OAK RIDGE NATIONAL LABORATORY LIBRARY
3 4456 0032500 2

US-Japan Workshop on 3-D MHD Studies

日米ワークショップ「三次元電磁流体力学シムレーションの研究」

MARCH 19-23, 1984
OAK RIDGE, TENNESSEE

QC
718.5
.M36
U48x
1984

Sponsored by

FUSION ENERGY DIVISION – OAK RIDGE NATIONAL LABORATORY

U. S. PROPERTY

QC
718.5.M36
U48X
1984

CONF-840370

PROCEEDINGS OF THE WORKSHOP

U.S.-JAPAN THEORY WORKSHOP ON 3-D MHD STUDIES

March 19-23, 1984

Oak Ridge, Tennessee

FUSION ENERGY DIVISION LIBRARY

B. A. Carreras, Editor

U.S.-Japan Exchange No. J-5

Sponsored by

OAK RIDGE NATIONAL LABORATORY
FUSION ENERGY DIVISION

Date Published May 1984

OAK RIDGE NATIONAL LABORATORY LIBRARY
3 4456 0032500 2

Sponsored by
U.S. Department of Energy
Office of Fusion Energy
Under Contract No. DE-AC05-840R21400
With Martin Marietta Energy Systems, Inc.

PREFACE

The US-Japan theory workshop on 3-D MHD studies was held at Oak Ridge, Tennessee on March 19-23, 1984. It was attended by 25 participants.

The main purpose of the workshop was to determine what important problems are ahead of us in 3-D MHD studies. In the meeting physics problems were addressed, as well as computational ones for different devices. The first day of the workshop was devoted to discussion of MHD equilibrium and stability issues related to stellarators. The MHD properties of RFP and compact torii were considered during the second day. Finally mirrors, EBT, and tokamaks were discussed on the last day of the workshop. The discussions were held in a very informal fashion, which allowed a frank and open exchange of views between the participants.

These proceedings include the manuscripts that were presented at the workshop. They cover most of the oral presentations and are organized in the way they were delivered. An attendance list, and the agenda are also included in the proceedings.

The Japanese delegation was led by Professor Tetsuya Sato of the Institute for Fusion Theory at Hiroshima. His cooperation in the organization of the workshop is gratefully acknowledged.

The workshop was sponsored by the Fusion Energy Division, Oak Ridge National Laboratory and could not have been successful without the efforts of many dedicated individuals - Session chairman, authors, participants, and last but not least, the workshop secretaries.

I would like to acknowledge special appreciation to: Janice Cox, who handled the problems of organization prior to the workshop in an efficient and professional manner; June Jernigan and Gladys Warren, who acted as workshop secretaries during the workshop, taking care of all the details and problems which normally are associated with such meetings in an excellent way. I am particularly grateful to June Jernigan and Gladys Warren for assembling the contributions of the proceedings, and handling much of the workshop paperwork.

Benjamin A. Carreras
Oak Ridge, Tennessee

CONTENTS

CALCULATION OF ISLAND WIDTHS IN THREE-DIMENSIONAL EQUILIBRIA
A. H. Reiman and A. H. Boozer..... 1

A 3D ALGORITHM FOR CALCULATING DRIFT ORBITS IN NONAXISYMMETRIC TOROIDAL DEVICES
K. Hanatani and K. Uo..... 7

EQUILIBRIUM STUDIES OF HELICAL AXIS STELLARATORS
T. C. Hender, B. A. Carreras, L. Garcia, J. H. Harris, J. A. Rome, J. L. Cantrell and V. E. Lynch..... 21

NON-LINEAR CALCULATIONS OF m = 1 INTERCHANGE MODE IN HELIOTRON E
M. Wakatani and H. Shirai..... 34

STELLARATOR EXPANSION STUDIES OF A HIGH-BETA TORSATRON
J. A. Holmes, B. A. Carreras, L. A. Charlton, H. R. Hicks and V. E. Lynch..... 42

REDUCED EQUATIONS IN THREE DIMENSIONAL GEOMETRY
M. S. Chu, T. H. Jensen, and J. S. Kim..... 58

THREE-DIMENSIONAL MHD IN THE REVERSED-FIELD PINCH
D. D. Schnack, D. C. Baxter, E. J. Caramana, R. A. Nebel, and R. A. Gerwin..... 68

NONLINEAR MHD SIMULATIONS OF THE SPHEROMAK AND THE REVERSED FIELD PINCH
A. A. Mirin, N. J. O'Neill, and A. G. Sgro..... 88

FINITE ELEMENT METHOD AND ITS APPLICATION TO 3D DYNAMIC SYSTEM
M. Aizawa and I. Kawakami..... 101

RAPIDLY CONVERGENT ALGORITHMS FOR 3-D TANDEM AND STELLARATOR EQUILIBRIA IN THE PARAXIAL APPROXIMATION
B. McNamara..... 113

MAGNETIC EQUILIBRIA FOR SQUARE AND CIRCULAR EBTs
C. L. Hedrick and L. W. Owen..... 126

THE TOTAL DEREDUCTION OF THE REDUCED EQUATIONS
R. Izzo, D. Monticello and J. DeLucia..... 138

3-D SIMULATIONS OF LIMITER STABILIZATION OF HIGH-BETA EXTERNAL KINK-TEARING MODES
J. K. Lee and N. Ohyabu..... 149

NONLINEAR EVOLUTION OF EXTERNAL KINK MODE IN TOKAMAK AND COMMENT ON RESISTIVE INTERNAL KINK MODE
T. Tsunematsu, G. Kurita, M. Azumi, T. Takizuka, and T. Takeda..... 158

CALCULATIONS IN TOROIDAL GEOMETRY WITH FULL M.H.D. EQUATIONS
L. A. Charlton, B. A. Carreras, J. A. Holmes, H. R. Hicks and V. E. Lynch..... 174

ATTENDANCE LIST..... 192

AGENDA..... 195

CALCULATION OF ISLAND WIDTHS IN THREE-DIMENSIONAL EQUILIBRIA

A. H. Reiman and A. H. Boozer
Plasma Physics Laboratory, Princeton University
P.O. Box 451
Princeton, New Jersey 08544

In three-dimensional MHD equilibria, pressure driven currents can resonate with rational surfaces in the plasma, producing magnetic islands and breaking up flux surfaces. This effect is of great practical importance for stellarators, where it gives an equilibrium β limit, and also limits the plasma aperture below that β limit. We have explored the physics of equilibrium island formation, and have obtained some estimates for island widths.[1] We have applied our theory to the Princeton heliac reference design.

Stellarator vacuum fields are constructed to have relatively good flux sufaces. The islands that exist are small relative to the minor radius. With finite β, the flux surfaces are shifted and distorted. It has been expected that the flux surfaces break up at some critical β. The convention has been to take the equilibrium β limit to be that value of β at which the magnetic axis shift equals half the minor radius. There have previously been no actual calculations of this β limit. In the following, we first describe our general analysis of island formation in three-dimensional equilibria, summarizing the general conclusions, and then detailing some of the mathematics by which we arrive at the conclusions. We finally apply the analysis to the particular example of the heliac device studied at Princeton.

For purposes of orientation, we contrast our picture of equilibrium island formation with the familiar picture of island formation in tokamaks. In tokamaks, the appearance of islands is usually due to symmetry breaking tearing instabilities, although it can also be caused by nonaxisymmetruc field errors. For nearly circular flux surfaces, the island width is proportional to the square root of the resonant fourier component of the radial magnetic field, B_{rmn}. This component is resonant in the sense that $n = \omega m$, where $\omega = 1/q$ is the rotational transform.

For the three-dimensional equilibria we are interested in, the geometry is considerably more complicated. The island width is now proportional to the square root of the resonant component of $B \cdot \nabla\psi$, as determined in an appropriate coordinate system (ψ, θ, ϕ). The island arises through the equilibrium equation, and is intrinsic to the equilibrium itself.

For an equilibrium with small islands, it is natural to use nearby flux coordinates, obtained by interpolating across the islands. The nearby ψ

coordinate is to coincide with the flux surfaces, except in the immediate vicinity of an island. The nearby flux coordinates define a magnetic field with good surfaces. The difference between this field and the exact field is small, relative to the magnitude of the exact field. This small difference is important, of course, because it contains all the information about the island structure. The nearby flux surfaces are not uniquely determined by the exact field, but this nonuniqueness is unimportant as long as the island widths are small.

The resonant component of the field is generated by a resonant component in the current. The resonant current is driven by the pressure, through the equilibrium equation

$$\nabla p = \underset{\sim}{j} \times \underset{\sim}{B} \quad , \tag{1}$$

due to a resonant term in the Jacobian, J. Here J is the Jacobian of the transformation from Cartesian coordinates to (ψ, θ, ϕ). It describes the geometry of the flux surfaces. The resonant term in the Jacobian, J_{nm}, corresponds to a resonant rippling of the flux surfaces. As β increases, the resonant current increases due to the direct dependence on β which comes from the ∇p term in Eq. (1), and also due to the dependence of J_{nm} on β.

The spectrum of the vacuum Jacobian typically has peaks at a few low values of m, n, and decays exponentially with increasing m, n. There is a peak at m = 1, n = 0, due to the toroidal curvature. For a helical axis stellarator there is a peak at m = 1 and n equal to the number of periods, due to the helical curvature. In addition, there are nonresonant terms with $m > 2$ which determine the shape of the flux surfaces. The resonant terms, with $\bar{n} = \omega m$, lie in the exponential tail of the spectrum.

Finite β gives a shift and distortion of the flux surfaces. The corresponding nonlinear coupling of the fourier components of the Jacobian gives a broadening of the fourier spectrum. The fourier amplitudes in the tail of the spectrum increase. In particular, the resonant component also increases.

The magnetic islands are intrinsic to the MHD equilibrium solution. When β is sufficiently large that the islands overlap, the flux surfaces are destroyed, and there is no equilibrium solution.

Now we present some of the mathematics by which we arrived at these conclusions. We rewrite Eq. (1) as the two equations

$$\underset{\sim}{j}_{\perp} = \underset{\sim}{B} \times \nabla p / B^2 \quad , \tag{2}$$

and

$$\underset{\sim}{B} \cdot \nabla(j_{\parallel}/B) = -\nabla \cdot \underset{\sim}{j}_{\perp} \quad . \tag{3}$$

To determine the integration constant for Eq. (3) we take the equilibrium to have zero net current inside each flux surface. This is appropriate for stellarator fields.

To solve the equations, we use an iterative method. To lowest order, we take $\underset{\sim}{B}$ equal to the vacuum field, with p constant on the vacuum flux surfaces. Equations (2) and (3) then give the lowest order plasma current. The lowest order correction to the field is determined by Ampere's law. To iterate, the corrected field is substituted back into Eqs. (2) and (3). We must go to second order in this iteration procedure to see all the physics we have previously described.

All results are expressed in terms of the fourier decomposition of the Jacobian,

$$J = J_o\left(1 + \sum_{n,m}{}' \delta_{nm} \cos(n\phi - m\theta)\right) \quad , \tag{4}$$

where the prime indicates that the n = 0, m = 0 term is omitted from the sum. In particular the solution for $\underset{\sim}{j}$ is,

$$\underset{\sim}{j} = J_o \frac{dp}{d\phi} \left[\nabla\phi \times \nabla\psi + \sum_{nm}{}' \frac{\delta_{nm}}{n-\omega m} \cos(n\phi - m\theta) \nabla\phi \times (m\nabla\theta - n\nabla\phi)\right] \quad . \tag{5}$$

At those rational surfaces where $n = \omega m$ and $\delta_{nm} \neq 0$, islands will form, so that $dp/d\psi = 0$ there.

The self-consistent set of equations is completed by Ampere's law,

$$\nabla \times \underset{\sim}{B} = \underset{\sim}{j} \quad . \tag{6}$$

One particular solution of Eq. (6) is

$$\underset{\sim}{H} = \left(\int_{\psi}^{\psi_a} J_o \frac{dp}{d\psi} d\psi\right)\nabla\phi + \left[J_o \frac{dp}{d\psi} \sum_{nm}{}' \frac{\delta_{nm}}{n-\omega m} \sin(n\phi - m\theta)\right]\nabla\psi \quad .$$

This has $\nabla \cdot \underset{\sim}{H} \neq 0$. The general solution to Eq. (6) can be written

$$\underset{\sim}{B} = \underset{\sim}{H} + \nabla F \quad , \tag{8}$$

with

$$\nabla^2 F = -\nabla \cdot \underset{\sim}{H} \quad . \tag{9}$$

We solve Eq. (9) by an expansion about the magnetic axis. To simplify further, we take the ellipticity of the flux surfaces to be small. We work in a helical coordinate system, first introduced by Mercier,[2] for which one of the coordinate axes coincides with the magnetic axis. Expressing the flux coordinates in terms of Mercier's coordinates, we get an inhomogeneous Bessel's equation for F. To make life easy, we take n/m small compared to the aspect ratio, so that the Bessel functions can be expanded.

To calculate the field explicitly, we need to specify a pressure profile. Taking a quadratic profile, we find the resonant correction to the field,

$$\frac{B_{1\rho nm}}{B_o} \simeq \beta \frac{L}{4\pi a^2} \delta_{nm} \left[\ln\left(\frac{a-\rho_o}{\rho_o}\right) + \sum_{j=1}^{2n+1} \frac{1}{j} + \frac{a}{\rho_o} \right] , \tag{10}$$

where L is the length of the magnetic axis, a is the minor radius, and ρ_o corresponds to the rational surface.

The resonant field given by Eq. (10) is proportional to the resonant fourier amplitude of the vacuum Jacobian. We have not yet obtained the broadening of the fourier spectrum. This appears in the next order.

In the next order, we need the nearby flux coordinates for the corrected field. The new flux coordinates are determined by

$$\left(\underset{\sim}{B}_v + \underset{\sim}{B}_1\right) \cdot \nabla\phi = 0 \tag{11}$$

and

$$\left(\underset{\sim}{B}_v + \underset{\sim}{B}_1\right) \cdot \nabla\theta = \left(\underset{\sim}{B}_v + \underset{\sim}{B}_1\right) \cdot \nabla\phi \quad , \tag{12}$$

where $\underset{\sim}{B}_v$ is the vacuum field and $\underset{\sim}{B}_1$ is the nonresonant part of the lowest order correction. We fourier decompose the difference between the old and new coordinates, and substitute into Eqs. (11) and (12), to obtain explicit expressions for the new coordinates in terms of the old.

The Jacobian is now reexpressed in terms of the new coordinates. To see what this looks like, we consider the case where only δ^v_{01} and δ^v_{N1} are nonzero for the vacuum Jacobian, where N is the number of periods. The fourier amplitudes of the Jacobian are then

$$\delta_{nm} \simeq \frac{1}{3}(2+m) \left[\delta^v_{01} J_{n/N}(\hat{\theta}_{N1}) J_{m-n/N-1}(\hat{\theta}_{01}) + \delta^v_{N1} J_{n/N-1}(\hat{\theta}_{N1}) J_{-m-n/N}(\hat{\theta}_{01}) \right]$$
$$+ \frac{1}{3}(2-m) \left[\delta^v_{01} J_{-n/N}(\hat{\theta}_{N1}) J_{-m+n/N-1}(\hat{\theta}_{01}) + \delta^v_{N1} J_{-n/N-1}(\hat{\theta}_{N1}) J_{-m+n/N}(\hat{\theta}_{01}) \right] ,$$

where the J's here are Bessel functions. This is probably not accurate for n or m large. Although the vacuum Jacobian has no resonant terms, the finite β Jacobian resonates with every rational surface.

Now we apply our analysis to the Heliac reference design. Here we are most concerned with the neighborhood of the magnetic axis, where $\omega \approx 1.5$, or $\omega/N \approx 0.5$. We cannot use our analysis directly, because $d\omega/d\rho$ vanishes at the axis. It is straightforward to modify all the formulas appropriately.

We obtain the δ^v_{nm}'s from a numerical fourier decomposition of the vacuum field.[3] To get a rough idea of the equilibrium β limit, we calculate the β at which our formulas predict an island width equal to half the minor radius of the plasma. For the direct resonance, due to the resonant fourier amplitude of the vacuum Jacobian, we get $\beta \approx 0.3\%$. This may be remedied by adjusting the tilt of the coils. The nonlinear resonance gives $\beta \approx 1.6\%$. This is not as easily remedied, coming from a coupling of the helical and toroidal curvature.

In the general design of stellarator vacuum fields, we might have expected the requirement of good vacuum flux surfaces to suppress the resonant field amplitudes. Our calculation for the heliac reference design shows that the amplitudes of the direct resonances may nonetheless be unacceptably large. We conclude that it is necessary to incorporate the constraints on the resonant δ^v_{nm} directly in the design procedure. Our application also shows that coupling of nonresonant components can give large islands, even for values of β at which the axis shift is small relative to the minor radius.

Our approximations have allowed us to obtain analytic estimates of island widths, for the direct resonances and for low n, m nonlinear resonances. Our simplifying approximations have also allowed us to explore and clarify the basic physics of island formation and surface destruction in three-dimensional equilibria. Clearly, the theory we have presented can be used do more accurate calculations, both analytically and using numerical methods. An extension of the calculation to higher order in β would allow the determination of island widths for higher m, n, and give a more complete description of the equilibrium β limit.

ACKNOWLEDGMENT

This work supported by U.S. Department of Energy Contract No. DE-AC02-76-CHO-3073.

We are grateful to H. Mynick for valuable comments and discussions.

REFERENCES

1. A. H. Reiman and A. H. Boozer, Princeton Plasma Physics Laboratory Report No. PPPL-2062 (November 1983).
2. C. Mercier, Lectures in Plasma Physics (Commission of the European Communities, Luxembourg, 1974), p. 74.
3. A. Ehrhardt, private communication.

A 3D Algorithm for Calculating Drift Orbits in Nonaxisymmetric Toroidal Devices

K. Hanatani and K. Uo

Plasma Physics Laboratory, Kyoto University
Gokasho, Uji, Kyoto, JAPAN

ABSTRACT

A three-dimensional (3D) interpolation technique for computing guiding-center drift orbits in nonaxisymmetric toroidal magnetic devices is described. The new technique, named "two-level interpolation scheme", uses a simple algorithm which splits given field quantities into symmetric (2D) and asymmetric (3D) parts. The interpolation scheme allows a fast and accurate drift orbits computation and also provides a direct means to examine the effects of symmetry-breaking perturbation as a part of the numerical procedure. The technique has been applied to study the toroidal drift of the particles in a vacuum heliotron field. It was found that the asymmetric part of the drift shows a vortex structure and this vortex reduces the net vertical drift in the peripheral region of the magnetic surface. A strong reduction in the net vertical drift occurs even near the magnetic axis when the magnetic axis is shifted inward by applying vertical field. The presence of the drift vortex is attributed to the absence of toroidal field coils in the heliotron field studied. An implication of the drift vortex on the diffusive and nondiffusive particle losses from the heliotron plasma is also commented.

INTRODUCTION

Lack of ignorable coordinate in stellarator and heliotron[1] implies that one must resort to 3D numerical techniques to examine the drift orbits. It also implies that the techniques must be fast and accurate to be useful in applications. Unfortunately, methods easy to implement do not simultaneously meet these requirements: Simplified analytic models may be inaccurate in the field modeling though they are time-saving. Conversely, integration of the Biot-Savart law is time-consuming though it is accurate. More advanced techniques, which are capable of achieving efficient drift orbit computation in the stellarator fields without sacrificing the reality in the modeling, have

been developed by several authors[2,3,4,5]. This paper proposes another simple technique which not only allows a fast and accurate drift orbit computation but also clarifies the effects of the symmetry-breaking perturbation on the drift orbits.

GUIDING CENTER EQUATION

A set of guiding-center drift equations which includes usual gradient and curvature drifts is used to track the charged particle orbits.

$$\frac{d\vec{x}}{dt} = v_{\parallel} \frac{\vec{B}}{B} + \vec{V}_D \tag{1a}$$

$$\frac{dv_{\parallel}}{dt} = - \frac{\mu}{m} H(\vec{x}) \tag{1b}$$

where

$$\vec{V}_D = \frac{v^2}{2\ \Omega_0\ R_0} (1 + \lambda^2) \vec{G}(\vec{x}) \tag{2a}$$

$$\vec{G}(\vec{x}) = B_0\ R_0 \frac{\vec{B} \times \nabla B}{B^3} \tag{2b}$$

$$H(\vec{x}) = \frac{\vec{B}}{B} \cdot \nabla B \tag{2c}$$

Here, λ (= $v_{\parallel}/v$) is the pitch of the particle, Ω_0 (= qB_0/m) denotes the cyclotron frequency, and μ (= $mv_{\perp}^2/2B$) denotes the magnetic moment which is assumed to be an adiabatic invariant. The velocities $v_{\parallel}$, $v_{\perp}$ and $v = (v_{\parallel}^2 + v_{\perp}^2)^{1/2}$ are the parallel, perpendicular and the total velocities of the guiding center. A nondimensional vector $\vec{G}(\vec{x})$ is a geometry-dependent (or particle-independent) part of the drift velocity $\vec{V}_D$; a scalar function $H(\vec{x})$ is the derivative of B in the direction of $\vec{B}/B$. We regard the drift $\vec{G}(\vec{x})$ and the derivative $H(\vec{x})$ as the field quantities (like the magnetic field $\vec{B}$) filling the whole space.

MAGNETIC FIELD GEOMETRY

The magnetic field model used to validate the new interpolation scheme is that of vacuum magnetic field produced by filamentary external helical windings. Integration of the Biot-Savart law provides the magnetic field quantities $\vec{B}$, $\vec{G}$ and H. In toroidal geometry, the most convenient way to specify the winding law is with quasi-toroidal coordinates (r, θ , ϕ). The heliotron winding (R_0; major radius, a; minor radius, L; pitch length) of multiplicity ℓ is simply defined by $\theta = \kappa\phi$, where $\kappa = 2\pi R_0/L$ is the twist number of the helical winding. The number of the field periods around the torus is then given by $\kappa\ell$. Besides the helical field (HF) windings, the heliotron configuration requires vertical field (VF) coils and allows, in general, toroidal field (TF) coils. The VF coils compensate the average vertical field produced by the HF coil. The VF coils also control the horizontal position of the magnetic axis.

THE INTERPOLATION METHOD

we propose here a two-level interpolation technique to speed up the drift orbit computations in the toroidal helical devices. Unlike conventional 3D interpolations, this technique makes full use of symmetry to evaluate asymmetric quantities. Basic idea is to decompose all relevant physical quantities into symmetric and asymmetric parts, both of which are more manageable than the original ones. Let P denote the helically symmetric part of any quantity Q. We then express Q as a sum of the principal part P and a residual part R:

any Quantity		Principal part		Residual part	
Q	=	P	+	R	(3)
(r, θ , ϕ)		(r, $\theta - \kappa\phi$)		(r, θ , ϕ)	
3D		2D		3D	

The principal part P is the dominant, symmetric part while the residual part R is the small asymmetric part. To evaluate the field quantity Q as the function of position, we interpolate P and R separately rather than interpolating Q itself. It must be emphasized that the right hand side of expression (3) is not an approximate expansion of the left hand side but a closed decomposition of Q as it literally means.

To evaluate the symmetric part P, one can use either analytic or numerical representation for Q in the equivalent, straight helically symmetric system. The analytical representation can be given by a series of modified Bessel functions; the numerical solution can be obtained by integrating the Biot-Savart law for infinitely long straight helical winding. In practice, however, we have not found them necessary. To obtain the desired representation for P, we simply extract the helically invariant components from the field quantity Q given in the finite aspect-ratio toroidal configuration. Here quantities that depend only on r and ζ (= $\theta - \kappa\phi$) are considered to be helically invariant. This extraction can be made by averaging the quantity Q "helically" over $2\pi/\kappa$,

$$P(r,\zeta) = \frac{\kappa}{2\pi}\int_0^{2\pi/\kappa} Q(r, \zeta + \kappa\phi, \phi)\, d\phi , \tag{4}$$

just as the calculation of zero order Fourier coefficient. Recently and independently, an averaging similar to (4) was used[6] to eliminate magnetic islands and stochasticity in a nonaxisymmetric vacuum 3D field. Once P is obtained, R can be calculated by Eq.(3). Untill now, notations Q, P and R are used only symbolically. In the following, Q, P and R actually represent the three components of $\vec{B}$, the three components of the nondimensional drift $\vec{G}$, and the directional derivative H that are necessary to solve the drift equation (1). From Eq.(3) one has

$$\begin{aligned} \vec{B}(\vec{x}) &= \vec{B}^{(0)} + \vec{B}^{(1)} , \\ \vec{G}(\vec{x}) &= \vec{G}^{(0)} + \vec{G}^{(1)} , \\ H(\vec{x}) &= H^{(0)} + H^{(1)} , \end{aligned} \tag{5}$$

where super-scripts (0) and (1) denote the symmetric and the asymmetric parts. In addition to $\vec{B}$, $\vec{G}$ and H, the decomposition can be applied to other quantities if necessary.

Above decomposition has a number of new advantages over standard methods. First of all, it allows us to investigate how and to what extent the symmetry-breaking perturbation affects the drift orbits. By directly examining the distribution of the residual parts, we may have clearer insight into the underlying orbit physics than by examining the integrated trajectory itself in full nonaxisymmetric complexity. We can also calculate drift surfaces in the corresponding, straight, helically symmetric system by artificially eliminating all the asymmetric parts from the drift equations(i.e., R = 0) and from the metric of the coordinates. This option permits us a close comparison between the unperturbed (2D) and the perturbed (3D) drift orbits. By this comparison, we can investigate the departure from the helical symmetry.

Secondly, the decomposition allows us to develop a simple and efficient computational scheme. The essential point is to choose suitable, different, interpolating formulas for P and R according to their relative importance and to the number of their dimensions. Although the original quantity Q is 3D, the principal part P reduces to 2D owing to the helical symmetry. Two-dimensional interpolations are, of course, much easier to implement, faster to execute and require less storage than 3D interpolations. We can, therefore, calculate the principal part P easily and quickly either by using bicubic spline with moderate mesh size or by using bilinear interpolation with finer mesh size. On the other hand, the residual part R is still 3D. The magnitude of this part is, however, typically by one order (a/R_0) smaller than that of the principal part P. We, therefore, need not use the same-accuracy formula as that used for the principal part, and a rough trilinear interpolation formula with coarse grids may be accurate enough. A volume-weighting method in the toroidal coordinates was used for this trilinear interpolation. Again, we can calculate the residual part R easily and quickly. Thus, we can handle both of the decomposed parts, P and R, in a more physically meaningful and numerically economical way than directly handle the original quantity Q.

The accuracy of the two-level interpolation scheme was tested by comparing the interpolated result with that of the direct calculation (the Biot-Savart law). We interpolate not only $\vec{B}$ but also $\vec{G}(\vec{x})$ and $H(\vec{x})$ in order to avoid the difference approximation in $\vec{B} \times \nabla B$ and $\vec{B} \cdot \nabla B$. The accuracy of $\vec{V}_D$ is, therefore, of the same order of that of $\vec{B}$. The convergence of the two-level scheme is faster than that of "single-level" trilinear interpolation. A possible weakness of the two-level scheme is that it may not work very efficiently in completely asymmetric fields. If the level of asymmetry is too strong, the magnitude of the residual part R becomes comparable to (or even greater than) that of the principal part P. In this extreme limit, the accuracy of the two-level scheme degrades to that of usual trilinear interpolation. Fortunately, however, many asymmetric magnetic confinement devices of practical importance such as stellarators and bumpy tori do have their neighboring symmetry and the levels of their asymmetry are usually weak or at most moderate.

We have compared the computing speed of two-level interpolation scheme with that of the direct calculation to estimate the figure of merit factor of the interpolation scheme. We compared the CPU times of the direct and the interpolation methods spent for one evaluation of the field quantities. As a reference, we also measured the CPU time of the single-level trilinear interpolation, which should give a minimum executing time of any interpolation methods. The comparison was made on FACOM/M-200 computer. The two-level scheme was faster than the direct method by more than two orders of magnitude, and it was slower than the single-level interpolation only about 30%.

APPLICATION

Let us apply the decomposition procedure to Heliotron E (see Fig.1) and to examine the effect of toroidal perturbation on the drift $\vec{V}_D$. From Eq.(2a), the normalized drift $\vec{G}(\vec{x})$ can be written as follows:

$$\vec{G}(\vec{x}) = \vec{G}^{(0)} + \vec{G}^{(1)} = \frac{\vec{V}_D}{U_{tor}} \tag{6}$$

$$U_{tor} = \frac{v^2}{2\ \Omega_0\ R_0} (1 + \lambda^2) \tag{7}$$

where $\vec{G}^{(0)}$ and $\vec{G}^{(1)}$ are the principal (symmetric) and the residual (asymmetric) parts of $\vec{G}(\vec{x})$. The characteristic velocity, U_{tor}, is the so-called "toroidal drift" velocity. If the magnetic field is produced only by a toroidal solenoid (TF coils), then $\vec{G}^{(0)}$ reduces to a zero vector and $\vec{G}^{(1)}$ reduces to a unit vertical vector $\hat{z}$. Accordingly, the drift velocity $\vec{V}_D$ reduces to a vertical drift $U_{tor}\ \hat{z}$.

The origin of the asymmetric drift, $\vec{G}^{(1)}$, in heliotron is different from that both of tokamaks and classical stellarators. In the latter two configurations, dominant contribution to $\vec{G}^{(1)}$ originates from the curvature and gradient of the toroidal field component B_t, which is produced by TF coils (toroidal solenoid). In heliotron, by contrast, $\vec{G}^{(1)}$ originates from the toroidal bending of the <u>helical winding</u>. Note that in heliotron both poloidal B_p and toroidal B_t field components can be produced by a single set of helical winding. The TF coils are dispensable or (at most) of secondary importance in the heliotron concept. For this reason, the perturbed drift, $\vec{G}^{(1)}$, in the heliotron need not be identical with those of tokamaks and classical stellarators.

A unique capability of the two-level interpolation scheme is that it allows us to visualize the "drift vector field" of the helically symmetric and the toroidally perturbing drifts, $\vec{G}^{(0)}$ and $\vec{G}^{(1)}$, part by part. Figure 2 shows the arrow map of the helically symmetric drift of Heliotron E. An interesting finding in the toroidal heliotron is a vortex structure in the perturbed drift, $\vec{G}^{(1)}$. In Fig. 3-(a),(b) and (c), the arrow map of the perturbed drift, $\vec{G}^{(1)}$, is similar to the toroidal drift , $U_{tor}\hat{z}$, near the minor axis. It is, however, substantially modified in the outer region of the magnetic surface and completely different in the separatrix region from $U_{tor}\hat{z}$ of simple toroidal solenoid. In particular, the drift $\vec{G}^{(1)}$ shows the vortex-like structure. The center of this "drift vortex" is located at the peripheral region of the magnetic surface. As a reference, arrow map of the toroidal solenoid is shown in Fig.4.

The numerical finding of the drift vortex prompts us to reconsider a question: what is the "toroidal drift" in nonaxisymmetric devices. To answer this question, we have examined the distribution of the perturbed drift $\vec{G}^{(1)}$ along the field line and along the drift orbit. Figure 5 shows the time variation of the unperturbed and the perturbed drift along the trajectory of a passing particle in the heliotron. The helically symmetric part, $\vec{G}^{(0)}$, asymmetric part and, $\vec{G}^{(1)}$, are clearly separated. we have averaged the vertical and horizontal components of the symmetric $\vec{G}^{(0)}$ and the asymmetric $\vec{G}^{(1)}$ parts along the field lines and along the drift orbits. The average was carried out along the line of force over 10 toroidal revolution around the torus. It was found that the net vertical drift resulting from the toroidal perturbation, $\vec{G}^{(1)} \cdot \hat{z}$, in the heliotron field is appreciably smaller than that expected from the geometric aspect ratio R_0/a of the device. This reduction is restricted in the peripheral region of the magnetic surface when the magnetic axis is centered on the minor axis. Effects of the VF coil field on the averaged vertical drift are also examined. When we shift the magnetic axis inward by the VF coils, a strong reduction (factor of two) in the vertical drift was obtained even near the magnetic axis (see Fig.6). This type of configuration was previously studied and referred to a "reduced Q" configuration[7].

These results indicate that the aspect ratio is effectively enhanced for the charged particles moving in the Heliotron E plasma. It must be emphasized that this enhancement of the aspect ratio is achieved not by introducing auxiliary coils (and hence extra complexity) into the system but by simply removing the TF coils from the system. When we increased the TF coil field in the calculation, the perturbed vertical drift approached to that of toroidal solenoid field as expected. We consider that the finding of the drift vortex is a good example illustrating a possibility of the optimization of field configuration. Since the reduction of the vertical drift are obtained even in a simplest combination of the helical winding and VF coils, one can expect further optimization of the drift by modifying the external coil system.

SUMMARY

We have outlined here a simple interpolation algorithm which enables us to develop an efficient 3D field line and drift orbit following code. This algorithm splits given field quantities into the symmetric and the residual parts and, therefore, is particularly powerful to evaluate asymmetric fields. Using this code (ATLAS), we have investigated the effects of the toroidal perturbation on drift orbits in the heliotron field, and found a vortex structure in the perturbed drift velocity. Such a "drift vortex" is that can not be expected from the usual toroidal drift in torus geometries. The presence of the drift vortex implies that the vertical drift of the particle in the heliotron plasma is substantially reduced than that frequently assumed in simplified analytical models for tokamaks and stellarators. This reduction in the vertical drift is important because it may reduces both diffusive and non-diffusive losses of the charged particles from the heliotron plasma.

So far, the two-level interpolation scheme has been applied only to the calculation of magnetic surfaces and drift orbits in the vacuum heliotron fields produced by filamentary helical windings. The ATLAS code can be a useful tool in investigating drift orbit related phenomena in nonaxisymmetric devices such as the calculation of velocity space loss region, neoclassical transport of thermal ions, slowing-down process of fast ions, and drift optimization of field configuration. The philosophy and the technique proposed here, however, may be equally applicable to wider classes of problems arising in various types of asymmetric 3D fields. Any magnetic fields obtained by other approaches than the Biot-Savart law that can provide reasonably accurate B and grad-B on the 3D grid points can be used as the input of the present decomposion procedure. For example, the scheme is in principle applicable to finite beta 3D equilibria by using the output of 3D MHD equilibrium codes. Incorporation with existing Monte-Carlo scattering algorithm and the inclusion of the electric filed remain the subjects of future studies.

REFERENCES

(1) K.Uo, Plasma Phys. 13 (1971) 243.

(2) G.Kuo-Petravic, A.H.Boozer, J.A.Rome and R.H.Fowler, Journal of computational physics 51 (1983) 261.

(3) W.Dommaschk, Z. Naturforsch 36a, 251 (1981).

(4) C.Gourdon, G.Lemarie, F.Roche, J.L.Soule, "Un Programme optimise de Calculs numeriques dans les configurations magnetiques toroidales" Rep. EUR-CEA-FC-449 (1968).

(5) R.E.Potok, P.A.Politzer and L.M.Lidsky, Phys. Rev. Lett. 45 1328 (1980). See also PFC/PR-80-15 (1980).

(6) J.R.Cary, Phys. of Fluids 27 (1984) 119.

(7) W VII-A Team and W.Lotz, presented by F.Rau, "On Toroidal Vacuum Fields and Particle Orbits in Modified Stellarator and Torsatrons" 9th Europ. Conf. on Contr. Fusion and Plasma Physics, Oxford Sept. (1979)

FIGURE CAPTIONS

Figure 1. the magnetic surface of Heliotron E (2π a/L = 1.4; R_0/a = 2.2/0.3). Field line tracing was carried out by the two-level interpolation scheme.

Figure 2. arrow map of helically symmetric drift $\vec{G}^{(0)}$. Note that the scale of the arrow length is different from that in figure (3),(4) and (6).

Figure 3. arrow map of asymmetric drift $\vec{G}^{(1)}$ at three different toroidal position (a),(b),(c).

Figure 4. drift arrow map of a reference tokamak (toroidal solenoid).

Figure 5. time evolution of vertical drift along the passing particle. Dots represent the helically symmetric part; solid line represents the asymmetric part.

Figure 6. arrow map of the asymmetric drift $\vec{G}^{(1)}$ in the case with increased (by 25%) vertical field. The magnetic surface is also shown.

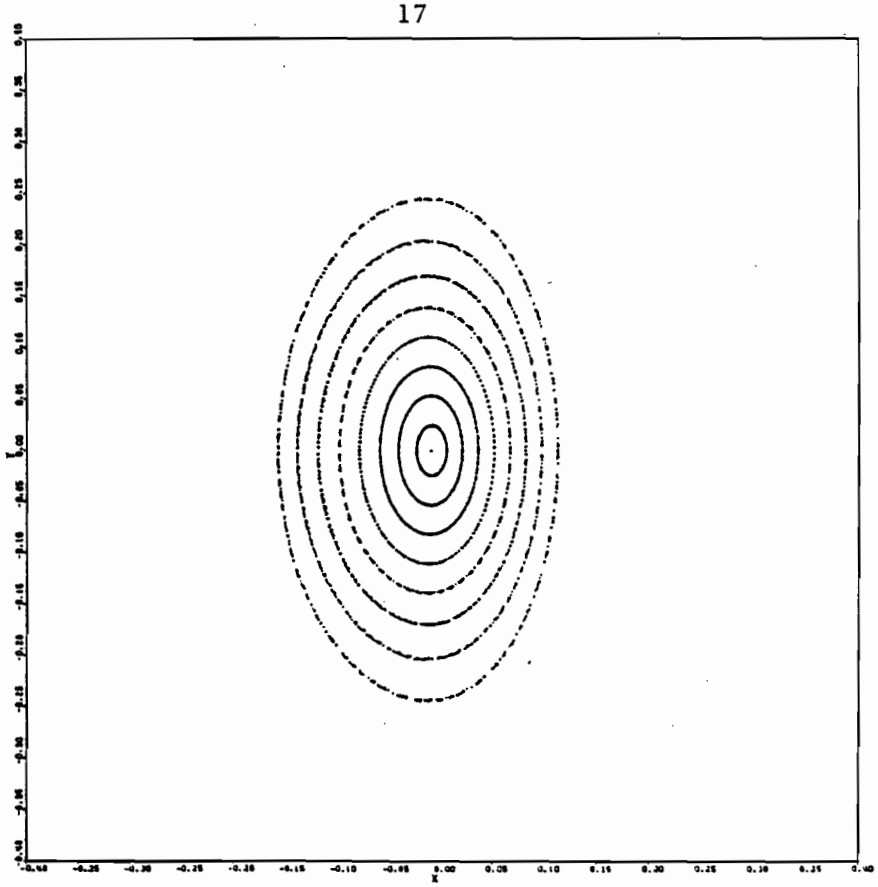

Figure 1.

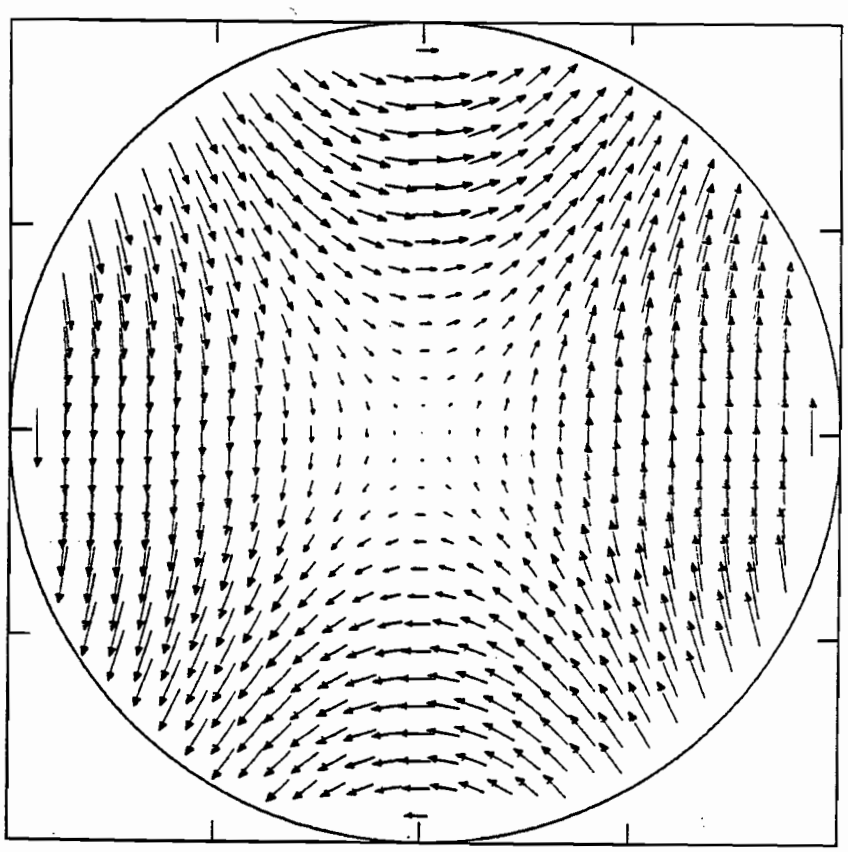

Figure 2.

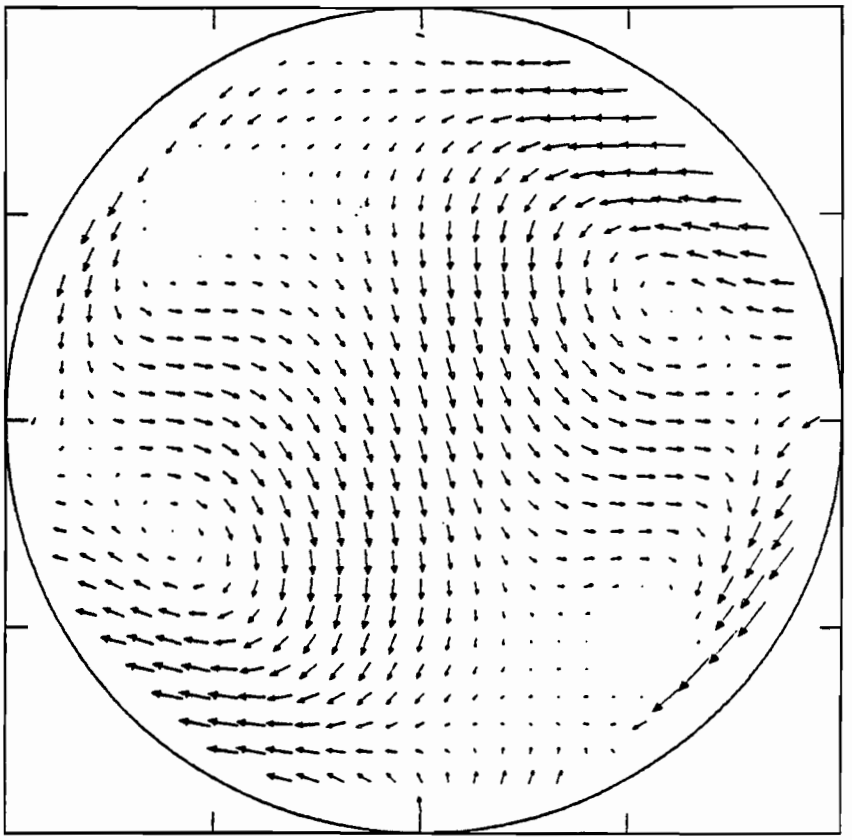

Figure 3-(a).

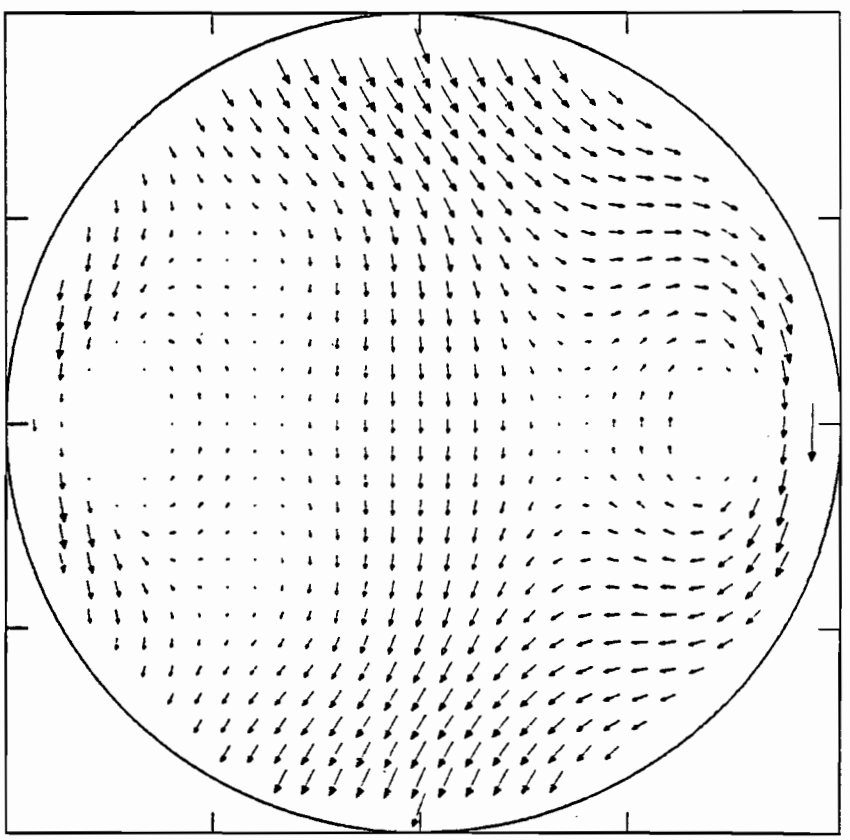

Figure 3-(b).

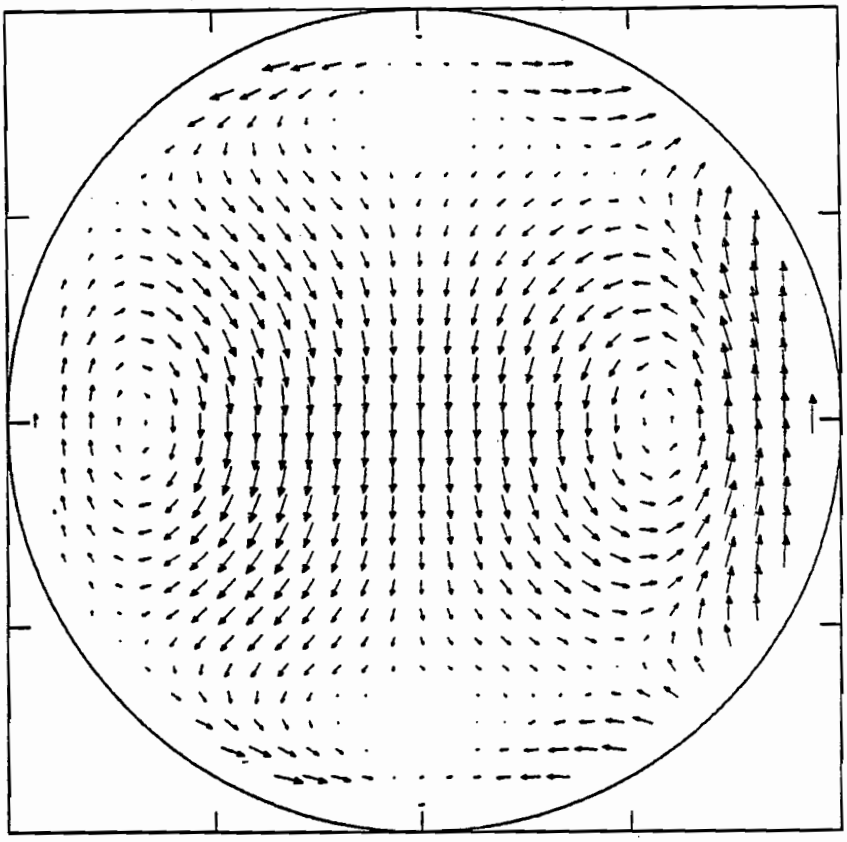

Figure 3-(c).

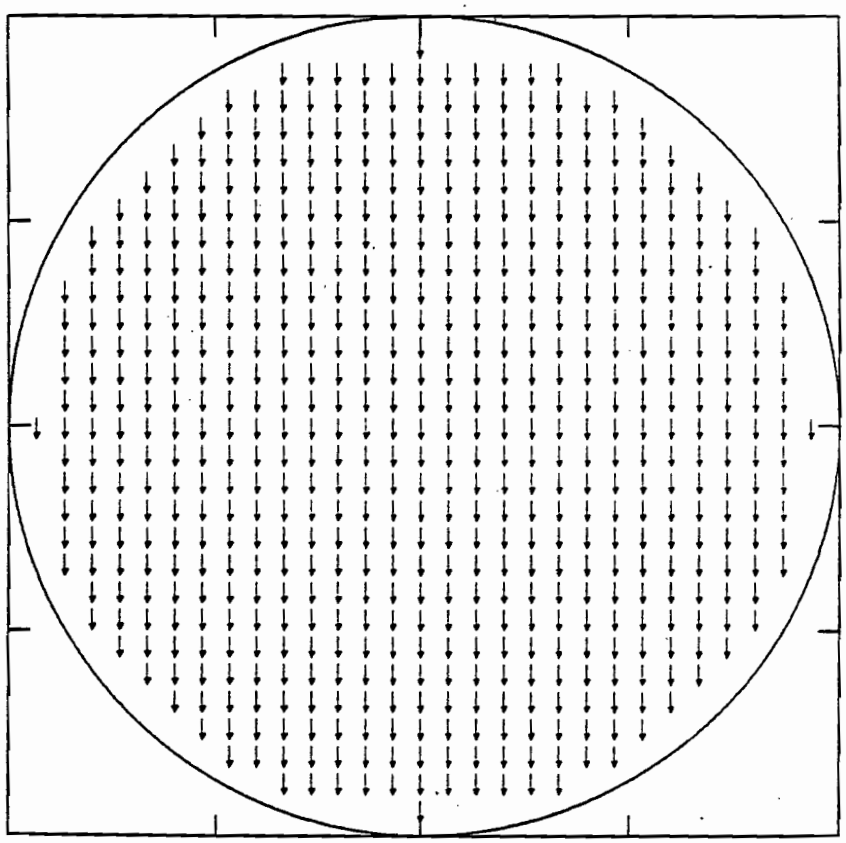

Figure 4.

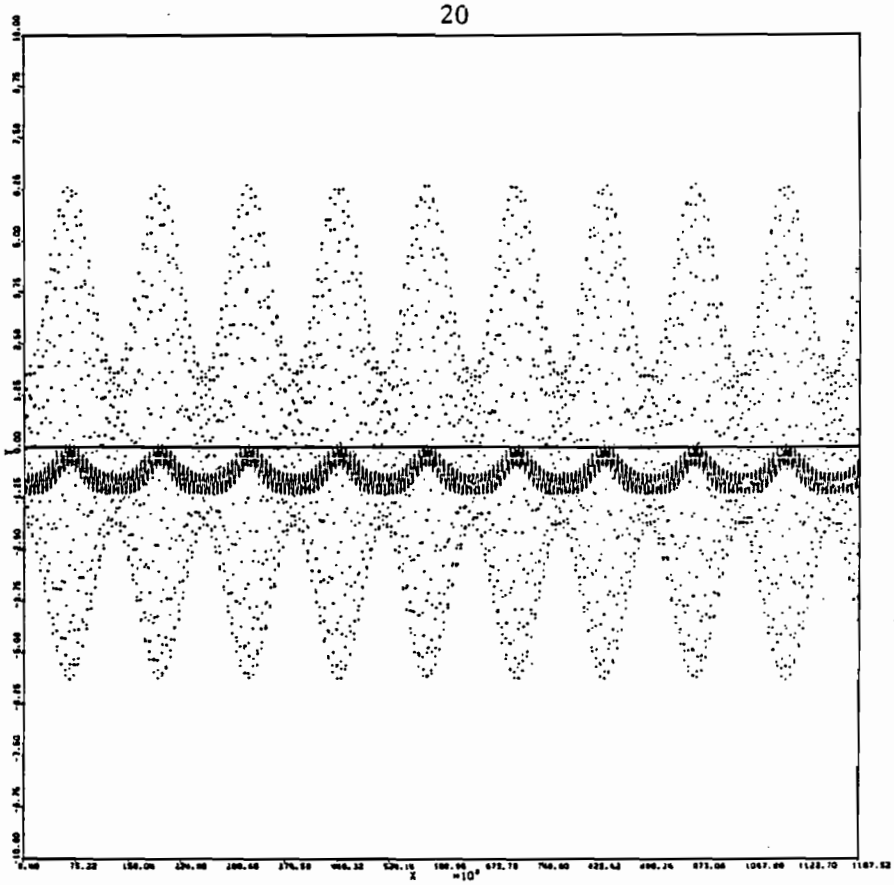

Figure 5.

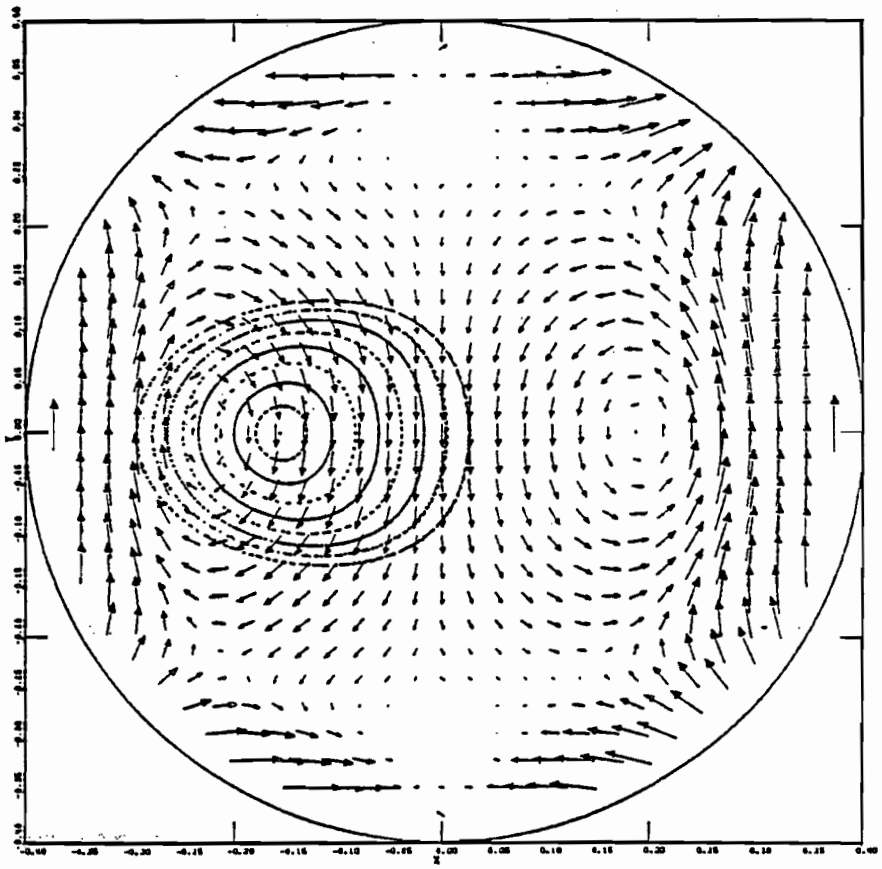

Figure 6.

By acceptance of this article, the publisher or recipient acknowledges the U.S. Government's right to retain a nonexclusive, royalty-free license in and to any copyright covering the article.

EQUILIBRIUM STUDIES OF HELICAL AXIS STELLARATORS*

T. C. Hender, B. A. Carreras, L. Garcia, J. H. Harris, J. A. Rome
Oak Ridge National Laboratory
Oak Ridge, Tennessee 37831

J. L. Cantrell and V. E. Lynch
Computer Science Division
Union Carbide Nuclear Division
Oak Ridge National Laboratory
Oak Ridge, Tennessee 37831

ABSTRACT

The equilibrium properties of helical axis stellarators are studied with a 3-D equilibrium code and with an average method (2-D). The helical axis ATF is shown to have a toroidally dominated equilibrium shift and good equilibria up to at least 10% peak beta. Low aspect ratio heliacs, with relatively large toroidal shifts, are shown to have low equilibrium beta limits (~5%). Increasing the aspect ratio and number of field periods proportionally is found to improve the equilibrium beta limit. Alternatively, increasing the number of field periods at fixed aspect ratio which raises ι and lowers the toroidal shift improves the equilibrium beta limit.

*Research sponsored by the Office of Fusion Energy, U.S. Department of Energy, under Contract No. W-7405-eng-26 with the Union Carbide Corporation.

1. Introduction

In this paper, the equilibrium properties of several types of helical axis stellarators will be studied. Previous stability studies of the heliac concept have shown the expectation of high β limits. In particular, detailed stability studies in the infinite aspect ratio, helically symmetric limit show favorable stability properties for "bean" shaped heliacs.[1] The equilibrium results given in this paper will focus on the finite aspect ratio regime where there is an interplay between toroidal and helical curvature effects. Studies by Reiman and Boozer indicate that such interactions may lead to island formation and flux surface destruction.[2]

The equilibrium properties of three types of helical axis device will be studied:

1) The helical axis ATF,[3] which is formed by imbalancing the currents in the helical windings of the ATF device.
2) Heliacs of the type studied at PPPL,[4] in which a set of toroidal field coils spiral about an interlocking, toroidally directed ring [Fig. 1(a)]. A large sequence of such heliacs, with varying helical and toroidal curvatures will be studied.
3) Helical axis stellarators formed by non-interlocking toroidal field coils. In particular, a system in which the axis of the coils defines a geodesic on a torus will be studied [Fig. 1(b)].

The above configurations have been studied with the 3-D equilibrium code NEAR, and also using an average method, which is applicable to helical axis systems. Details of these methods will be given in the next section and results of the calculations will be presented in Sec. 3.

2. Numerical and Semi-Analytic Methods

Both the average method and 3-D NEAR code are based on a set vacuum flux coordinates $(\rho_v, \theta_v, \phi_v)$, described by Boozer. These coordinates are defined by their relationships to the vacuum magnetic field

$$\vec{B}_v = B_0\rho_v \vec{\nabla}\rho_v \times \vec{\nabla}(\theta_v - \iota_v\phi_v) = F_v\vec{\nabla}\phi_v \tag{1}$$

and by the additional constraints that $B_0\rho_v^2/2$ is the vacuum toroidal flux and that the constant F_v should be such that ϕ_v varies by 2π in traversing the torus once toroidally. The $(\rho_v, \theta_v, \phi_v)$ coordinates and associated metric elements are derived numerically from given coil configurations, using a modified version of a code developed at ORNL.

The 3-D NEAR code uses the $(\rho_v, \theta_v, \phi_v)$ coordinates as its Eulerian frame of reference. The dependent variables are represented as doubly periodic Fourier series in θ_v and ϕ_v. Thus, for example, the contravariant component of the magnetic field is represented as

$$B^\rho(\rho_v,\theta_v,\phi_v,t) = \sum_{m,n} B^\rho(\rho_v,t)\ \sin(m\theta_v + n\phi_v)\ . \tag{2}$$

The equilibrium problem is solved, using this representation, by a steepest descent method in the manner described by Chodura and Schlüter.[5] A fictitious force $\vec{F}$ is introduced

$$\vec{F} = \vec{J} \times \vec{B} - \vec{\nabla}P \tag{3}$$

which in turn is related to a velocity $\vec{V}$, by a conjugate gradient iteration scheme.[5] The magnetic field and pressure are advanced subject to the constraints of flux and mass conservation:

$$\frac{\partial \vec{B}}{\partial t} = \nabla \times (\vec{V} \times \vec{B}) \tag{4}$$

and

$$\frac{\partial P}{\partial t} = -\vec{V} \cdot \vec{\nabla} P - \gamma P \nabla \cdot \vec{V} \ . \tag{5}$$

The wall boundary condition is given by an infinitely conducting wall at the last closed flux surface.

The other approach which has been used in these studies is an average method. The average method was first applied to the stellarator equilibrium problem by Greene and Johnson.[6] Their averaging was in real toroidal angle and relies on the dominance of the toroidal magnetic (B_T) field over the rapidly varying helical component ($\tilde{B}_v$), where $|\tilde{B}_v|/B_T \sim \delta \ll 1$. The averaging method described in this paper makes the same assumption but averages are performed in the flux coordinate toroidal angle (ϕ_v) at fixed ρ_v, θ_v. Thus the average magnetic field is

$$\langle \vec{B} \rangle = \frac{1}{2\pi} \int_0^{2\pi} \vec{B} \, d\phi_v \tag{6}$$

To leading order, the averaged equilibrium equations reduce to a Grad-Shafranov type equation:

$$\frac{1}{\rho_v} \frac{\partial}{\partial \rho_v} \left(\rho_v \langle \bar{g}^{\rho\rho} \rangle \frac{\partial \psi}{\partial \rho_v} + \langle \bar{g}^{\rho\rho} \rangle \frac{\partial \psi}{\partial \theta_v} \right) + \frac{1}{\rho_v} \frac{\partial}{\partial \theta_v} \left(\langle \bar{g}^{\rho\theta} \rangle \frac{\partial \psi}{\partial \rho_v} + \frac{\langle \bar{g}^{\theta\theta} \rangle}{\rho_v} \frac{\partial \psi}{\partial \theta_v} \right)$$

$$+ \frac{B_0 F}{F_v} \left[\frac{1}{\rho_v} \frac{\partial}{\partial \rho_v} \left(\rho_v^2 \iota_v \langle \bar{g}^{\rho\rho} \rangle \right) + \frac{1}{\rho_v} \frac{\partial}{\partial \theta_v} \left(\rho_v \iota_v \langle \bar{g}^{\rho\theta} \rangle \right) \right]$$

$$= \frac{-F_v}{B_0} \frac{1}{D_v} \frac{dP}{d\psi} - F \frac{dF}{d\psi} \tag{7}$$

where

$$\frac{B^{\rho}}{D_v} = \frac{1}{\rho_v}\frac{\partial\psi}{\partial\theta_v} \quad \text{and} \quad \frac{B^{\theta}}{D_v} = -\frac{\partial\psi}{\partial\rho_v}$$

here D_v is the Jacobian and $F \equiv \langle B_\phi \rangle$. The equivalence of Eq. (7) to the Grad-Shafranov equation derived by Greene and Johnson may be demonstrated. Equation (7) is, however, equally applicable to planar and helical axis configurations; provided the toroidal shift dominates. A Poisson type equation for $\tilde{B}_\phi$ (the toroidally varying toroidal field) has also been derived. Thus higher order corrections to the averaged equilibrium may be computed. Numerical methods have been developed to solve both this Poisson equation and the Grad-Shafranov equation [Eq. (7)]. Comparisons between 3-D equilibria and average method calculations will be given in the next section.

3. Results

(a) Helical Axis ATF

By imbalancing the currents in the helical field coils of the ATF device, a helical axis plasma is formed. The low iota bar per field period (~0.1) and relatively low aspect ratio, result in the equilibrium shift being toroidally dominated. The average method described in the previous section is thus applicable. Figure 2 shows a comparison of the flux surfaces, for the helical axis ATF, computed with 3-D NEAR code and with the average method at $\beta_0 = 2.6\%$ (the vacuum flux surfaces are also shown for reference). To make this comparison more qualitative, the equilibrium shifts (Δ_ρ) computed with NEAR (3-D) and the average method are compared in Fig. 3. The average and 3-D computations agree well. Good equilibria have been found for the helical axis ATF for central beta's up to 10%. However, the importance of resonant harmonics (whose importance is accentuated by the low shear) has not been examined in detail.

(b) Heliacs and Geodesic Helical Axis Stellarators.

A wide range of heliacs have been studied. Two fixed pitch scans have been examined in detail [Pitch = (Number field periods)/(Aspect ratio)]. The particular configurations studied in these pitch scans are summarized Fig. 4. In general, it is found that low aspect ratio heliacs have low equilibrium beta limits. Figure 5 shows a comparison between the equilibrium flux surfaces computed with the Chodura-Schlüter[5] code and the NEAR code, for the M = 4, R = 4 heliac (M is the number of field periods). The distortions to the flux surfaces, shown in Fig. 5, are caused by the beating of the dominant toroidal shift with the helical harmonics generated by the coils. At higher betas (~10%) these distortions grow without limit and destroy the equilibrium. The equilibrium beta limits can be raised by reducing the toroidal equilibrium shift. This may be achieved either by raising the total ι or by raising the aspect ratio at fixed pitch. Figure 6 shows equilibrium flux surfaces at β_0 = 5% for the M = 8, R = 8 and M = 8, R = 4 heliacs. These correspond to raising the total ι (M = 8, R = 4) and raising the aspect ratio (M = 8, R = 8), relative to the M = 4, R = 4 case. The improvement in equilibrium quality is evident in Fig. 6. The results of the M/R = 1 scan are summarized in Fig. 7, where the toroidal shift (Δ_T) and helical shift (Δ_H) as function of β_0 are plotted for the configurations studied. The helical shifts remain practically invariant for all configurations in the pitch scan, while the toroidal shifts decline as the inverse aspect ratio. This is because in a fixed pitch scan the helical curvature remains constant as the toroidal curvature varies.

Finally, the potential of reducing the toroidal shift by winding the toroidal coil axis as a geodesic on a torus, has been examined [Fig. 1(b)]. Figure 8 shows equilibrium flux surfaces at β_0 = 5% for this configuration. The toroidal shift is of the same order as the M = R = 4 heliac (shown in Fig. 2); there appears to be little benefit in winding the axis as a geodesic. Further studies are however required to clarify this point.

Conclusions

A wide range of helical axis stellarators have been studied with the 3-D equilibrium code NEAR and with an average method applicable to helical axis configurations. The helical axis variant of the ATF device is found to have a toroidally dominated equilibrium shift. Studies of the helical axis ATF with NEAR (3-D) and the average method indicate good equilibria exist up to at least 10% central beta.

Two sequences of fixed pitch heliacs have been examined to clarify the effects of toroidal and helical curvature on the equilibrium. In general, it is found that heliacs which have large toroidal shifts, have low equilibrium beta limits. This is because the beating of toroidal shift with the helical harmonics of the coils produces gross distortions to the flux surfaces. This process is the same as that described by Reiman and Boozer.[3] Raising the total ι by increasing M at fixed aspect ratio improves the equilibrium beta limit in heliacs. Alternatively increasing the aspect ratio at fixed pitch also raises the equilibrium beta limit.

Finally, the potential of reducing the toridal shift by winding the toroidal field coil axis as geodesic [Fig. 1(b)] has been examined. Initial results indicate there is little reduction toroidal shift by winding the coils in such a manner.

Acknowledgments

We should like to thank J. L. Johnson and A. H. Boozer for several useful discussions. This work was sponsored by the Office of Fusion Energy, U.S. Department of Energy, under Contract No. W-7405-eng-26 with the Union Carbide Corporation.

REFERENCES

[1]D. A. Monticello, R. L. Dewar, H. P. Furth and A. H. Reiman, Princeton Plasma Physics Laboratory Report PPPL-2036, 1983.

[2]A. H. Reiman, A. H. Boozer, Princeton Plasma Physics Laboratory Report PPPL-2062, 1983.

[3]J. F. Lyon, et al., Oak Ridge National Laboratory Report No. ORNL/TM-8496, 1983.

[4]A. H. Boozer, et al., Plasma Physics and Controlled Nuclear Fusion Research (IAEA, Vienna, 1983), Vol. 3, p. 129.

[5]R. Chodura and A. Schlüter, J. Comput. Phys. 41, 68 (1981).

[6]J. M. Greene and J. L. Johnson, Phys. Fluids 4, 875 (1961).

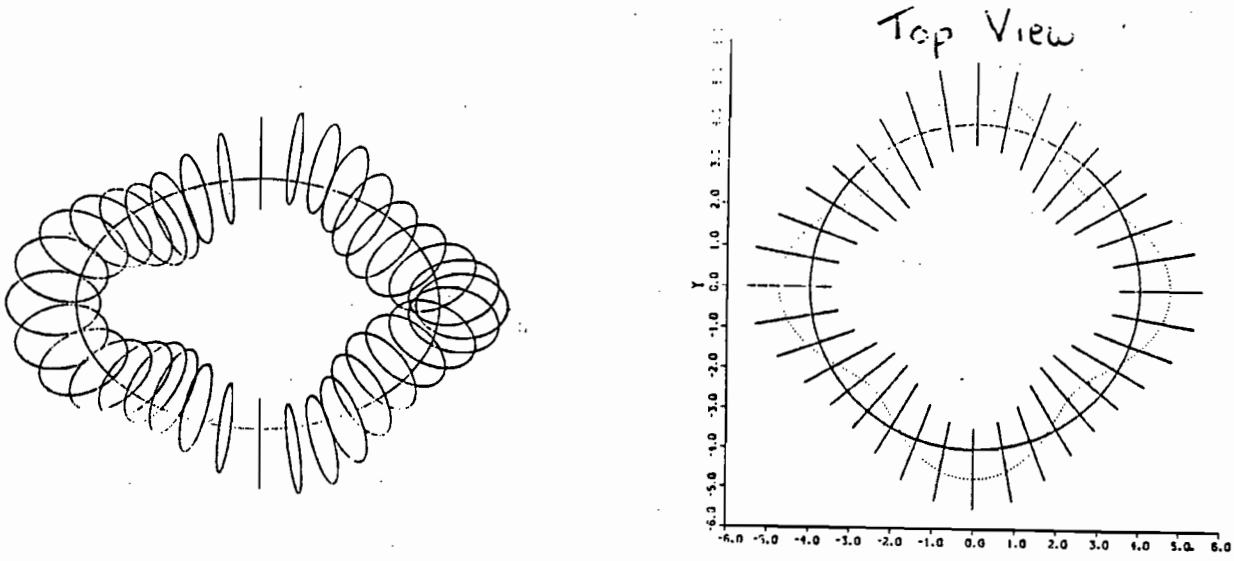

Fig. 1(a). Coil set for M = R = 4 heliac.

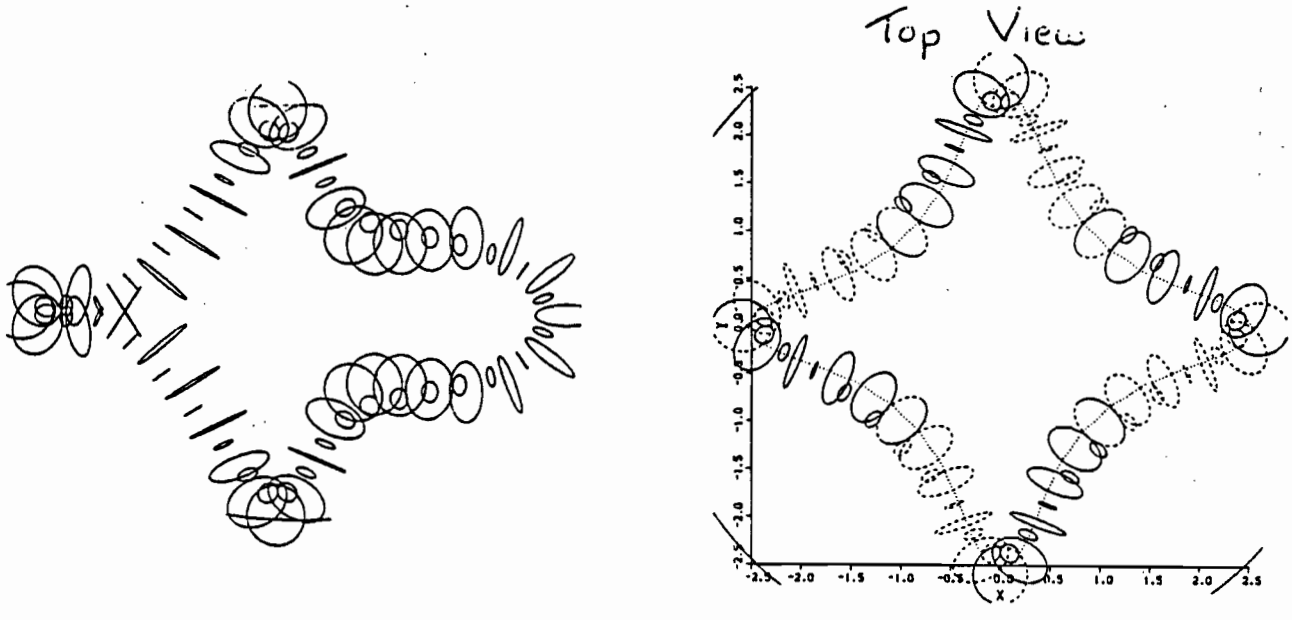

Fig. 1(b). Coil set for geodesic helical axis stellarator.

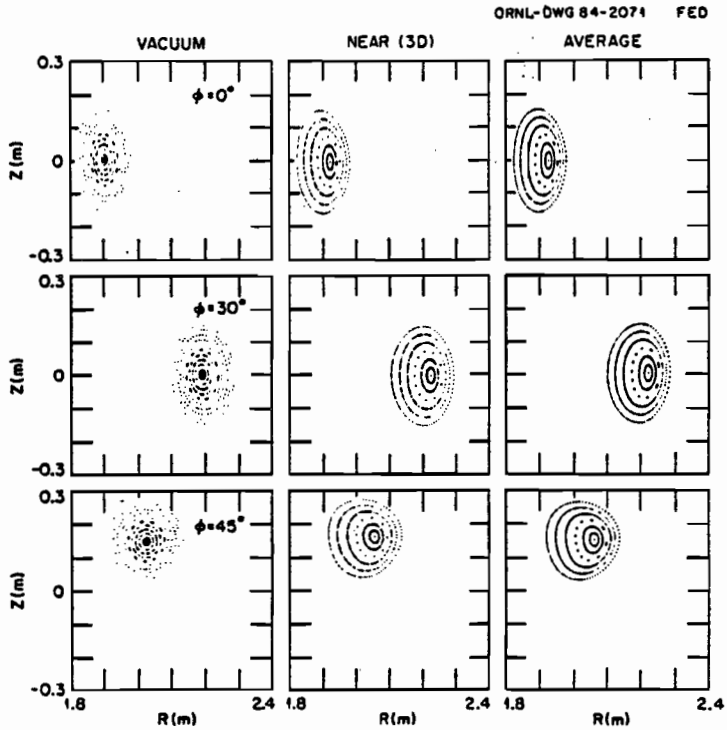

Fig. 2. Comparison between equilibrium flux surfaces computed with NEAR (3-D) and average method (β_0 = 2.6%, $\langle P \rangle \propto \psi^2$) for helical axis ATF. Vacuum flux surfaces are also shown for comparison.

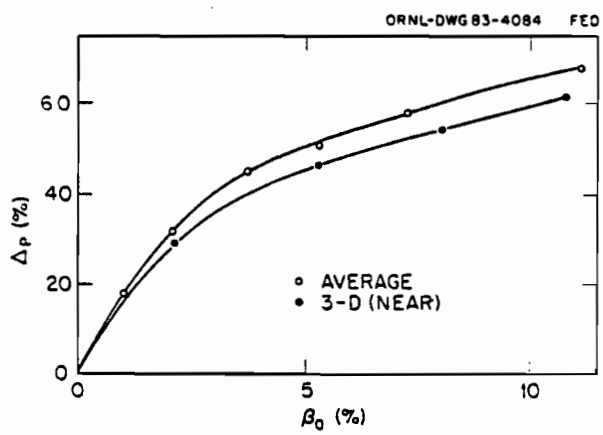

Fig. 3. Shift (Δ_p) as a function of β_0 for the helical axis ATF.

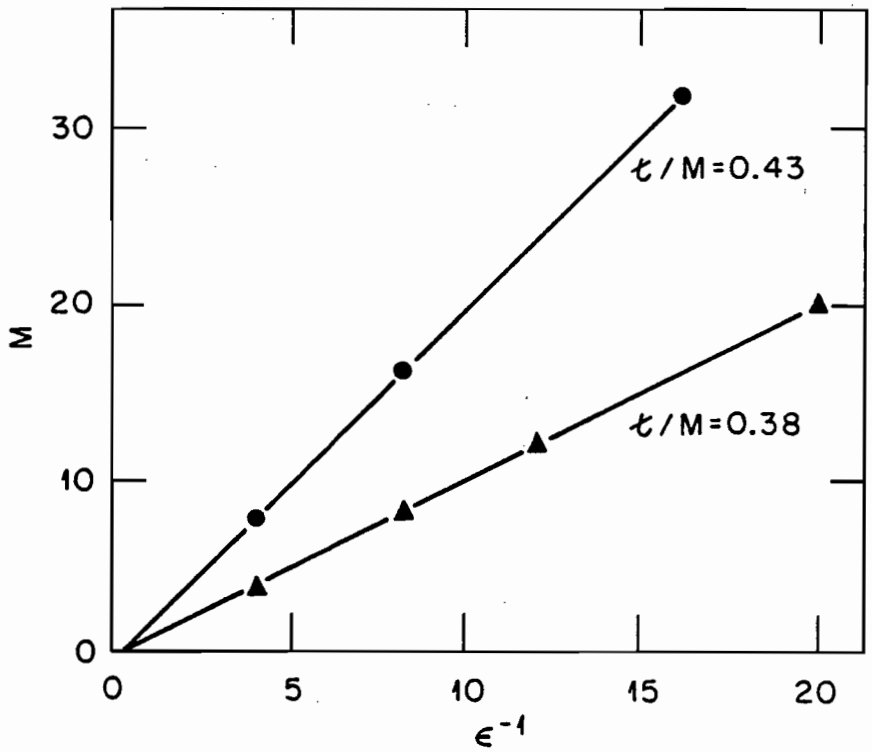

Fig. 4. Plot of number of field periods (M) v Aspect ratio; summarising the heliac configurations studied in the fixed pitch scans.

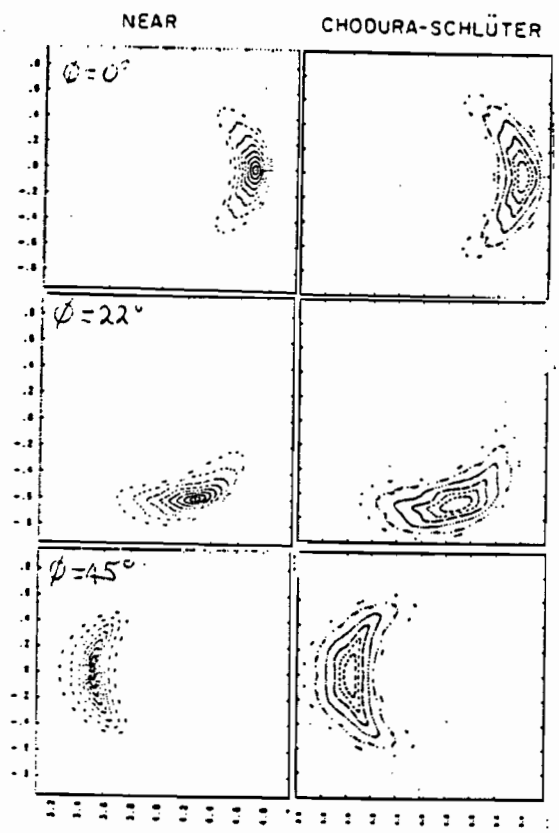

Fig. 5. Comparison of equilibrium flux surfaces for M = R = 4 heliac between NEAR (β_0 = 5%) and Chodura-Schlüter code (β_0 = 3%).

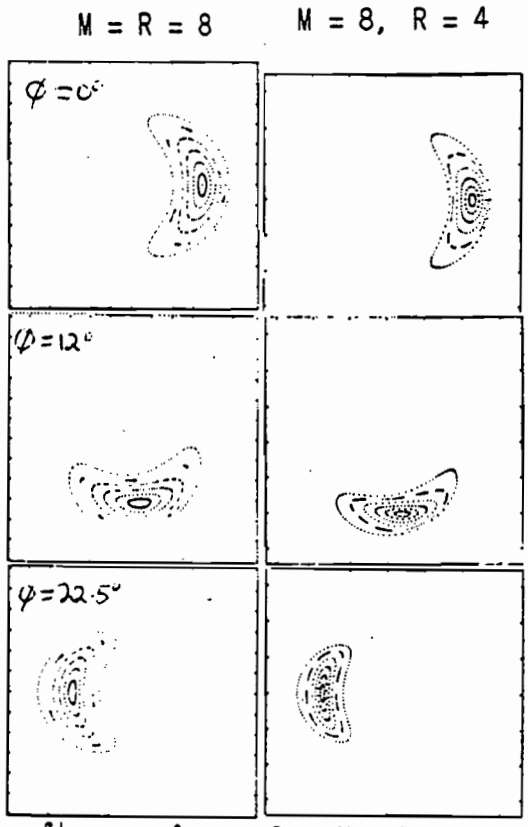

Fig. 6. Equilibrium flux surfaces for M = R = 8 and M = 8, R = 4

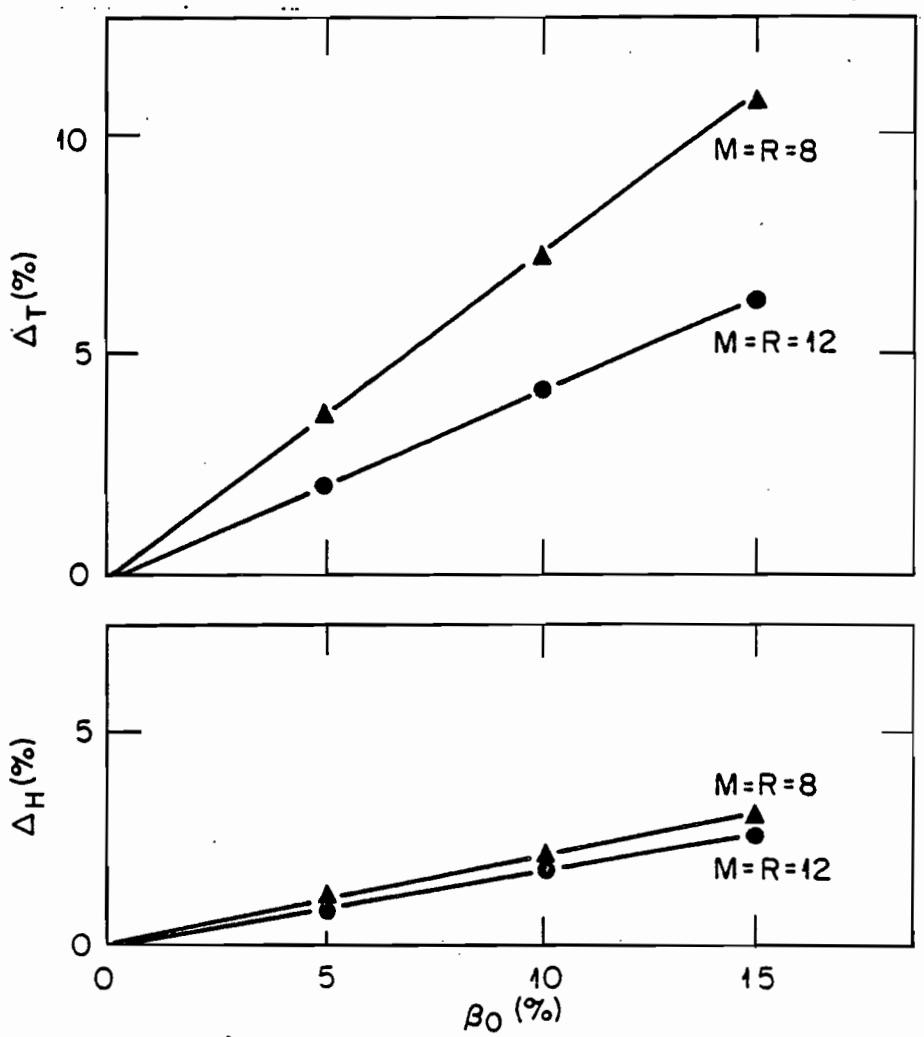

Fig. 7. Toroidal equilibrium shift (Δ_T) and helical shift (Δ_H) as a function of β_0 for configurations studied in M/R = 1 scan.

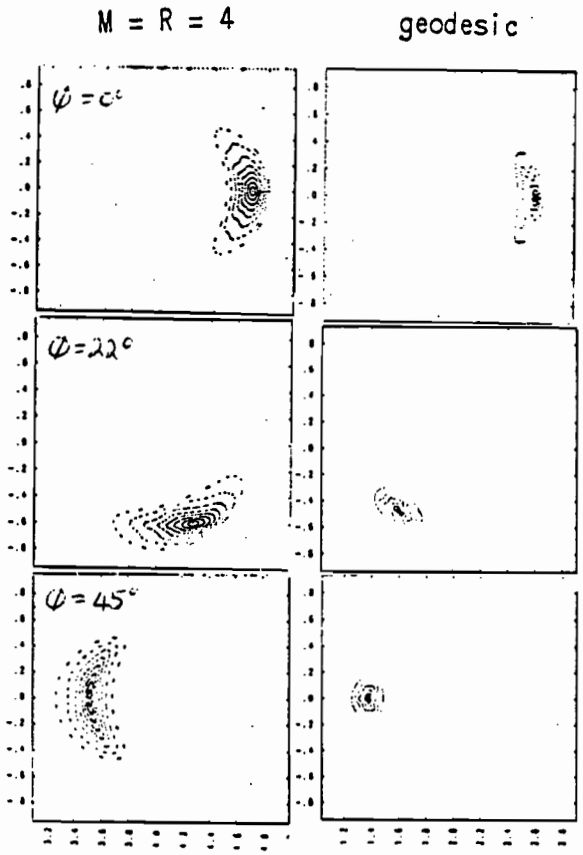

Fig. 8. Equilibrium flux surfaces for geodesic axis stellarator (β_0 = 5%); also shown for comparison are the M = R = 4 case flux surfaces at β_0 = 5%.

Non-linear Calculations of m = 1 Interchange Mode in Heliotron E

M. Wakatani and H. Shirai

Plasma Physics Laboratory
Kyoto University
Gokasho, Uji
Kyoto, Japan

In the heliotron with large rotational transform, $\iota(a) \sim 2$, the dominant stabilizing mechanism against MHD instabilities is shear. The linear MHD stability of the heliotron configuration was studied against the low n pressure-driven modes both for the cylindrical [1] and the toroidal configuration [2], where n is a toroidal mode number. It is found that (i) the equilibrium averaged beta limit exceeds 7% since both ι and the aspect ratio, R/a, is large, and (ii) the stability beta limit depends on the pressure profile and broad profiles give large stability margin.

Recently two types of discharge are observed in Heliotron E which depend on the gas puffing condition during the neutral beam injection. In the weak gas puffing case, for $\beta(0) \gtrsim 2\%$, internal disruption with precursor fluctuations appears in the soft x-ray measurements as shown in Fig. 1 (S mode). On the other hand, when the intense gas puffing is applied, the fluctuations of the

soft x-ray become weak or disappear (Q mode). In the S mode, density fluctuations and magnetic fluctuations are also observed. At the time of the internal disruption energy flow to the edge region was detected by the bolometric measurement.

The estimated mode number from the measured precursor oscillations is m = 1/ n = 1, where m denotes a poloidal mode number. The main difference between the S mode and the Q mode is the pressure profile. The S mode has a peaked profile, while the Q mode has a broader one. The stability of the Q mode is consistent with the linear stability analyses which predicts a higher beta limit for a broader pressure profile.

In order to investigate the physical mechanism of the S mode, the reduced non-linear MHD equations describing the stellarator plasma [3],

$$(1)\quad \frac{d}{dt}\nabla_\perp^2 u = \{B_{z0}\vec{e}_z + \vec{\nabla}(\psi_J + \psi_h) \times \vec{e}_z\}\cdot \vec{\nabla}(\nabla_\perp^2\psi_J) + \vec{\nabla}\Omega \times \vec{\nabla}P\cdot\vec{e}_z,$$

$$(2)\quad \frac{\partial}{\partial t}\psi_J = \{B_{z0}\vec{e}_z + \vec{\nabla}(\psi_J + \psi_n) \times \vec{e}_z\}\cdot \vec{\nabla}u + \eta\nabla_\perp^2\psi_J,$$

$$(3)\quad \frac{dP}{dt} = K_{eff}\nabla_\perp^2 P$$

are solved in the straight plasma model,

where

$$\psi_h = \frac{B_0\varepsilon h^2 l}{2\varepsilon^2 hr^2} I_1'(hr)\, I_1(hr)$$

$$\Omega = \frac{4}{q(a)R}\frac{G(hr)}{F'(hr)},$$

$$F(hr) = \frac{2}{hr} I_l(hr)\ I_l'(hr),$$

$$G(hr) = [I_l'(hr)]^2 + (1 + \frac{l^2}{h^2r^2})\ I_l^2(hr).$$

Here u denotes a stream function, ψ_J a flux function due to plasma current, ε_h a magnitude of the helical magnetic field and l and h characterize the helical field structure. In the pressure equation (3), the thermal diffusion K_{eff}, is included to take into account the rapid energy transport due to the instability and to remove the singular profile at the saturation of the unstable ideal MHD mode. In the numerical calculations, K_{eff} is given by $\alpha\eta$, where α is a constant and η denotes resistivity. It is assumed that the mode coupling due to the toroidal geometry may be weak for the m = 1/ n = 1 mode resonate at ι = 1 surface. The resistivity in eq. (2) allows reconnection of the magnetic field lines in the non-linear stage of the ideally unstable mode.

Without η and K_{eff} in eqs. (1) ~ (3), the linear stability analyses against the ideal m = 1/ n = 1 interchange mode give $\beta_c(0) \simeq 2.5\%$ for the pressure profile, $P = P_0(1 - (r/a)^2)^2$, and below this value the resistive m = 1/ n = 1 interchange is destabilized by η. In the non-linear analyses of these modes we assume single helicity. The time evolution of kinetic energy is shown in Fig. 2. Figure 3 shows plasma pressure profiles at four different times. T = 132 (normalized by the poloidal Alfven transit time) corresponds to the growing stage of the unstable mode, at T = 164 the reconnection of the magnetic field lines

starts and T = 292 corresponds to the saturated stage. The pressure profile deforms due to both the non-linear development of the m = 1/ n = 1 mode and the thermal diffusion. From the time evolution of the pressure profile we can estimate the soft x-ray signal in the experiment by assuming that the pressure corresponds to electron temperature and the plasma column rotates rigidly. We also assume the soft x-ray is proportional to P^3. Figure 4 shows the estimated fluctuations for the central cord and the cord through about the half radius. It is seen that the fluctuation level is large in the outer region and the phase of the central cord is about 180° different from the outer region cord. These are consistent with the experimental data of Fig. 1.

Now we will discuss the time scale of the internal disruption. In Fig. 1 it starts at T = 471.6 msec and ends at T = 472.8 msec. Therefore, the saturation time may be 1.2 msec. The saturation time in Fig. 2 is about $T \simeq 280\ T_0$. From the experimental data the unit time T_0 is estimated 0.5 sec. By comparing these members, there is about 8 times difference between the experiment and the numerical results. Still there is ambiguity about both the beta value and the pressure profile just before the internal disruption. More detailed measurements of the temperature profile and the density profile are required. The fluctuation before T ≃ 471.6 msec is assumed the resistive instability with m = 1 and n = 1.

In summary, main characteristics of S mode can be explained by the non-linear evolution of the m = 1/ n = 1 interchange mode at nearly marginal stability.

References

[1] M. Wakatani, et al., J. Phys. Soc. Jpn. 47 (1979) 974.

[2] M. Wakatani, IEEE Trans. Plasma Science, PS-9 (1981) 243.

[3] H.R. Strauss, Plasma Physics 22 (1980) 733.

Figure Captions

Fig. 1 An example of soft x-ray fluctuations in the case of internal disruption for $\beta(0) \sim 2.5\%$.

Fig. 2 Time evolution of kinetic energy of $m = 1/\ n = 1$ interchange instability for $P = P_0(1 - (r/a)^2)^2$ and $\beta(0) = 2.6\%$. Magnetic Reynolds number $S = 5 \times 10^3$ and $K_{eff} = 2\eta$.

Fig. 3 Pressure profiles along $\theta = 0$ and $\theta = \pi$ line for the instability shown in Fig. 2.

Fig. 4 Soft x-ray fluctuations from time evolution of pressure profile by assuming rigid rotation of the plasma column. (a) shows the central cord and (b) the cord through about the half radius for $\beta(0) = 3.7\%$, $K_{eff} = 5\eta$ and $S = 5 \times 10^3$.

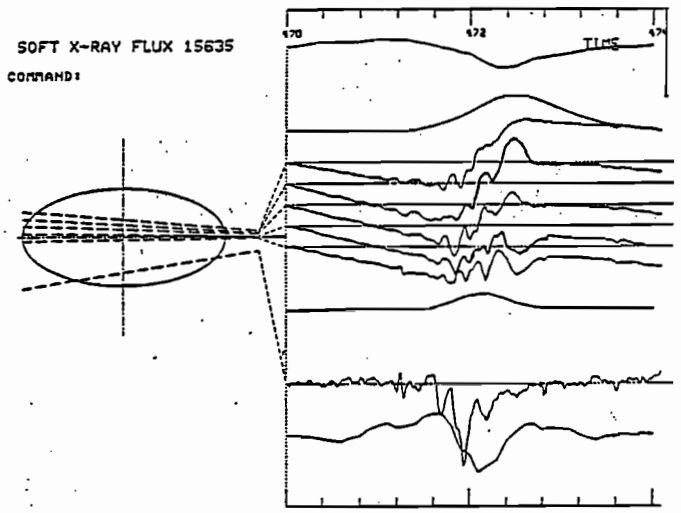

Fig. 1

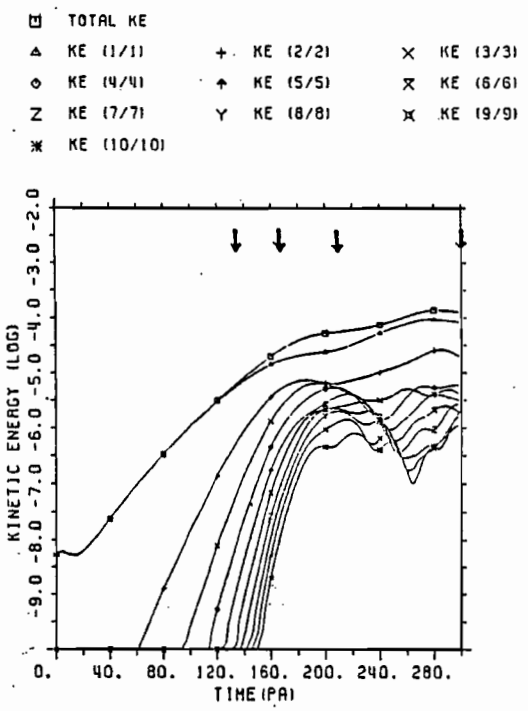

Fig. 2

TIME DEVELOPMENT OF KE

RUN NUMBER= 34.

STEP= 13200. TIME(PA)= 132.

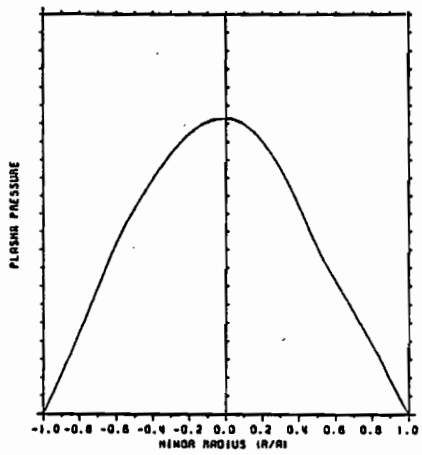

PLASMA PRESSURE PROFILE

RUN NUMBER= 34.

STEP= 16400. TIME(PA)= 164.

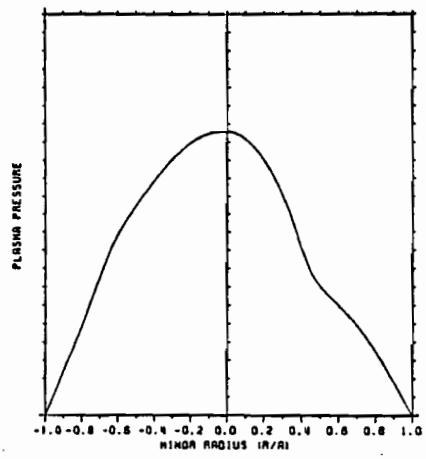

PLASMA PRESSURE PROFILE

RUN NUMBER= 34.

STEP= 21200. TIME(PA)= 212.

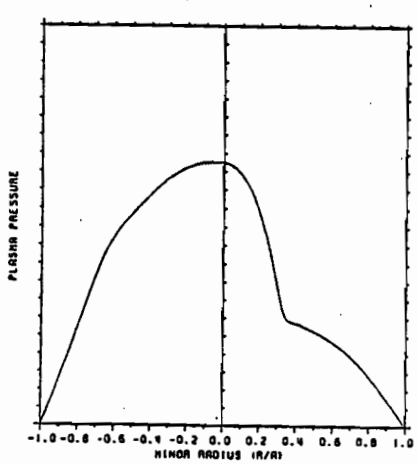

PLASMA PRESSURE PROFILE

RUN NUMBER= 34.

STEP= 29200. TIME(PA)= 292.

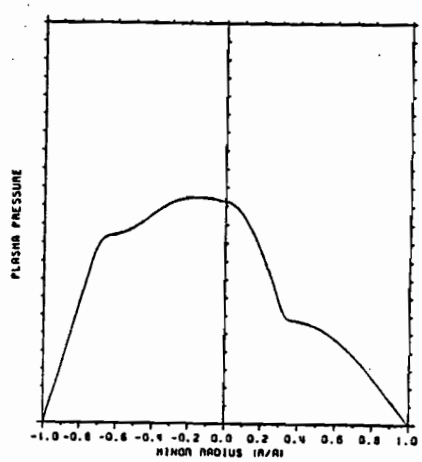

PLASMA PRESSURE PROFILE

Fig. 3

RUN NUMBER=30.

ANGLE=60.0

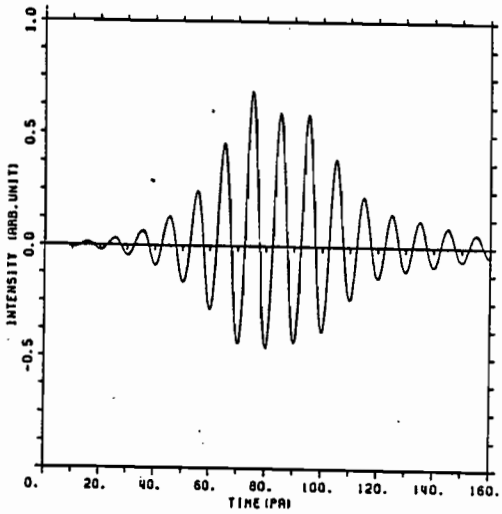

SOFT X RAY INTENSITY (3)

Fig. 4 (b)

RUN NUMBER=30.

ANGLE=88.5

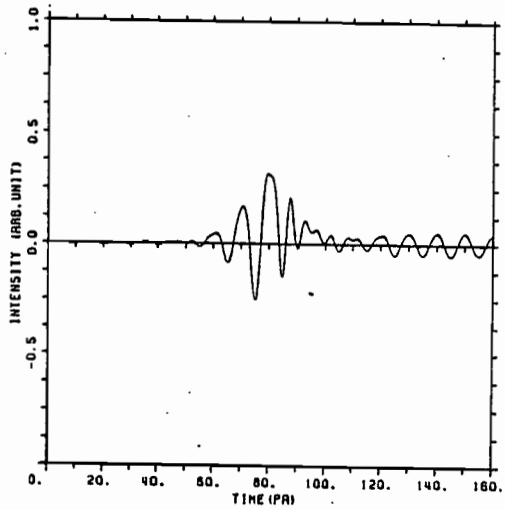

SOFT X RAY INTENSITY (3)

Fig. 4 (a)

By acceptance of this article, the publisher or recipient acknowledges the U.S. Government's right to retain a nonexclusive, royalty-free license in and to any copyright covering the article.

STELLARATOR EXPANSION STUDIES OF A HIGH-BETA TORSATRON*

J. A. Holmes, B. A. Carreras,** L. A. Charlton,
H. R. Hicks, and V. E. Lynch

Computer Sciences at
Oak Ridge National Laboratory
Oak Ridge, Tennessee 37831 USA

1. INTRODUCTION

ATF is a medium aspect ratio ($R_c/a_c = 7$) $\ell = 2$ continuous torsatron with twelve field periods ($M = 12$). This configuration has been demonstrated, using the stellarator expansion,[1] to have good MHD equilibrium and stability properties[2] with increasing β.

Present studies are directed toward improving the flexibility of the ATF design by determining means of controlling important plasma parameters, such as the magnetic well and the rotational transform profile. We concentrate here on the use of the ATF vertical-field (VF) coil system in providing this control.

The stellarator expansion equilibrium and stability calculations carried out using the system of computer codes developed at Oak Ridge[2-4] feature a fixed-boundary approach. This method provides convenient control of the equilibrium shaping and is useful for rapidly producing and considering a wide range of cases. However, with the demonstrated desirability of the ATF configuration from an MHD equilibrium and stability standpoint and with the capability of the VF coil system for controlling plasma parameters as discussed here, the need to study the free-boundary equilibrium and stability of ATF becomes important. To carry out this work, we have recently obtained Princeton Plasma Physics Laboratory's free-boundary stellarator expansion equilibrium and stability codes.[5-8] We present here the results of our initial free-boundary calculations for ATF.

---

*Research sponsored by the Office of Fusion Energy, U.S. Department of Energy, under Contract No. DE-AC05-840R21400 with Martin Marietta Energy Systems, Inc.

**Fusion Energy Division.

2. THE STELLARATOR EXPANSION EQUATIONS AND THEIR SOLUTION

The stellarator expansion was originally derived by Greene and Johnson[1] using an ordering scheme with the ratio of the helical and toroidal magnetic-field strengths as the basic parameter. In this scheme, toroidal effects are assumed to enter in second order. The crucial feature of the stellarator expansion is the reduction of the equilibrium calculation from three to two dimensions through toroidal averaging over a field period. This feature makes the systematic computational treatment of a large number of cases possible. With this reduction, one solves an equilibrium equation for the averaged poloidal flux function

$$\Delta^* (\Psi - \Psi_v^*) = -R^2 \frac{dP}{d\Psi} - (F + F^*) \frac{dF}{d\Psi} , \tag{1}$$

which closely resembles the Grad-Shafranov equation for tokamaks. In Eq. (1), $\Psi(R,Z)$ is the averaged poloidal flux function, $\Psi_v^*(R,Z)$ is the averaged poloidal flux function of the vacuum, R is the major radius coordinate, Z is the vertical position, $P(\Psi)$ is the pressure, $F^*(R,Z)$ is the helical-curvature term, and the averaged toroidal flux function $F(\Psi)$ is adjusted to give either strict flux conservation ($\iota = \iota_v$) or zero net toroidal current within each flux surface ($\langle J_\phi \rangle_\Psi = 0$). The quantities Ψ_v^* and F^* depend only upon the vacuum magnetic field. While the details are discussed in Refs. 1 and 2, it suffices for present purposes to state that F^* depends only upon the helical magnetic field and that $\Psi_v^* = \Psi_0 + \Psi^*$, where Ψ^* depends only on the helical field and Ψ_0 contains only axisymmetric contributions. In particular, Ψ_0 is obtained by solving $\Delta^* \Psi_0 = 0$ with the boundary condition $\vec{B}_{0_\perp} = \frac{1}{R} \vec{\nabla}_\perp \Psi_0 \times \hat{\zeta}$, where $\vec{B}_{0_\perp}$ is the poloidal vacuum field averaged over a field period. Hence, the effect of the axisymmetric VF coil system in these calculations enters entirely through the quantity Ψ_0. Because the stellarator expansion is not an exact model for three-dimensional equilibrium and stability (being derived in the limit of small helical-field variations, large aspect ratio, and low β), tests have been conducted comparing the results with those of full

three-dimensional equilibrium calculations. As shown in Ref. 2, good agreement is obtained.

Both the fixed- and the free-boundary equilibrium codes used in this work have been adapted to accept averaged numerical vacuum data, rather than model fields, from the actual ATF design. The vacuum magnetic fields are calculated using the Biot-Savart law, together with filamentary coil specifications.

Both the fixed- and free-boundary equilibrium codes solve Eq. (1) on a rectangular coordinate grid. While the fixed-boundary code can produce either flux-conserving or zero net current equilibria, the free-boundary code solves only the latter. In both programs the averaged pressure is modeled by $P(\Psi) = c\ (\Psi - \Psi_a)^k$ where the constant c determines the peak β, Ψ_a is the value at the zero pressure boundary, and the exponent k determines the steepness of the pressure profile. We take $k = 2$ in this work.

The main difference between the fixed- and free-boundary equilibrium codes is the treatment of the boundary. In the fixed-boundary code, a flux surface of Ψ_v^* is chosen to be the computational boundary. The boundary conditions are taken to be $P = 0$ and $\Psi = 0$, and the calculation is carried out entirely inside this conducting wall boundary. The free-boundary code calculates a solution over an entire rectangular region with the boundary conditions applied at the edges. The location of the flux surface of zero pressure is determined by the intersection of the flux surfaces with a specified limiter. Interior to this surface one obtains a solution to Eq. (1) with pressure, while the exterior solution is an averaged vacuum solution. The boundary conditions on the edge of the computational grid are determined from the plasma currents using Green's functions.[7] The control of the shape and location of the $P = 0$ surface in the free-boundary method is carried out completely through the specification of the VF coil currents.

The fixed-boundary stability calculations for low-n modes are carried out using a reduced set of equations for stellarators that was derived by Strauss[9] using the stellarator expansion ordering. These calculations (described in Ref. 2) use an initial-value approach. The free-boundary code for low-n stability, described in Refs. 7 and 8,

uses a δW approach, with an optional conducting wall that can be placed at any multiple of the plasma radius between 1 and ∞. This free-boundary system of codes is a modification of the tokamak MHD equilibrium and stability PEST code[5,6] to do the stellarator expansion.

3. ROTATIONAL TRANSFORM CONTROL USING THE ATF VF COIL SYSTEM

For fixed-vacuum configurations, zero net current equilibrium sequences show significant deformation of the rotational transform profile with increasing β. As can be seen for the standard ATF reference vacuum in Fig. 1, with increasing β the rotational transform increases on the magnetic axis, decreases at the (fixed) plasma boundary, and forms intermediate minima. Such major variations of the rotational transform could lead to resistive instabilities and degradation of confinement. To control the rotational transform of zero net current sequences of equilibria, let us now consider the ATF VF coil system.

The VF coil system for ATF consists of the three pairs of axisymmetric coils shown in Fig. 2. Each pair is located symmetrically about the horizontal midplane, and the currents in the upper and lower members of each pair are equal. By varying the currents in the three sets of coils, it is possible to alter the magnetic configuration quite flexibly. Such features as the position, the total external flux linked, and the cross-section shape of the magnetic surfaces can be controlled in this manner. For example, by changing the relative currents between the inner and outer sets of coils, it is possible to shift the magnetic surfaces in or out along the major radius. Reference 2 shows how this technique can be used to control the magnetic well and, hence, the stability of the resulting equilibria.

With three sets of coils, it is possible to control three degrees of freedom, or to satisfy three constraints, in the magnetic-field configuration. One such constraint could be to determine the position of the plasma, using the VF coils to shift the surfaces in or out as desired. Another such constraint is to determine the total external flux linked by the plasma. Having satisfied these two constraints, one degree of freedom remains, and this is related to the cross-section shape of the magnetic configuration. This is discussed in a quantitative way in Ref. 10. For the calculations to be presented in

this section, we have chosen to maintain the plasma position and the external flux linked by the plasma to be constant and equal to that for the standard, reference ATF vacuum configuration. This leaves one remaining degree of freedom in the relative coil currents. Since the standard ATF vacuum configuration is obtained with zero current in the VFB coils (Fig. 2), we parameterize this degree of freedom by I_b, the current in the VFB coils normalized to the current in the helical-field coils. The constraint of constant external flux linked by the plasma is in keeping with the conditions of a dynamic adjustment of the coil currents during a discharge, during which changes in the flux would lead to surface currents in the plasma.

As the VF coil currents are changed in a manner to maintain constant external flux linkage and plasma position, the shape of the magnetic surfaces becomes elongated/shortened with increasing/decreasing I_b. For a given plasma β, ι_0 decreases as the surfaces become elongated ($I_b \geq 0$). For large enough values of I_b, $I_b \gtrsim 0.3$, the vacuum ι_0 becomes zero, and a separatrix forms, leading to a doublet configuration. Since ι_0 increases with increasing β for a fixed-vacuum configuration and decreases with increasing I_b for fixed β, it is possible to increase I_b with increasing β at a rate just sufficient to maintain ι_0 constant. Such flux-controlled curves of constant ι_0 are plotted in the $\beta_0 - I_b$ plane in Fig. 3.

We shall now describe our results for a typical flux-controlled curve depicted in Fig. 3. The equilibria in this sequence have been calculated by varying the coil currents with β to maintain constant ι_0 such that at $\beta = 0$ the vacuum is the standard ATF reference case. Throughout this sequence the vacuum-averaged flux surface chosen for the boundary is taken such that $\iota_a = 1$, which is consistent with the notion of a natural limiter at the plasma boundary. The elongation of the magnetic surfaces required to maintain constant ι_0 as β is increased is shown in Fig. 4.

A favorable property of the flux-controlled equilibrium path is a reduction of the magnetic axis shift at given β when compared with that of the standard vacuum coil current configuration (Fig. 5). This decrease can be understood as a consequence of a reduction in the Pfirsch-Schlüter currents with increasing I_b.

Although one might expect a decrease in the magnetic well in conjunction with the reduced axis shifts and Pfirsch-Schlüter currents, the shaping of the magnetic surfaces accompanying these reductions prevents such a decrease.

4. FREE-BOUNDARY CALCULATIONS

Our initial work with free-boundary equilibrium and stability has concentrated on comparison with existing fixed-boundary cases. This comparison has been carried out for a fixed VF coil current configuration. The equilibrium parameters compare quite closely for the two methods. In Fig. 6 we show plots of $\langle\beta\rangle$ and the magnetic axis shift δ/R_0 vs β_0 for the fixed- and free-boundary models. The free-boundary calculations have been carried out here using an additional vertical field to keep the plasma centered as β is increased. The rotational transform profiles also agree quite well in Fig. 7. The difference at the outside boundary is due to a different choice of limiter in the two calculations, but the trend in ι_a vs β is the same for both methods.

We have not, at this time, observed any global instabilities for the ATF configuration. Although Rewoldt and Johnson[11] have reported a global $n = 1$ kink mode for an $\langle\beta\rangle = 2.6\%$ equilibrium, this calculation was made using a vacuum field configuration that has been computationally superseded. In this vacuum configuration, the computational boundary for the toroidal averaging was taken to be a square box. To keep this box from intersecting the (circular) projection of the helical-field coils, it was necessary to omit substantial regions containing good flux surfaces (Fig. 8). In addition, the helical magnetic fields were calculated using a potential function Φ_h such that $\vec{\nabla}\Phi_h = \vec{B}_h$, with the derivatives evaluated numerically. Since then, the vacuum calculations have been modified to use the circular region, which more nearly matches the projection of the helical-field coils. With this larger region it is possible to include more good surfaces. As seen in Fig. 8, using the old method (square box) on the standard ATF vacuum, the rotational transform is cut off at $\iota = 0.82$, while with the circular region, surfaces with $\iota > 1.1$ are included. We now also calculate the vacuum helical fields more accurately using the Biot-Savart law, which avoids the necessity

of numerical differentiation. Finally, higher resolution is now obtained in the average vacuum calculations by using a 100 x 100 mesh, rather than the 65 x 65 mesh as used previously. While we have been able to duplicate the results of Rewoldt and Johnson by using the same "old" vacuum file they used, we find no global instabilities for the same configuration when the "new" vacuum calculations are used. At present we are working on separating the effects of box size, numerical differentiation versus Biot-Savart, and resolution to determine which factors are instrumental in changing the stability results.

ACKNOWLEDGMENT

We thank John Johnson and Greg Rewoldt for providing us with the PPPL free-boundary stellarator expansion equilibrium and stability codes.

REFERENCES

1. J. M. Greene and J. L. Johnson, Phys. Fluids 4, 875 (1961).
2. B. A. Carreras, H. R. Hicks, J. A. Holmes, V. E. Lynch, L. Garcia, J. H. Harris, T. C. Hender, and B. F. Masden, Phys. Fluids 26, 3569 (1983).
3. V. E. Lynch, B. A. Carreras, H. R. Hicks, J. A. Holmes, and L. Garcia, Comput. Phys. Commun. 24, 465 (1981).
4. J. A. Holmes, Y-K. M. Peng, and S. J. Lynch, J. Comput. Phys. 36, 35 (1980).
5. J. L. Johnson et al., J. Comput. Phys. 32, 212 (1979).
6. R. C. Grimm, J. M. Greene, and J. L. Johnson, p. 253 in Methods in Computational Physics, vol. 16, ed. J. Killeen, Academic Press, New York, 1976.
7. G. Anania, J. L. Johnson, and K. E. Weimer, Phys. Fluids 26, 2210 (1983).
8. G. Anania and J. L. Johnson, Phys Fluids 26, 3070 (1983).
9. H. R. Strauss, Plasma Phys. 22, 733 (1980).

10. B. A. Carreras, H. R. Hicks, J. A. Holmes, V. E. Lynch, and G. H. Neilson, to be published.
11. G. Rewoldt and J. L. Johnson, PPPL-2088, Princeton Plasma Physics Lab., New Jersey, 1983.

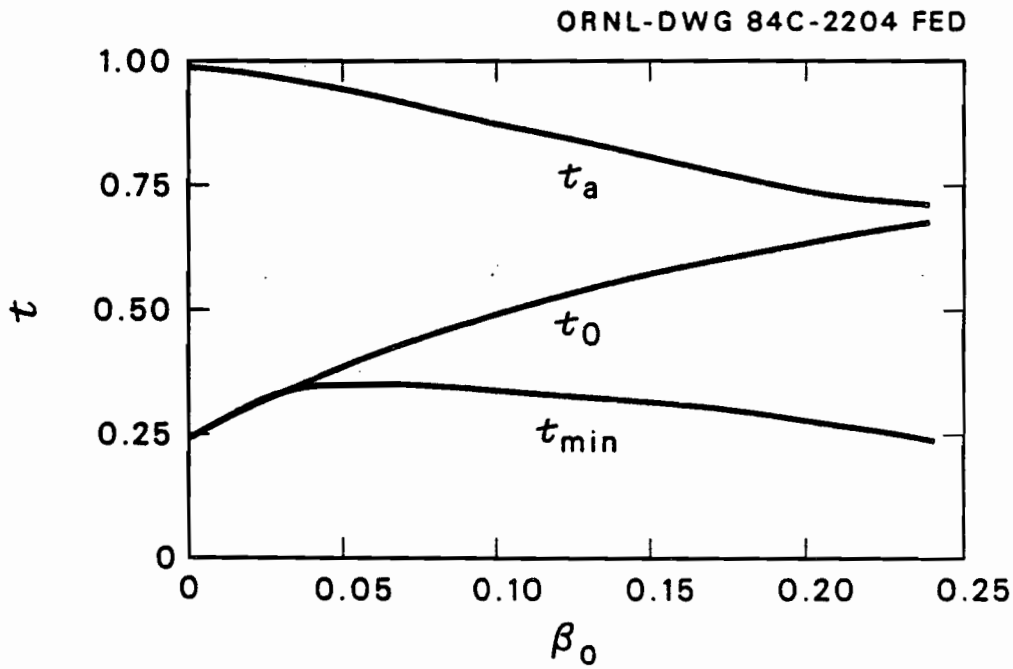

Fig. 1. Rotational transform profiles of zero net current equilibria at several values of β for the standard ATF VF coil currents.

ORNL-DWG 84C-2248 FED

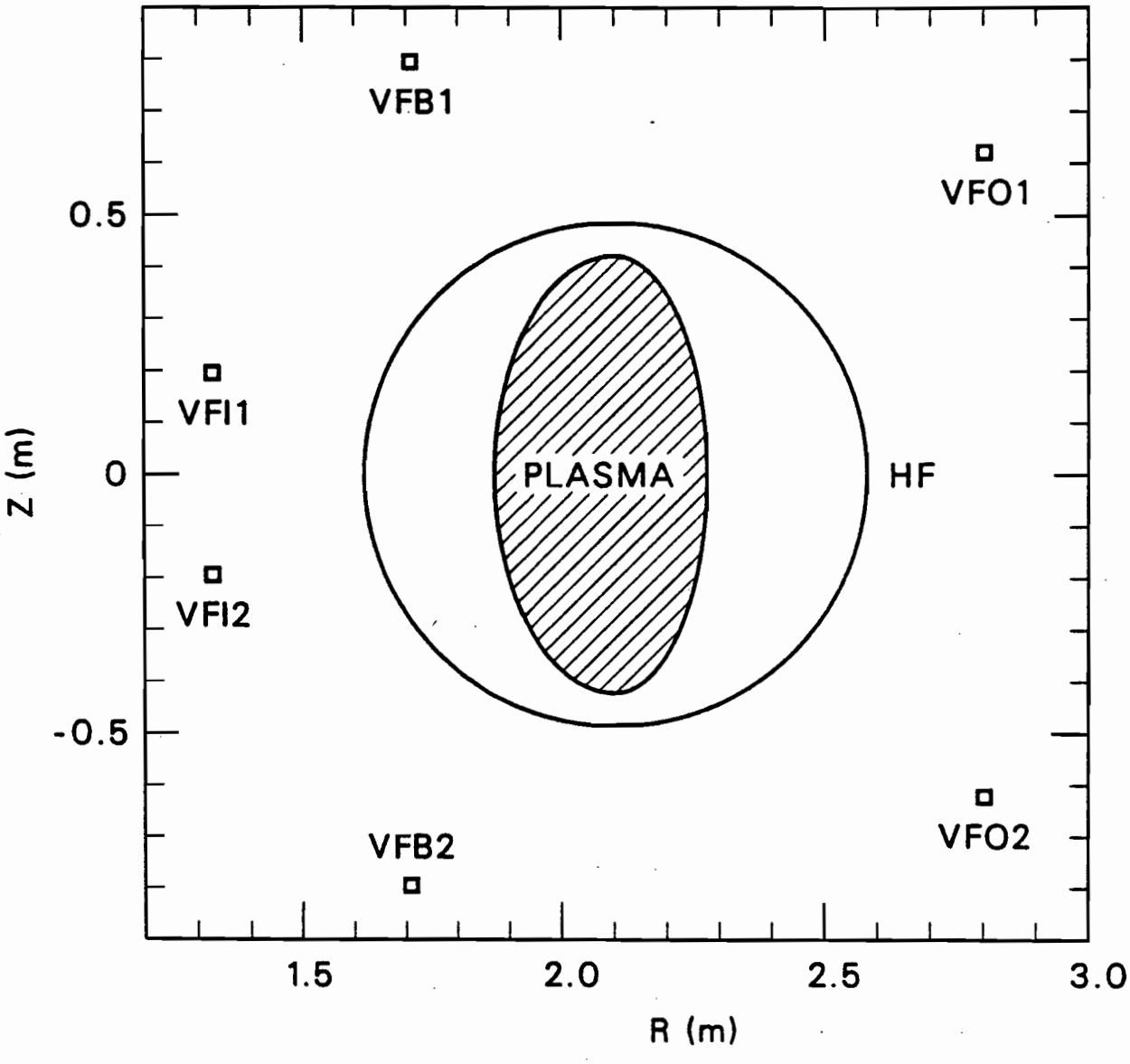

Fig. 2. The ATF coil system showing the helical coils and the three pairs of axisymmetric VF coils.

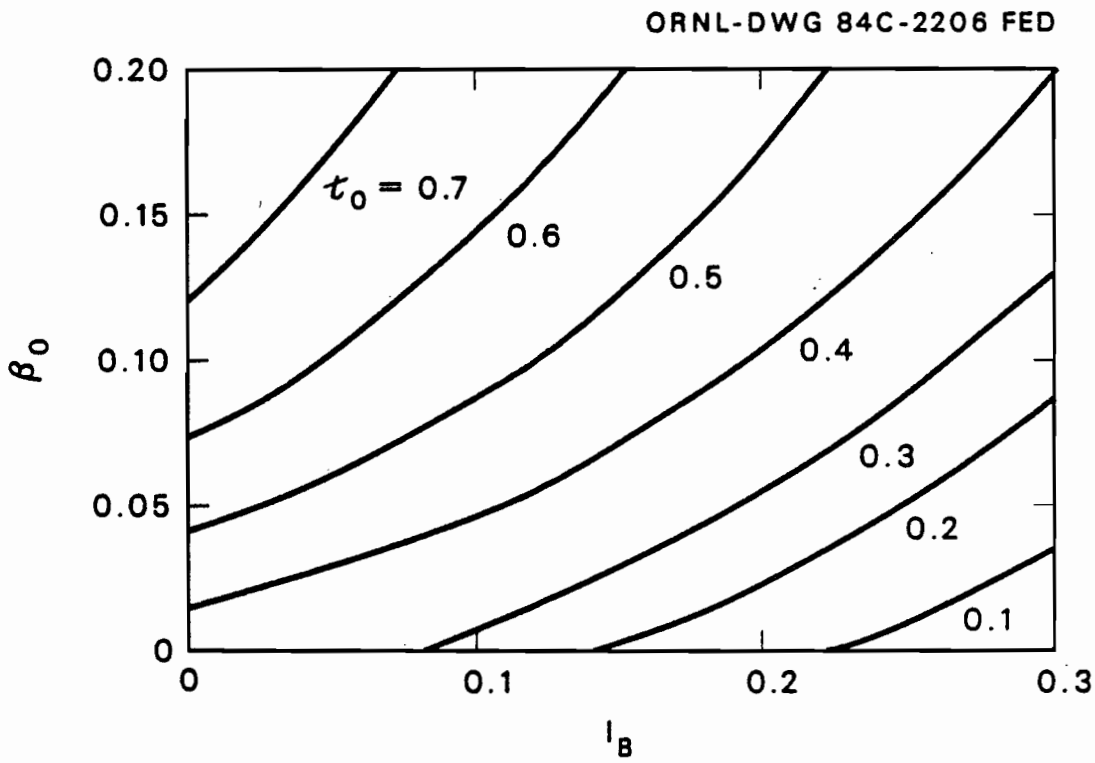

Fig. 3. Paths of constant ι_0 for zero net current equilibria can be followed to high β by increasing I_b with β.

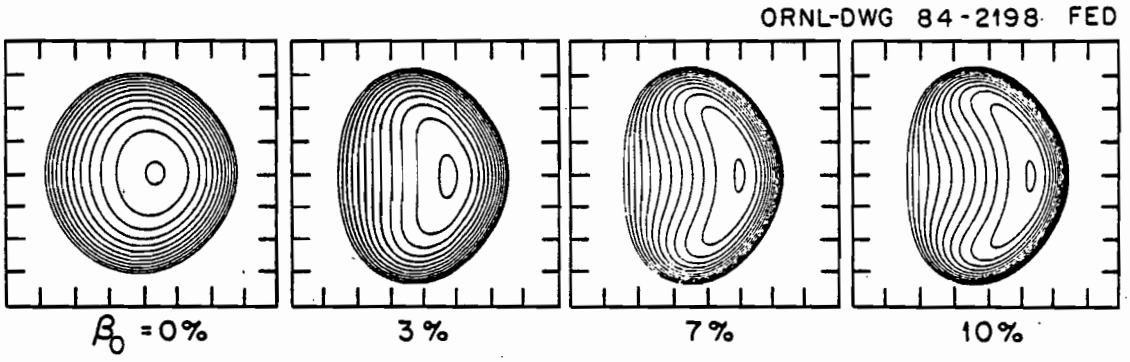

Fig. 4. Increasing I_b elongates the plasma, leading to constant ι_0 for zero net current equilibria as β is increased.

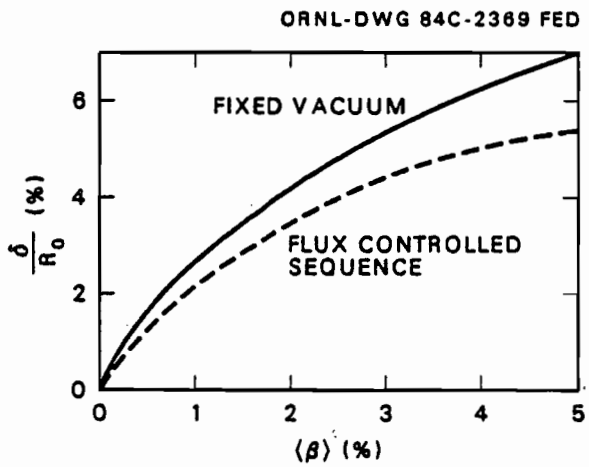

Fig. 5. The magnetic axis shifts are reduced for the flux-controlled sequence.

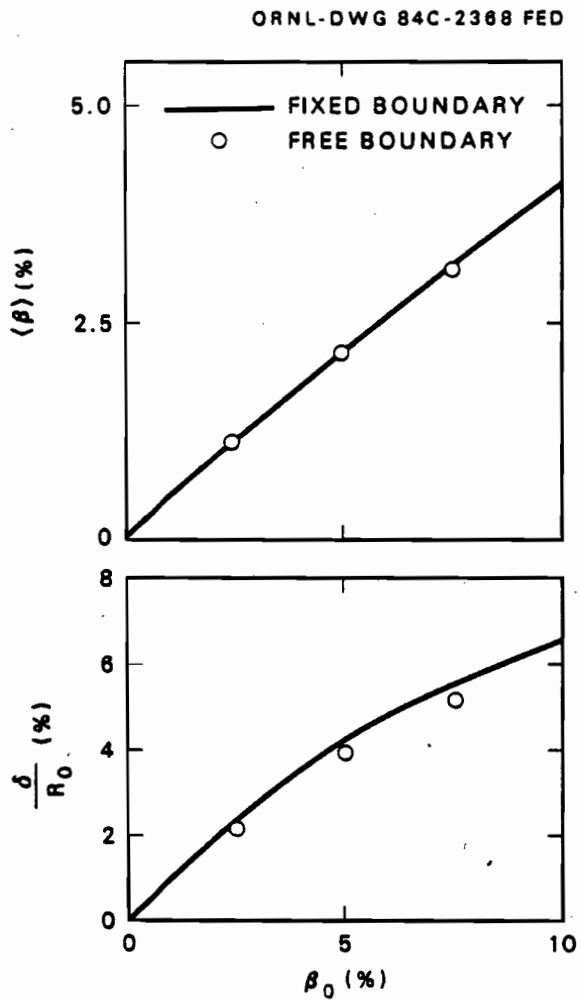

Fig. 6. ⟨β⟩ and magnetic axis shifts δ/R_0 compare well for the fixed- and free-boundary equilibria.

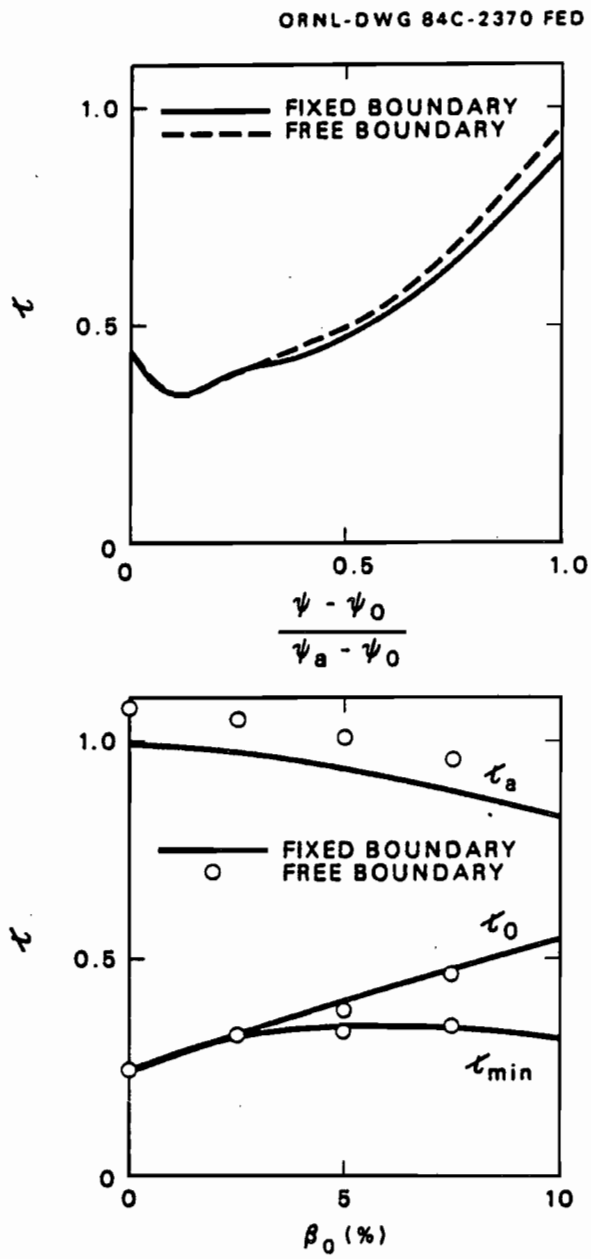

Fig. 7. Rotational transform agreement is good between the fixed- and free-boundary equilibrium codes.

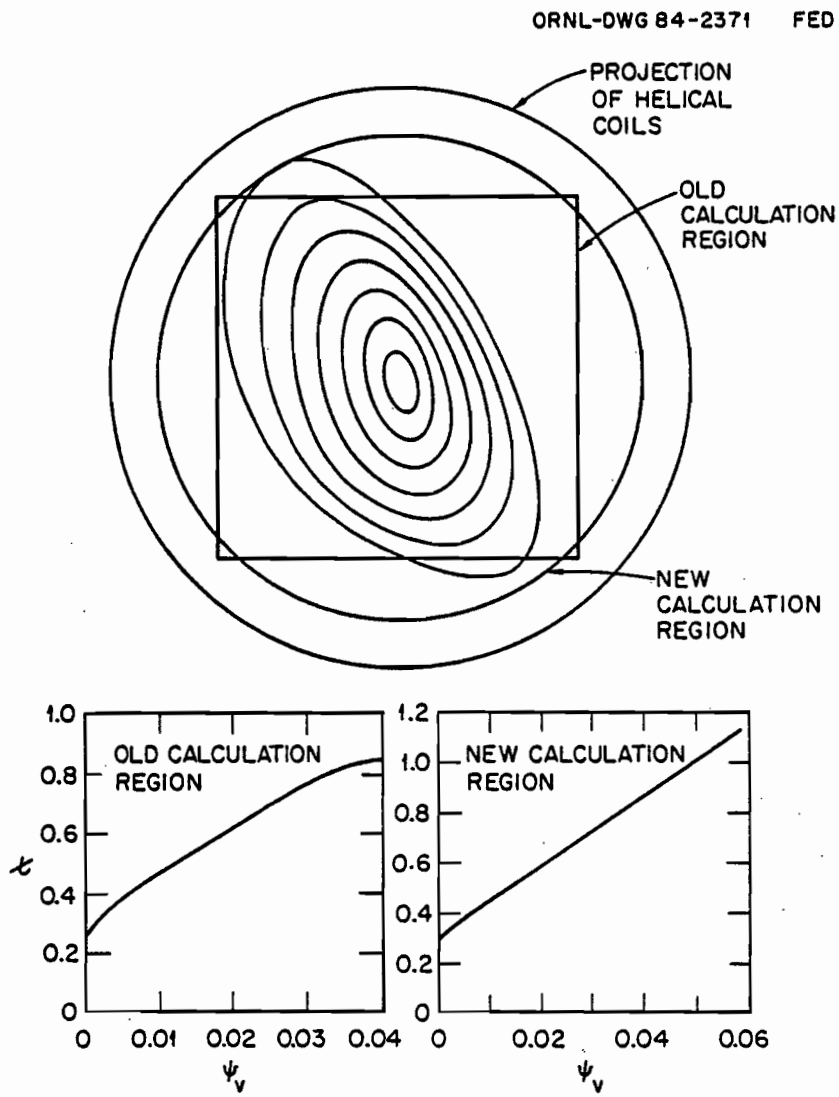

Fig. 8. The present vacuum field calculations incorporate more magnetic surfaces using a circular region than did the previous method using a square box.

REDUCED EQUATIONS IN THREE DIMENSIONAL GEOMETRY

M. S. Chu, T. H. Jensen, and J. S. Kim

GA Technologies Inc.
San Diego, California 92138

ABSTRACT

The nature of the resistive MHD equations is examined in terms of a set of gauge functions based on the magnetic field. A set of reduced equations may be arrived at in this gauge by making the simple assumption that the compressional motion is decoupled from the shear motion. The equations reduce to those first proposed by Strauss and by Chance et al. when the perpendicular perturbation wavelength is much shorter than the equilibrium length scale.

I. INTRODUCTION

The basic nature of the reduced equations[1-3] is that they provide a concise description of the interaction of the shear Alfvén waves in the system. One of the key assumptions in the original Strauss equations is that in the plasma there is a predominant (axially symmetric) toroidal magnetic field. Due to this strong toroidal field, the phenomena under study could be decoupled from the magnetoacoustic branch. As a matter of fact, the magnetoacoustic branch is completely eliminated. In a general fusion configuration, the plasma may evolve into a state in which the magnetic field does not have any predominant symmetry direction. Examples of these devices are the spheromak,[4] stellarator, the various high current pinches (RFP, OHTE,[5] bumpy Z-pinch,[6] etc.), and the very low aspect ratio tokamak. It is the purpose of this paper to extend the formulation of the reduced equations to these configurations.

By representing the electric field in a special gauge, simple assumptions can be made which allow the easy elimination of the magnetoacoustic waves and the clear decoupling of the magnetoacoustic branch from the Alfvén waves. This gauge facilitates the decomposition of the primitive set of equations into links of equation chains with easily solvable links. The gauge functions play the essential role of the Langrangian coordinates[7] for the magnetic field.

The plasma state is no longer specified by the eight variables $(\vec{B},\vec{v},p,\rho)$. Their evolution, instead, is aided by the information on the evolution of the gauge functions ψ, χ and u, specifying the electric field. Further specific assumptions about them provide self-consistent simplifications on the system without affecting the structure of the equations.

II. "REDUCED" EQUATIONS IN AN ARBITRARY CONFIGURATION

The primitive MHD equations which we start with are:

$$\frac{\partial\rho}{\partial t} + \vec{\nabla}\cdot(\rho\vec{v}) = 0 \quad , \tag{1}$$

$$\rho\,\frac{\partial\vec{v}}{\partial t} + \rho(\vec{v}\cdot\vec{\nabla})\vec{v} = -\,\vec{\nabla}p + \vec{J}\times\vec{B} \quad , \tag{2}$$

$$\frac{\partial\vec{B}}{\partial t} = -\,\vec{\nabla}\times\vec{E} \quad , \tag{3}$$

$$\vec{E} = \eta\vec{J} - \vec{v}\times\vec{B} \quad , \tag{4}$$

$$\frac{\partial p}{\partial t} + \vec{v}\cdot\vec{\nabla}p + \Gamma p\vec{\nabla}\cdot\vec{v} = T \quad , \tag{5}$$

and

$$\vec{J} = \vec{\nabla}\times\vec{B} \quad . \tag{6}$$

A completely equivalent description of the plasma state may be specified by adopting the gauge of the electromagnetic field as

$$\vec{E} = -\frac{\partial\psi}{\partial t}\vec{B} - \vec{\nabla}\frac{\partial\chi}{\partial t} \times \vec{B} + \vec{\nabla}u \quad . \tag{7}$$

This gauge is motivated by noting that the fluid velocity $\vec{v}$ is obtained from Eq. (4) as (for plasmas close to MHD equilibria):

$$\vec{v} = \frac{\vec{\nabla}u\times\vec{B}}{B^2} + \vec{\nabla}_\perp\frac{\partial\chi}{\partial t} - \frac{\eta}{B^2}\vec{\nabla}p + \frac{v_\parallel\vec{B}}{B^2} \quad . \tag{8}$$

We see from Eq. (8) that $\vec{v}$ is decomposed into parts which can be identified as the shear motion around the field line, $\vec{\nabla}u\times\vec{B}/B^2$; the compressional motion $\vec{\nabla}_\perp(\partial\chi/\partial t)$; the slippage of the plasma with respect to the field line, $\eta/B^2(\vec{\nabla}p)$; and the motion parallel to the field line $v_\parallel\vec{B}/B^2$. We associate u with the shear Alfvén wave and $\partial\chi/\partial t$ with the magnetoacoustic mode. A description of the plasma state may therefore be obtained by regarding $\vec{B},\psi,\chi,u,\rho,p$ as dependent variables and recast the set of Eqs. (1) through (6) in terms of them. In this set of variables, the decoupling of the shear motion and the compressional motion is relatively easily implemented.

Here ψ is the inductive volt seconds linked by a field line. Its evolution in time is obtainable from the parallel component of Eq. (4) as

$$\frac{\partial\psi}{\partial t} = \frac{1}{B^2}(\vec{B}\cdot\vec{\nabla}u - \eta\vec{J}\cdot\vec{B}) \quad , \tag{9}$$

The elimination of the compressional Alfvén wave is equivalent to the neglect of the mass density in the equation of motion for the compressional component. Or when mass density is ignored, we have the equilibrium relation:

$$\vec{\nabla}p = \vec{J}\times\vec{B} \quad , \tag{10}$$

The compressional component can be used as a dynamical constraint for determining $\nabla_\perp(\partial\chi/\partial t)$. By differentiating Eq. (10) with respect to time, we find

$$\vec{\nabla}\frac{\partial p}{\partial t} - \frac{\partial\vec{J}}{\partial t}\times\vec{B} - \vec{J}\times\frac{\partial\vec{B}}{\partial t} = 0 \quad . \tag{11}$$

In Eq. (11), the time rate of change of the magnetic field consists of two parts

$$\frac{\partial\vec{B}_\psi}{\partial t} = \vec{\nabla}\times\left(\frac{\partial\psi}{\partial t}\vec{B}\right) \quad , \tag{12}$$

$$\frac{\partial\vec{B}_\chi}{\partial t} = \vec{\nabla}\times\left(\vec{\nabla}\frac{\partial\chi}{\partial t}\times\vec{B}\right) \quad . \tag{13}$$

By utilizing Eq. (5), and Eqs. (12) and (13), Eq. (11) can be shown as the Euler equation for the following functional L_χ for a plasma satisfying Eq. (10), with

$$L_\chi\left(\vec{\nabla}_\perp\frac{\partial\chi}{\partial t}\right) = L^\perp_{MHD}\left(\vec{\nabla}_\perp\frac{\partial\chi}{\partial t}\right) = \int\left(\vec{\nabla}_\perp\frac{\partial\chi}{\partial t}\cdot\vec{S}_\chi\right)d\tau \quad , \tag{14}$$

In Eq. (14)

$$L^\perp_{MHD}(\vec{\xi}_\perp) = \frac{1}{2}\int d\tau\ \{[\vec{\nabla}\times(\vec{\xi}_\perp\times\vec{B})]^2 + \vec{J}\cdot\vec{\xi}_\perp\times\vec{\nabla}\times(\vec{\xi}_\perp\times\vec{B})$$
$$+ (\vec{\nabla}_\perp\cdot\vec{\xi}_\perp)(\vec{\xi}_\perp\cdot\vec{\nabla}p + \Gamma p\vec{\nabla}_\perp\cdot\vec{\xi}_\perp)\} \quad , \tag{15}$$

and

$$S_\chi = \left[\left(\nabla \times \frac{\partial \vec{B}_\psi}{\partial t}\right) \times \vec{B}\right] + \left(\vec{J} \times \frac{\partial \vec{B}_\psi}{\partial t}\right) - \vec{\nabla} P_c \quad , \tag{16}$$

and P_c is due to pressure changes.

For the non-equilibrium state under consideration as in usual non-equilibrium dynamics, we regard the function $\partial\chi/\partial t$ minimizing Eq. (14) as the desired solution. This minimizing function $\partial\chi/\partial t$ is the resultant response of the plasma through the eliminated compressional waves. We note that $L^{\perp}_{MHD}$ is the same as the L_{MHD} functional given by Bernstein et al.,[8] except that $L^{\perp}_{MHD}$ allows the displacement to be only in the direction perpendicular to the magnetic field. If the plasma evolves through a sequence of ideal MHD stable equilibria, then $L_{MHD} \geq 0$, the minimizing function, definitely exists. The appropriate boundary condition in Eq. (14) for $\partial\chi/\partial t$ is $\partial\chi/\partial t = 0$ and $\vec{\nabla}(\partial\chi/\partial t) = 0$ at the boundary.

In this manner, the velocity $\vec{v}$ in Eq. (8) is completely determined. To determine the time rate of change of u, we take the $\vec{B}\cdot\vec{\nabla}\times$ component of Eq. (2) to obtain:

$$\frac{\partial}{\partial t}\left[-\vec{\nabla}\cdot\rho\vec{\nabla}u + (\vec{B}\cdot\vec{\nabla})\rho\,\frac{\partial\psi}{\partial t} - \vec{\nabla}\times(\rho\vec{B})\cdot\vec{\nabla}\,\frac{\partial\chi}{\partial t}\right]$$
$$= (\vec{B}\cdot\vec{\nabla})(\vec{J}\cdot\vec{B}) - (\vec{J}\cdot\vec{\nabla})B^2 + S^u_{NL} \quad , \tag{17}$$

where S^u_{NL} is a nonlinear source term.

The terms on the left-hand side of Eq. (17) contain second derivative terms in time. These make the solution of this equation more complicated. We assume that they are negligible in this equation. This is the other major assumption necessary in the decoupling of the equations in this coordinate system. As shown in the next section, the assumption of short perpendicular wavelength in comparison to the parallel wavelength is sufficient to justify this assumption. For a plasma with constant density, this assumption also

is identical to that of the Coulomb gauge condition $\vec{\nabla}\cdot\vec{A} = 0$, which is verified by the chosen gauges.

To complete the listing of the equations, we note that

$$\rho \frac{\partial v_{\parallel}}{\partial t} = - \vec{B}\cdot\vec{\nabla}p - \rho\vec{B}\cdot(\vec{v}\cdot\vec{\nabla})\vec{v} - \rho\vec{v}\cdot \frac{\partial\vec{B}}{\partial t} \quad . \tag{18}$$

The equations for determining ρ and p are the same as Eqs. (1) and (5).

Therefore, we have arrived at a set of first order differential equations in time, Eqs. (1), (5), (9), (17), and (18) for the evolution of ρ, p, ψ, $\nabla^2 u$, and $v_{\parallel}$. The auxiliary functional L_χ in Eq. (14) has to be minimized for $\partial\chi/\partial t$, and the three-dimensional Laplacian ∇^2 has to be inverted to determine $\partial u/\partial t$ from $\nabla^2(\partial u/\partial t)$. The result of the elimination of the compressional Alfvén wave is the minimization of Eq. (14) for $\partial\chi/\partial t$, and the decoupling of $(\partial\chi/\partial t)$ from the equation [Eq. (17)] for $\nabla^2 u$ keeps the equations structurally simple. These equations are the structural equivalent of the Strauss equations in a general configuration.

Although the inversion of ∇^2 is not complicated, the minimization of L_χ to find $\partial\chi/\partial t$ is not very easy in general. In practice, some physical assumptions should be adopted in simplifying the minimization of L_χ. In here, we mention one such possible subsidiary assumption; in L_χ we assume the perpendicular perturbation wavelength can be taken to be much shorter than the equilibrium wavelength. We then obtain

$$L_{MHD}(\vec{\xi}) \approx \int d\tau \; (B^2 + \Gamma p)(\vec{\nabla}\cdot\xi)^2 \quad , \tag{19}$$

$$\vec{S}_\chi \approx - \vec{\nabla}P_c \quad . \tag{20}$$

The minimization of L_χ then leads to

$$(B^2 + \Gamma p)\nabla^2 \frac{\partial \chi}{\partial t} = - P_c \quad . \tag{21}$$

with the boundary condition of $\chi = 0$ at the conducting boundary.

With this last simplification, we have arrived at the systems of Eqs. (1), (5), (9), (17), (18), and (21) for advancing ρ, p, ψ, $\nabla^2 u$, $v_\parallel$, and $\nabla^2\chi$, with two three-dimensional Laplacian equations to be inverted for $\partial u/\partial t$ and $\partial\chi/\partial t$. The sequence of the solution of the equations should be starting with a configuration determined by $\vec{B}$, ψ, χ, u, $v_\parallel$, p, and ρ; Eq. (9) is first used to advance ψ. Equation (24) is used to solve for $\partial\chi/\partial t$, the velocity $\vec{v}$ in Eq. (8) is then determined, Eqs. (1), (5), (17), and (18) can then be used to determine $\partial\rho/\partial t$, $\partial p/\partial t$, $\partial u/\partial t$, and $\partial v_\parallel/\partial t$. Written in this fashion, we did not actually reduce the amount of information in the original set of equations.

However, the structure of the equations makes the introduction of additional physical assumptions easy, such as ignoring $v_\parallel$ or the compressional motion $\vec{\nabla}(\partial\chi/\partial t)$, and results in real reduction.

III. NONLINEAR EVOLUTION WITH "LOCALIZED" PERTURBATIONS

We start with the ordering that the plasma has an equilibrium specified by $\vec{J}_0 \sim \vec{B}_0 \sim P_0 \sim 1$, with equilibrium gradient length $\vec{\nabla}_0 \sim 1$, except that $\vec{B}_0 \times \vec{\nabla}_0(\vec{J}_0 \cdot \vec{B}_0) \sim 1/\varepsilon$. For the perturbation, we assume $\vec{J}_1 \sim 1$, $\partial p/\partial t \sim \varepsilon$, $\partial/\partial t \sim 1$, $\psi \sim \varepsilon^2$, $\chi \sim \varepsilon^3$, $u \sim \varepsilon^2$, $\vec{\nabla}_\parallel \sim 1$, $\vec{\nabla}_\perp \sim 1/\varepsilon$, $\vec{v} \sim \varepsilon$, and $\eta \sim \varepsilon^2$.

Then

$$\frac{\partial \vec{B}}{\partial t} = \left(\vec{\nabla}\frac{\partial\psi}{\partial t} \times \vec{B}\right) - \nabla^2 \frac{\partial\chi}{\partial t}\vec{B} \sim O(\varepsilon) \quad . \tag{22}$$

Since $\partial\vec{B}/\partial t \sim O(\varepsilon)$, we do not need to update $\vec{B}$ for $t \lesssim 1/\varepsilon$. The equilibrium relation [Eq. (12)] gives

$$\nabla^2 \frac{\partial \chi}{\partial t} = \frac{1}{B^2} \frac{\partial p}{\partial t} \quad . \tag{23}$$

This relation is the same as Eq. (21), except we see that in Eq. (23) the natural ordering for pressure is $p_0 \sim \varepsilon$. p_0 has been ordered to be of lower order so that parallel sound wave effect would be kept. Then from Eq. (4) to leading order

$$\rho\vec{v} = \rho \frac{\vec{\nabla}u\times\vec{B}}{B^2} + \rho \frac{v_\parallel \vec{B}}{B^2} \qquad \sim O(\varepsilon) \quad , \tag{24}$$

The perpendicular velocity is dominated by the rotational part of the fluid flow. It is quite easy to write down that

$$\frac{\partial \rho}{\partial t} = \rho\Big[\frac{\vec{\nabla}\times\vec{B}}{B^2}\cdot\vec{\nabla}u - (\vec{B}\cdot\vec{\nabla})\frac{v_\parallel}{B^2} + \vec{\nabla}\cdot\Big(\frac{\eta}{B^2}\vec{\nabla}p\Big) - \frac{1}{B^2}\frac{\partial p}{\partial t}\Big]$$

$$- \frac{\vec{\nabla}u\times\vec{B}}{B^2}\cdot\vec{\nabla}\rho \qquad \sim O(\varepsilon) \quad , \tag{25}$$

$$\Big(1 + \frac{\Gamma p}{B^2}\Big)\frac{\partial p}{\partial t} = -\frac{\vec{\nabla}u\times\vec{B}}{B^2}\cdot\vec{\nabla}p - \Gamma p\Big[(\vec{B}\cdot\vec{\nabla})\Big(\frac{v_\parallel}{B^2}\Big) + \vec{\nabla}\cdot\frac{\vec{\nabla}u\times\vec{B}}{B^2}$$

$$- \vec{\nabla}\cdot\Big(\frac{\eta}{B^2}\vec{\nabla}p\Big)\Big] \qquad \sim O(\varepsilon) \quad , \tag{26}$$

$$\frac{\partial \psi}{\partial t} = \frac{1}{B^2}(\vec{\nabla}u\cdot\vec{B} - \eta\vec{J}\cdot\vec{B}) \qquad \sim O(\varepsilon^2) \quad , \tag{27}$$

$$\frac{\partial}{\partial t}\vec{\nabla}\cdot(\rho\vec{\nabla}u) = -(\vec{B}\cdot\vec{\nabla})(\vec{J}\cdot\vec{B}) + (\vec{J}\cdot\vec{\nabla})B^2 - \vec{\nabla}_\perp\cdot\vec{\nabla}(\rho\nabla^2 u) \quad , \tag{28}$$

$$\rho \frac{\partial v_\parallel}{\partial t} = - (\vec{B}\cdot\vec{\nabla})p - \rho(\vec{v}_\perp\cdot\vec{\nabla})v_\parallel \quad . \tag{29}$$

This set of nonlinear coupled differential equations [Eqs. (25) through (29)] may be used for the study of the nonlinear evolution of small amplitude localized Alfvén wave perturbations. In the linear regime, $\vec{v} = 0$ at equilibrium, the density equation [Eq. (25)] is decoupled from the rest of the equations. By denoting $\gamma = \partial/\partial t$, we obtain

$$\left(1 + \frac{\Gamma p}{B^2}\right) \gamma p = - \frac{\vec{\nabla}p_0\times\vec{\nabla}u\cdot\vec{B}_0}{B_0^2} - \Gamma p_0\left[(\vec{B}_0\cdot\vec{\nabla})\left(\frac{v_\parallel}{B_0^2}\right) + \nabla\cdot \frac{\vec{\nabla}u\times\vec{B}_0}{B_0^2}\right.$$

$$\left. - \vec{\nabla}\cdot\left(\frac{\eta}{B_0^2}\vec{\nabla}p\right)\right] \quad , \tag{30}$$

$$\gamma\psi = + \frac{\vec{B}_0\cdot\vec{\nabla}u - \eta\vec{J}_1\cdot\vec{B}_0}{B_0^2} \quad , \tag{31}$$

$$\gamma\rho_0\nabla_\perp^2 u = - (\vec{B}_0\cdot\vec{\nabla})\vec{J}_1\cdot\vec{B}_0 - (\vec{B}_1\cdot\vec{\nabla})\vec{J}_0\cdot\vec{B}_0 + (\vec{J}_1\cdot\vec{\nabla})B^2$$

$$+ (\vec{J}_0\cdot\vec{\nabla})(B^2)_1 \quad , \tag{32}$$

$$\gamma\rho_0 v_\parallel = - (\vec{B}_1\cdot\vec{\nabla})p_0 - (\vec{B}_0\cdot\vec{\nabla})p \quad , \tag{33}$$

By substituting Eq. (22) into Eqs. (30) through (33), we note this set is similar to the set which has been used by Strauss with $\Gamma = 5/3$, $\psi = A_\parallel/B$, $v_\parallel \to v_\parallel B_0$, and $J_0 \to -J_0$, to study the resistive ballooning mode. This set is also identical to the high n ordering equations used by Chance et al.[9] except that the current density gradient term has been kept. This is appropriate for intermediate n numbers in which the effect of current density gradient and the pressure gradient and curvature force both affect the shear Alfvén wave.[10]

IV. CONCLUSION

In conclusion, a new approximate reduced set of equations for the interaction of shear Alfvén waves in a general magnetic configuration is given by the set of equations, Eqs. (1), (5), (17), (18) and (21), with auxiliary conditions given by Eqs. (8) and (12). The assumption of localized modes with perpendicular wavelength much shorter than the equilibrium wavelength reduces the set to that given by Strauss and Chance et al. The numerical implementation for a high current pinch configuration is particularly simple. It could be modified from the known schemes for the Strauss equation, such as HIB.[11]

The authors would like to acknowledge stimulating discussions with Drs. C. S. Liu, Y. C. Lee, and J. K. Lee. This work was supported by U.S. DOE Contract DE-AT03-84ER53158.

V. REFERENCES

[1]H. R. Strauss, Phys. Fluids 20, 1354 (1977); and H. R. Strauss, Phys. Fluids 24, 2004 (1981).

[2]R. Schmalz, Phys. Lett. 82A, 14 (1981); and E. Edery et al., Computer Phys. Comm. 24, 427 (1981).

[3]B. A. Carreras et al, Phys. Fluids 24, 66 (1981); and J. A. Holmes et al., Phys. Fluids 25, 800 (1982).

[4]M. N. Rosenbluth and M. N. Bussac, Nucl. Fusion 19, 489 (1979).

[5]T. Ohkawa et al., Nucl. Fusion 20, 1464 (1980).

[6]T. H. Jensen and M. S. Chu, J. Plasma Phys. 25, 459 (1981).

[7]A. Schlüter and U. Schwenn, Computer Phys. Comm. 24, 263 (1981).

[8]I. B. Bernstein et al., Proc. Roy. Soc. 244, 17 (1957).

[9]M. S. Chance et al., in Plasma Physics and Controlled Thermonuclear Fusion Research (IAEA, Vienna, 1978), Vol. I, p. 677.

[10]C. Chu et al., Proceedings of 1983 Sherwood Theory Meeting, paper 1C2.

[11]W. Park et al., Bull. Am. Phys. Soc. 23, 779 (1978).

THREE-DIMENSIONAL MHD IN THE REVERSED-FIELD PINCH*

D. D. Schnack, D. C. Baxter
Applied Plasma Physics and Technology Division
Science Applications, Inc.
La Jolla, CA 92038

E. J. Caramana, R. A. Nebel, R. A. Gerwin
Los Alamos National Laboratory
Los Alamos, NM 87544

I. INTRODUCTION

It is now well established that multidimensional nonlinear resistive magnetohydrodynamics (MHD) is an excellent model for the description of the macroscopic dynamics of present magnetic fusion experiments. Two-dimensional simulation of these processes has become commonplace [1-3]. Such calculations have provided valuable insights into the interpretation of experimental diagnostics [4], and the nonlinear behavior of unstable modes in various devices [1,5,6,7].

It has recently been recognized that two-dimensional motions, while enlightening, do not represent the true state of plasma dynamics, and that fully three-dimensional calculations are required [8,9]. For tokamak plasmas, where one component of the magnetic field is everywhere large, it is possible to derive a reduced set of equations that adequately describes the dynamics of these devices [10]. Three-dimensional simulations of these equations have provided a detailed picture of plasma evolution [8,9,11]. These calculations can proceed much faster than solutions of the original equations. In other magnetic fusion devices, such as the spheromak and the reversed field pinch, no such generally applicable set of reduced equations exists at present, and one must solve the primitive equations. Incompressibility may provide some computational relief [12] but this assumption can only be justified a posteriori.

*Work supported by U.S. DOE contract DE-AC03-83ER53150.

The periodic nature of the poloidal and toroidal directions in many fusion devices allows solutions to be represented by Fourier series in these coordinates. Simulations of tokamak plasmas with reduced equations have found that only a handful of these modes are important to the dynamics [13]. Codes developed for the solution of such problems have made use of this fact by introducing a mode selection process whereby only a few modes are retained in the calculation [14]. This procedure has also been used in incompressible simulations of the primitive equations [12]. The convolution sums that arise from the Fourier representation of quadratic nonlinearities in configuration space are then computed directly.

In fusion devices such as the Reversed-Field Pinch or the Spheromak no a priori mode selection is possible. Indeed, there is reason to believe that many large scale modes will be equally important [7]. Thus a large number of mode interactions are probable. These large scale motions may serve to drive small scale MHD turbulence, which may be responsible for such important physical effects as dynamo action and profile maintenance. Also, the particular path taken in the cascade of energy from long to short wavelength (along with the possibility of inverse cascades from short to long wavelength) is unknown and may be important. A large number (>100) of modes must therefore be retained in such calculations.

The physical and computational problems described above are similar to those encountered in the simulation of turbulent hydrodynamic flows. Accurate and efficient methods have been developed for the solution of these problems [15-20]. These spectral methods are based on the use of the Fast Fourier Transform (FFT), which allows the convolution sums to be evaluated in $O(N\ln_2 N)$ operations, as opposed to $O(N^2)$ operations for direct summation [15]. This allows many modes to be used in the simulation. In this paper we describe codes based on these methods [21], and briefly present some results.

II. BASIC EQUATIONS

The study of large-scale dynamics in fusion and astrophysical plasmas involves the description of motions that occur on long time scales. In these cases the plasma acts as an electrically conducting fluid whose motions are adequately described by the single-fluid resistive magnetohydrodynamic (MHD) equations. In a suitable non-dimensional form, they are

$$\frac{\partial \underline{B}}{\partial t} = -\underline{v} \cdot \nabla \underline{B} + \underline{B} \cdot \nabla \underline{v} - \underline{B} \nabla \cdot \underline{v} + \eta_o \nabla^2 \underline{B} - \nabla \eta_o x (\nabla \times \underline{B}) \tag{1a}$$

$$\frac{\partial \underline{v}}{\partial t} = -\underline{v} \cdot \nabla \underline{v} + \frac{1}{\rho} \underline{B} \cdot \nabla \underline{B} - \frac{1}{2\rho} \nabla (p + B^2) \tag{1b}$$

$$\frac{\partial \rho}{\partial t} = -\underline{v} \cdot \nabla \rho - \rho \nabla \cdot \underline{v} \tag{1c}$$

$$\frac{\partial p}{\partial t} = -\underline{v} \cdot \nabla p - \gamma p \nabla \cdot \underline{v} + 2(\gamma - 1)\ \eta_o (\nabla \times \underline{B})^2 - \frac{p}{\tau} \tag{1d}$$

where $\underline{B}$ is the magnetic field measured in units of a characteristic field B_o, $\underline{v}$ is the velocity measured in units of the Alfvén velocity $v_A = B_o/\sqrt{4\pi\rho_o}$, ρ is the mass density measured in units of a characteristic density ρ_o, p is the thermodynamic pressure measured in units of $p_o = B_o^2/8\pi$, γ is the ratio of specific heats, and all lengths are measured in units of a characteristic length a. The coefficient η_o is a nondimensional resistivity that may be a function of the dependent variables. When the resistivity is constant in space and time, η_o is the inverse of the Lundquist number $S = t_R/t_A$, where $t_R = c^2\eta/4\pi a^2$ is the resistive diffusion time and $t_A = a/v_A$ is the Alfvén transit time. Note that S is defined in terms of the normalization constants, and is not to be confused with the magnetic Reynolds number R_M, which is defined in terms of local quantities. The last term in Eq. (1d) represents energy losses not directly encompassed by the model, and is included to control the effects of Joule heating on plasma beta ($\beta \equiv 8\pi p/B^2$).

When η_o vanishes, Eqs. (1a)-(1d) define the ideal MHD model. A finite value of η_o relaxes the flux topology constraints of these equations with the result that previously unallowed motions are possible [22]. These new dynamical processes are essential for an adequate description of fusion and astrophysical plasmas. The inclusion of further dissipative processes, such as ion viscosity or thermal conduction, removes no further constraints on the magnetic topology. We thus exclude these effects from the model.

We note that the compressible nature of Eqs. (1a)-(1d) admits the propagation of Alfvén (fast magnetosonic) waves perpendicular to the field. These waves evolve on a time scale defined by a cross-field scale length divided

by the Alfvén velocity. For a diffuse pinch this length scale is the minor radius. Since many phenomena of interest occur on much longer time scales, this presents a computational problem. In tokamaks one component of the magnetic field is everywhere large. This allows a self-consistent ordering in which the plasma becomes incompressible, and the magnetosonic wave is eliminated [10]. The remaining high-frequency normal mode is the shear Alfvén wave propagating parallel to the field. This wave evolves on a time scale defined by a parallel scale length divided by the Alfvén velocity. In fusion experiments in which the incompressible ordering is valid, this scale length is the major radius. Thus in these cases the fast time scale is increased by a factor that is of the order of the aspect ratio, thereby greatly reducing the computational requirements. However, in general such orderings are not possible, and there is no a priori justification for eliminating compressibility from the model. Indeed, for highly sheared, low q devices such as the reversed field pinch a shear Alfvén wave travelling near the field reversal surface evolves on a time scale that is on the order of the minor radius divided by the Alfvén velocity, i.e., the same order as that of the compressible wave. We thus retain compressibility in our model.

III. NUMERICAL METHODS

In the numerical solution of Eqs. (1a)-(1d) in cylindrical geometry (r,θ,ς) the state variable $\underline{U} = (B_r, B_\theta, B_\varsigma, v_r, v_\theta, v_\varsigma, \rho, p)$ is represented on mesh of $N_r \times N_\theta \times N_\varsigma$ grid points $(r_i,\ i = 1,N_r;\ \theta_j,\ j = 1,N_\theta;\ \varsigma_k,\ k = 1,N_\varsigma)$. The spacing in the poloidal (θ) and toroidal (ς) directions is uniform such that $\Delta\theta = 2\pi/N_\theta$, $\Delta^\varsigma = 2\pi/N_\varsigma$. We allow for nonuniform mesh spacing in the radial coordinate, but in practice a uniform spacing $\Delta r = a/(N_r-1)$ is used.

The periodic nature of the solution vector $\underline{U}$ with respect to the θ and ς coordinates allows a spectral representation to be employed for the finite approximation of spatial operators in these directions, since this representation is uniformly convergent at the boundaries 0 and 2π. The radial coordinate is treated by the method of finite differences.

When the periodic function $u(\theta,\varsigma)$ is approximated by MxN data points (e.g., stored on a mesh), it can be represented by the finite Fourier series

$$U_{MN}(\theta_j,\varsigma_k,t) = \sum_{n=-M/2+1}^{M/2} \sum_{n=-N/2+1}^{N/2} a_{m,n}(t)e^{i(m\theta_j + n\varsigma_k)} \quad , \tag{2}$$

with

$$a_{m,n}(t) = \frac{1}{MN} \sum_{j=1}^{M} \sum_{k=1}^{N} U_{MN}(\theta_j \varsigma_k, t) e^{-i(m\theta_j + n\varsigma_k)} \quad . \tag{3}$$

Here $U_{MN}(\theta_j, \varsigma_k, t)$ is the MN-term approximation to the function $U(\theta, \varsigma, t)$ evaluated at the mesh point (θ_j, ς_k) at time t; $\theta_j = (j - 1)2\pi/M$ and $\varsigma_k = (k - 1)2\pi/N$. The derivatives $\partial u/\partial\theta$ and $\partial u/\partial\varsigma$ at the point (θ_j, ς_k) and time t are given by

$$\left(\frac{\partial u_{MN}}{\partial\theta}\right)_{j,k} = \sum_{m=-M/2+1}^{M/2} \sum_{n=-N/2+1}^{N/2} ima_{m,n}(t) e^{i(m\theta_j + n\varsigma_k)} \quad . \tag{4a}$$

$$\left(\frac{\partial u_{MN}}{\partial\varsigma}\right)_{j,k} = \sum_{m=-M/2+1}^{M/2} \sum_{n=-N/2+1}^{N/2} ina_{m,n}(t) e^{i(m\theta_j + n\varsigma_k)} \quad . \tag{4b}$$

The spectral representation of the equations of motion is obtained by employing Eqs. (2) and (4) in some appropriate manner in the right hand side of the Eq. (1a-d). If this is done in a straight forward manner, the quadratic nonlinearities inherent in these equations leads to convolution sums whose direct evaluation requires $O(N^2)$ operations, making such methods excessively expensive except when a handful of modes is employed. However, when fast Fourier Transforms are used [23], the operation count is reduced to $O(N\ell nN)$, making it comparable in speed to finite differences. These methods are called pseudospectral.

The pseudospectral approximation takes advantage of the fact that multiplication is most efficiently performed in configuration space and differentiation is most accurately performed in Fourier space. Fast Fourier Transforms are used to communicate between the two representations. In principle it is irrelevant whether the dependent variables are the N Fourier coefficients or the values of $u(x_j)$ stored at the N mesh points x_j in configuration space. In the first case the transformation is made to configuration space to perform the convolution; in the second case the transformation is made to Fourier space to

perform the differentiation. Both methods have the same accuracy. Because of its familiarity, we have chosen the configuration space representation.

It is well known that these methods can lead to a physically realistic and rapidly convergent approximation to a linear equation. When nonlinearities are present, as discussed above, these methods are subject to aliasing errors [15,17,18,20] that arise from the generation by quadratic nonlinearities of modes with wavelengths shorter than $\pi/\Delta x$. These errors are caused by modes in the "high" end of Fourier space; they can be prevented by removing the offending modes from the problem. This is accomplished by truncating Fourier space at some value M^*. Modes outside this range are set to zero, since it is these terms that contain the aliasing errors. It can be shown that it is sufficient to set $M^* < N/3$, where N is the number of mesh points in a periodic direction. Since $k_{max} = N/2$, aliasing errors are prevented by using 2/3 of available Fourier space.

We employ explicit leapfrog with averaging for the temporal approximation to the advective terms. The diffusive terms are treated implicitly in Fourier space.

IV. RESULTS OF THREE-DIMENSIONAL SIMULATIONS

We have previously studied the nonlinear evolution of $m = 1$ tearing modes in RFP plasmas in single helicity [7]. To study three-dimensional mode coupling effects, we pose an initial value problem consisting of an equilibrium [7] and two unstable $m = 1$ modes with axial mode numbers $n = -10$ and $n = -11$. We use a mesh with 65 radial, 8 poloidal, and 64 axial points. In Fig. 1 we show the evolution of the radial magnetic energy in these modes as a function of time for both single helicity and three-dimensional simulations. We see that saturation occurs sooner and at a lower level when three-dimensional effects are included. This is because the mode coupling to a larger part of Fourier space allows energy to be drained from the $m = 1$ modes. This is illustrated in Fig. 2, where we plot the energy in various $m = 0$ and $m = 2$ modes for the three-dimensional case. Note that $m = 2$ possesses more energy than $m = 0$ [24].

In Fig. 3 we plot the evolution of $q(o)$, the safety factor at $r = 0$, as a function of time for both single helicity and multi-helicity simulations. We see that the rise in $q(o)$ is significantly slowed when the extra three-dimensional mode couplings are included.

V. REDUCED RELAXATION MODEL FOR DRIVEN SYSTEMS

A problem of interest in RFP and CT plasmas is the dynamics of relaxation to a force-free state [25]. Recent experimental schemes for providing steady-state current and flux regeneration in both RFPs [26] and spheromaks [27] probably depend in part on the existence of these relaxation phenomena. In order to assess these schemes and to understand their utility, these inherently three-dimensional problems must be addressed. However such motions occur on time scales long compared to Alfvén times, and hence present computational difficulties if the model described in the previous sections is employed.

In this section we present a computational model for the simulation of these processes. Codes based on this model are presently under development. We assume that the plasma relaxes to a force-free state through the action of perpendicular perturbation currents alone; the pressure is ignored. Fast time scales are eliminated by replacing the time derivative in the momentum equation with a phenomenological drag. Thus displacements away from the force-free state are damped; the plasma always relaxes. With these assumptions, the combination of Ampéres law and Ohm's law yields an anisotropic diffusion equation for the vector potential that completely describes the response of the system to electric fields driven at the boundaries. With the proper choice of gauge a tractable computational model is obtained. The model is similar to one previously used to compute three-dimensional force-free equilibria [28].

We picture a system in which the plasma is continually driven away from a force-free state by the imposition of slowly varying electric fields at the boundary. We are not interested in the details of the flow during the ensuing relaxation; it merely provides a means by which the relaxation can take place. We thus replace the time derivative in the momentum equation by a phenomenological drag coefficient ν, and ignore the pressure. (The latter is strictly justified only when $\delta p \ll \delta B^2$, but it is in the spirit of the model.) Then using the resulting velocity in Ohm's law yields

$$\underline{E} = \underline{\underline{\eta}} \cdot \underline{J} = \eta_\perp \underline{J}_\perp + \eta_\parallel \underline{J}_\parallel \tag{5}$$

where $\eta_{\parallel} = \eta_0$, and $\eta_{\perp} = \eta_{\parallel} + B^2/\rho\nu$ is an effective perpendicular resistivity that damps the perturbations. Introducing the vector potential $\underline{B} = \nabla\times\underline{A}$, we find

$$\frac{\partial \underline{A}}{\partial t} = -\underline{\underline{\eta}}\cdot\underline{J} \quad , \tag{6}$$

$$\underline{J} = \nabla \times \nabla \times \underline{A} \quad . \tag{7}$$

If we choose the gauge $A_r = 0$ (in cylindrical coordinates), and specify $E_\theta(t)$ and $E_z(t)$ at the outer boundary, Eqs. (6) and (7) become a coupled set of diffusion equations in the unknowns A_θ and A_z:

$$\frac{\partial A_\theta}{\partial t} = -\eta_{\theta r}J_r - \eta_{\theta\theta}J_\theta - \eta_{\theta z}J_z \quad , \tag{8}$$

$$\frac{\partial A_z}{\partial t} = -\eta_{zr}J_r - \eta_{z\theta}J_\theta - \eta_{zz}J_z \quad . \tag{9}$$

By introducing a staggered mesh, finite representations that preserve the properties of the continuum can be obtained.

Nonlinearities in Eqs. (8) and (9) arise because the Euler angle transformation required to define the space centered components of $\underline{\underline{\eta}}$ is a function of the instantaneous fluctuating magnetic field. We treat these nonlinearities by writing

$$\frac{\partial \underline{A}}{\partial t} = -\underline{\underline{\eta}}\cdot\underline{\underline{J}}\cdot\underline{A} \quad , \tag{10}$$

where $\underline{A}$ and $\underline{\underline{\eta}}$ contain both mean and fluctuating parts. Taking the spatial average of (10) allows these components to be separated. We find

$$\frac{\partial \underline{A}_0}{\partial t} = -\underline{\underline{\eta}}_0\cdot\underline{\underline{J}}_0\cdot\underline{A}_0 - \langle\delta\underline{\underline{\eta}}\cdot\underline{\underline{j}}\cdot\underline{a}\rangle \tag{11a}$$

$$\frac{\partial \underline{a}}{\partial t} = - \underline{\underline{\eta}}_0 \cdot \underline{\underline{j}} \cdot \underline{a} - \delta \underline{\underline{\eta}} \cdot \underline{\underline{J}}_0 \cdot \underline{A}_0 \tag{11b}$$

The operators $\underline{\underline{\eta}}_0 \cdot \underline{\underline{J}}_0$ and $\underline{\underline{\eta}}_0 \cdot \underline{\underline{j}}$ are now linear. These equations are solved iteratively.

REFERENCES

1. B. V. Waddell, M. N. Rosenbluth, D. A. Monticello, and R. B. White, Nucl. Fusion 16, 528 (1976).
2. B. Carreras, B.V. Waddell, H.R. Hicks, and S.J. Lynch, Phys. Rev. A 18, 735 (1978).
3. D. Schnack and J. Killeen, J. Comp. Phys. 35, 110 (1980).
4. G.L. Jahns, M. Soler, B.V. Waddell, J.D. Callen, and H.R. Hicks, Nucl. Fusion 18, 609 (1978).
5. D. Schnack and J. Killeen, Nucl. Fusion 19, 877 (1979).
6. D.D. Schnack, J. Killeen, and R.A. Gerwin, Nucl. Fusion 21, 447 (1981).
7. E.J. Caramana, R.A. Nebel, and D.D. Schnack, Phys. Fluids 26, 1305 (1983).
8. B.V. Waddell, B. Carreras, H.R. Hicks, and J.A. Holmes, Phys. Fluids 22, 896 (1979).
9. B. Carreras, H.R. Hicks, J.A. Holmes, and B. Waddell, Phys. Fluids 23, 1811 (1980).
10. H. Strauss, Phys. Fluids 19, 134 (1976).
11. B. Carreras, H.R. Hicks, and D.K. Lee, Phys. Fluids 24, 66 (1981).
12. A.Y. Aydemir and D.C. Barnes, J. Comp. Phys. 53, 100 (1984).
13. B.A. Carreras, M.N. Rosenbluth, and H.R. Hicks, Phys. Rev. Letters 46, 1131 (1981).
14. H.R. Hicks, B.A. Carreras, J.A Holmes, D.K. Lee, and B.V. Waddell, J. Comp. Phys. 44, 46 (1981).
15. S.A. Orszag, Stud. App. Math. 50, 293 (1971).
16. S.A. Orszag, J. Fluid Mech. 49, 75 (1971).
17. S.A. Orszag, Stud. App. Math. 51, 253 (1972).
18. G.S. Patterson, Jr., and S.A. Orszag, Phys. Fluids 14, 2538 (1971).
19. D.G. Fox and S.A. Orszag, J. Comp. Phys. 11, 612 (1973).

20. D. Gottlieb and S.A. Orszag, "Numerical Analysis of Spectral Methods: Theory and Applications," SIAM, Philadelphia (1977).
21. D. D. Schnack, D. C. Baxter, and E. J. Caramana, Science Applications, Inc. report SAI02383-477LJ/APPAT-14, September 1983, accepted for publication in J. Comp. Phys. (1984).
22. H.P. Furth, J. Killeen, and M.N. Rosenbluth, Phys. Fluids 6, 459 (1963).
23. C. Temperton, Comp. Phys. Comm. 26, 331 (1982).
24. J. A. Holmes, B. A. Carreras, T. C. Hender, H. R. Hicks, and V. E. Lynch, Bull. Am. Phys. Soc. 28, 1230 (1983).
25. J. B. Taylor, Phys. Rev. Lett. 33, 1139 (1974).
26. M. K. Bevir and J. W. Gray, Proc. RFP Theory Workshop, LA-8944-C, Los Alamos Report (1980).
27. T. Jarboe, private communication (1983).
28. M. S. Chu, T. H. Jensen, and B. Dy, Phys. Fluids 25, 1611 (1982).

FIGURE CAPTIONS

Fig. 1. Energy in the (a) m = 1, n = -10, and (b) m = 1, n = -11 modes as a function of time for both single helicity and three-dimensional evolution.

Fig. 2. Energy in the (a) m = 0, n = 1; (b) m = 0, n = 2; (c) m = 2, n = -21; and (d) m = 2, n = -22 modes of the radial magnetic field as a function of time for the three-dimensional low-β case.

Fig. 3. q(o) as a function of time for the single helicity evolution of (a) the m = 1, n = -10 mode; (b) the m = 1, n = -11 mode; and (c) the fully three-dimensional, high-β case.

Fig. 4. Field line plots (surfaces of section) in the (r,z) plane at various times for evolution at low-β.

Fig. 5. Field line plots (surfaces of section) in the (r,z) plane at various times for the evolution at high-β.

Fig. 6. m = 0 magnetic islands for n = 1, 2, and 3 for the low-β case of Fig. 4.

Fig. 7. m = 0 magnetic islands for n = 1, 2, and 3 for the high-β case of Fig. 5.

Fig. 8. (a) axial magnetic flux contained within the field reversal surface r_v; (b) m = 0, n = 0 component of the poloidal electric field at the field reversal surface; and (c) poloidal mode contributions to the mean poloidal electric field at the field reversal surface, as functions of time for the three-dimensional high-β case.

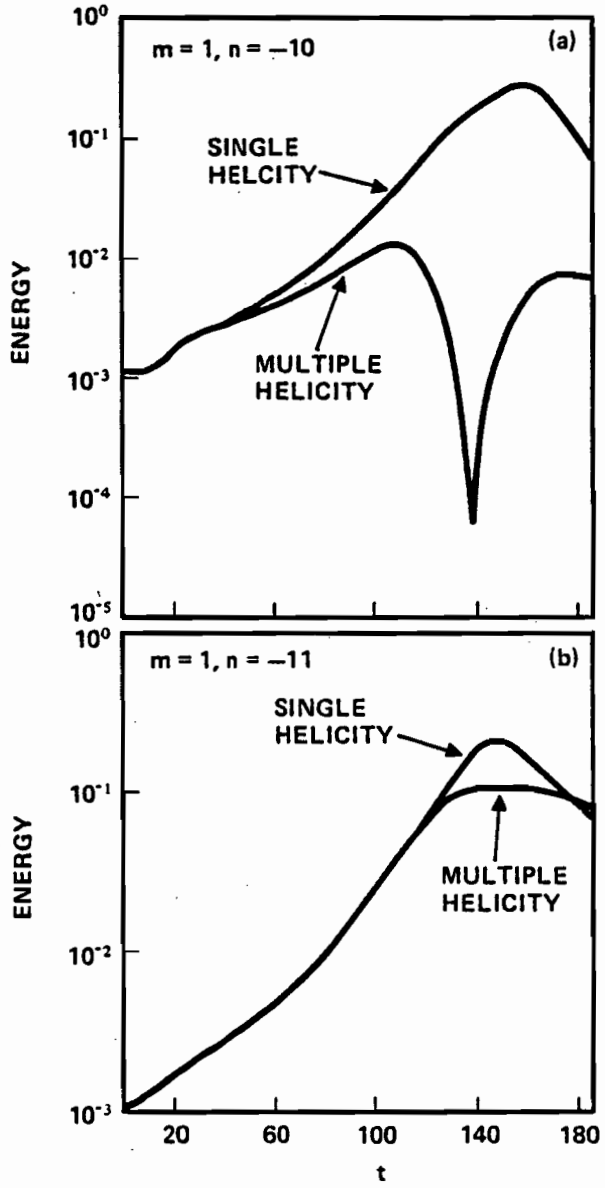
m = 1, n = –10
(a)
SINGLE
HELCITY
MULTIPLE
HELICITY
ENERGY
10^0
10^{-1}
10^{-2}
10^{-3}
10^{-4}
10^{-5}
m = 1, n = –11
(b)
SINGLE
HELICITY
MULTIPLE
HELICITY
ENERGY
10^0
10^{-1}
10^{-2}
10^{-3}
20
60
100
140
180
t

Figure 1

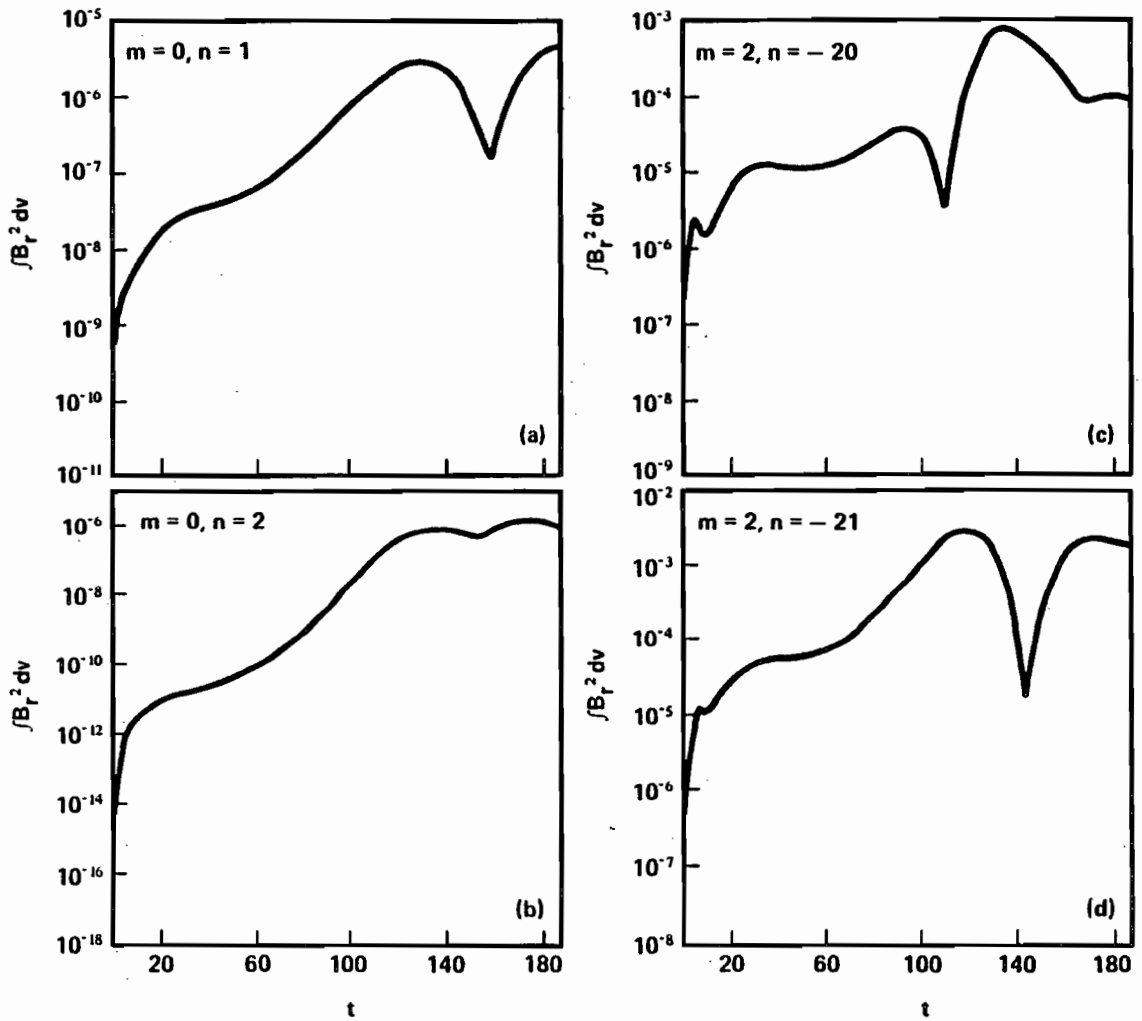

Figure 2

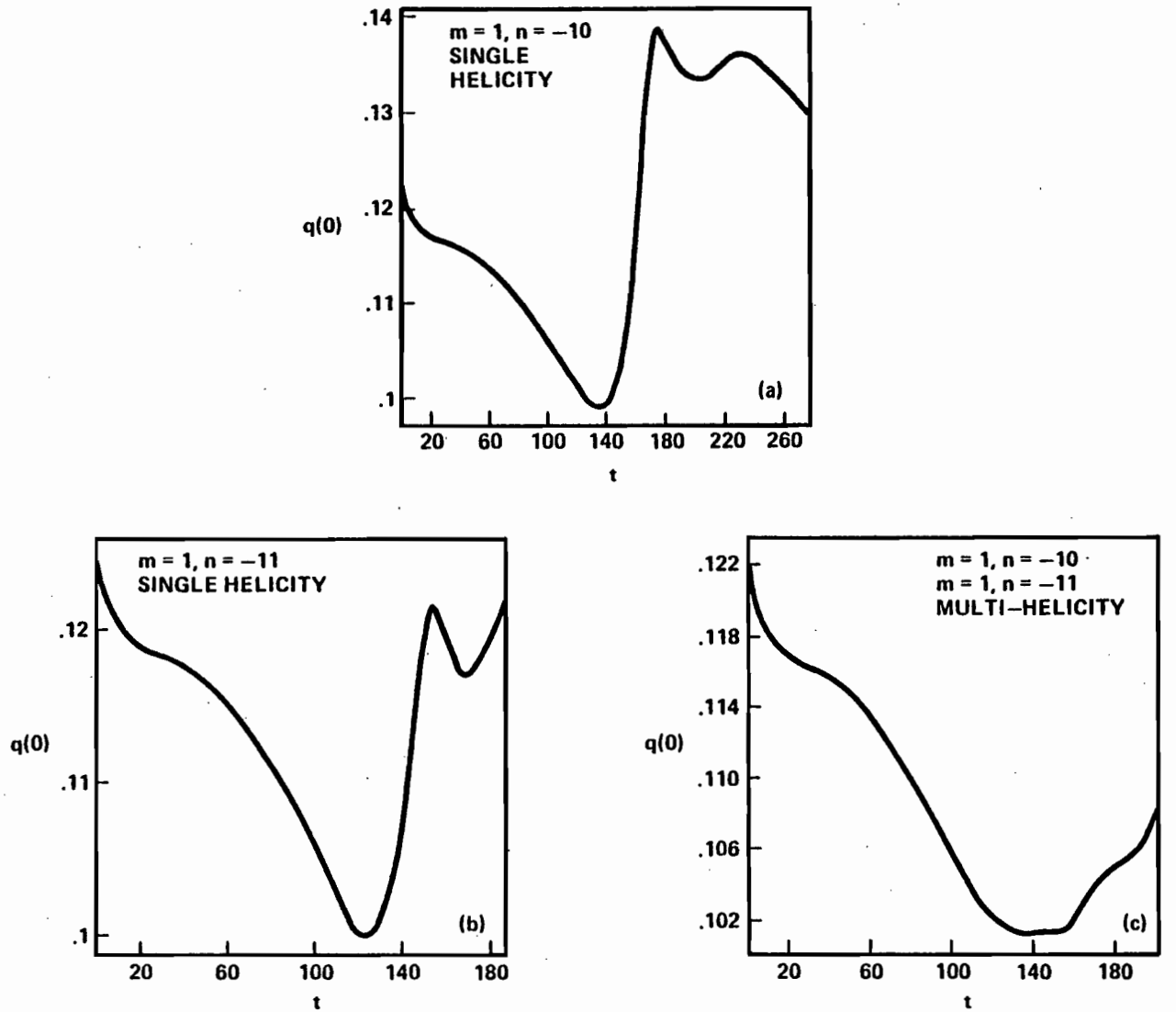
m = 1, n = −10
SINGLE
HELICITY
(a)
q(0)
.14
.13
.12
.11
.1
20
60
100
140
180
220
260
t
m = 1, n = −11
SINGLE HELICITY
(b)
q(0)
.12
.11
.1
20
60
100
140
180
t
m = 1, n = −10
m = 1, n = −11
MULTI−HELICITY
(c)
q(0)
.122
.118
.114
.110
.106
.102
20
60
100
140
180
t

Figure 3

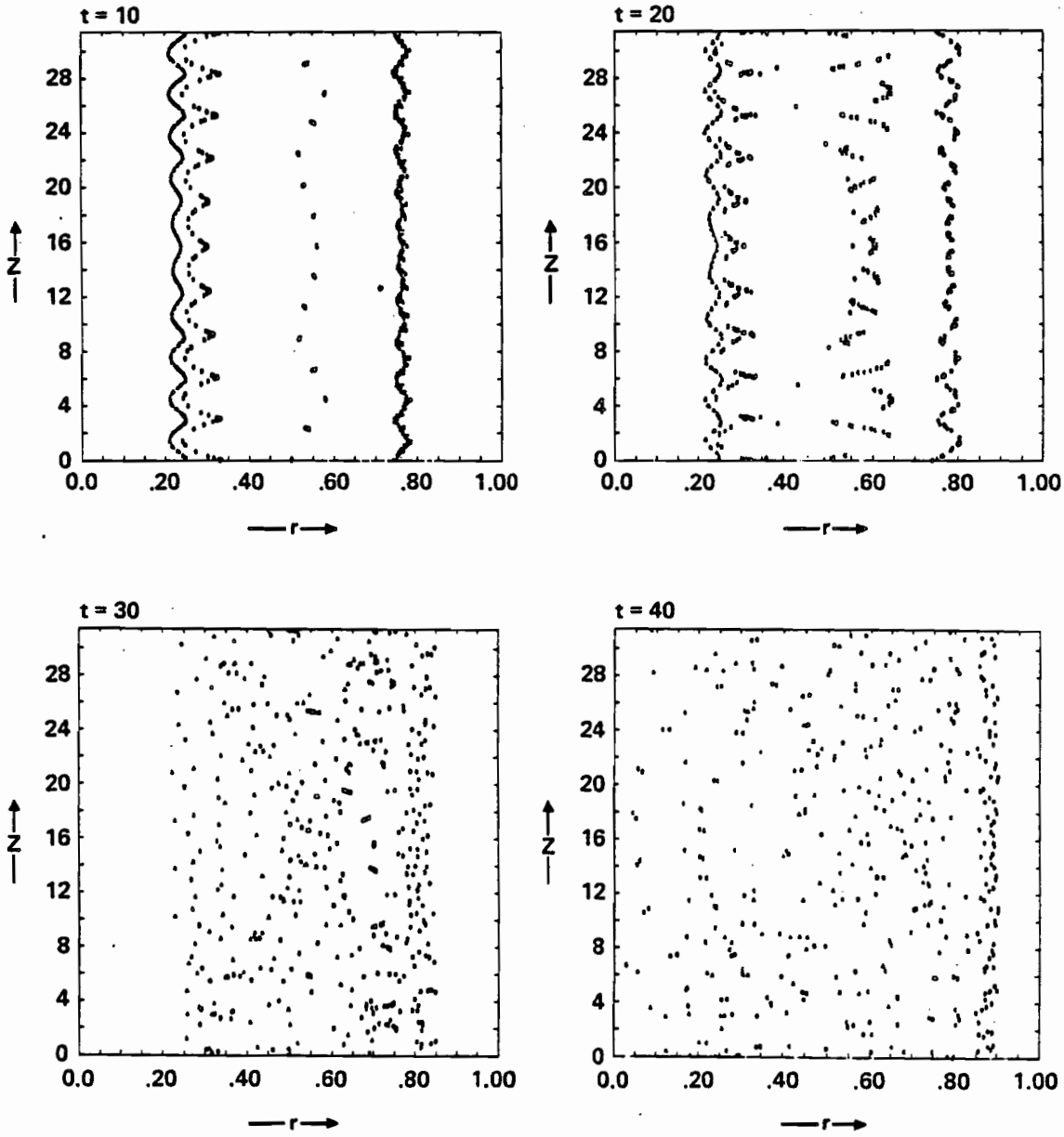

Figure 4

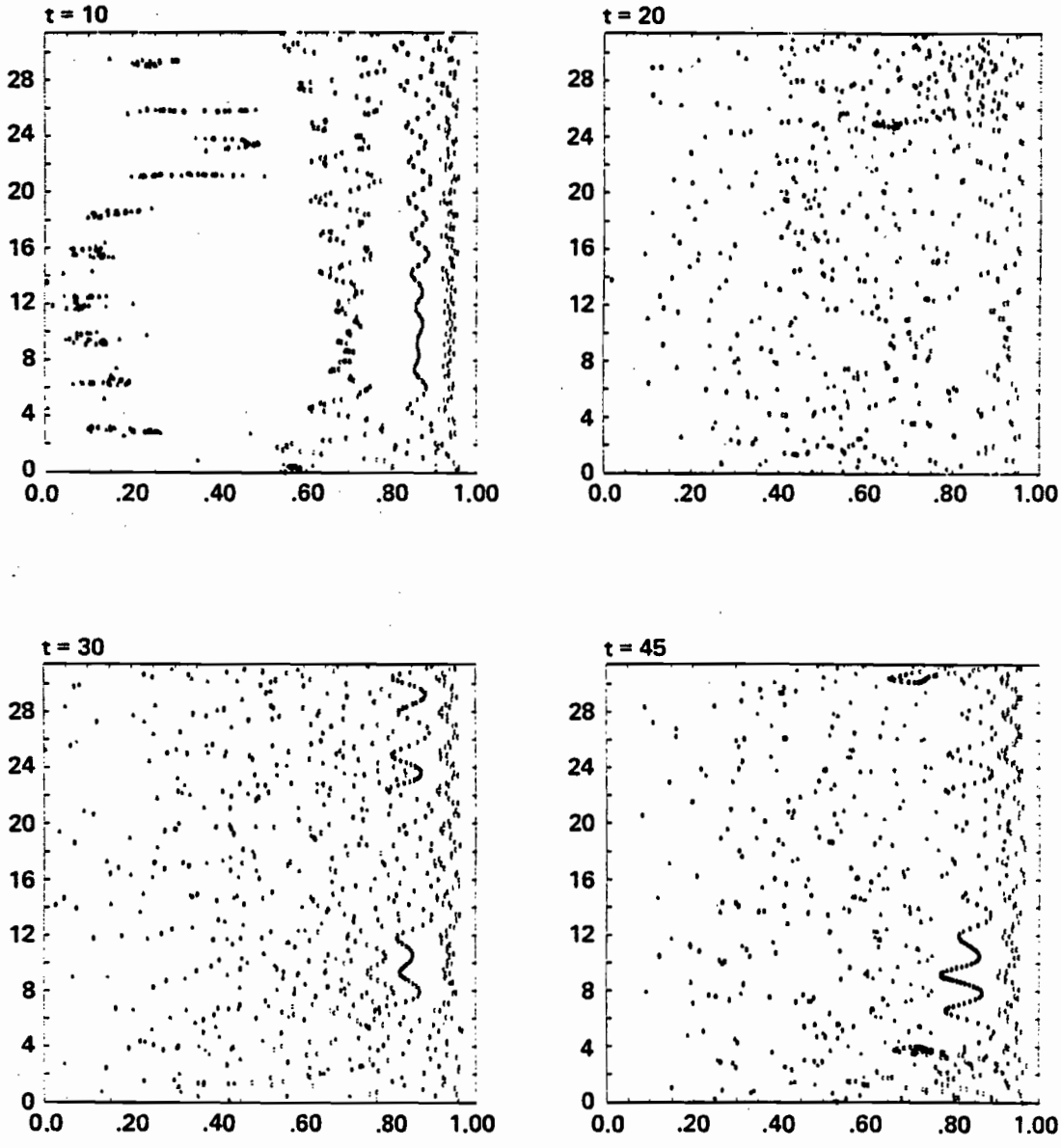

Figure 5

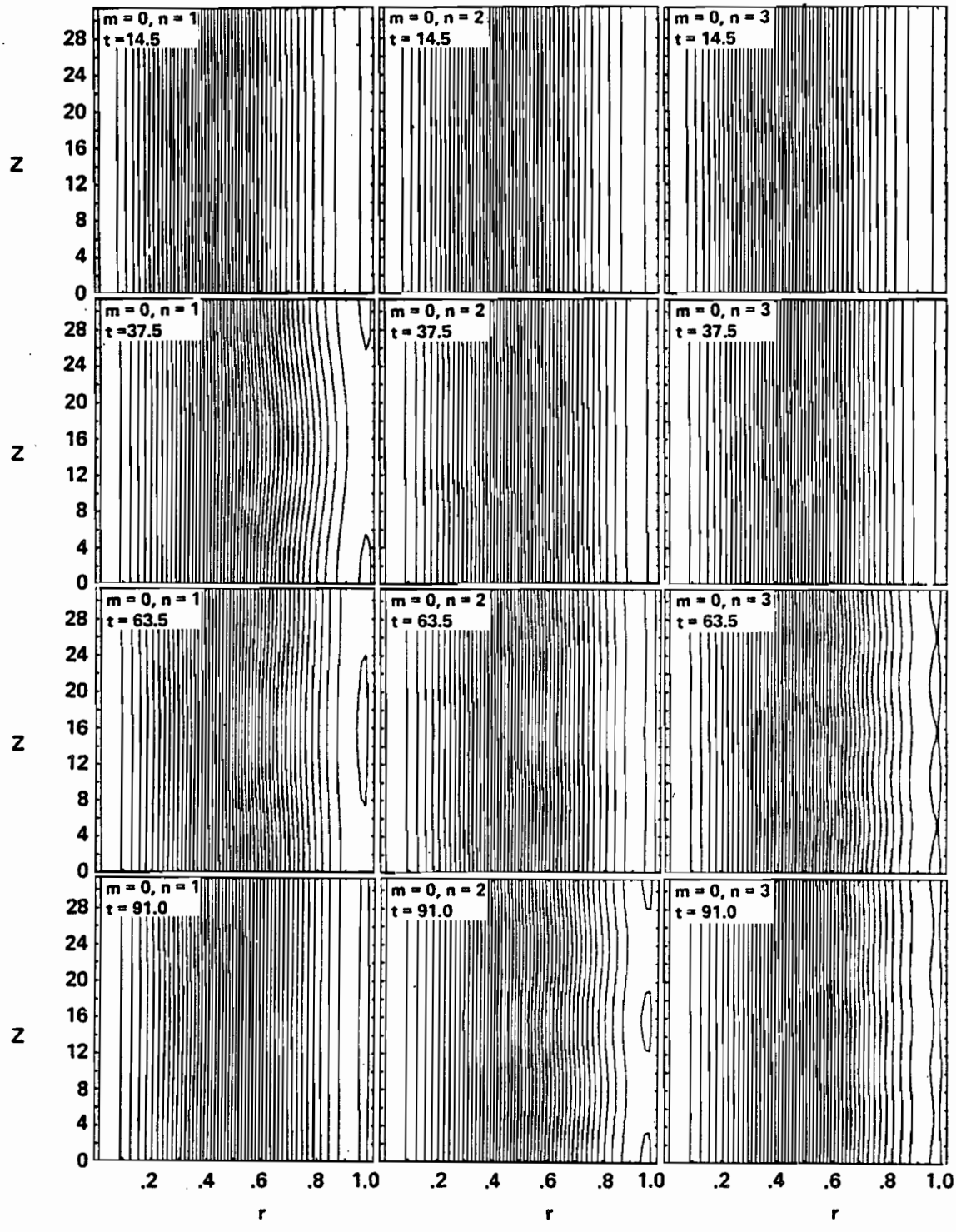
m = 0, n = 1
t = 14.5
m = 0, n = 2
t = 14.5
m = 0, n = 3
t = 14.5
m = 0, n = 1
t = 37.5
m = 0, n = 2
t = 37.5
m = 0, n = 3
t = 37.5
m = 0, n = 1
t = 63.5
m = 0, n = 2
t = 63.5
m = 0, n = 3
t = 63.5
m = 0, n = 1
t = 91.0
m = 0, n = 2
t = 91.0
m = 0, n = 3
t = 91.0
z
0
4
8
12
16
20
24
28
.2
.4
.6
.8
1.0
r

Figure 6

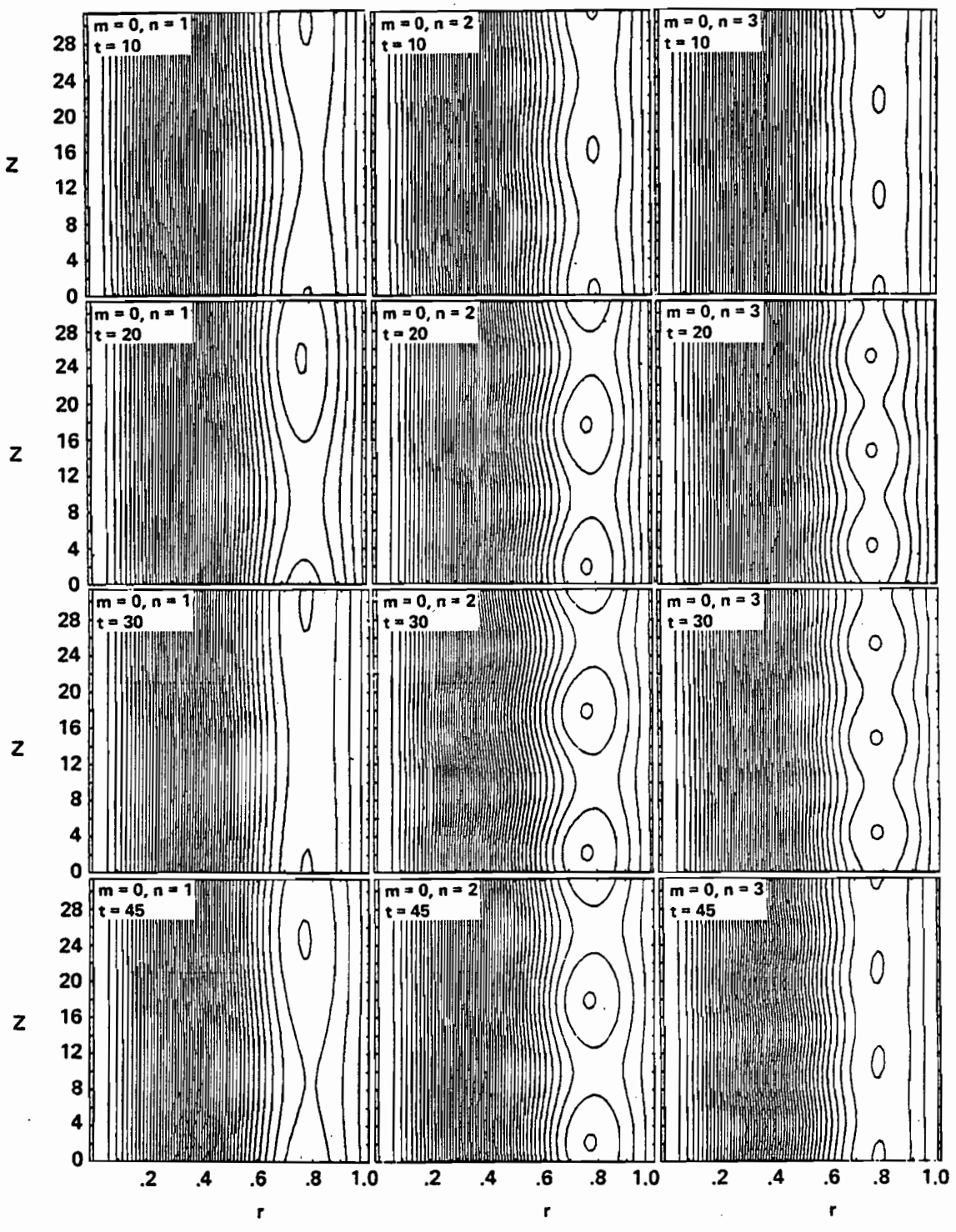
m = 0, n = 1
t = 10
m = 0, n = 2
t = 10
m = 0, n = 3
t = 10
m = 0, n = 1
t = 20
m = 0, n = 2
t = 20
m = 0, n = 3
t = 20
m = 0, n = 1
t = 30
m = 0, n = 2
t = 30
m = 0, n = 3
t = 30
m = 0, n = 1
t = 45
m = 0, n = 2
t = 45
m = 0, n = 3
t = 45
z
0
4
8
12
16
20
24
28
.2
.4
.6
.8
1.0
r

Figure 7

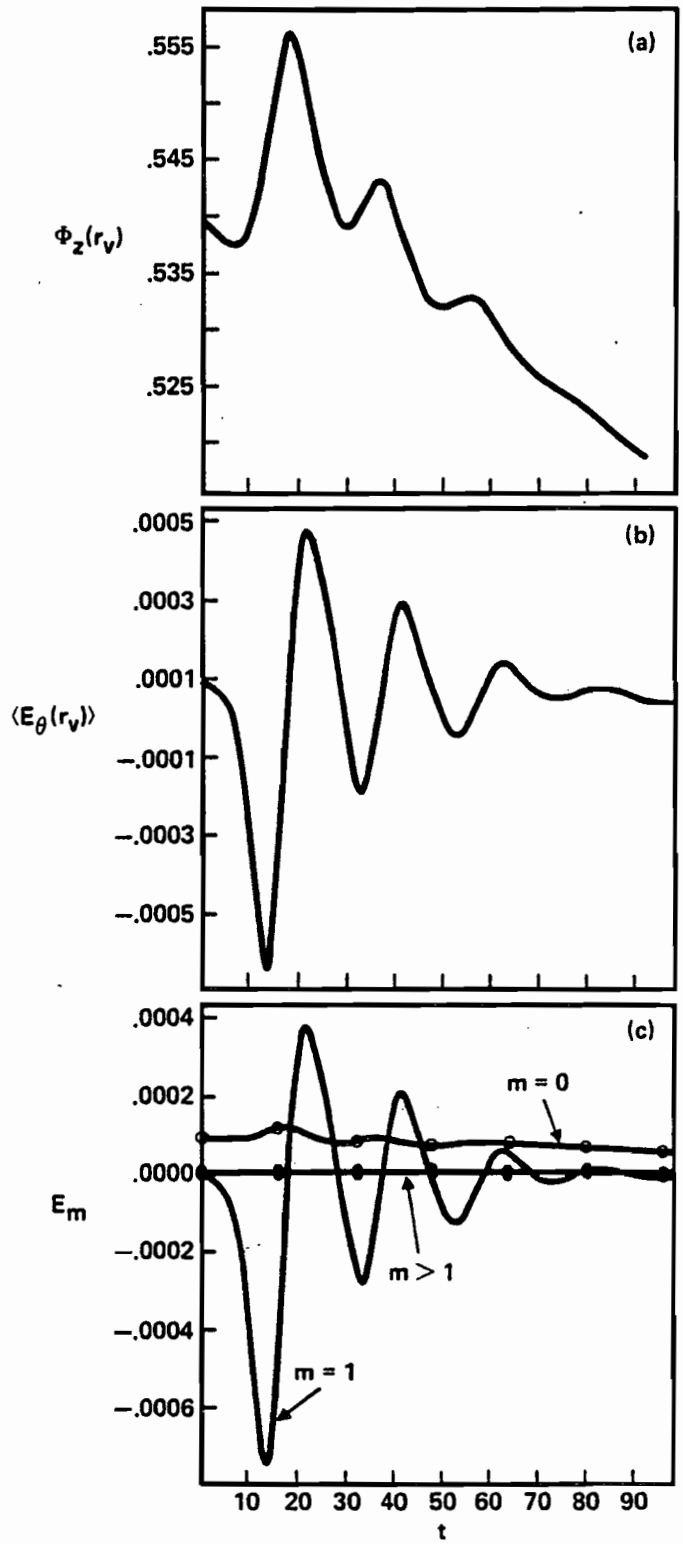
(a)
.555
.545
.535
.525
$\Phi_z(r_v)$
(b)
.0005
.0003
.0001
−.0001
−.0003
−.0005
$\langle E_\theta(r_v)\rangle$
(c)
.0004
.0002
.0000
−.0002
−.0004
−.0006
E_m
m = 0
m > 1
m = 1
10 20 30 40 50 60 70 80 90
t

Figure 8

Nonlinear MHD Simulations of the Spheromak and The Reversed Field Pinch*

A.A. Mirin and N.J. O'Neill
National Magnetic Fusion Energy Computer Center
Lawrence Livermore National Laboratory
Livermore, California 94550

and

A.G. Sgro
Los Alamos National Laboratory
Los Alamos, New Mexico 87544

Introduction

MHD simulations applicable to both the CTX gun-injected Spheromak[1] at Los Alamos National Laboratory and to the various Reversed Field Pinches (e.g. ZT40 at LANL[2]) are presented. The evolution of the Spheromak is simulated using the three-dimensional, finite-beta, compressible, nonlinear, resistive MHD code TEMCO[3]. The code uses cylindrical coordinates (r,ϕ,z) and hence is applicable to both cylindrical and toroidal geometries. The effect of Hall terms on resistive interchange modes in a Reversed Field Pinch is studied using the cylindrical, linear, compressible, finite-beta initial value code ODRIC[4]. Extensions of this work to three dimensions will be presented at a later date. (A nonlinear study exclusive of Hall terms is presented in Reference [3]).

Basic Equations

The nondimensional equations are as follows:

$$\frac{\partial \rho}{\partial t} + \nabla\cdot(\rho \underline{v}) = 0 \qquad (1)$$

*Work performed under the auspices of the U.S. Department of Energy by the Lawrence Livermore National Laboratory under Contract No. W-7405-ENG-48.

$$\frac{\partial T}{\partial t} + \underline{v}\cdot\nabla T = -(\gamma-1)\, T\, \nabla\cdot\underline{v}$$

$$+ \frac{2(\gamma-1)}{\rho}\, \underline{J}\cdot(\underline{E} + \underline{v}\times\underline{B})$$

$$+ \frac{(\gamma-1)}{\rho}\, \underline{\underline{\Pi}} : \nabla\underline{v} + \frac{(\gamma-1)}{\rho}\, \nabla\cdot(\kappa\nabla T) \tag{2}$$

$$\frac{\partial \underline{v}}{\partial t} + \underline{v}\cdot\nabla\underline{v} = -\frac{1}{2}\nabla T - \frac{T}{2\rho}\nabla\rho$$

$$+ \frac{1}{\rho}\, \underline{J}\times\underline{B} + \frac{1}{2\rho}\, \nabla\cdot\underline{\underline{\Pi}} \tag{3}$$

$$\frac{\partial \underline{B}}{\partial t} = -\nabla\times\underline{E}, \tag{4}$$

with the auxiliary conditions

$$\underline{J} = \nabla\times\underline{B} \tag{5}$$

$$\underline{E} = -\underline{v}\times\underline{B} + \frac{\eta}{S}\,\underline{J} + \underline{E}_{Hall} \tag{6}$$

$$\underline{E}_{Hall} = \frac{\upsilon}{\rho}\left[\underline{J}\times\underline{B} - \frac{g}{2}\nabla(\rho T)\right] \tag{7}$$

In Eqs. (1)-(7), ρ is the mass density, T is the energy per unit mass, $\underline{v}$ is the velocity, $\underline{B}$ is the magnetic field, γ is the ratio of specific heats, S is the magnetic Reynolds number τ_R/τ_A, the ratio of resistive diffusion time to Alfven time, $\underline{\underline{\Pi}}$ is the viscous stress tensor, κ is the thermal conductivity, η is the resistivity, $\nu = (\omega_{ci}\tau_A)^{-1}$ and g is the fraction of pressure in the electrons. Time is measured in Alfven units.

The resistivity η and thermal conductivity κ are taken as isotropic. The Hall contribution to the electric field is optional. The viscous stress tensor $\underline{\underline{\pi}}$ is based on an isotropic coefficient of viscosity, so that

$$\nabla \cdot \underline{\underline{\pi}} = \tilde{\mu} \; [\nabla^2 \underline{v} + \frac{1}{3}\nabla(\nabla \cdot \underline{v})], \tag{8}$$

as in Dibiase and Killeen [5]. The fact that the resistivity, thermal conductivity and viscosity are taken as isotropic is a matter of expediency. Although classical tensor representations of these quantities have been derived [6], their applicability is questionable due to the extremely long parallel mean free path.

Representation of Variables in TEMCO

The principal dependent variables are represented in a 1-D Fourier series:

$$U(r,\phi,z) = U_o(r,z) + \sum_{m=1}^{M} [U_{mc}(r,z)\cos m\phi + U_{ms}(r,z)\sin m\phi]. \tag{9}$$

Because only low mode numbers are of interest, the ϕ direction is treated in a purely spectral manner, with the exception of an option to compute $1/\rho$ pseudo-spectrally. Finite differencing is performed in the r and z directions.

Numerical Methods in TEMCO

Letting $\underline{U} = (\rho, T, v_r, v_\phi, v_z, B_r, B_\phi, B_z)^t$, the basic equations can be written in the form

$$\frac{\partial \underline{U}}{\partial t} = L_A(\underline{U}) + L_\eta(\underline{U}) + L_\mu(\underline{U}) + L_\kappa(\underline{U}) + L_\upsilon(\underline{U}). \tag{10}$$

Here, L_η represents the resistive terms in Eq. (4), L_μ represents the viscous terms in Eq. (3), L_κ represents the thermal conduction terms in Eq. (2), L_υ represents the Hall terms in Eq. (4), and L_A represents everything else. Eq. (10) is solved using operator splitting. Standard spatial central differencing coupled with an explicit time advancement is used in L_η, L_μ, L_κ and L_υ. In Eq. (4) the term $-\nabla x(\frac{\eta}{S}\nabla xB)$ is expressed as $\frac{\eta}{S}\nabla^2 B - \nabla(\frac{\eta}{S})x\nabla xB$. This is found to be helpful in reducing errors in the divergence of B. The operator L_A is advanced using either a two step Lax-Wendroff method or a leapfrog method. In the latter case temporal smoothing is occasionally employed. Artifical smoothing of ρ and $\underline{v}$ is sometimes necessary. The timestep is determined in accordance with the courant condition associated with L_A. The other operators are advanced using a smaller timestep if necessary.

Boundary Conditions in TEMCO

At $r = 0$, the boundary conditions depend on the mode number m. Generally speaking all variables are 0, except as follows: For $m = 0$, ρ, T, v_z and B_z have vanishing radial first derivatives, as do v_r, v_ϕ, B_r and B_ϕ for $m = 1$. At the wall radius $r = r_w$, $v_r = B_r = 0$, $\frac{\partial\rho}{\partial r} = 0$, $\frac{\partial T}{\partial r} = \frac{2v_\phi^2}{r}$, $\frac{\partial}{\partial r}(rv_\phi) = \frac{\partial v_z}{\partial r} = 0$ and $\frac{\partial}{\partial r}(rB_\phi) = \frac{\partial B_z}{\partial r} = 0$. Alternative boundary conditions ar $r = r_w$ may be applied as the physics dictates. For a cylindrical system periodic boundary conditions are used in the z direction. In the case of a toroidal system $\frac{\partial\rho}{\partial z} = 0$, $\frac{\partial T}{\partial z} = 0$, $\frac{\partial v_r}{\partial t} = 0$, $\frac{\partial V_\phi}{\partial z} = 0$, $\frac{\partial B_r}{\partial z} = 0$ and $\frac{\partial B_\phi}{\partial z} = 0$ at the z-walls. All boundary conditions are second order accurate.

Numerical Methods in ODRIC

ODRIC is merely a linearization of the cylindrical form of TEMCO. Equilibrium quantitities $\rho_o(r)$, $T_o(r)$, $B_{\phi o}(r)$ and $B_{zo}(r)$ are specified. Perturbed variables are expressed in the form $f_1(r,t)\exp[i(m\phi+nkz)]$ where m and n are the poloidal and toroidal mode numbers and k is the inverse aspect ratio. Equations for the perturbed variables are then integrated in time using a fully implicit algorithm. Central differencing is used in the radial

direction, and the boundary conditions are first order accurate. Complex growth rates are calculated using the algorithm of Buneman[7].

Spheromak Applications

The dynamical relaxation of an unstable Spheromak equilibrium is modeled using the three-dimensional nonlinear code TEMCO. This equilibrium is calculated as follows: A zero-beta equilibrium in its minimum energy state is evolved in time using the noncircular transport code MINERVA[8]. The resistivity profile corresponds to that of a $Z_{eff} = 1$ plasma having a temperature of 23 eV at the magnetic axis and 4.5 eV at the boundary. The plasma evolves until the safety factor q on axis drops below 0.5, at which time the equilibrium becomes unstable to an n = 2 kink instability. This unstable equilibrium, combined with an n = 2 perturbation at the $\varepsilon = 10\%$ level as computed by a linear stability code of Marklin[9], serves as initial data for TEMCO.

Standard Case. The dimensions of the poloidal domain are $0 \leq r \leq 1.125$ and $0 \leq z \leq 1$. There are 73 meshpoints in the radial direction and 65 points in the z direction; both meshes are uniformaly spaced. The calculation is performed at "zero beta", i.e., $T \equiv 0.001$, and the density ρ is set uniformly equal to 1.0. The thermal conductivity and viscosity coefficients are set to zero and the Hall terms are ignored. The ratio of specific heats γ is set to 5/3, and the Lundquist number $S = \tau_R/\tau_A$ is equal to 1×10^4. Toroidal mode numbers n = 0 and 2 are included in the computation. Artificial smoothing of the velocity components is performed. The simulation is run for 107 Alfven times, which corresponds to 8000 timesteps.

The 3D magnetic fields are fed into the TUBE code[10], which outputs puncture plots in various poloidal planes. It can be seen that the unstable perturbation initially grows and the plasma moves closer to the boundary (see Fig. 1). At around t = 12 (Fig. 1b) the displacement reverses itself and the plasma moves in the opposite direction, crossing its original position at about t = 40 (Fig. 1c). The displacement continues opposite to its original motion until about t = 53 (Fig. 1e), during which time the magnetic topology becomes less coherent (Fig. 1f) and the kinetic energy sharply increases. By

$t = 61$ (Fig. 1g) the magnetic structure seems to have settled down and the kinetic energy has begun to drop. The calculation is stopped at $t = 107$. By this time the kinetic energy has dropped from its maximum value by over two orders of magnitude and the magnetic energy has dropped from its value at $t = 0$ by about thirty percent. It is difficult to tell whether the plasma has actually reached a stable equilibrium or whether it will undergo some gross motion at a later time.

A result of this evolution is that the plasma is closer to a minimum energy state than at the beginning of the relaxation. For a force-free plasma, $\underline{J} = \lambda \underline{B}$. In general, λ is a function of position, but in a minimum energy state it is a constant λ_0. At the beginning of the MHD simulation λ at the outer boundary is much less than its value at the magnetic axis, as a result of the initial resistive evolution. During the dynamical relaxation λ becomes more uniform, as can be seen by examining contours of the function $\chi = J \cdot B/\lambda_0 B^2$ (see Fig. 2). Furthermore, the number of meshpoints at which $|\chi - 1|$ is less than 0.1 increases by 50% during the course of the simulation. This indicates that the plasma has moved closer to a minimum energy state.

Variation with Magnetic Reynolds Number. When the MHD simulation is repeated at $S = 10^3$ instead of 10^4, the configuration is seen to diffuse toward a Taylor state. By $t = 24$, the number of meshpoints at which $|\chi - 1| < 0.1$ has trebelled and the fractional magnetic energy in the $n = 2$ mode has dropped by two orders of magnitude. (When $S = 10^4$ this fraction is roughly constant.) This is consistent with transport code results which show that at $S = 10^3$, the minimum energy state $q(\psi)$ profile is recovered after 75 Alfven times, but at $S = 10^4$ the change in $q(\psi)$ is much less pronounced.

Perturbation Size. When ε equals 0.01 instead of 0.1, the $n = 2$ mode grows approximately linearly until it reaches an amplitude of about $\varepsilon = 0.03$, at which time nonlinearities appear to set in. This indicates that the original $\varepsilon = 0.1$ level is a reasonable, but perhaps slightly large initial perturbation size. It is difficult to tell exactly when nonlinearities develop since the initial conditions, having been computed by Marklin's ideal code[9], are not an eigenfunction of TEMCO.

Comparison with Linear Code. The ideal stability code of Marklin[9] is compared to a linearized version of TEMCO, obtained by ignoring nonlinear convolution terms and zeroth order resistive diffusion terms. A comparison of contour plots and growth rates indicates excellent agreement between the two codes. Marklin computes a growth rate of 0.1, whereas TEMCO obtains 0.13 for $S = 10^3$ and 0.20 for $S = 10^4$. The calculation fails when run on a 37 by 33 mesh, indicating that a mesh size of at least 73 by 65 is necessary. Verification that a 73 by 65 mesh is adequate will have to be forthcoming, as the present version of the code does not fit on the MFECC D machine if the mesh is made any larger.

Number of Toroidal Harmonics. The standard case includes only modes $n = 0$ and 2. It is quite likely that higher modes must be included. This too will have to wait for the future due to lack of storage.

Artificial Smoothing. A significant amount of artificial smoothing must be added to the velocity components. The extent to which this distorts the physics cannot be ascertained without using a much finer mesh. This will also have to wait for the future.

Variable Density. The standard case is redone allowing the density to vary according to Eq. (1). For $0 \leq t \leq 40$ the evolution of the magnetic field is almost identical, but the velocity variables look quite different. Meanwhile the $n = 2$ density component has been growing steadily, and by $t = 40$ its amplitude exceeds that of the $n = 0$ density component, causing the density to become negative at some locations. The cause of this, including the extent to which it is due to not carrying enough toroidal harmonics, is under investigation.

RFP Applications

The effect of Hall terms on resistive interchange modes in a Reversed Field Pinch is studied using the linear initial value code ODRIC. The equilibrium used is that of Robinson[11], which is known to be stable to tearing modes. It satisfies

$$\mu \equiv \frac{rB_z}{B_\phi} = 2\left(1 - \frac{r^2}{8} - \frac{r^4}{400}\right) \tag{11}$$

$$C_1 \equiv -\frac{p'}{2rB_z^2}\left(\frac{\mu}{\mu'}\right)^2 \leq 0.125 \tag{12}$$

Unless otherwise specified, in the results to follow $C_1 = 0.1$ and the wall radius r_w equals 3. The inverse aspect ratio is taken to be $k = 0.2$. Since ODRIC is an initial value code, it computes only the fastest growing mode. The growth rate of the variable f is defined as

$$\gamma + i\omega = \frac{\partial f}{\partial t}/f \; ; \tag{13}$$

in the absence of Hall terms $\omega = 0$.

Linear g-mode studies exclusive of Hall terms have been presented recently[4]. The principal observations are as follows:

a) For $m = 0$, as S increases from 10^3 to 10^7, the growth rate first increases and then decreases; there is a wider range of toroidal mode numbers which are unstable; and the n value of the most unstable mode increases. Preliminary results indicate the same trends for $m > 0$.

b) For $m = 0$, $n = 25$ and S between 10^6 and 10^7, $\gamma \sim S^{-0.26}$ (vs. $S^{-0.33}$ as predicted by Finn and Manheimer[12]); for S between 10^4 and 10^7, the jump in the logarithmic derivative of B_r, Δ', behaves as predicted in Reference [12].

c) For $m = 0$, $n = 25$ and S between 3×10^4 and 3×10^6, the growth rate decreases much more rapidly with decreasing C_1 as C_1 gets smaller, in qualitative agreement with Reference [12].

In studying the effects of Hall terms, it is convenient to initially consider the situation in which there is no temperature perturbation. The first case under study satisfies $m = 0$, $n = 25$ and $S = 10^4$. In the absence of Hall terms ($\nu = 0$; see Eq. (7)), the growth rate (γ,ω) equals $(2.71 \times 10^{-3}, 0)$, and the resulting mode is recognized to be the "odd mode" of Finn and Manheimer[12]; that is, the radial velocity is an odd function with respect to the singular radius. As ν increases, γ decreases monotonically until $\nu \simeq 0.12$, at which point γ becomes negative and the mode has been stabilized. At the same time ω increases until it hits a maximum at $\nu = 0.07$, at which point it begins to decrease slowly. In all cases considered the odd mode is the fastest growing mode.

A similar situation occurs for $m = 1$, $n = -6$ and $S = 10^3$. As ν increases from 0 to 0.5, γ decreases monotonically until the mode is stabilized. As with $m = 0$ above, the odd mode is the fastest growing mode. These results are in qualitative agreement with Delucia, et al., who study the effect of Hall terms on resistive instabilities in the Spheromak[13].

If the temperature perturbation is included, however, the situation becomes more complicated. For zero thermal conductivity, when $m = 0$, $n = 25$ and $S = 10^4$, then in the absence of Hall terms $\gamma = 2.97 \times 10^3$. As the Hall parameter ν increases, the real part of the growth rate decreases until about $\nu = 0.064$, at which point $\gamma = 8 \times 10^{-4}$. During this time the odd mode has continued to be the fastest growing mode. However at $\nu = 0.064$, γ suddenly starts increasing and eventually reaches 7.1×10^{-2}, more than twenty times its value at $\nu = 0$ (see Fig. 3). It is now the even mode which is the fastest growing mode; the odd mode has presumably been stabilized.

This increase in the growth rate may be negated through inclusion of the thermal conductivity. For $\nu = 0.2$ (applicable to ZT-40) and $\kappa = 0$, the growth rate (γ,ω) is $(8.66 \times 10^{-3}, 5.68 \times 10^{-3})$ and the even mode prevails. As κ increases from zero, γ decreases monotonically and ω increases monotonically until $\kappa = 1.05 \times 10^{-4}$, at which point the mode is stabilized. The even mode does continue to prevail, however. It is difficult to attach a significance to the value of κ since this model assumes isotropic thermal

conductivity, which is known to be a rather poor approximation. A similar situation occurs for $m = 1$, $n = -6$ and $S = 10^3$.

References

[1] T.R. Jarboe, et al., Phys. Fluids 27, No. 1 (1984), 13.

[2] D.A. Baker, et al., Plasma Physics and Controlled Nuclear Fusion Research (IAEA, Vienna, 1982), I, 587.

[3] A.A. Mirin and J. Killeen, "Nonlinear Three-Dimensional MHD Calculations of Resistive Instabilities in a Reversed Field Pinch," US-Japan Workshop on 3-D MHD Studies for Magnetically Confined Plasmas, Nagoya (1983).

[4] A.A. Mirin and N.J. O'Neill, "Modeling of Resistive g-Modes in a RFP," Bull. Am. Phys. Soc. 28 (APS Meeting, Los Angeles, 1983), 1186.

[5] J.A. Dibiase and J. Killeen, "Numerical Studies of Resistive Instabilities in Diffuse Pinches," J. Comp. Phys. 24, No. 2 (1977), 158.

[6] S.I. Braginskii, in Reviews of Plasma Physics 1 (Consultants Bureau, New York, 1965), 205.

[7] O. Buneman, J. Comp. Phys. 29 (1978), 295.

[8] A.G. Sgro, et al., "Quasistatic Evolution of Compact Toroids," Tenth Conf. on Numerical Simulation of Plasmas, San Diego (1983), 2C16.

[9] G.J. Marklin, "MHD Stability of the Spheromak," U. Maryland Report PL83-039 (1983).

[10] N.J. O'Neill and A.A. Mirin, "TUBE, a Field Line Integrator Code," LIBRIS Abstract P81, NMFECC, Livermore; see also J. Killeen, et al., LLNL Report UCRL-50161 (1967).

[11] D.C. Robinson, Nucl. Fusion 18 (1978), 939.

[12] J.M. Finn and W.M. Manheimer, Phys. Fluids 25, No. 4 (1982), 697.

[13] J. DeLucia, et al., "Resistive Stability of the Cylindrical Spheromak," Princeton Plasma Physics Lab. Report PPPL-2054 (1983).

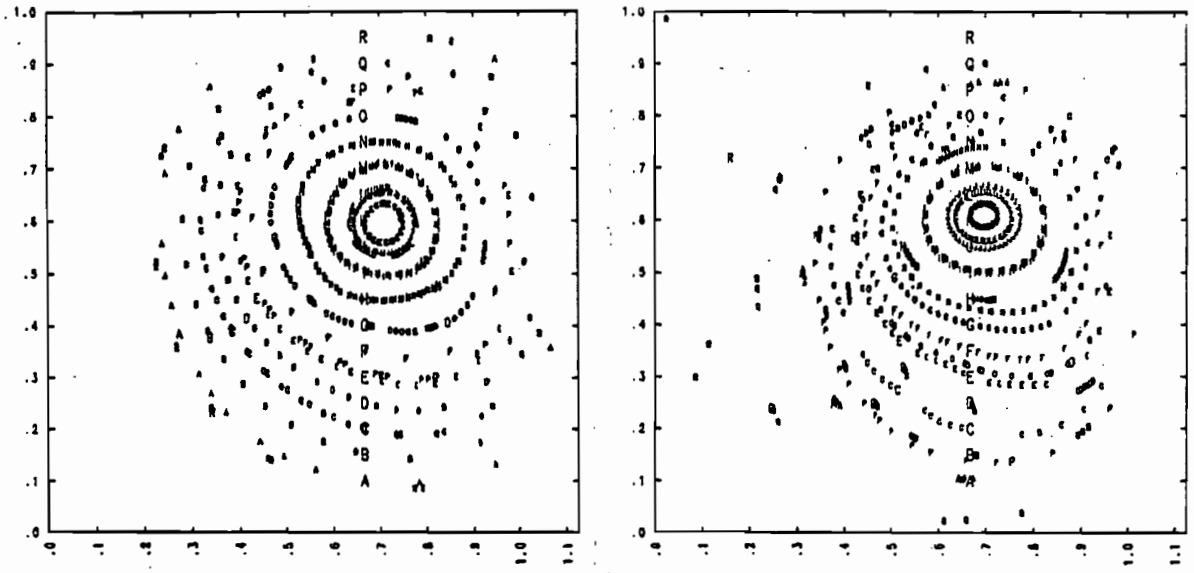

(a) t = 1

(c) t = 40

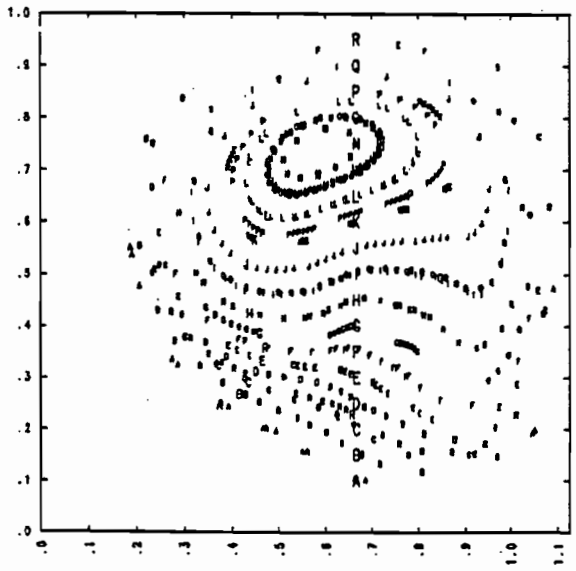

(b) t = 12

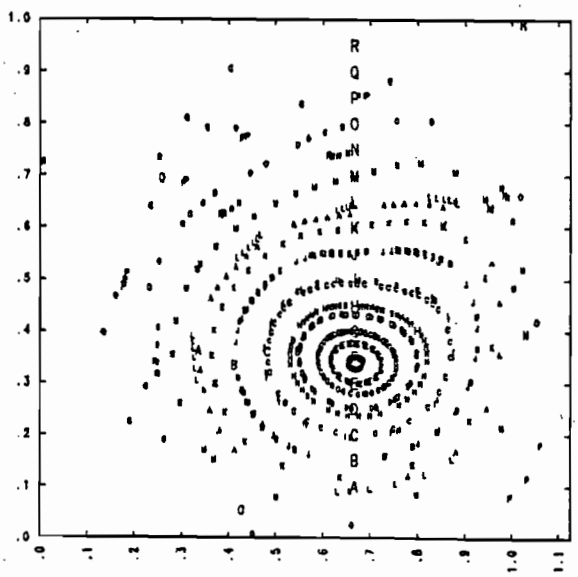

(d) t = 51

Fig. 1 Puncture plots for the standard Spheromak case at $\phi=0$; r is the horizontal variable and z is the vertical variable.

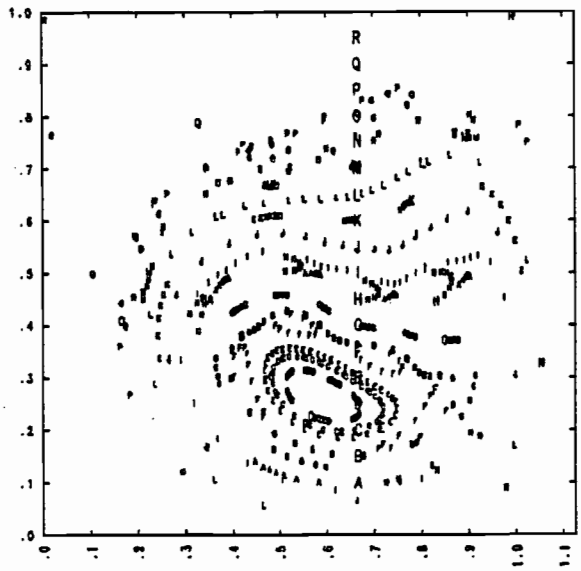

(e) t = 53

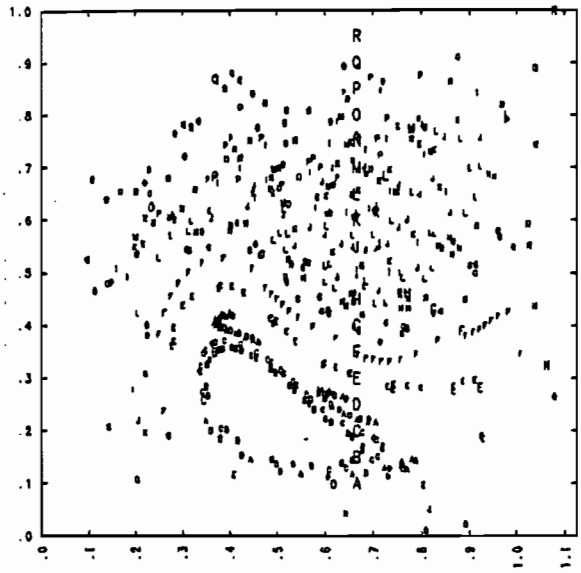

(g) t = 61

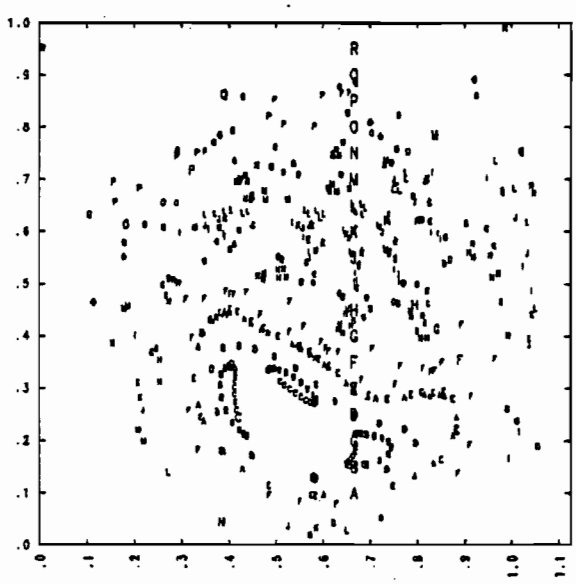

(f) t = 56

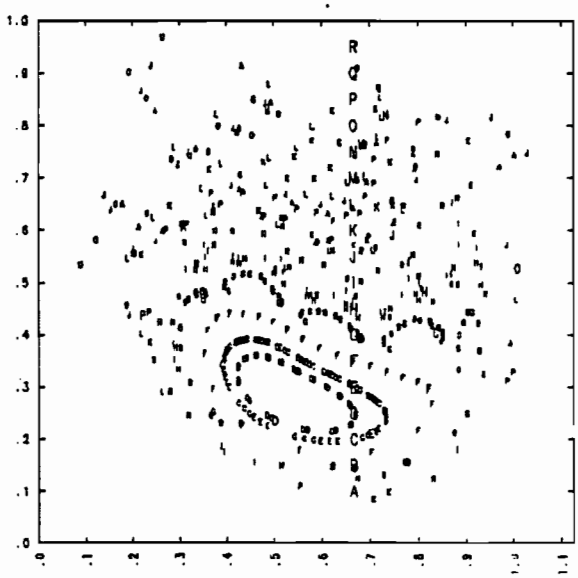

(h) t = 107

Fig. 1 Continued

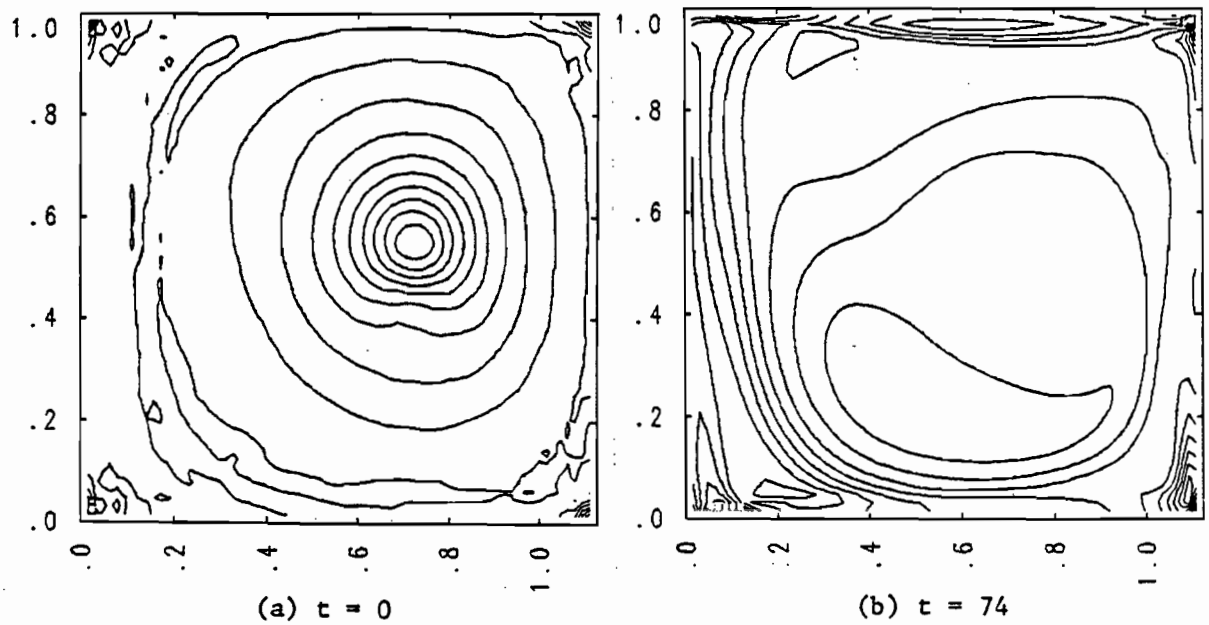

Fig. 2 Contours of $\chi = J \cdot B/\lambda_0 B^2$ for the standard Spheromak case; r is the horizontal variable and z is the vertical variable.

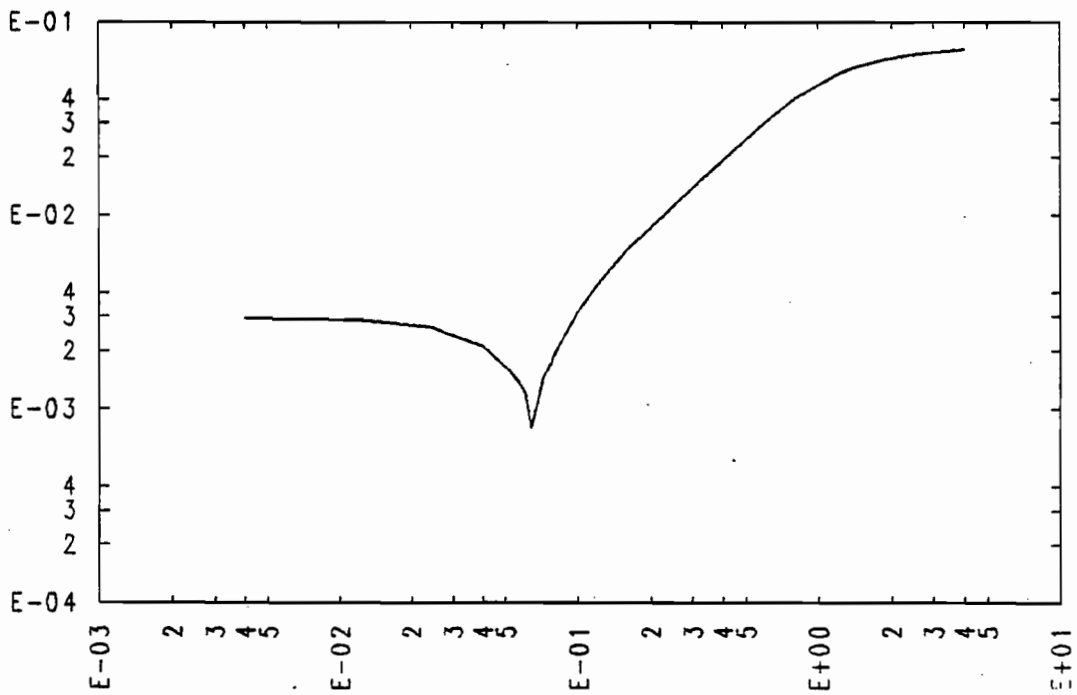

Fig. 3 Real growth rate γ (ordinate) vs. Hall parameter ν (abscissa) for a cylindrical RFP in which k=.2, m=0, n=5 and $S=10^4$; the temperature perturbation is included.

FINITE ELEMENT METHOD AND ITS APPLICATION TO 3D DYNAMIC SYSTEM

M. Aizawa and I. Kawakami
Atomic Energy Research Institute
College of Science and Technology
Nihon University

Mar. 19-23, 1984, at Oak Ridge
National Laboratory

1. Introduction

A numerical method for solving a system of 3D-MHD equations is proposed in this paper.

The method is based on and formulated with the finite element method (FEM) with elements in motion, that is, arbitrary Lagrangian and Eulerian (ALE) method. This method is called "FEMALE".

Numerical methods for solution of the nonlinear hyperbolic system stemmed from Lax's work[1]. The two-step Lax-Wendroff-scheme which is currently and widely used, is regarded as one of tough method of numerical solution. It contains Friedrichs scheme, which introduce large diffusion. The discretization which is necessary for numerical simulations, divides fluid into three dimensional bodies, and large energy input to them near the discontinuity makes kinetic energy of bodies large. Then these bodies become oscillatory and overshot.

To suppress this overshooting, the kinetic energy have to be converted into thermal energy.

This is just the reason of introduction of numerical diffusion. However, the discontinuity disappears because of this diffusion. In studying MHD plasma quantitatively, it is important that we have to discriminate differences between physical and numerical diffusions in computation. For this purpose, we propose here a finite element method which is little or no numerical diffusion.

2. Formulation

2. 1 Basic equations

Our basic MHD equations can be written as a conservation form,

$$\frac{\partial U}{\partial t} + \mathrm{div}\ \vec{F}(U) = 0 \ . \qquad (2 - 1)$$

U is a 8-column vector whose components are unknown scalar variables:

$$U = (\rho,\ \rho\vec{v}\ ,\ \varepsilon\ ,\ \vec{B}\ )^T\ , \qquad (2 - 2)$$

where

$$\varepsilon \equiv \frac{1}{2}\rho v^2 + \frac{3}{2}p + \frac{B^2}{2\mu_o} \ .$$

T denotes transposition of matrix, and other notations have usual meanings. $\vec{F}$ is a flux vector corresponding to U ,

$$\vec{F} = (\rho\vec{v}\ ,\ \tilde{P}\ ,\ \vec{g}\ ,\ \tilde{E}^*)^T\ , \qquad (2 - 3)$$

where

$$\tilde{P} \equiv (p + \frac{B^2}{2\mu_o})\tilde{I} + \rho\vec{v}\vec{v} - \frac{1}{\mu_o}\vec{B}\vec{B}$$

$$\vec{g} \equiv (p + \varepsilon)\vec{v} + \frac{1}{\mu_o}(\vec{v}_\perp B^2 + \eta\vec{J}\times\vec{B})$$

$$\tilde{E}^* \equiv \vec{v}\vec{B} - \vec{B}\vec{v} + \frac{\eta}{\mu_o}((\vec{\nabla}\vec{B})^T - \vec{\nabla}\vec{B}) \ .$$

Hereafter, we choose the resistivity $\eta = 0$, or we assume that eq. (2 - 1) is hyperbolic.

2. 2 Shape Functions

The space Ω , occupied by plasma, is divided into Ne elements Re :

$$\Omega = \bigcup_{e=1}^{Ne} Re \qquad (2 - 4)$$

and they are not overlapped. To define elements, N nodes are defined. Let the position of the μ-th node by $\vec{x}_\mu \varepsilon \Omega$. A series of N-functions is introduced,

$$\{\phi^1(\vec{x}, t), \phi^2(\vec{x}, t), \cdots\cdot, \phi^N(\vec{x}, t)\} \qquad (2- 5)$$

such that $\sum_\mu \phi^\mu(\vec{x}, t) = 1, \quad \vec{x}\varepsilon\Omega,$

$$\phi^\mu(\vec{x}_\nu, t) = \delta^{\mu\nu} ,$$

where $\delta^{\mu\nu}$ is Kronecker's delta. We assume that $\phi^\mu(\vec{x}, t)$ is a class of functions which satisfy

$$\frac{\partial\phi^\mu}{\partial t} + \vec{v}_g \cdot \text{grad } \phi^\mu = 0 , \qquad (2 - 6)$$

where $\vec{v}_g$ is the grid velocity. Eq. (2 - 6) shows the elements are ALE. When $\vec{v}_g = 0$ then method is Eulerian, and when $\vec{v}_g = \vec{v}$ then it is Lagrangian. Though this grid velocity is arbitrary here, its value has large effect on accuracy of computation.

2. 3 Basic equations for numerical simulation

For the conservation equation (2 - 1), we interpolate U, $\vec{F}$ and $\vec{v}_g$ as

$$U \cong U' = \sum_{\mu} \phi^{\mu}(\vec{x}, t) U_{\mu}(t) \ , \qquad (2 - 7a)$$

$$\vec{F} \cong \vec{F}' = \sum_{\mu,i} \phi^{\mu}(\vec{x}, t) F_{i\mu}(t) \vec{e}_i \ , \qquad (2 - 7b)$$

$$\vec{v}_g \cong \vec{v}_g{}' = \sum_{\mu,i} \phi^{\mu}(\vec{x}, t) v_{gi\mu}(t) \vec{e}_i \ , \qquad (2 - 7c)$$

where $\vec{e}_i$ is unit basis vector. U', $\vec{F}'$ and $\vec{v}_g{}'$ coincide with U, $\vec{F}$ and $\vec{v}_g$ at the nodes. For simplicity we drop the dash in what follows.

According to Galerkin method[2], we take

$$\int_{\Omega} d\Omega \ \phi^{\mu}(\frac{\partial U}{\partial t} + \text{div } \vec{F}) = 0 \ , \qquad (2 - 8)$$

and substituting eqs. (2 - 6), (2 - 7) into (2 - 8)

$$\sum_{\nu} \alpha^{\mu\nu} \frac{dU_{\nu}}{dt} = C^{\mu} \qquad (2 - 9)$$

where

$$C^{\mu} = \int_{\Omega} d\Omega \phi^{\mu}(\vec{v}_g \cdot \text{grad } U - \text{div } \vec{F})$$

$$= \sum_{\nu} \vec{R}^{\mu\nu} \cdot \vec{v}_{g\nu} - S^{\mu}$$

$$\alpha^{\mu\nu} = \int_{\Omega} d\Omega \phi^{\mu} \phi^{\nu}$$

$$\vec{R}^{\mu\nu} = \sum_{\rho} \vec{\beta}^{\mu\nu\rho} U_{\rho}$$

$$S^{\mu} = \sum_{\nu,i} \beta_i^{\mu\nu} F_{i\nu}$$

$$\vec{\beta}^{\mu\nu\rho} = \int_{\Omega} d\Omega \phi^{\mu}\phi^{\nu} \mathrm{grad}\phi^{\rho}$$

$$\beta_i^{\mu\nu} = \int_{\Omega} d\Omega \phi^{\mu} \mathrm{div}(\phi^{\nu}\vec{e}_i)$$

$\alpha^{\mu\nu}$, $\vec{\beta}^{\mu\nu\rho}$ and $\beta_i^{\mu\nu}$ are geometrical coefficients independent of U_{μ}. Eq. (2 - 9) is a system of ordinary differential equations for U_{μ}, if $\vec{v}_{g\nu}$ is specified. The nodal position is obtained by solving

$$\frac{d\vec{x}g}{dt} = \vec{v}_{g\mu} \ . \qquad (2 - 10)$$

Eq. (2 - 9) and (2 - 10) are our basic equations for numerical simulation, and solve these ordinary differential equations under prescribed initial and boundary conditions.

The properties of eq. (2 - 9) should be noted. Taking ϕ^{μ} linear function in the one-dimensional problem, eq. (2 - 9) is equal to the conjugate approximation[3] of equation

$$\frac{dU}{dt} = v_g \frac{\partial U}{\partial x} - \frac{\partial F}{\partial x} \ , \qquad (2 - 11)$$

and if equally grid spacing Δx is taken, $\frac{\partial U_{\mu}}{\partial t}$ is equal to the compact differencing[4] of eq. (2 - 11) which is accurate to $O((\Delta x)^4)$.

Finally, ICED ALE equation[5]

$$\frac{d}{dt}\int_{Re} d\Omega U = \int_{Re} d\Omega \mathrm{div}(U\vec{v}_g - \vec{F}) \qquad (2 - 12)$$

is regarded as a special case where $\phi^{\mu}(\vec{x}, t) = 1$ for $\vec{x} \varepsilon Re$, and vanishes otherwise. This can be seen by noting that eq. (2 - 9) is written as

$$\frac{d}{dt}\int_{\Omega} d\Omega\phi^{\mu}U = \int_{\Omega} d\Omega\phi^{\mu}\mathrm{div}(U\vec{v}_g - \vec{F}) \ . \qquad (2 - 13)$$

3. Optimization of Accuracy with Specifying the Grid Velocity

3. 1 Effects of grid velocity

In many cases, $\vec{v}_g$ can be arbitrarily specified, and eq. (2 - 9) can be numerically integrated. However, when one or some kinds of discontinuities exist, the value of $\vec{v}_g$ is crucially important.

As the example, the problem of single rectangular pulse propagation can be considered.

$$\frac{\partial\rho}{\partial t} + \frac{\partial\rho v}{\partial x} = 0 \ , \quad v = \mathrm{const.} \ . \qquad (3 - 1)$$

When $v_g \neq v$, the computation results show that the fluctuation is observed around discontinuity. When $v_g = v$, this fluctuation disappears.

The application of eq. (2 - 9) to eq. (3 - 1)

$$\begin{aligned}\sum_{\nu} \alpha^{\mu\nu}\frac{d\rho_{\nu}}{dt} = \frac{1}{6}\{&(v_{g\mu+1} - v)(\rho_{\mu+1} - \rho_{\mu}) \\ &+ 2(v_{g\mu} - v)(\rho_{\mu+1} - \rho_{\mu-1}) \\ &+ (v_{g\mu-1} - v)(\rho_{\mu} - \rho_{\mu-1})\} \ , \end{aligned} \qquad (3 - 2)$$

thus for $v_g = v$, $\frac{d\rho_{\mu}}{dt} = 0$. This explains above results.

3. 2 Optimization of accuracy with generalized Rankine-Hugoniot relation

The results of previous section suggest us that one of the best way of determining the value $\vec{v}_g$ is the one which $C^{\mu} = 0$ in

eq. (2 - 9).

Here we examine the shock tube problem as non-trivial example. We should note that

$$C^{\mu} = \int_{\Omega} d\Omega \phi^{\mu} (\vec{v}_g \cdot \text{grad } U - \text{div } \vec{F}) = 0 \ , \qquad (3 - 3)$$

is the FEM representation of generalized Rankine-Hugoniot relation (R-H relation). It should be noted the relation (3 - 3) lead us to the best way of determining grid velocity in the pulse propagation problem. We consider one dimensional shock tube probelm, where at t = 0

$$U(x, 0) = \begin{cases} U_{L0} & x < 0 \\ U_{R0} & x > 0 \end{cases} \ . \qquad (3 - 4)$$

We shall find the solution for t > 0. C^{μ} is

$$C^{\mu} = \int dx \phi^{\mu} (v_g \frac{\partial U}{\partial x} - \frac{\partial F}{\partial x}) \ . \qquad (3 - 5)$$

Let the discontinuities, the shock front and the contact discontinuity, be at x_{μ},

$$U = U_L + \theta(x - x_{\mu})(U_R - U_L) \qquad (3 - 6a)$$

$$F = F_L + \theta(x - x_{\mu})(F_R - F_L) \qquad (3 - 6b)$$

$\theta(x)$ is Heaviside function. U_L, U_R are value of U on the left and on the right, respectively, and have to satisfy the generalized Rankine-Hugoniot relation:

$$(U_R - U_L)S = F_R - F_L \ , \qquad (3 - 6)$$

where S is the speed of the discontinuity. Substitution eqs. (3 - 6) into (3 - 5) yields

$$C^{\mu} = (U_R - U_L)v_g(x_{\mu}) - (F_R - F_L) \qquad (3 - 7)$$

and $C^{\mu} = 0$ if $v_g(x_{\mu}) = S$. Thus, C^{μ} vanishes in the shock tube problem, if v_g is the shock speed at the shock front and fluid velocity at the contact discontinuity.

For the rarefaction wave, $\frac{\partial U}{\partial x}$ is an eigenstate of Jacobian $\frac{\partial F}{\partial U}$ with eigenvalue $\xi = \frac{x}{t}$, which is a velocity of single wave, and

$$v_g \frac{\partial U}{\partial x} - \frac{\partial F}{\partial x} = (v_g - \xi) \frac{\partial U}{\partial x} = 0 \qquad (3 - 8)$$

if $v_g = \xi$. So eq. (2 - 9) is reduced to

$$\frac{dU_{\mu}}{dt} = 0 \qquad (3 - 9)$$

$$\frac{dx_{g\mu}}{dt} = v_{g\mu} \quad (\mu = 1, 2, \cdots N)$$

in the all region of the shock tube problem if $v_{g\mu}$ is a local wave front velocity. When $v_{g\mu}$ is exact, then numerical solution U_{μ} is also exact.

3. 3 General case

Unfortunately, $C^{\mu} = 0$ is not generally satisfied by a single $\vec{v}_{g\mu}$, since $C^{\mu} = 0$ ($\mu = 1, 2 \cdots N$) is 8N linear simulateneous equations for determining 3N unknowns, $\vec{v}_{g\mu}$. From previous discussions, we require that $\vec{v}_{g\mu}$ is determined by the condition $\sum_{\mu} \| C^{\mu} \|_2$ is minimum. Usually, this condition does not determine

$\vec{v}_g$ uniquely, so we also require that $\sum_\mu \|\vec{v}_{g\mu}\|_2$ is minimum among $\vec{v}_g$ which minimize $\sum_\mu \|C^\mu\|_2$.

As numerical method to this end, we used the Conjugate Gradient method (CG). It is known that this method can obtain Moore-Penrose solution of the simulateneous equations, and this solution satisfy above condition if starting value of iteration is taken to be zero. After $\vec{v}_g$ is obtained. Eq. (2 - 9) is solved by using Incomplete Cholesky-Conjugate Gradient method (ICCG), then differential equations for U_μ are solved by using the implicit Adams method.

4. Application

We developed the 3D code, ATLAS, based on the FEMALE method. The element is tetrahedron.

To check the ability of this code, the 3D shock tube problem in which the waves propagate in z direction is simulated. The numerical solution $\vec{v}_g$ of R-H relation, $C^\mu = 0$, agree with the local wave front velocities. It needs careful attention to determine $\vec{v}_g$ numerically. The results of this simulation are shown in Fig. 1, where solid line is exact solution and dots show numerical one. As the references, we show the results of Lagrangian ($\vec{v}_g = \vec{v}$) and Lax-Wendroff methods in Figs. 2 and 3, which are obtained by 1D code.

References

[1] P. D. Lax

Comm. Pure and Appl. Math 7 (1954) 159

[2] C. A. J. Fletcher

"Computational Galerkin Method"

Springer-Verlag, (1984)

[3] J. T. Oden

"Finite Elements of Nonlinear Continua"

McGrow-Hill Inc. (1972)

[4] R. S. Hirsh

J. Comp. Phys. 11 (1973) 38

[5] C. W. Hirt, A. A. Amsden and J. L. Cook

J. Comp. Phys. 14 (1974) 227

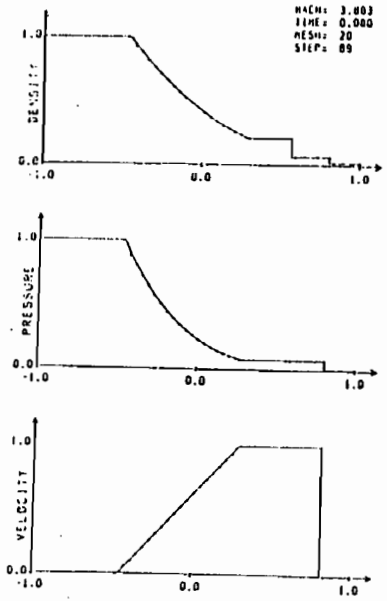

Fig. 1

FEMALE method

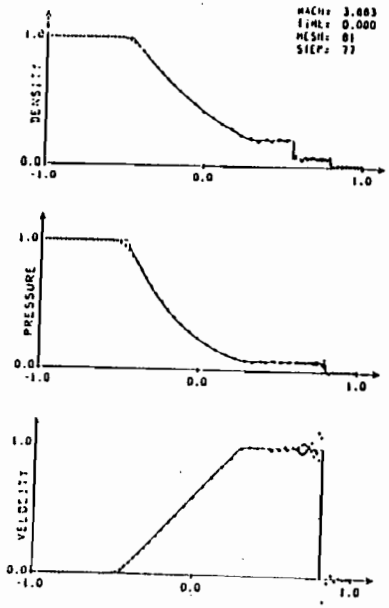

Fig. 2

Lagrangian method

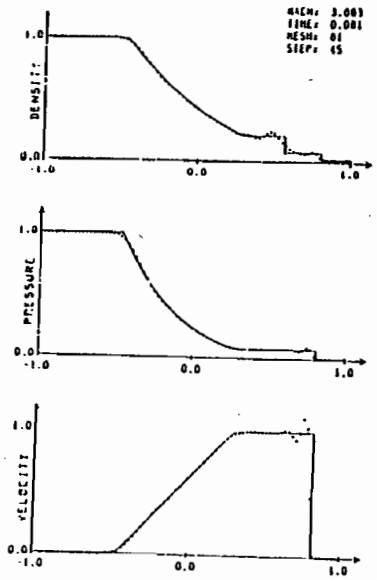

Fig. 3

Two-step Lax-wendroff method

RAPIDLY CONVERGENT ALGORITHMS FOR 3-D TANDEM AND STELLARATOR EQUILIBRIA IN THE PARAXIAL APPROXIMATION

BRENDAN McNAMARA,

Lawrence Livermore National Laboratory, University of California, Livermore, California.

Tandem and stellarator equilibria at high β have proved hard to compute and the relaxation methods of Bauer et al. [1], Chodura and Schluter[2], Hirshman [3], Strauss [4], and Pearlstein et al. [5] have been slow to converge. This paper reports an extension of the low-β analytic method of Pearlstein, Kaiser, and Newcomb [6] to arbitrary β for tandem mirrors which converges in 10-20 iterations. Extensions of the method to stellarator equilibria are proposed and are very close to the analytic method of Johnson and Greene [7] - the "stellarator expansion". Most of the results of all these calculations can be adequately described by low-β approximations since the MHD stability limits [8] occur at low β. The tandem mirror, having weak curvature and a long central cell, allows finite Larmor radius effects to eliminate most ballooning modes and offers the possibility of really high average β. This is the interest in developing such three-dimensional numerical algorithms.

2. CONNECTION BETWEEN KINETIC AND FLUID MODELS

Tandem mirrors have very large mirror ratios and large flux-surface distortions and so any numerical representation of the equilibrium must use the field lines as the basis of the coordinate system to place mesh points where they are needed. This is done by defining the magnetic field in terms of two scalars (ψ,θ) as

$$\underline{B} = \nabla\Psi \times \nabla\theta \qquad (1)$$

which ensures that $\nabla\cdot\underline{B}=0$. In a Stellarator the field lines lie on magnetic surfaces which naturally identify a set of flux surfaces, ψ. In tandem mirrors the field lines are open and there are no natural magnetic surfaces. However, the systems are designed so that confined particles move on closed drift surfaces and, in many designs, these are arranged to be the same surfaces for almost all particles whose orbits intersect the same field line. These are the so-called omnigenous drift surfaces of Hall and McNamara [9] and are physically the relevant choice for ψ. The second flux-line coordinate, θ, is an angle-like variable chosen to satisfy eqn.1. Even in systems which are not everywhere omnigenous for particles moving in the vacuum field alone it is speculated that the plasma transport processes set up radial electric fields which re-align the drift orbits much closer to an omnigenous set and this is to be expected also in toroidal systems. The assumption of omnigenity allows one to connect the microscopic distribution functions with macroscopic density and pressure profiles most easily. Most fusion systems now have neutral beam or high-power RF inputs which directly affect distribution functions and thereby affect the equilibria, effects which need to be modelled.

Tandem mirrors tend to self-anneal for a number of reasons which need further explanation. In stationary electric and magnetic fields the strong constants of motion of a single particle of charge, e, mass, m, and velocity, v are the energy,

$$H = \frac{1}{2} m v_{\parallel}^{2} + \mu B + e\Phi \qquad (2)$$

and the magnetic moment,

$$\mu = \frac{m v_{\perp}^{2}}{2B} \qquad (2)$$

The magnetic moment is an adiabatic invariant and is destroyed by plasma oscillations at or above the cyclotron frequency, but is not affected by the global geometry of the field, provided the Larmor parameter, ε = (Larmor radius)/(radial scale) is small. The longitudinal adiabatic invariant, Λ, is the action in the bounce motion,

$$\Lambda = \int v_{\parallel}\, dl \qquad (3)$$

$$= \int \left(\frac{2}{m}(H - \mu B - e\Phi)\right)^{1/2} ds \qquad (4)$$

In the paraxial equilibrium theory [10] it is found that $B=B(\psi,s)$ in a mirror cell at high β. (β= the ratio of plasma to magnetic pressure). The distance s along a field line is approximately the distance, z, along the axis of the system and so $\Lambda = \Lambda(H,\mu,\psi)$ if Φ is small. The drifts are dominated by the ∇B drift and the surfaces are locally omnigenous.

At low β, B is independent of ψ and so the drift surfaces are determined by the difference between s and z due to the weak field line curvature. At this point I introduce Newcomb's [10] notation for the covariant components of the field line curvature,

$$\underline{k} = \hat{b}\cdot\nabla\hat{b}$$

$$= R\nabla\psi + \Xi O\nabla\theta \qquad (5)$$

Then, it can be shown that the net drift off a surface, ψ, in one bounce of a particle is

$$\Delta\psi = -\left(\frac{m}{e}\right)\int (v_{\parallel}^{2} + \mu B)\, \Xi O\, \frac{dz}{v_{\parallel}} \qquad (6)$$

If B is symmetric about the center of this cell then the integral will vanish if ΞO is designed to be antisymmetric and the drift surfaces will be omnigenous.

In the paraxial limit the potential is determined by the requirement of local quasineutrality and then $\Phi=\Phi(B,\psi)$. Even in a low-β mirror cell which is not omnigenous in the vacuum magnetic field, omnigenity is restored by the potential, determined by radial losses and events in neighbouring cells. An example of just such a case is the GAMMA-VI experiment [11], in which the end plugs are aligned so that fans of field lines enetering the center-cell from the plugs are both vertical. There are NO confined magnetic drift surfaces in the centre cell and so the choice of ψ is determined by the drift surfaces of the high-temperature plasma in the plugs. These are omnigenous locally, with a

circular section at the midplane of each plug. These cicles map into an elliptic cross-section flux tube in the center cell. When the center cell is filled with plasma the radial losses lead to radial potential drops of $\Phi \simeq 3\text{-}4\ T_{ic}$ and the drifts are dominated by the $\underline{E}\times\underline{B}$ drifts and so the <u>total</u> system becomes omnigenous. Reasonable models of the total pressure tensor can be given in the forms

$$\underline{P} = \underline{P}(\Psi,B)$$

$$= \omega(\Psi)(\hat{p}_{\parallel}(\Psi,B)\underline{I} + \hat{b}\hat{b}\hat{p}_{\perp}(\Psi,B)) \tag{11}$$

where most of the Ψ-dependence has been extracted in the density profile factor ω, and $\underline{\hat{P}}$ depends only on weakly varying functions like the mirror ratio, or on the radial variation of Φ. The electric fields have not been included in the rest of this paper but will be essential in a fuller model of the tandem mirror equilibria.

3. THE CURRENT BALANCE ALGORITHM.

Newcomb and Strauss have derived the paraxial form of the equilibrium equations from the static and dynamical equations respectively. I therefore present only the most direct definition of the required relations. In addition to the requirement that $\nabla\cdot\underline{B}=0$, which is satisfied by the representation in eqn. (1), the three-dimensional equilibrium of a guiding center plasma is described by the force-balance equation,

$$\underline{J}\times\underline{B} = \nabla\cdot\underline{P} \tag{12}$$

and Ampere's law,

$$\nabla\times\underline{B} = \underline{J} \tag{13}$$

In Strauss' reduction of the dynamical equations, the leading order equilibrium condition, $O(\lambda^0)$, comes from the perpendicular components of the force-balance. Eqns. 12 and 13 can be combined to give

$$\nabla_{\perp}(B^2/2 + p_{\perp}) = \underline{k}(B^2 + p_{\perp} - p_{\parallel}) \tag{14}$$

In the paraxial approximation the curvature is small, $O(\lambda^2)$, and, on dropping the curvature, eqn. 14 may be integrated to give

$$B^2/2 + p_{\perp} = B_v(z)^2/2 \tag{15}$$

This is to be solved for $B(\Psi,z)$ to establish perpendicular pressure balance, where z is the distance along the axis of the system and B_v is the vacuum field on the axis. The next order equilibrium condition is obtained from the parallel component of the force balance, which is

$$\hat{\underline{b}}\cdot\nabla \cdot \underline{P}=0 \tag{16}$$

This arises from conservation of (H,μ). The pressure gradient is now determined in flux coordinates, along with the perpendicular current flow. It remains to find the parallel current and the actual shape of the flux surfaces. At this point, the Lagrangian representation of the field is introduced in terms of the position of a field line as

$$\underline{X} = \underline{X}(\Psi,\theta,s) \tag{17}$$

so that

$$\underline{B} = \hat{b}B = \underline{X}'B \tag{18}$$

and $\underline{X}'=\partial\underline{X}/\partial s$ is the tangent vector. The parallel current per unit flux, i, is defined as

$$\underline{B} \cdot \underline{J} = iB^2 \qquad 19)$$

$$= B\underline{X}'\cdot\nabla\times\underline{X}'B$$

$$= B\underline{X}'\cdot(\nabla B\times\underline{X}' + B\,\nabla\times\underline{X}')$$

$$= B^2\underline{X}'\cdot\nabla\times\underline{X}' \tag{19}$$

In the paraxial approximation only the axial current contributes and so

$$i_1 = i(\Psi,\theta,z) = \frac{\partial X'}{\partial y} - \frac{\partial Y'}{\partial x}$$

$$= B([X',X] + [Y',Y]) \tag{20}$$

where (x,y,z) are Cartesian coordinates and (X,Y,z) the position of a field line. The conversion to (Ψ,θ,z) coordinates introduced the bracket notation for

$$[f,g] = \frac{\partial f\partial g}{\partial\Psi\partial\theta} - \frac{\partial f\partial g}{\partial\theta\partial\Psi} \tag{19}$$

$$= f_\Psi\, g_\theta - f_\theta\, g_\Psi \tag{21}$$

and the Jacobian, in this approximation is

$$\frac{1}{B} = [X,Y] \tag{22}$$

The definition of the parallel current involves only local quantities, the position of the field lines, but the equilibrium equations also demand that

$$\nabla\cdot\underline{J} = 0$$

$$= \nabla\cdot\underline{J}_\perp + \underline{B}\cdot\nabla\, i \tag{23}$$

After substituting for $\underline{J}_\perp$ from the force balance eqn. (12), and a little maniputlation, i is found to be the field-line integral

$$i(\Psi,\theta,s) = \frac{1}{\sigma}\int_{-L}^{s} \hat{\underline{b}}\cdot\underline{k} \times \nabla(\sigma B^2)\frac{dl}{B^2} + i_{-L} \tag{24}$$

where

$$\sigma = 1 + \left(\frac{p_\perp - p_\parallel}{B^2}\right) \tag{25}$$

The initial plane, s=-L, can be an arbitrary plane in the vacuum outside the tandem mirror where the integration constant, i_{-L}, is zero. In the paraxial approximation,

$$i_p = i(\Psi,\theta,z) = \frac{1}{\sigma}\int_{-L}^{z} 2\Psi O \frac{\partial\bar{p}}{\partial\Psi}\frac{dl}{B^2} + O(\lambda^3) \tag{26}$$

where

$$\bar{p} = (p_\perp + p_\parallel)/2 \tag{27}$$

The current balance algorithm moves the field lines to equate the local expression, (20), and the integral expression (26)

$$i_l = i_p \tag{28}$$

This is equivalent to setting the integral of the parallel component of the curl of the force balance to zero in Strauss' dynamical model.

The starting position for the tandem-mirror field lines is obtained from one vacuum field line close to the axis of the system of an actual coil configuration. This gives the field strength, $B_v(z)$, and the ellipticity factor, $c_v(z)$ for the field line coordinates

$$X = \rho \cos\theta \; e^{c_v(z)}$$

$$Y = \rho \sin\theta \; e^{c_v(z)} \tag{29}$$

The radial factor, ρ, is chosen to give the correct Jacobian, (13), with $B(\Psi,z)$ calculated from the pressure balance, (18):

$$\rho^2 = \int_0^{\Psi} \frac{d\Psi}{B(\Psi,z)} \tag{30}$$

This choice of ρ takes care of the diamagnetism of the plasma and usually provides most of the displacement of the field lines from their equilibrium positions.

Subsequent movement of the field lines must be done incompressibly so as to preserve the pressure balance,(15), and also the Jacobian, (22), conservation of which is used as numerical test of the accuracy of the calculations. Such a motion is determined by a velocity potential or two-dimensional 'Hamiltonian', u, for the (X,,Y) motion in each z-plane as

$$d\underline{X}(\Psi,\theta,z)/dt = \nabla u \times \hat{z} \tag{31}$$

If the displacement is small then

$$\underline{X} = \underline{X}_0 + \nabla(\int u\, dt) \times \hat{z} + O(\Delta X^2)$$

$$= \underline{X}_0 + \nabla U \times \hat{z} \tag{32}$$

or, in (Ψ,θ,z) coordinates,

$$X = X_0 + B[X_0,U]$$

$$Y = Y_0 + B[Y_0,U] \tag{33}$$

This may be substituted into the current balance eqn.(28), and i_1 linearised to give the equation for U

$$\nabla^2 \frac{(BU)'}{B} = (i_0 - i_p) + [U,i_0] - B[X_0,BU[X_0,\frac{B'}{B}]]$$

$$-B[Y_0,BU[Y_0,\frac{B'}{B}]] + O(U^2) - \frac{1}{2}I_p \tag{34}$$

where

$$i_0 = B([X_0',X_0] + [Y_0',Y_0]) \tag{35}$$

Since it does not linearise conveniently, the integral is evaluated, to all orders in U, from the field line positions at the previous step in the iteration process. The right hand side of (34) is evaluated on each plane and the elliptic operator is inverted. The boundary conditions for the tandem mirror are that U=0 on the symmetry planes, $\theta=0,\pi/2$, and at a distant wall, $\Psi=\Psi_{wall}$.

The last piece in (34) is needed to symmetrize the numerical representation of the equation. The tandem mirror has ying-yang symmetry about the mid-point and so computations are done only in an octant of the configuration. By definition, every term of (34) has this symmetry exactly, except for the integral, i_p, which is done from z=-L. Without the symmetrizing addition, which goes separately to zero at equilibrium, the midplane is driven away from equilibrium. Needless to say, some meditation was needed to introduce this correction to ther numerics.

A final integration then yields:

$$U = \frac{1}{B}\int_0^z (BU)'\, dz + \frac{\Phi(\Psi,\theta)}{B(\Psi,z)}$$
$$= U_A + \frac{\Phi}{B} \qquad (36)$$

The integration constant, Φ, on each field line is now determined by the condition that the integral form of the current should vanish in the symmetrically placed vacuum at z=+L.

$$\frac{I_p}{\omega_\Psi} = \frac{i_p(\Psi,\theta,L)}{\omega_\Psi}$$
$$= \oint \frac{dz}{B}\frac{2\bar{p}_\Psi}{\omega_\Psi}\left(X_{0\theta}\, X_0'' + Y_{0\theta} Y_0''\right)$$
$$+ \oint \frac{dz}{B}\frac{2\bar{p}_\Psi}{\omega_\Psi}\left(\left(B[X_0,U_A]_\theta\, X_0'' + X_{0\theta}(B[X_0,U_A])''\right) + (X\to Y)\right)$$
$$+ a\Phi_{\theta\theta} + b\Phi_{\Psi\theta} + c\Phi_\Psi + d\Phi_\theta + e\Phi + O(U^2)$$
$$= 0 \qquad (37)$$

The function Φ and its derivatives come out of the integral, yielding a second-order parabolic equation! This is somewhat strange for an equilibrium problem and is a consequence of the paraxial approximation and the conversion of the corresponding axial boundary condition on the dynamical formulation into an integral constraint. It does not occur in the fully three-dimensional treatments (cf. Hall and Mcnamara). The coefficients (a-e) are the corresponding pieces of the integrals over U_A and need not be written explicitly here, except for 'a' which turns out to be the flute stability integral

$$a = \oint \frac{dz}{B}\frac{2\,R\,\bar{p}_\Psi}{\omega_\Psi} \qquad (38)$$

This would vanish at the flute stability boundary, with dire consequences for the algorithm , but this would always be at betas above the stability limit for ballooning or rigid-displacement modes.

The factor $1/(\omega_\Psi)$, is inserted in the integrals to keep all the coefficients finite near the plasma boundary, where the whole equation would otherwise vanish, leaving no useful means of defining Φ. This would also allow the equation to be extended into the vacuum region but Φ will then never satisfy any particular radial boundary condition. There is no current in the vacuum driven by plasma pressure and it seems incorrect to use the constraint on these field lines. This leaves Φ completely unspecified in the vacuum and it can therefore be chosen to be any smooth function which matches to the plasma Φ and which satisfies $\Phi=0$ at $\Psi=\Psi_{wall}$.

The other boundary conditions on Φ are therefore $\Phi=0$ on the symmetry planes $\theta=0,\pi/2$ and, because of the overall quadrupole symmetry of tandem mirrors, at $\theta=\pi/4$, about which Φ is actually anti-symmetric. Only one boundary condition in the Ψ-direction can be specified in the plasma, $\Phi(\Psi=0) = 0$, and this parabolic equation is then integrated outwards from the magnetic axis. This completes the definition of U and the field line displacements needed to achieve equilibrium.

This completes the description of the basic algorithm.

4. APPLICATION TO STELLARATORS.

I have not written a code for the Stellarator version of this method but believe it is a straightforward modification. The first change is to insert an appropriate analytic guess at the initial conditions, similar to eqns (29-30). The next point is to confine the problem volume to one period of the Stellarator and apply periodicity conditions to the calculation. Thus, the integration constant, i_{-L}, in eqn (24) is a given function of Ψ, corresponding to the net induced current flowing on each surface.

The constraint on the parallel current flow is that it be periodic , which yields a pair of conditions on the integration constant Φ and its surface average. Thus, $i_p(\Psi,\theta,L)=i_p(\Psi,\theta,2L)=i_p(\Psi,\theta,nL)$. The second part of this leads to the requirement that the surface average of the parallel current should equal $i_{-L}(\Psi)$. The first part is constructed by iterating the mapping of the field line positions at z=0 to their positions at z=L to get the locations at z=2L. The periodicity requirement then gives an eqn similar to (37).

5. A TMX-UPGRADE EXAMPLE

This particular example was the first case successfully brought to equilibrium by L.D.Pearlstein with the dynamical code in some 11,000 time steps. The result shown is very close to that and both are close to the TEBASCO result from the low-β analytic theory.

The first figure shows the axial magnetic field profile as $B_{kG}(Z_{cm})$.

Improved accuracy is obtained by stretching the z coordinate and Fig2 shows B(s(z)). The initial analytic guess at equilibrium gives the parallel current profile of Fig. 3 at z=0 from the local expression and the profiles of Fig 4. from the integral. They are far from agreement and the local form shows current flowing in the vacuum. The axial variation of the local and integral currents are shown in fig. 5 for a field line in the plasma and one in the vacuum. The differences supply most of the source for eqn. (34). The initial flow patterns in the mid-plane, which is all octupole and higher, and the end plane are in Figs 6,7. The average beta in a plane has a maximum of 8.3%, peak central beta being 25% with $\omega=(1-\Psi/\Psi_{plas})^2$. This case converged in ten steps to 1% accuracy everywhere. Current balance is shown in fig 8 and the convergence behaviour in Figs. 9-12. Note the total current constraint is $O(\beta)$ smaller than the other measures. Flux surface shapes in equilibrium show the characteristic diamond distortion for a stable equilibrium.

These results agree closely with the dynamical code and quite well with Tebasco, the low-beta analytic equilibrium calculation. The principal differences are that the parallel current is about 15% higher in the finite-β calculation and the geodesic curvatures are somewhat larger. The principal curvature, and hence the MHD stability are hardly altered by the plasma.

At higher betas the code may fail to converge because the initial guess is simply too far from the answer. Also, in tandems with more cells , numerical accuracy becomes a problem. Work is continuing on extending the domain of applicability of the code.

ACKNOWLEDGEMENTS

I would like to thank L.S. Hall, T.B.Kaiser, L.D.Pearlstein for many useful conversations.

REFERENCES.

1. F.Bauer,O.Betancourt, P.Garabedian, A Computational Method for Plasma Equilibrium. Springer, 1978

2. R. Chodura, A. Schluter, J. Comp. Phys,41,68-88,(1981)

3. S. Hirshman, Phys. Fluids, 1983

4. H.R. Strauss, Nucl. Fusion, 22(1982) 893

5. L.D.Pearlstein, B.McNamara, T.B.Kaiser, Bull. A.P.S., Nov. 1983

6. L.D.Pearlstein, T.B.Kaiser, W.A.Newcomb, Phys Fluids, 24(1981)1326

7. J.Johnson, J. Greene, Phys Fluids, 1961

8. R.H.Bulmer et al., Proc. IAEA Conf. on Fusion, 1982 9. L.S.Hall, B. McNamara,Phys. Fluids 18(1975) 552

10. W.A.Newcomb, J. Plasma Phys., 26(1981) Pt3,529

11. T. Kawabe, Private Communication.

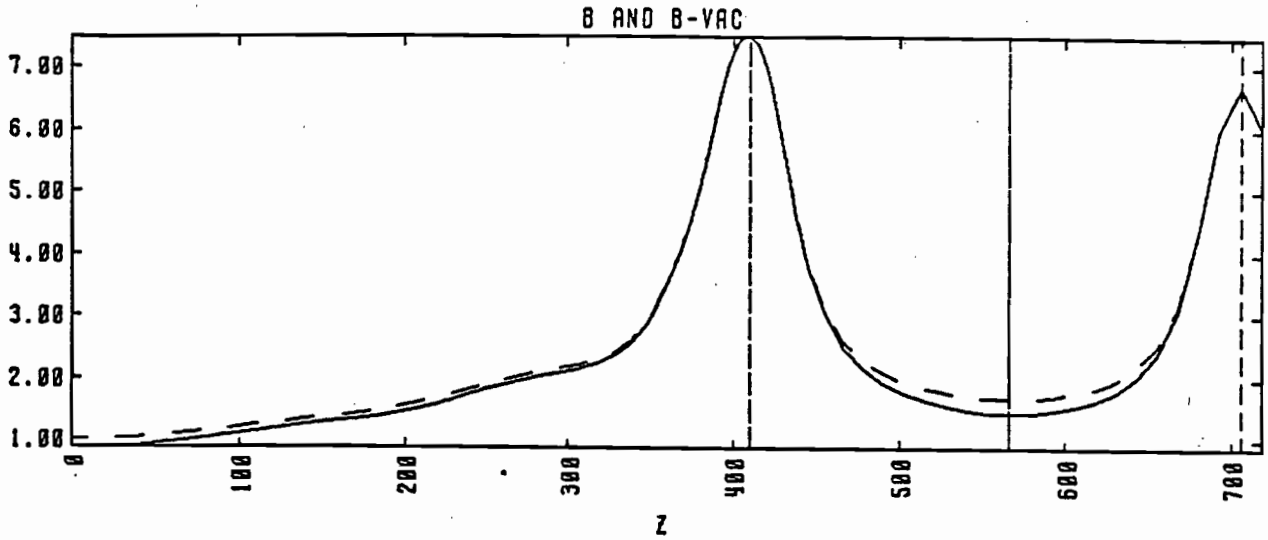

Figs. 1,2. Axial magnetic field strength vs z and the stretched coordinate s(z) to improve accuracy.

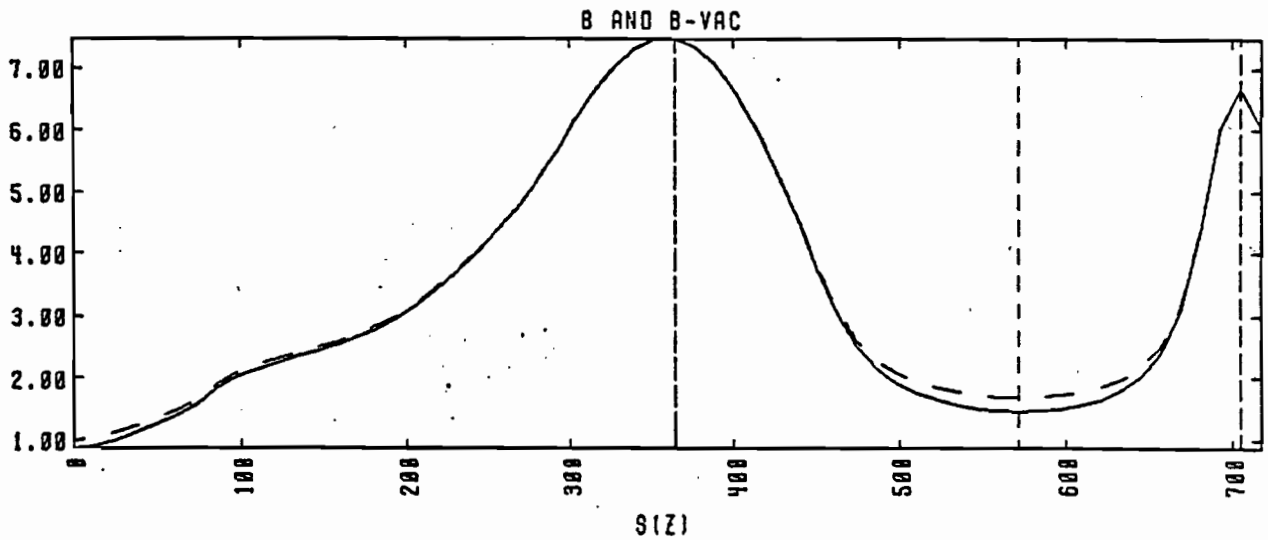

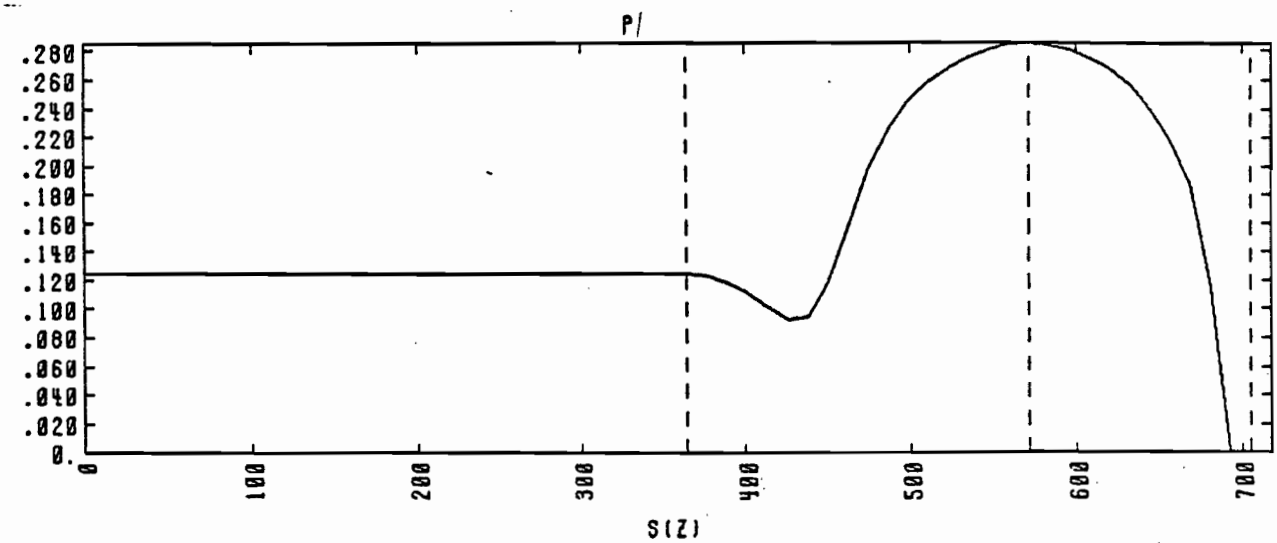

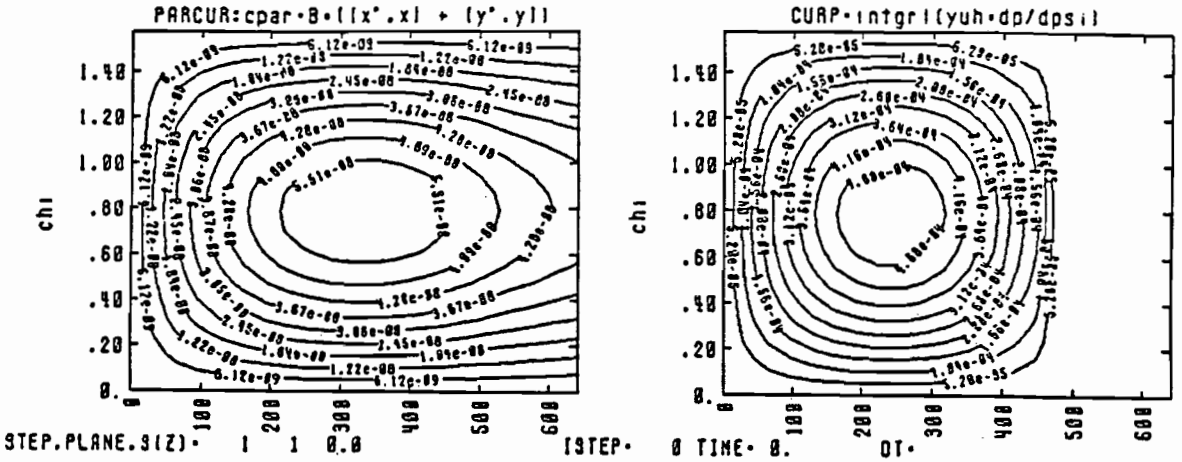

Figs. 3,4. Compare local and integral values of the mid-plane parallel current from the initial guess.

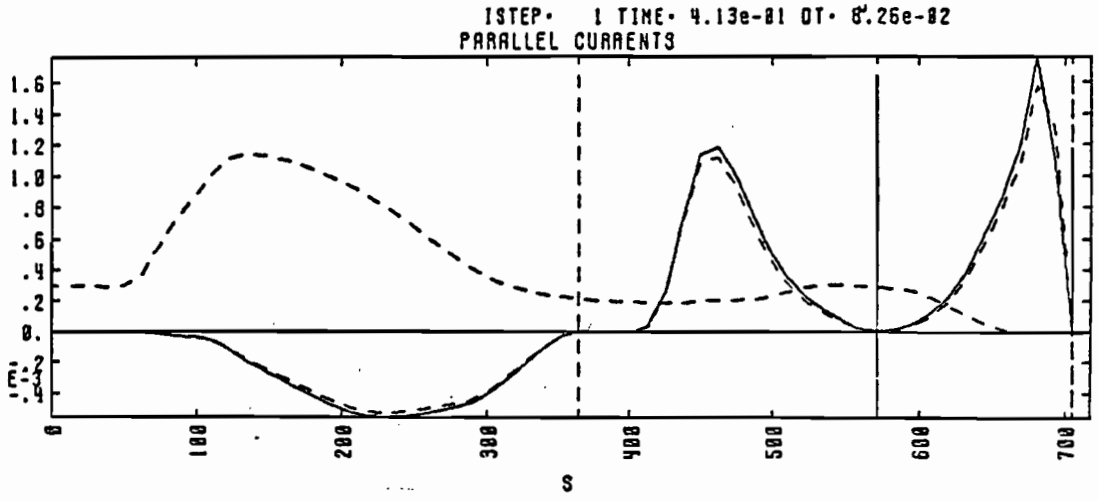

Figs. 5. Solid line is parallel current at $\psi = \psi_{plas}/2$, $\theta = \pi/10$. Nearby dotted line at ψ near ψ wall. Other dotted line is integral value of current on $(\psi_{plas}/2, \pi/10)$.

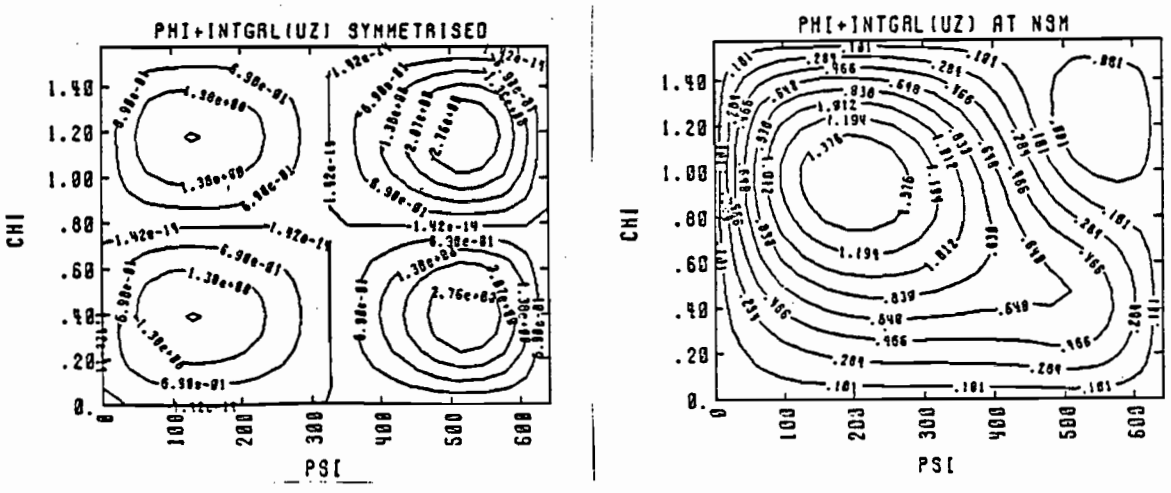

Figs. 6,7. Initial flow pattern in mid-plane and end-plane to approach current balance.

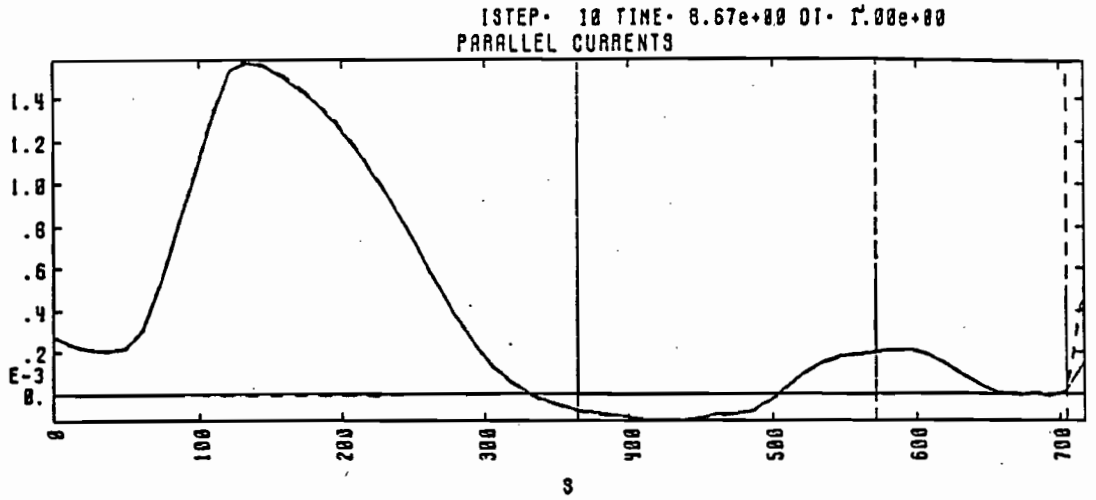

Fig. 8. Local and integral currents balanced in 10 steps. Vacuum currents reduced to zero.

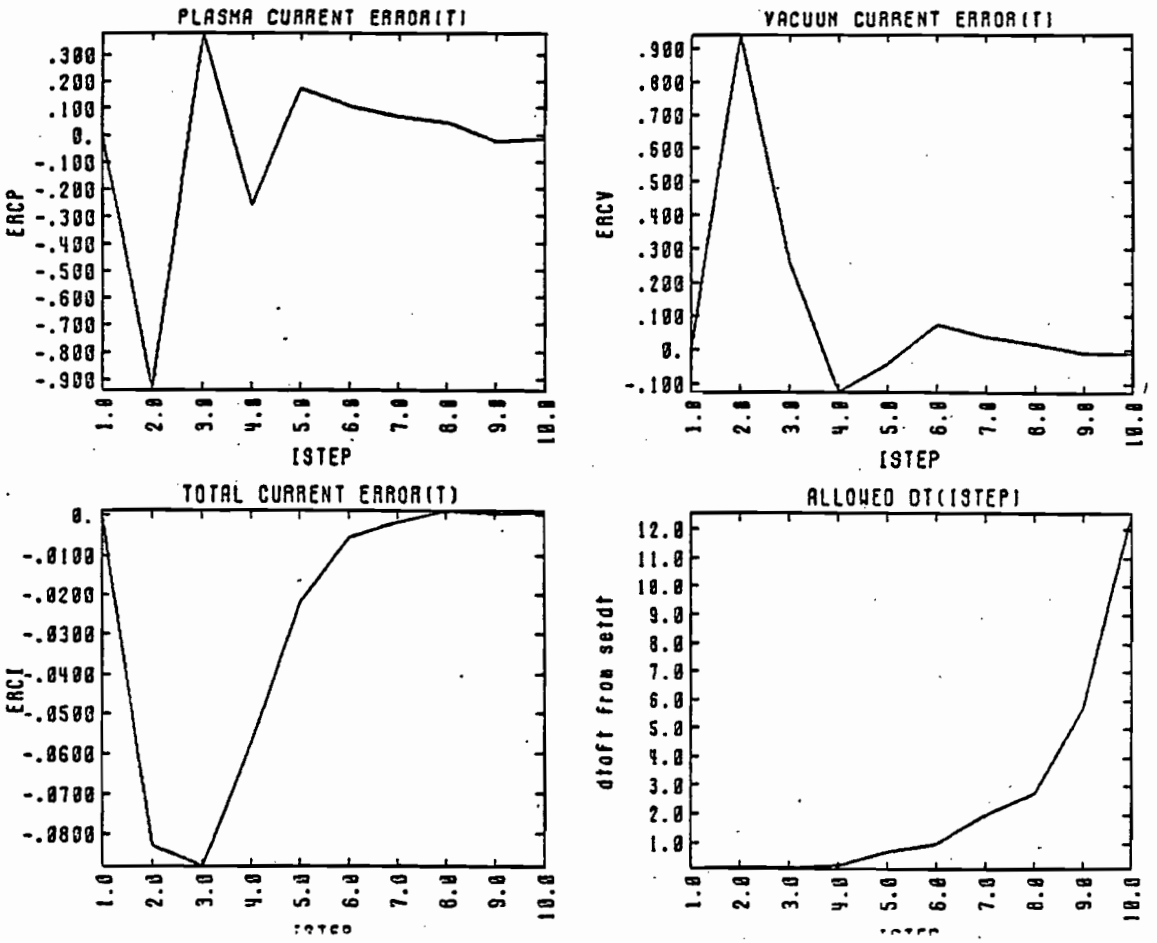

Figs. 9-12. Convergence of relative errors in current balance, vacuum current, and total current constraint. Also maximum timestep allowed for conserving Jacobian.

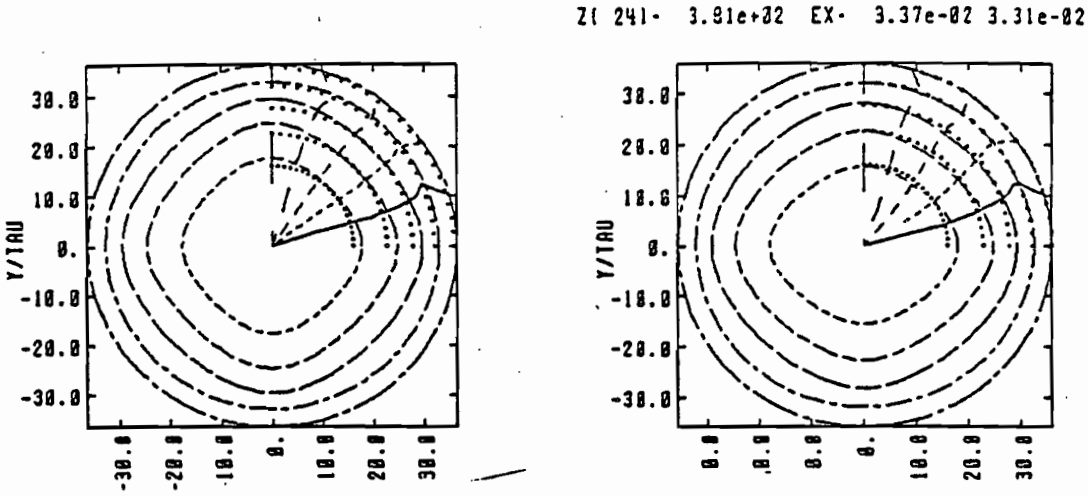

Figs. 13,14. Flux surface shapes in mid-plane and first mirror throat. Coordinates normalized so dotted vacuum shapes are circular.

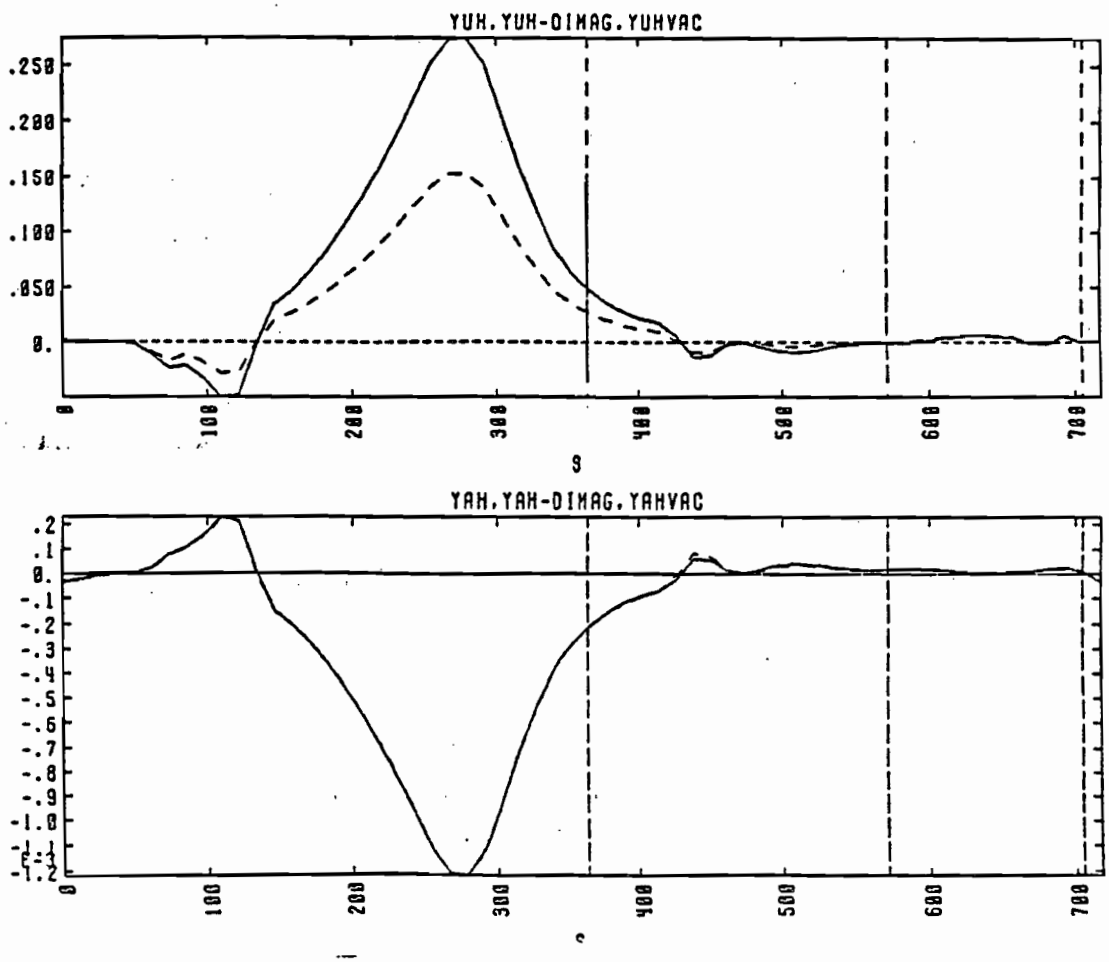

Figs. 15,16. Geodesic and principal curvatures compared with dotted vacuum values.

By acceptance of this article, the publisher or recipient acknowledges the U.S. Government's right to retain a nonexclusive, royalty-free license in and to any copyright covering the article.

Magnetic Equilibria for Square and Circular EBTs

C. L. Hedrick and L. W. Owen

For closed magnetic field line devices, scalar pressure MHD implies that the pressure surfaces are the same as surfaces of constant $\oint d\ell/B$. This relation can also be developed from the drift kinetic equation. Here we contrast this result with that obtained from the bounce averaged drift kinetic equation. We consider a collisionality regime such that the collision frequency is much less than the bounce frequency but comparable (within an order of magnitude) to the poloidal precession frequency. Under these circumstances it is reasonable to assume that scattering causes the distribution function to be approximately isotropic and that J is not conserved on a drift time scale. This assumption allows us to make a direct comparison to the MHD results which would not be possible for lower collisionality where the distribution function would be anisotropic and approximately a function of ϵ, μ, and J. Our motivation for discussing this collisionality regime lies in its possible application to the EBT-I/S and NBT-IM experiments as well as to configurations projected for the near future such as the ELMO Bumpy Square.

There are several ways of obtaining the MHD result that the pressure surfaces are the same as surfaces of constant $\oint d\ell/B$ for closed magnetic field lines. One of the algebraically most compact procedures follows from the equilibrium algorithm introduced by Lortz [1] (extended to tensor pressure by Grad [2] and others [3], [4]). This approach makes use of the fact that $\nabla \cdot \vec{j} = 0$ implies that a Clebsch representation can be used for the current: $\vec{j} = \nabla\varsigma \times \nabla p$. By extracting the perpendicular current from this equation and comparing it to that obtained from pressure balance; $j_\perp = \vec{B} \times \nabla p/B^2$ one finds that $\partial\varsigma/\partial\ell = 1/B$. This result allows one to impose single-valuedness of the current in the Clebsch representation and obtain

*Research sponsored by the Office of Fusion Energy, U.S. Department of Energy, under contract No. DE-AC05-84OR21400 with Martin Marietta Energy Systems, Inc.

$$\nabla \oint \frac{d\ell}{B} \times \nabla p = 0 \tag{1}$$

A second approach, which more closely follows the procedure which is convenient for kinetic treatments again begins with the time independent expression of charge conservation:

$$\nabla \cdot \vec{j} = 0 \tag{2}$$

Here one begins with the observation that $\nabla \cdot \vec{j}_{\parallel} = B\frac{\partial}{\partial \ell}(j_{\parallel}/B)$ and integrates Eq. (2) around a field line to obtain

$$\oint \frac{d\ell}{B} \nabla \cdot \vec{j}_{\perp} = 0 \tag{3}$$

From $\vec{j} \times \vec{B} = \nabla p$, $\vec{j}_{\perp} = \vec{B} \times \nabla p/B^2$; which yields after a little manipulation

$$\nabla \cdot \vec{j}_{\perp} = \nabla p \cdot \left[\nabla \times \vec{B} + 2\vec{B} \times \nabla \ell n B\right]/B^2 \tag{4}$$

Noting that ∇p is perpendicular to $\vec{B}$ one next uses the vector identity for $\nabla(\vec{B} \cdot \vec{B})$ to obtain

$$\nabla \cdot \vec{j}_{\perp} = \frac{\nabla p}{B^2} \cdot \left[\vec{B} \times (\vec{\kappa} + \nabla \ell n B)\right] \tag{5}$$

where the curvature vector is given by

$$\vec{\kappa} = (\hat{b} \cdot \nabla)\hat{b} \tag{6}$$

At this juncture, it is convenient to introduce the Clebsch representation for the magnetic field:

$$\vec{B} = \nabla\alpha \times \nabla\beta \tag{7}$$

and note that α and β are constant along field lines. Since p is constant along field lines

$$\nabla p = \frac{\partial p}{\partial \alpha}\nabla\alpha + \frac{\partial p}{\partial \beta}\nabla\beta \tag{8}$$

and Eq. (5) becomes

$$\nabla \cdot \vec{j}_\perp = \left[-\frac{\partial p}{\partial \alpha}\vec{U}_\beta + \frac{\partial p}{\partial \beta}\vec{U}_\alpha\right] \cdot (\vec{\kappa} + \nabla \ell n B) \tag{9}$$

where

$$\begin{aligned} \vec{U}_\alpha &\equiv (\nabla\beta \times \vec{B})/B^2 \\ \vec{U}_\beta &= (\vec{B} \times \nabla\alpha)/B^2 \end{aligned} \tag{10}$$

and have the properties that

$$\begin{aligned} \vec{U}_\alpha \cdot \nabla\alpha &= 1 \quad ; \quad \vec{U}_\alpha \cdot \nabla\beta = 0 \\ \vec{U}_\beta \cdot \nabla\alpha &= 0 \quad ; \quad \vec{U}_\beta \cdot \nabla\beta = 1 \end{aligned} \tag{11}$$

Inserting Eq. (9) into Eq. (3) and noting that p and its α, and β derivatives are independent yields

$$-\frac{\partial p}{\partial \alpha}\oint \frac{d\ell}{B}\left[\vec{U}_\beta \cdot (\vec{\kappa} + \nabla \ell n B)\right] + \frac{\partial p}{\partial \beta}\oint \frac{d\ell}{B}\left[\vec{U}_\alpha \cdot (\vec{\kappa} + \nabla \ell n B)\right] = 0 \quad (12)$$

One next notes that for closed field lines and arbitrary S

$$\frac{\partial}{\partial \alpha}\oint d\ell S = -\oint d\ell\, S\, \vec{U}_\alpha \cdot \left[\vec{\kappa} - \nabla \ell n\, S\right]$$

$$\frac{\partial}{\partial \beta}\oint d\ell\, S = -\oint d\ell\, S\, \vec{U}_\beta \cdot \left[\vec{\kappa} - \nabla\, \ell n\, S\right] \quad (13)$$

Setting S = 1/B in Eq. (13) one finds that Eq. (12) becomes

$$\frac{\partial p}{\partial \alpha}\frac{\partial}{\partial \beta}\oint \frac{d\ell}{B} - \frac{\partial p}{\partial \beta}\frac{\partial}{\partial \alpha}\oint \frac{d\ell}{B} = 0 \quad (14)$$

Equation (14) is simply Eq. (1) written in component form.

We now turn to the drift kinetic equation [5]

$$\frac{\partial f_j}{\partial t} + v_\parallel \cdot \nabla f_j + \vec{V}_{Dj} \cdot \nabla f_j = C_j \quad (15)$$

Here f_j is a function of ϵ, μ and $\vec{x}$, the position of the guiding center. (We will soon consider time independent solutions and drop the time derivative of f_j.) The previous MHD analysis suggests that we integrate over velocity to form the lowest moment of Eq. (15) and then multiply by the charge, e_j, and sum over species to obtain the charge conservation relation

$$\frac{\partial \rho}{\partial t} + \nabla \cdot \vec{j} = 0 \tag{16}$$

which reduces to Eq. (2) for time independent solutions. Here

$$\nabla \cdot \vec{j}_{\parallel} = \sum_j e_j \int d^3v \; v_{\parallel} \cdot \nabla f_j = \sum_j e_j \; n_j \langle v_{\parallel} \rangle_j \tag{17}$$

and

$$\nabla \cdot \vec{j}_{\perp} = \sum_j e_j \int d^3v \; \vec{v}_{Dj} \cdot \nabla f_j \tag{18}$$

with

$$\vec{V}_{Dj} = \frac{\frac{1}{2}mv^2}{e_j B} \hat{b} \times \left[2\varsigma^2 \vec{\kappa} + (1 - \varsigma^2) \nabla \ell n \; B\right] \tag{19}$$

and

$$\varsigma \equiv v_{\parallel}/v \tag{20}$$

Note that for simplicity we have not included an electrostatic potential and the resultant $\vec{E} \times \vec{B}$ drifts. [Retaining such terms leads to small corrections of order $(\rho/en)\; e\phi/T$ times the ratio of scale lengths — usually negligible because of quasi-neutrality: $\rho/en \ll 1$.]

For isotropic distribution functions, $\partial f_j/\partial \mu = \partial f_j/\partial \varsigma = 0$ and the only pitch angle dependence in the integral of Eq. (18) occurs through the form factor $[2\varsigma^2 \vec{\kappa} + (1 - \varsigma^2) \nabla \ell n \; B]$ appearing in Eq. (19). Accordingly, it is convenient to define an average drift velocity by

$$\langle \vec{V}_D \rangle = \frac{T}{(\frac{1}{2}mv^2)} \int_0^1 d\varsigma \; \vec{V}_D \tag{21}$$

or

$$\langle \vec{V}_D \rangle = \frac{\frac{2}{3}T}{|e|B} \hat{b} \times [\vec{\kappa} + \nabla \ell n\, B] \tag{22}$$

and note that since

$$\frac{3}{2}p = \sum_j \int d^3v \, \frac{1}{2} mv^2 f_j \tag{23}$$

$$\nabla \cdot \vec{j}_\perp = \nabla p \cdot \left[\frac{\frac{3}{2}|e|\langle \vec{V}_D \rangle}{T}\right] \tag{24}$$

Inserting Eq. (22) into Eq. (24) yields the MHD result, Eq. (5), and one again obtains Eq. (14). It is instructive to follow a slightly different procedure. If we form the $\oint d\ell/B$ average of the charge conservation Eq. (16), the divergence of the parallel current vanishes and in steady state

$$\frac{1}{\oint \frac{d\ell}{B}} \oint \frac{d\ell}{B} \nabla \cdot \vec{j}_\perp$$

$$= \frac{1}{\oint \frac{d\ell}{B}} \oint \frac{d\ell}{B} \nabla p \cdot \left[\frac{\frac{3}{2}e\langle \vec{V}_D \rangle}{T}\right] = 0 \tag{25}$$

Using Eqs. (22) and (13) we find that

$$\frac{1}{\oint \frac{d\ell}{B}} \oint \frac{d\ell}{B} \nabla \alpha \cdot \langle \vec{V}_D \rangle = \left[\frac{\frac{2}{3}T}{e}\right] \frac{1}{\oint \frac{d\ell}{B}} \frac{\partial}{\partial \beta} \oint \frac{d\ell}{B} \tag{26}$$

$$\frac{1}{\oint \frac{d\ell}{B}} \oint \frac{d\ell}{B} \nabla\beta \cdot \langle \vec{V}_D \rangle = -\left[\frac{\frac{2}{3}T}{e}\right] \frac{1}{\oint \frac{d\ell}{B}} \frac{\partial}{\partial\alpha} \oint \frac{d\ell}{B} \tag{27}$$

Thus if we define

$$\langle\langle \vec{V}_D \rangle\rangle = \frac{1}{\oint \frac{d\ell}{B}} \left\{ \vec{U}_\alpha \oint \frac{d\ell}{B} \nabla\alpha \cdot \langle \vec{V}_D \rangle + \vec{U}_\beta \oint \frac{d\ell}{B} \nabla\beta \cdot \langle \vec{V}_D \rangle \right\} \tag{28}$$

then

$$\langle\langle \vec{V}_D \rangle\rangle = \left[\frac{\frac{2}{3}T}{|e|}\right] \frac{1}{\oint \frac{d\ell}{B}} \left[\frac{\nabla \oint \frac{d\ell}{B} \times \hat{b}}{B}\right] \tag{29}$$

and Eq. (25) can be written

$$\nabla p \cdot \left[\frac{\frac{3}{2}e}{T} \langle\langle \vec{V}_D \rangle\rangle\right] = 0 \tag{30}$$

or

$$\nabla p \cdot \langle\langle \vec{V}_D \rangle\rangle = 0 \tag{31}$$

Equations (31) and (29) may be interpreted as meaning that $\oint d\ell/B$ is a constant of motion for an "average particle". The relation between p and U may be interpreted as meaning that the pressure is constant on an "average" drift surface.

We notice that the $\oint d\ell/B$ average arose because $v_{\parallel}\partial f/\partial \ell$ in the drift kinetic equation [Eq. (15)] led to $\nabla \cdot \vec{j}_{\parallel}$ in the charge conservation equation. We also notice that f in Eq. (15) is a function of ϵ, μ, α, β and ℓ. For cases where the collision frequency is small compared to the bounce or transit frequency we expect that the dependence of f on ℓ will be very weak so that $\partial f/\partial \ell \simeq 0$. If the relation $\partial f/\partial \ell = 0$ holds for all species then $\nabla \cdot \vec{j}_{\parallel} = 0$ and the motivation for performing the $\oint d\ell/B$ average vanishes.

For collision frequencies well below the bounce frequency we expect that the distribution function will satisfy (approximately) the bounce (or transit) averaged drift kinetic equation:

$$\frac{\partial f_j}{\partial t} + \left[\frac{1}{\tau_j}\oint \frac{d\ell}{v_{\parallel}} V_{Dj}\right] \cdot \nabla f_j(\epsilon,\mu,\alpha,\beta) = \hat{C}_j \tag{32}$$

where

$$\langle \vec{V}_D \rangle_b = \frac{1}{\tau_j}\oint \frac{d\ell}{v_{\parallel}} \vec{V}_{Dj} = \frac{\nabla J \times \hat{b}}{e_j B \tau_j}$$

$$= \frac{1}{e_j \tau_j}\left\{\vec{U}_\alpha \frac{\partial J}{\partial \beta} - \vec{U}_\beta \frac{\partial J}{\partial \alpha}\right\} \tag{33}$$

As before we can obtain the equation of charge conservation by multiplying Eq. (32) by e_j, integrating over velocity space and summing over species. The time independent result is

$$\nabla \cdot \vec{j}_{\perp} = \sum_j e_j \int d^3v \, \langle \vec{V}_{Dj} \rangle_b \cdot \nabla f_j = 0 \tag{34}$$

We notice that if collisions are so infrequent that C_j can be neglected in Eq. (32) then $\langle \vec{V}_{Dj} \rangle_b \cdot \nabla f_j = 0$ and Eq. (34) is automatically satisfied. On the other hand if collisions are so infrequent that J is

approximately invariant, one cannot construct an isotropic distribution function for all α and β — except in certain highly degenerate cases.

In some cases of interest the collision frequency is comparable to the poloidal precession frequency but well below the bounce and transit frequency. In this instance it is possible to construct an isotropic distribution function for all α and b. This intermediate collisional case allows us to draw comparisons between the pressure surfaces arising from Eq. (32) and those arising from Eq. (15) or MHD. We thus suppose that f_j is independent of the adiabatic invariant μ:

$$f_j = f_j(\epsilon,\alpha,\beta) \tag{35}$$

As before, the lack of pitch angle (or μ) dependence of f_j allows us to pass it through the pitch angle integral implicit in Eq. (34) and we obtain the analog of Eq. (31):

$$\nabla \cdot \vec{j}_\perp = \nabla p \cdot \langle\langle \vec{W}_D \rangle_b \rangle \tag{36}$$

Note however that the average drift velocity in Eq. (36) is now given by

$$\langle\langle \vec{W}_D \rangle_b \rangle = \left[\frac{T}{(\frac{1}{2}mv^2)}\right] \left\{ \vec{U}_\alpha \int_0^1 d\varsigma_0 \, \langle \vec{V}_D \rangle_b \cdot \nabla\alpha \right.$$

$$\left. + \vec{U}_\beta \int_0^1 d\varsigma_0 \, \langle \vec{V}_D \rangle \cdot \nabla\beta \right\} \tag{37}$$

where $\vec{U}_\alpha$, $\vec{U}_\beta$, $\nabla\alpha$, $\nabla\beta$ and

$$\varsigma_0 \equiv \sqrt{1 - \mu B_0/\epsilon}$$

are to be evaluated at the arbitrary point, $\vec{X}_0$, where ∇p is evaluated

in Eq. (36). The pitch-angle like variable ς_0 has been chosen to make the correspondence to the earlier formalism more transparent.

In comparing Eqs. (31) and (36) we see that the α-component of $\langle\langle\vec{V}_D\rangle\rangle$ in Eq. (28) is given by

$$\langle\langle\vec{V}_D\rangle\rangle_\alpha = \left\{\frac{1}{\oint\frac{d\ell}{B}}\oint\frac{d\ell}{B}\int_0^1 d\varsigma\ \nabla\alpha\cdot\vec{V}_D\right\}\cdot\frac{T}{(\frac{1}{2}mv^2)} \tag{38}$$

while in Eq. (37) we have

$$\langle\langle\vec{W}_D\rangle_b\rangle_\alpha = \left(\frac{T}{\frac{1}{2}mv^2}\right)\int_0^1 d\varsigma_0\,\frac{1}{\tau}\oint\frac{d\ell}{v_\parallel}\nabla\alpha\cdot\vec{V}_D \tag{39}$$

and similarly for the β-components. We are thus led to invert the order of integration in Eq. (35). To facilitate this, we note that

$$\mu = \frac{\epsilon}{B}(1-\varsigma^2) = \frac{\epsilon}{B_0}(1-\varsigma_0^2) \tag{40}$$

so that

$$\frac{d\ell}{B}\,d\varsigma = \frac{1}{B_0}\frac{\varsigma_0}{\varsigma}\,d\ell d\varsigma_0 = \frac{1}{B_0}\frac{v_{\parallel p}}{v_\parallel}\,d\ell d\varsigma_0 \tag{41}$$

and

$$\langle\langle\vec{V}_D\rangle\rangle_\alpha = \left(\frac{T}{\frac{1}{2}mv^2}\right)\left[\frac{1}{B_0\oint\frac{d\ell}{B}}\right]\int_0^1 d\varsigma_0\ V_{\parallel,0}\oint\frac{d\ell}{v_\parallel}(\nabla\alpha\cdot\vec{V}_D) \tag{42}$$

or

$$\langle\langle\vec{V}_D\rangle\rangle_\alpha = \int_0^1 d\varsigma_0\ g(\langle\vec{V}_D\rangle_b\cdot\nabla\alpha)\left[\frac{T}{\frac{1}{2}mv^2}\right] \tag{43}$$

where

$$g = \frac{v_{\parallel 0}\,\tau}{B_0 \oint d\ell/B} \tag{44}$$

and similarly for the β component.

We notice that Eq. (43) would reduce to the bounce averaged case Eq. (37) if the weighting factor, g, were unity. However as given by Eq. (44), the weighting factor associated with the relatively high collisionality regime of MHD is not constant. Suppose that the point $\vec{X}_0$ corresponds to a minimum in B (along a field line). Referring to Eq. (44) we see that if we attempt to apply the high collisionality (or MHD) formalism to the intermediate collisionality regime, trapped particles are weighted too weakly ($v_{\parallel 0}$). We also note that τ becomes large for transitional particles, so that the high collisionality (or MHD) formalism weights transitional particles too heavily.

The net effect then is that the MHD result overestimates the pressure shift when the collision frequency is comparable to the drift frequency. For EBT-I/S, this overestimate is nearly a factor of 2 too large. For EBS where all particle orbit shifts are small, the pressure shift is also small. Applying the MHD result makes a larger percentage error than in EBT because transitional particles contribute relatively more to the pressure shift and MHD overemphasizes these particles. For EBS the MHD result for the shift is a factor of 3 or 4 too large.

REFERENCES

[1] D. Lortz, Z. Angew, Math. Phys. 21 (1970) 196.

[2] H. Grad, in Vol. III (pg. 229) of "Proc. of the 4th Int. Conf. on Plasma Phys. and Nucl. Fusion Research," Madison, Wisconsin, USA, June 17-23, 1971.

[3] C. L. Hedrick, G. E. Guest and D. B. Nelson, "Some Techniques for Determining Tensor Pressure Equilibria," ORNL/TM-4076 (March 1973).

[4] L. S. Hall and B. McNamara, Phys. Fluids 18 (1975), pg. 552 and references cited therein.

[5] R. D. Hazeltine, Plasma Physics, 15 (1973), pp. 77-80.

The Total Dereduction of the Reduced Equations

R. Izzo, D. Monticello and J. DeLucia
Princeton Plasma Physics Laboratory
P.O. Box 451, Princeton, NJ 08544

We have recently reported on the expansion of the Magnetohydrodynamics (MHD) equations to 4th order in the aspect ratio.[1] This high order expansion (2 orders past leading order) was necessary in order to calculate correctly the stability and nonlinear evolution of the internal kink. We report here on the expansion of the MHD equations to 5th order in the aspect ratio. Our motivation is the study of finite beta resistive modes. The work of Glasser, Greene, and Johnson[2] has shown that the coupling of the stable interchange modes to the unstable tearing modes can, at high enough temperature, lead to a stabilization of the latter. This stabilization is not in the 4th order reduced equations. The modificatons of the 4th order equations are quite simple. We use 6 scalar quantities to define general velocity and magnetic vector fields:

$$V = R^2 \nabla u \times \nabla \zeta + \nabla_\perp \chi + R\, V_\zeta \nabla \zeta \,, \tag{1}$$

$$B = \nabla \psi \times \nabla \zeta + \frac{1}{R} \nabla_\perp \left(\frac{\partial f}{\partial \zeta}\right) + I \nabla \zeta \,. \tag{2}$$

Using a model density $\rho \sim 1/R^2$ we find the following modifications to the 4th order equations (see Ref. (1)),

$$\frac{dP}{dt} = - \Gamma P \nabla \cdot V \,, \tag{3}$$

$$I \nabla_\perp I = - R^2 \nabla_\perp P - R^2 J_\zeta (B \times \hat{\zeta}) + I \frac{\partial B_\perp}{\partial \zeta} - I B_R \hat{\zeta} - R^2 \frac{\partial V_{\perp o}}{\partial t} \,, \tag{4}$$

where

$$V_{\perp o} = R^2 \nabla u \times \nabla \zeta \ .$$

The $4^{\underline{th}}$ order equations contain only a $\nabla \cdot V_{\perp o}$ in Eq. (3) and the $V_{\perp o}$ in Eq. (4) was dropped due to a small inertia approximation. The inclusion of the term $\nabla \cdot V$ gives the sound wave that is necessary for stabilization of the tearing modes. However, dropping this compression in Eq. (4) means that we have eliminated the unwanted fast wave that travels in the poloidal plane.

Next, we take ohms law as

$$E + V \times B = \eta j \tag{5}$$

and make a subsidiary ordering of these equations in η. By ordering the variables as

$$\gamma \sim \eta^{1/3},$$

$$U,\ \psi,\ \phi \sim 1,$$

$$I,\ P,\ V_s \sim \frac{1}{\gamma}\ ,$$

$$B \cdot \nabla,\ \chi,\ f \sim \gamma\ .$$

We find that we are able to recover the equations of Coppi, Greene, and Johnson,[3] for finite beta tearing modes and that to do so it is necessary to keep the two terms mentioned above.

To verify the qualitative and quantitative applicability of our equations we have run comparisons in the cylinder with exact codes. HILO is the code that advances our 5th order equations. It is seen from Fig. (1) and (2) that our formulation gives excellent agreement with an exact formulation (shooting code) for ideal modes. The eigenfunctions have also been compared and there are no significant differences between the eigenfunctions the two codes produce.

We have also run comparisons for the resitive modes and again find that our formulation gives excellent quantitative results. Figure (3) is a plot of the growth rate for $\beta=0$ tearing modes. It shows the agreement between our formulation and analytic theory for small resistivity. Fig (3) also shows the excellent agreement, for all values of resistivity, between an exact code (FMHD) and HILO. Figure (4) show that this agreement continues to hold for finite β interchange modes (distabilizing pressure profile). The dashed line is the growth rate found from a boundary layer analysis code (MATCH), and the solid line is that for HILO and FMHD. Again the MATCH code only gives good agreement at very small values of η. The last figure (Fig. (5)) is a plot of the perturbed flux as a function of time, for a stabilizing (reversed) pressure profile. Both HILO and FMHD give the same values of growth rate and frequency for these modes, where as the MATCH code is off by a large factor (~5). We do not, at this time, understand the reason for this large discrepancy.

We would like to point out several advantages of HILO over an exact formulation. First the numerics are simpler because the fast wave that travel across the poloidal plane in time a/V_A has been eliminates, in fact only 4 waves, not 6, remain in the problem. Secondly, the equilibrium force balance is exact, so these equations could be used to find 3-d equilibrium such as

stellarator equilbria. The present formulation also allows one to identify the source of new physics by turning off higher order terms. Lastly, if one desires, the dynamics can easily be made exact and implicit simply by taking $V_{\perp o} \rightarrow V_{\perp}$ in Eq. (4) and by following the advancement scheme in Ref. (1). This then is the reason for the title of this paper.

Acknowledgments

This work supported by U.S. DoE Contract No. DE-AC02-76-CHO-3073.

References

[1]R. Izzo, D. A. Monticello, H. R. Strauss, W. Park, J. Manickam, R. C. Grimm, and J. DeLucia, Phy. Fluids 26, 3066 (1983).

[2]A. H. Glasser, J. M. Greene, and J. L. Johnson, Phy. Fluids 18, 875 (1975).

[3]B. Coppi, J. M. Greene, and J. L. Johnson, Nucl. Fusion, 6, 101 (1966).

Figure Captions

Fig. 1 Growth rate vs beta on axis, for $\beta = \beta_o(1-3r^2 + 2r^3)$ and inverse aspect ratio equal $\varepsilon = 0.1$.

Fig. 2 Same as Fig. (1) except here ε is varied.

Fig. 3 Growth rate vs resistivity for $\beta = 0$, $\varepsilon = 0.1$.

Fig. 4 Same as Fig. (3) except here $\beta=\beta_o(1 - 3r^2 + 2r^3)$.

Fig. 5 Perturbed flux vs time for $\eta=4\times10^{-9}$ and $\beta = 0.25(0.001 + 0.028r^2 - 0.059r^4 + .03r^6)$.

*Note the growth rates and the resistivity in these plots have been scaled by $1/\varepsilon$ from those units given in the text. Likewise the time in Fig. 5 has been scaled by ε.

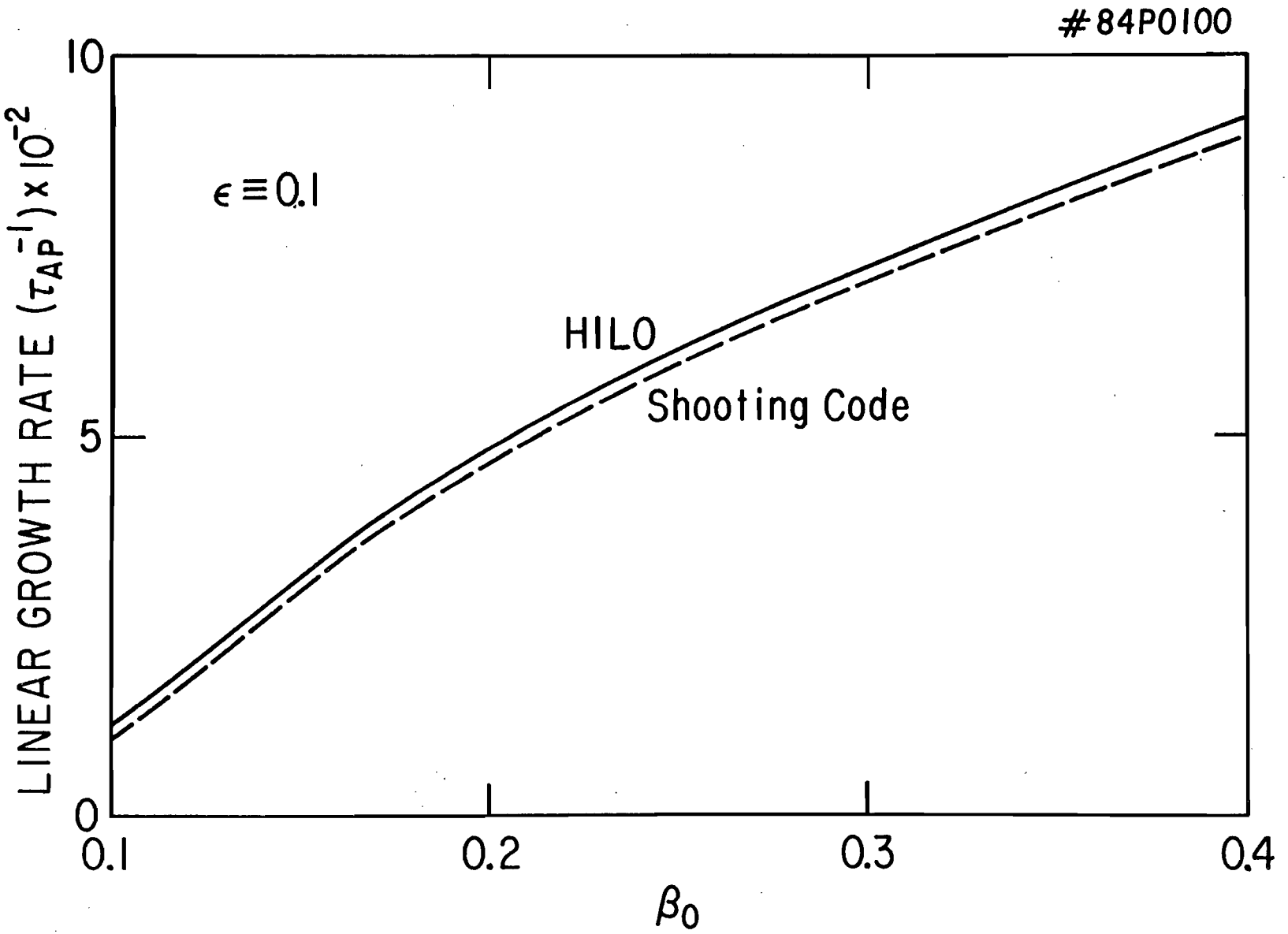
#84P0100
10
5
0
LINEAR GROWTH RATE $(\tau_{AP}^{-1}) \times 10^{-2}$
$\epsilon \equiv 0.1$
HILO
Shooting Code
0.1
0.2
0.3
0.4
β_0

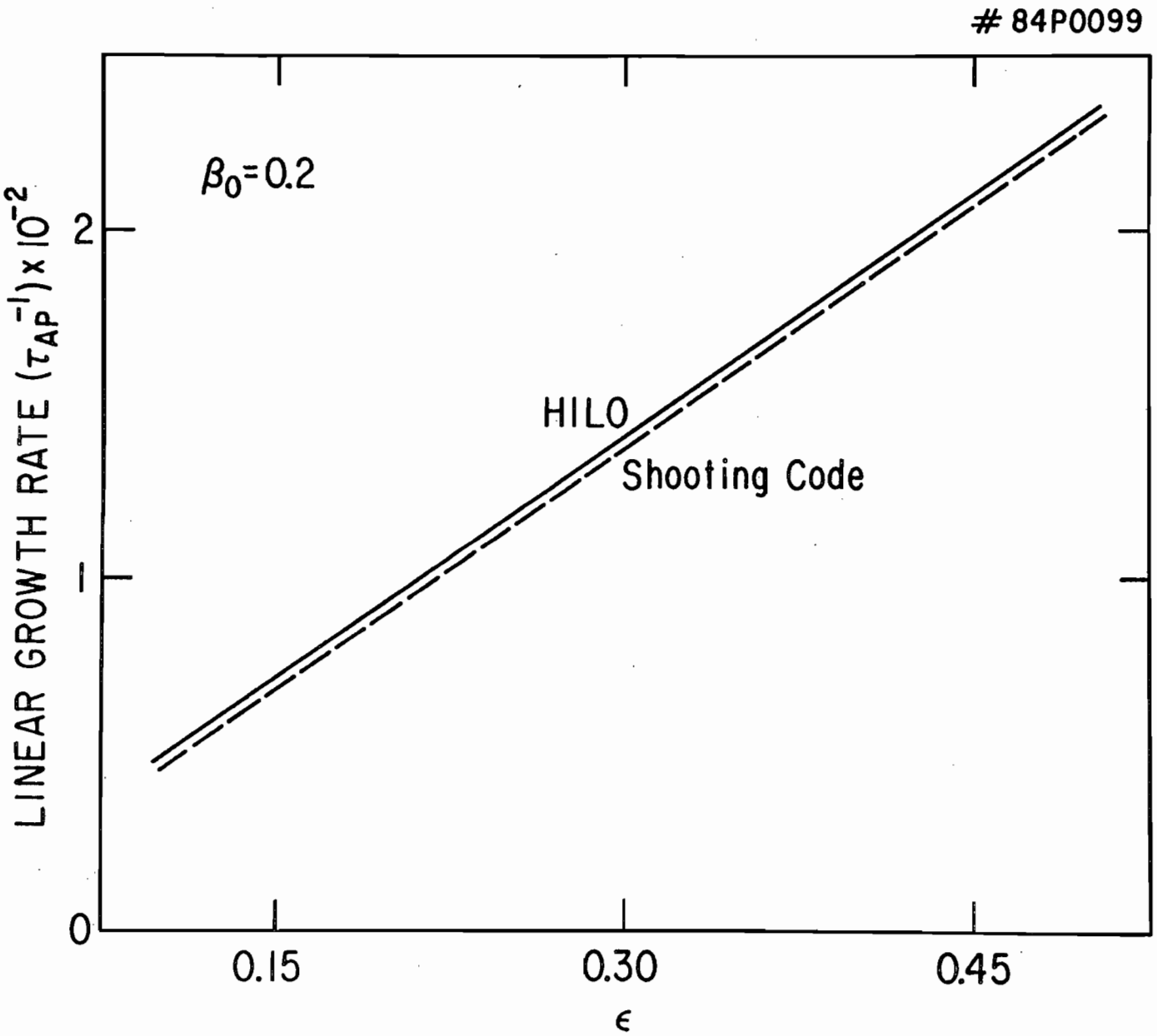
84P0099
$\beta_0 = 0.2$
HILO
Shooting Code
LINEAR GROWTH RATE $(\tau_{AP}^{-1}) \times 10^{-2}$
0
1
2
0.15
0.30
0.45
ϵ

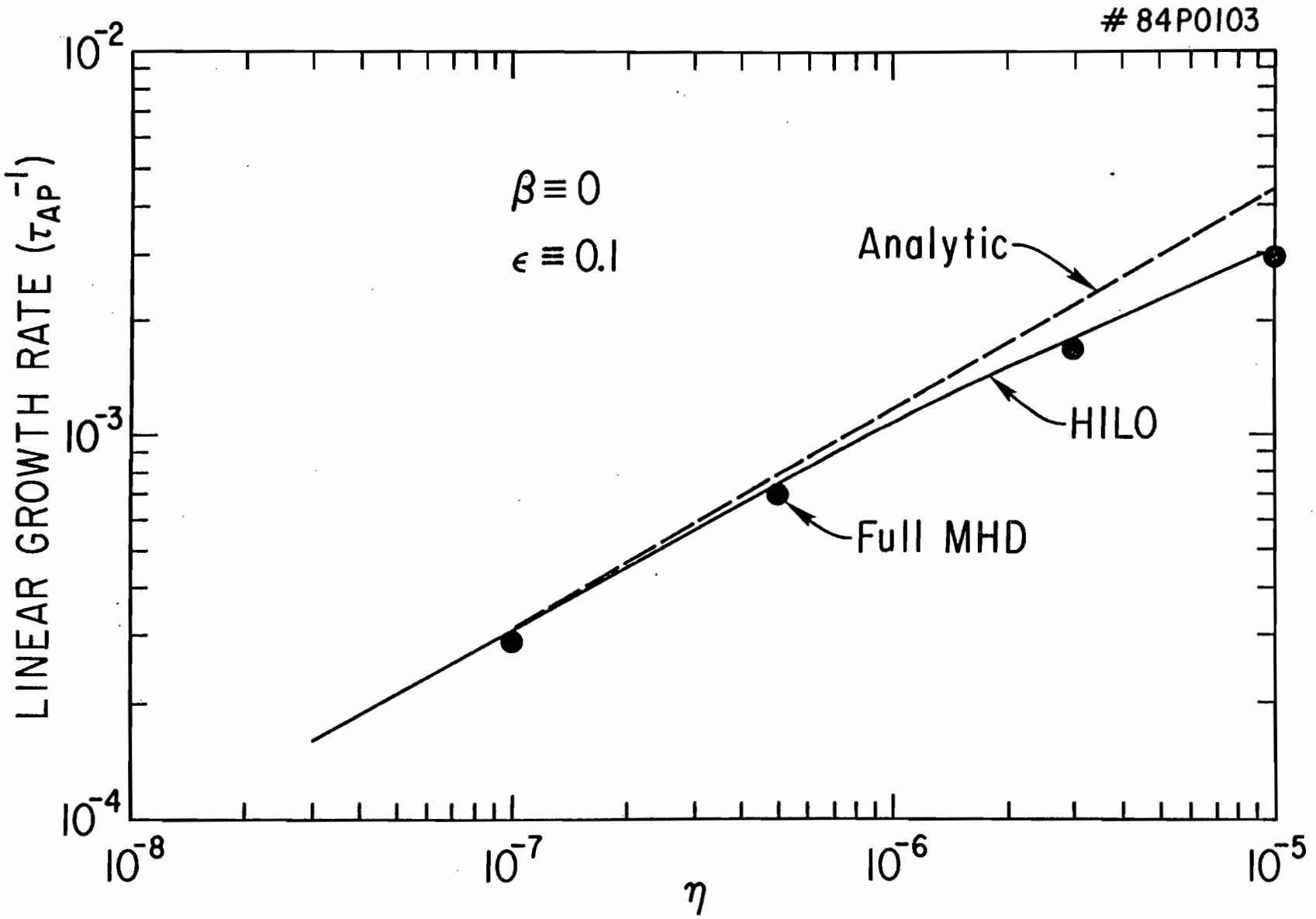
84P0103
$\beta \equiv 0$
$\epsilon \equiv 0.1$
Analytic
HILO
Full MHD
LINEAR GROWTH RATE (τ_{AP}^{-1})
10^{-2}
10^{-3}
10^{-4}
10^{-8}
10^{-7}
10^{-6}
10^{-5}
η

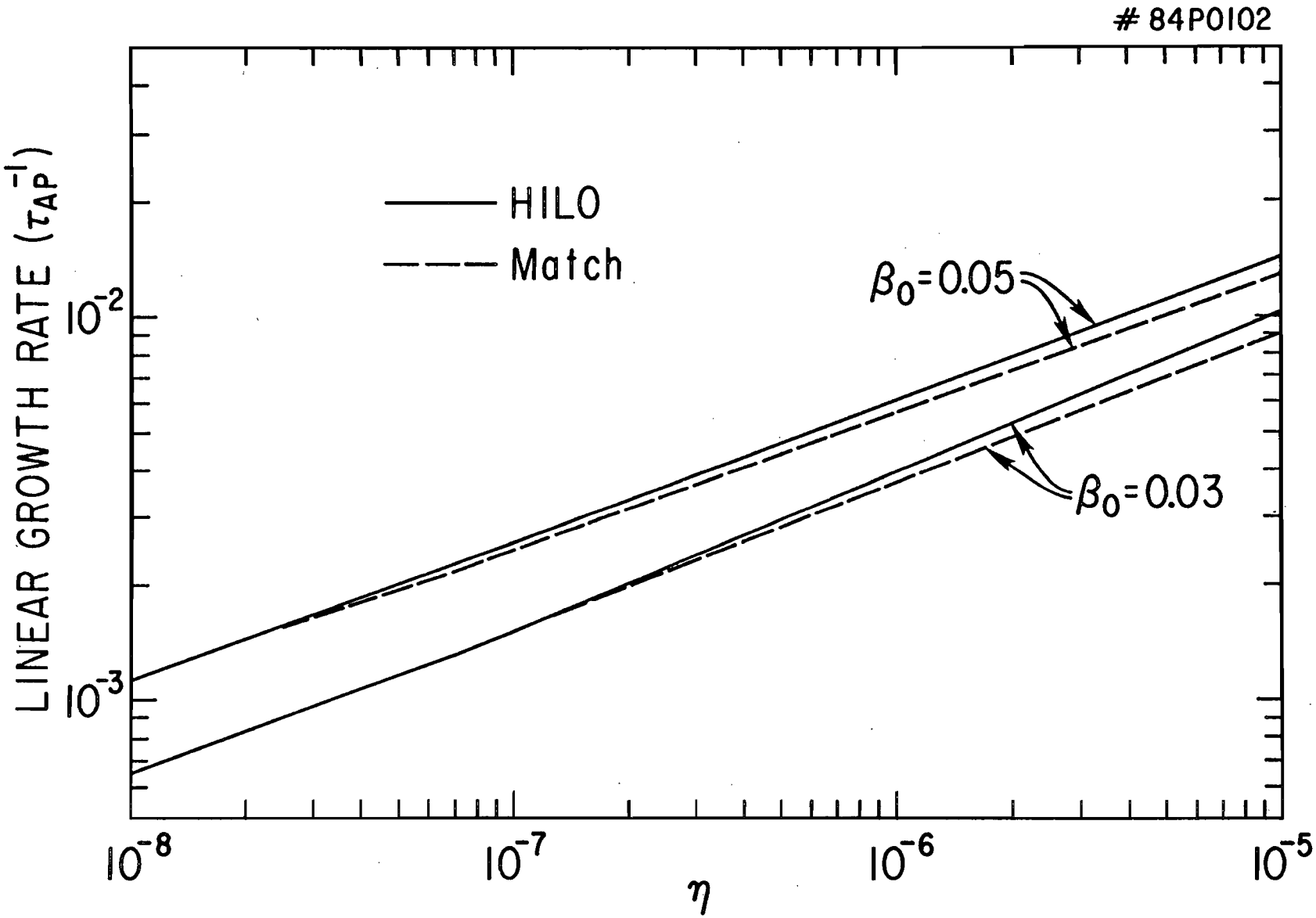
84P0102
HILO
Match
$\beta_0 = 0.05$
$\beta_0 = 0.03$
LINEAR GROWTH RATE (τ_{AP}^{-1})
10^{-2}
10^{-3}
10^{-8}
10^{-7}
10^{-6}
10^{-5}
η

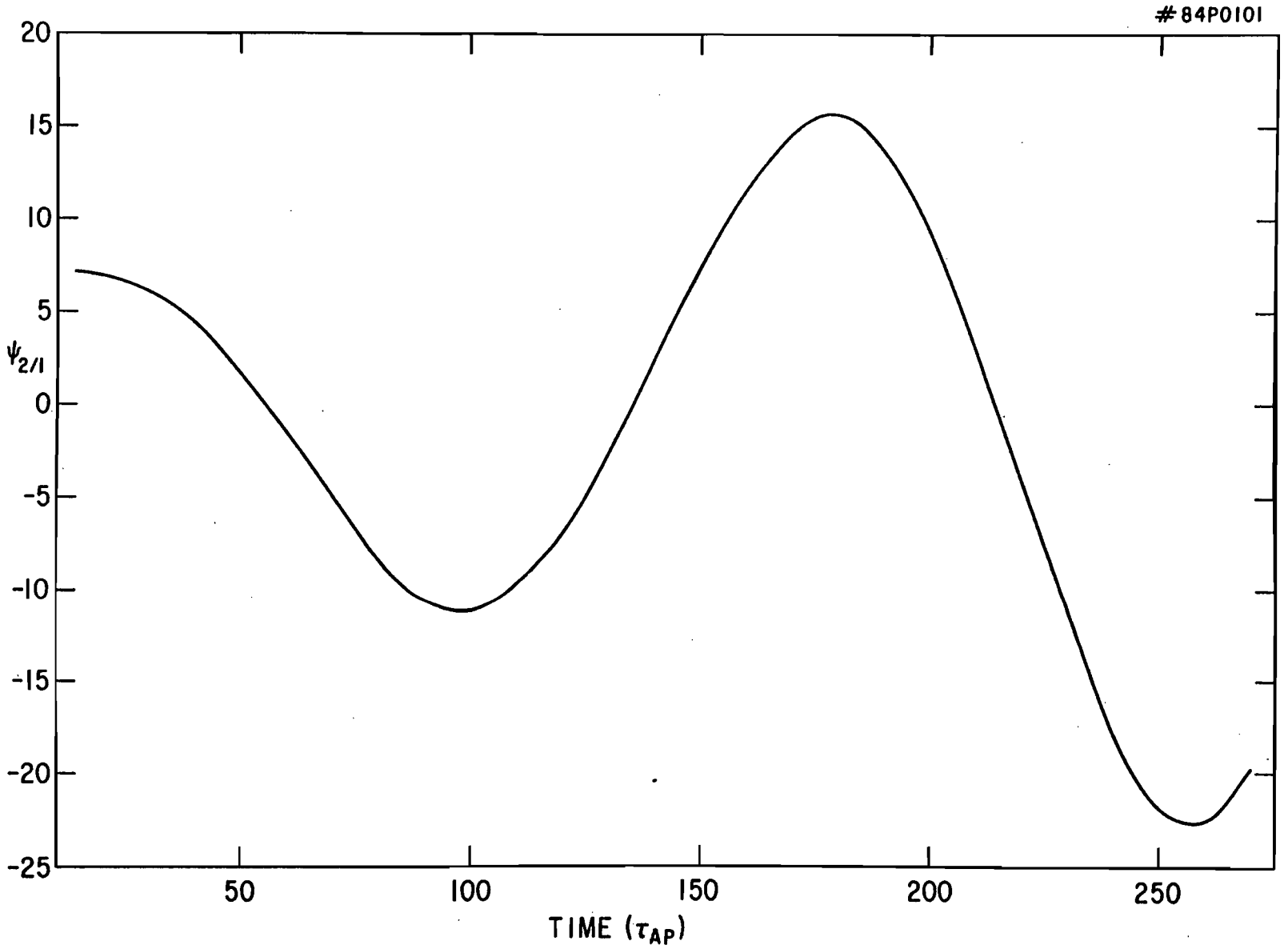
#84P0101
20
15
10
5
0
-5
-10
-15
-20
-25
$\psi_{2/1}$
50
100
150
200
250
TIME (τ_{AP})

3-D SIMULATIONS OF LIMITER STABILIZATION OF HIGH-BETA EXTERNAL KINK-TEARING MODES

Jae Koo Lee and N. Ohyabu
GA Technologies Inc.
San Diego, California

ABSTRACT.

The effects of finite-size poloidal limiters, toroidal limiters, and general mushroom limiters are examined for high-beta finite-resistivity tokamak plasmas in free boundary. Even for a linear stability analysis, a 3-D simulation is necessary, in which many poloidal and toroidal modes are coupled because of the limiter constraint and finite-beta. When the plasma pressure and resistivity are small, a poloidal limiter is effective in reducing the growth rate with a small limiter-size, while a toroidal limiter requires a large size for a comparable effect. As the plasma pressure or resistivity increases, a toroidal limiter becomes more effective in reducing the growth rate than a poloidal limiter of the same size. A small optimized mushroom limiter might have a stabilizing effect similar to a conducting shell.

The plasma instability most widely studied in connection with a major disruption of a high-beta tokamak has been the pressure and current driven external kink-tearing mode[1,2]. This magnetohydrodynamic mode in general has the largest growth rate at toroidal mode number n=1. Being a global mode, it shows large perturbations not only throughout the whole plasma but also in the vacuum region. This finite perturbation in the plasma-vacuum region can be easily affected by placing a conducting shell or a finite size limiter. Since a conducting shell is inconvenient in many practical purposes, a limiter covering only a small fraction of the tokamak circumference is desirable if it can be as effective as an all-the-way-around conducting shell in suppressing or slowing down the unstable mode.

For a low-beta ideal plasma in a straight cylinder, it has been found[3] that a poloidal limiter is very effective in suppressing the external kink mode, while a toroidal limiter is not. For a high-beta ideal and resistive tokamak plasma, a toroidal limiter of a various size has been found[4] to be effective in reducing the growth rate if the size, i.e., the poloidal extent of the limiter is finite. The objective of this paper is to examine the comparative effect of a finite-size poloidal limiter, toroidal limiter, and general mushroom-type limiter for a high-beta finite-resistivity tokamak plasma. For the latter two limiters, our analyses allow three-dimensional linear mode coupling, so that toroidal as well as poloidal modes are coupled when the size of the limiter is finite. We use an initial value code HIB[5] with appropriate boundary conditions on perturbed quantities to simulate the limiter effect; namely, perturbations are allowed to vanish in the region where the limiter is located.

Our results show that a poloidal limiter of a small but finite size reduces the unstable mode's growth rate substantially and is more effective than a toroidal limiter of a comparable size when the plasma beta and resistivity are low. These results recover the previous results[3] if the size of the limiter is allowed to be finite rather than infinitesimal as mentioned in Ref. 3. As the $\varepsilon\beta_p$ (ε is the ratio of minor to major radius and β_p is the ratio of plasma thermal energy to

poloidal magnetic energy) or the plasma resistivity increases, a toroidal limiter of a finite size becomes more effective than a poloidal limiter. A general mushroom-type limiter whose size is finite both in poloidal and toroidal extents can be optimized in size for a significant slowing-down of the unstable mode, thus making feasible a passive feed-back stabilizing scheme.

The method of the present analyses was described in details in Ref. 4 together with numerical procedure and parameters for equilibrium and linear stability. The boundary condition for a finite-size poloidal limiter or a general limiter is similar to that for a finite-size toroidal limiter[4]. For a general limiter covering a poloidal area from $\theta=\delta$ to $\theta=-\delta$ and a toroidal area from $\zeta=\Delta$ to $\zeta=-\Delta$, this boundary condition is

$$\tilde{\phi}_{mn}(r) = \phi_{mn}(r) - \frac{1}{\pi^2}\int_{-\delta}^{\delta} d\theta \int_{-\Delta}^{\Delta} d\zeta \sin m\theta \sin n\zeta \sum_{m',n'} \phi_{m'n'}(r) \sin m'\theta \sin n'\zeta$$

$$= \phi_{mn}(r) - \left(\delta - \frac{f\sin 2m\delta}{2m}\right)\left(\Delta - \frac{f\sin 2n\Delta}{2n}\right)\frac{\phi_{mn}(r)}{\pi^2}$$

$$- \sum_{m'\neq m}\sum_{n'\neq n}\left[\frac{\sin(m-m')\delta}{m-m'} - \frac{f\sin(m+m')\delta}{m+m'}\right]\left[\frac{\sin(n-n')\Delta}{n-n'} - \frac{f\sin(n+n')\Delta}{n+n'}\right]\frac{\phi_{m'n'}(r)}{\pi^2}$$

$$- \left(\delta - \frac{f\sin 2m\delta}{2m}\right)\sum_{n'\neq n}\left[\frac{\sin(n-n')\Delta}{n-n'} - \frac{f\sin(n+n')\Delta}{n+n'}\right]\frac{\phi_{mn'}(r)}{\pi^2}$$

$$- \left(\Delta - \frac{f\sin 2n\Delta}{2n}\right)\sum_{m'\neq m}\left[\frac{\sin(m-m')\delta}{m-m'} - \frac{f\sin(m+m')\delta}{m+m'}\right]\frac{\phi_{m'n}(r)}{\pi^2},$$

where $f=1$ for perturbed velocity stream function ϕ and $f=-1$ for perturbed poloidal magnetic flux function ψ. This boundary condition has been imposed both for ψ and ϕ.

For the three types of limiter, the growth rates in the unit of the poloidal Alfven frequency ω_A are shown in Fig. 1. Here, the equilibrium has the safety factor on the axis and at the limiter $q_0=1.05$

and q_ℓ=1.7, and $\varepsilon\beta_p$=0.11. The rest of the parameters are the same as in Ref. 4. When the plasma resistivity is small as in the bottom three curves with $\eta=10^{-6}$ ($\eta=1/\tau_r\omega_A$ with τ_r denoting the resistive diffusion time) a poloidal limiter is very effective in reducing the growth rate even with a small limiter size. For example, a factor of five reduction in growth rate is obtained with F=1/8 where F is the ratio of the limiter size to the total circumference area. A toroidal limiter, however, is not as effective as a poloidal limiter, thus requiring a large size to have a comparable effect as a poloidal limiter.

These results for a finite β_p recover the previous results[3] for a zero-β_p straight tokamak if the limiter size is finite rather than vanishingly small as orginally described in Ref. 3. The results for a poloidal limiter in Ref. 3 are applicable only to a finite-size poloidal limiter, not to a zero-size poloidal ring limiter. This is because the term k^2r^2 was neglected in comparison with the m^2-term in the poloidal limiter constraint equation as well as in the unconstrained eigenfunction solution and equation such as Eqs. (4) and (5) of Ref. 3. This neglect is justifiable only for a finite-size poloidal limiter.

As the plasma resistivity becomes large to make the unstable mode dominated by a resistive tearing mode, a toroidal limiter reduces the growth rate to a greater extent than a poloidal limiter as shown in the upper three curves of Fig. 1 with $\eta=10^{-3}$. This is also observed in higher-β_p cases as in Fig. 2.

An optimized general limiter is usually more effective than a poloidal limiter of the same size as seen in Fig. 1 both for small and large resistivity. This is because the unstable mode structure is shifted outward with respect to the tokamak major axis, thus making a limiter at the smaller major radius side less effective.

The numerical convergence is 1/N, where N indicates the total mode number used in the calculation. A typical case is shown in the inset of Fig. 1, where four calculations for a poloidal limiter of F=1/8 with different total toroidal mode number found a single growth rate

corresponding to $N=\infty$. Nine poloidal modes are kept in these calculations (typically from $m=-3$ to $m=5$); thus, nine poloidal modes and six to ten toroidal modes are all coupled to simulate a finite-size poloidal limiter. For a finite-size toroidal limiter[4], toroidal modes are uncoupled and poloidal modes are coupled depending on the magnitude of $\varepsilon\beta_p$; for this case, approximately twenty poloidal modes are used. Most of the results in the following are based on this numerical convergence $1/N$ with at least two different N values.

The effect of β_p are shown in Fig. 2, where three values of β_p for an otherwise same equilibria are used. Here, a broader pressure profile with $\upsilon=2$ (as in Ref. 4) is employed in contrast to a more peaked one with $\upsilon=4$ in Fig. 1. It is shown that a toroidal limiter with a small size $F=1/8$ is more effective at high-β_p in reducing the growth rate than a poloidal limiter of the same size, while an opposite conclusion is drawn at low-β_p. A poloidal or toroidal limiter of a finite size usually falls between the fixed boundary curve (i.e., with $F=1$) and the complete free boundary curve (i.e., with $F=0$). This allows a smooth transition in the stability boundary from the free boundary to the fixed boundary through a limiter of a finite size.

Since it is clear that the fixed and free boundary limits are the two limiting boundary for a limiter with a finite size, it is helpful to examine a normalized growth rate Γ, where $\Gamma = (\gamma-\gamma_1)/(\gamma_0-\gamma_1)$ with γ_1 and γ_0 being the fixed and free boundary value respsectively. These normalized growth rates are plotted in Fig. 3, showing that a toroidal limiter is increasingly more effective with increasing $\varepsilon\beta_p$ and that a poloidal limiter becomes increasingly effective with decreasing $\varepsilon\beta_p$.

The present results are based on a linear analysis. The nonlinear amplitudes are shown in general[6] to increase monotonically with the linear growth rates. Thus, a reduction in the linear growth rate could bring a reduction in the nonlinear amplitude as well.

In summary, the stabilizing effects of poloidal, toroidal, and general limiters become significant as the limiter size increases. A small (on the order of 10% of a conducting shell) optimized mushroom-type general limiter might have a stabilizing effect similar to a conducting shell.

ACKNOWLEDGMENTS

This work was supported by the U. S. Department of Energy, Contract No. DE-AT03-84ER53158.

REFERENCES

[1] V. D. Shafranov, Sov. Phys.-Tech. Phys. 15, 175 (1970).

[2] B. V. Waddell, B. Carreras, H. R. Hicks, J. Holmes, D. K. Lee, Phys. Rev. Lett. 41, 1386 (1978); R. B. White, D. A. Monticello, M. N. Rosenbluth, Phys. Rev. Lett. 39, 1618 (1977).

[3] J. P. Freidberg, J. P. Goedbloed, and R. Rohatgi, Phys. Rev. Lett. 51, 2105 (1983).

[4] J. K. Lee, Phys. Fluids 27, No.4 (1984).

[5] W. Park, D. A. Monticello, R. B. White, A. M. M. Todd, Bull. Am. Phys. Soc. 23, 779 (1978); H. R. Strauss, W. Park, D. A. Monticello, R. B. White, S. C. Jardin, M. S. Chance, A. M. M. Todd, A. H. Glasser, Nucl. Fusion 20, 628 (1980).

[6] J. K. Lee, M. S. Chu, F. J. Helton, and W. Park, Phys. Fluids 27, 607 (1984); Proc. Eleventh Europ. Conf. on Controlled Fusion and Plasma Physics, Aachen, Germany, p.231 (1983).

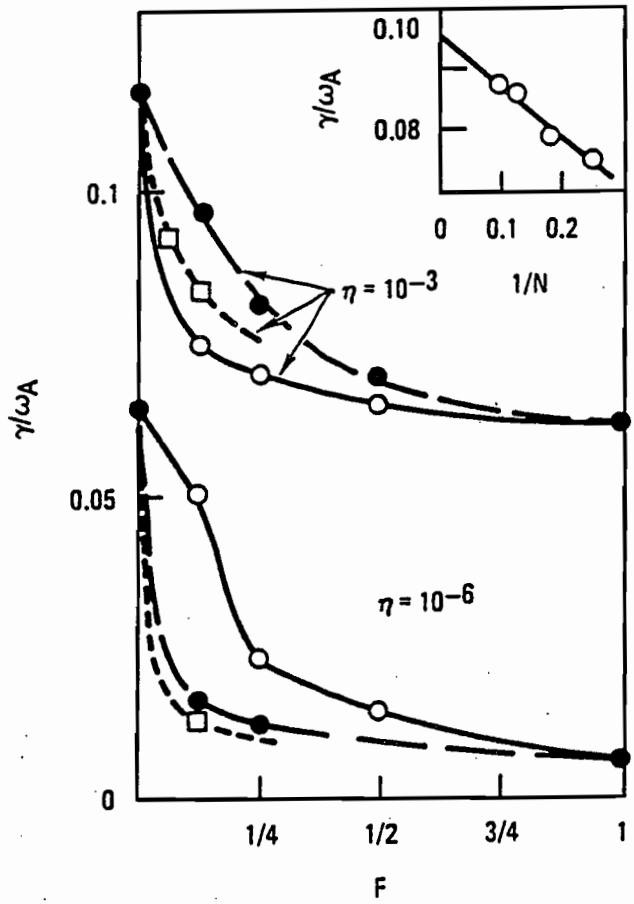

Fig. 1. Linear growth rates for weakly resistive (bottom three curves) and highly resistive (top three curves) plasmas as a function of the limiter size F. Results for toroidal limiters are open circles; those for poloidal limiters are filled circles; those for general limiters are rectangles. The numerical convergence is shown in the insert.

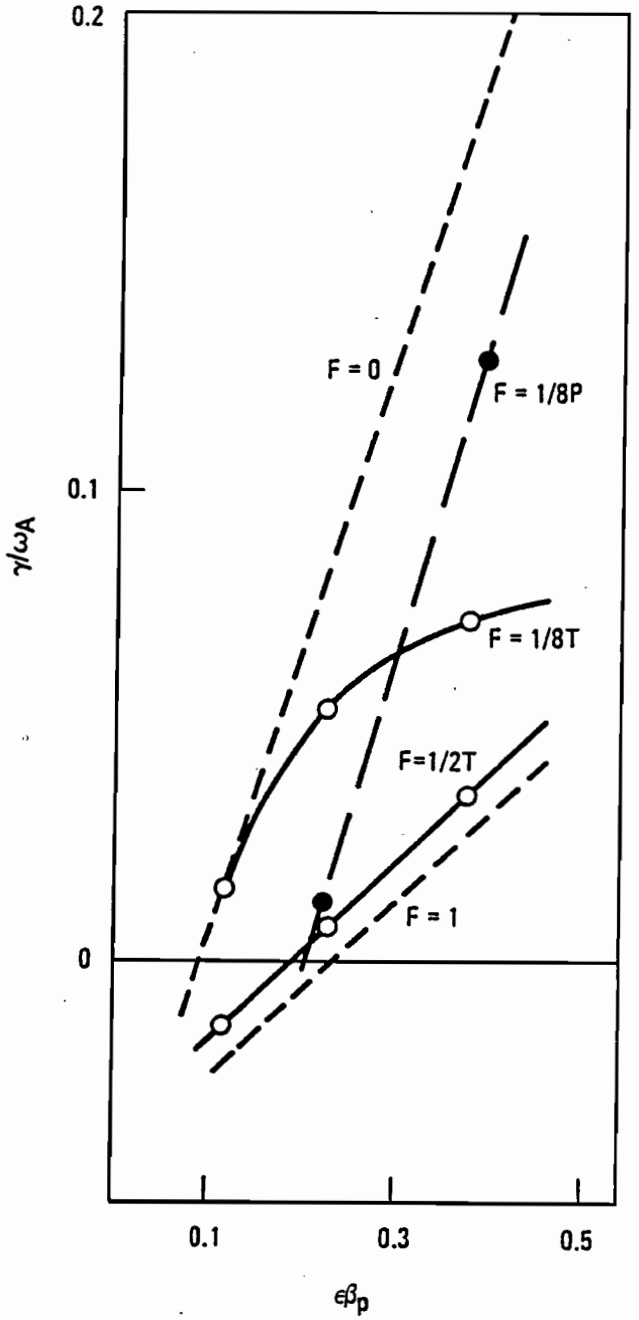

Fig. 2. Dependence of growth rates on $\epsilon\beta_p$. Results for poloidal limiters with the size F=1/8 are indicated as a dashed line; those for toroidal limiter with F=1/8 and F=1/2 are indicated as solid curves marked F=1/8T and F=1/2T. The fixed boundary and no-limiter free boundary results are shown as dotted lines with F=1 and F=0.

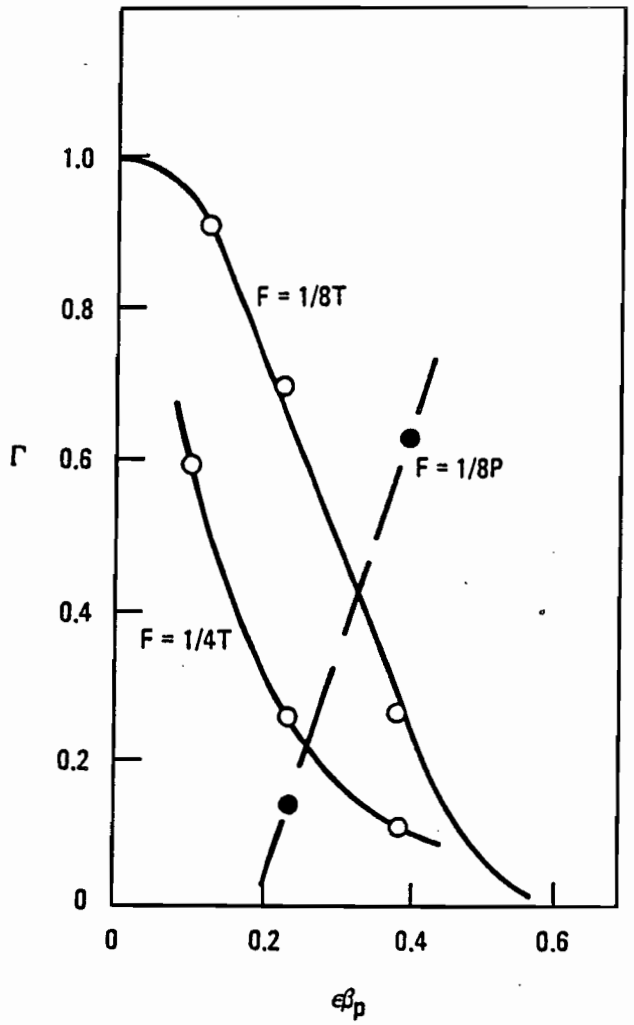

Fig. 3. Normalized external kink growth rates as a function of $\varepsilon\beta_p$ for the cases of Fig. 2.

Extended Abstract of Nonlinear Evolution of External Kink Mode in Tokamak and Comment on Resistive Internal Kink Mode

Toshihide TSUNEMATSU, Gen-ichi KURITA, Masafumi AZUMI
Tomonori TAKIZUKA and Tatsuoki TAKEDA

Japan Atomic Energy Research Institute
Tokai-mura, Naka-gun, Ibaraki-ken 319-11, Japan

1. Introduction

Since the first workshop on the 3-D MHD simulation we have studied the disruptive processes in tokamaks from the view point of the resistive MHD instabilities{1-4} and we have extended our models to ones for the high-beta and the toroidal plasmas. The results show that the major disruption process is caused by the nonlinear coupling between the tearing modes with different helicities as pointed out by Waddell et al.{5} and that the high-beta or the toroidal effect does not give the essential effects. The experiments also indicate that this instability can be suppressed by the control of the profile of the plasma current when the safety factor at the plasma surface, q_a, is greater than 2. When $q_a \sim 2$, the major disruption occurs except for the case of the conducting wall close to the plasma surface. This fact indicates that the m=2/n=1 free boundary mode plays an important role in the major disruption process. In this workshop, we show the model of the resistive free boundary plasma and the validity of our model as the first step to study the role of the free boundary mode in the major disruption

process. In the next section we study the structure of the external kink mode as the candidate of the unstable free boundary mode in the linear theory and the nonlinear evolution of the mode to estimate the level of the saturation.

As for the high-beta effect on the internal disruption, we have shown that the saturation of the m=1 magnetic island due to the pressure-driven instability in the cylindrical geomerty{2} and have also pointed out the importance of the toroidal effect on the m=1 mode{4}. The other effect on this mode such as kinetic effect was pointed out by Biskamp{6}. We make some comments on the kinetic effect on the internal disruption process in tokamaks in section 3.

2. Nonlinear Evolution of External Kink Mode

2.1 Model and Basic Equations

In the usual analysis of the external kink mode, the plasma is considered to be surrounded by the vacuum region. The equations are solved seperately both in the plasma and in the vacuum, and the connection of the two solutions at the plasma surface gives the dispersion relation of the external kink mode. This model is, however, very difficult to study in the nonlinear numerical computation because the motion of the plasma surface has to be precisely traced. In stead of a real vacuum we put a highly resistive and a small-current region ($a<r<b$) outside the plasma column with the radius a (Fig.1). The conducting wall is places at r=b. The resistivity, η, increases steeply at r=a from $\eta_0=\eta(r=0)$ to $\eta_e=\eta(r=b)$. The plasma current is given by $J=E_w/\eta(r)$, where E_w is the electric field at the conducting wall. The plasma density, ρ, decrease steeply at r=a from $\rho_0=\rho(r=0)$ to $\rho_e=\rho(r=b)$. The width of the steep change of the equilibrium quantities is denoted by δ in Fig.1. In the highly resistive region the perturbed current dissipates rapidly and this region is expected to behave as the vacuum.

We solve the following reduced set of equations through the whole region in the cylindrical geometry.

$$\frac{\partial U}{\partial t} + V_\perp \cdot \nabla_\perp U = B \cdot \nabla J \tag{1}$$

$$\frac{\partial \Psi}{\partial t} + V_\perp \cdot \nabla_\perp \Psi = \eta J - E_w(t) + B_z \frac{\partial \Phi}{\partial z} \tag{2}$$

$$\frac{\partial \eta}{\partial t} + V_\perp \cdot \nabla_\perp \eta = 0 \tag{3}$$

$$U = \nabla_\perp^2 \Phi \tag{4}$$

$$J = \nabla_\perp^2 \Psi \tag{5}$$

where $\nabla_\perp \equiv \partial/\partial r\ \nabla r + \partial/\partial\theta\ \nabla\theta$, $V_\perp = \mathbf{e}_z \times \nabla_\perp \Phi$, $B_\perp = \mathbf{e}_z \times \nabla_\perp \Psi$. The quantities Ψ, Φ, U and J denote the magnetic flux, stream function, vorticity and longitudinal current density, respectively. The extension to the toroidal geometry is straightforward.

2.2 Linear Analysis

For the linear analysis we use the linearized equations of eqs.(1)-(3) with respect to the small perturbation, $V_\perp$. By using the Fourier expansion, $(\Phi,\Psi,\eta)=(\Phi,\Psi,\eta)_{m,n}\exp i(m\theta - nz/R_0)+\gamma t$, and the finite difference method to the radial direction, we have the asymmetric eigenvalue equation,

$$\gamma Ax = Bx \tag{6}$$

For $\eta_0=0$, $\eta_e=\infty$ and $\delta=0$ (the case of the uniform current density), we have the analytic solution and the growth rate is given by

$$\gamma^2 = \gamma_E^2/S \tag{7}$$

where

$$S = 1 + \frac{\rho_e}{\rho_0}\frac{1 + (a/b)^{2m}}{1 - (a/b)^{2m}} \tag{8}$$

and

$$\gamma_E^2 = 2(B_\theta/a)^2(m-nq)\left[1 - \frac{m-nq}{1-(a/b)^{2m}}\right]. \tag{9}$$

The quantity γ_E in eq.(9) is the growth rate of the external kink mode for the uniform current distribution. As ρ_e decreases the growth rate, γ, tends to γ_E.

Figure 2 shows the growth rate of the m=2/n=1 mode as the function of the ratio ρ_e/ρ_0 for $\eta_0=10^{-7}$ and $\eta_e=1.0$ obtained by solving eq.(6). In this case the m=2/n=1 rational surface and the conducting wall are placed at r=1.2a and b=2a,respectively. The numerical result (solid line) for $\delta/a \ll 1$ agrees well with the analytic one (dashed line). In spite of the decrease of the growth rate the structure of the eigenmode is unchanged by the increase of ρ_e/ρ_0. This fact encourages us to study the nonlinear evolution without the reduction of the Alfven transit time. Next we study the effect of the external resistivity, η_e. Figure 3(a) shows the growth rate as the function of η_e by fixing $\eta_0=10^{-7}$. For $\eta_e<10^{-4}$ the growth rate scales as $\gamma \sim \eta^{3/5}$. This means the mode tends from the external kink mode to the tearing mode. The structures of the m=2/n=1 component of the plasma current for the differnt η_e also show the change of the mode (Fig.3(b), (c) and (d)).

The linear analysis shows that this model describes both the external kink mode and the tearing mode by changing η_e and that the structure of the eigenmode is insensitive to ρ_e.

2.3 Nonlinear Evolution

For the study of the nonlinear evolution of the external kink mode we integrate eqs.(1)-(5) in time by using the Fourier expansion to both the azimuthal and the longitudinal directions and the finite difference method to the radial direction. In the cylindrical geometry we can use the approximation of the single helicity. Typical numbers of the modes, M, and the radial meshes, N_r are M=5 and N_r=201. Eigensolution of the linear equations is used as the initial perturbation to save the computational time. The resistivity used in the nonlinear study is

$\eta_0=10^{-2}$ and $\eta_c=1$.

Figure 4(a) and (b) show the time evolution of the magnetic energy and the kinetic energy, respectively. The m=2/n=1 rational surface and the conducting wall are placed at r=1.2a and b=2a, respectively, and $\delta/a=0.1$. Both energies saturate at $t \sim 30\tau_{PH}$. Here τ_{PH} is the poloidal Alfven transit time at r=a. The evolution of the magnetic flux surface is shown in Fig.5 at t=0 (Fig.5(a)) and $t=30\tau_{PH}$ (Fig.5(b)), respectively. The dense lines denote the contors of the resistivity. From Fig.5(b) we have the saturation level of the plasma surface, $\xi/a \sim 0.1$, which corresponds to the saturation level of the magnetic field fluctuation, $\tilde{B}_r/B_\theta \sim 0.03$. The dependence of $\tilde{B}_r/B_\theta$ on the position of the rational surface, r_s, is shown in Fig.6. The saturation level increses as the rational surface becomes close to the plasma surface. The level and the dependence on r_s agree with the result of neighbouring equilibrium theory given by Itoh{7}.

Our preliminary results show that the highly resistive region outside the plasma column can describe the external kink mode in nonlinear evolution.

3. Comment on Resistive Internal Kink Mode

The intense heating by NBI in the JFT-2 tokamak has shown the transition from the sawtooth oscillation to the continuous oscillation of the soft X-ray signal{8}. We have studied this transition from the view point of the m=1/n=1 resistive MHD mode and have shown the saturation of the m=1/n=1 magnetic island due to the pressure-driven mode in the cylindrical geometry{2}. The m=1/n=1 ideal internal kink mode is, however, always unstable for the finite-beta value in the cylindrical model and the saturation width of the magnetic island is independent of the beta value. In the last workshop we have shown the toroidal effect plays an essential role in this mode{4}, and proposed the new reduced set of equations by using $\nabla \cdot V/R^2=0$ in stead of $\nabla_\perp \cdot V_\perp/R^2=0$. The new equation covers both the resistive equations and the imcompressible ideal equations.

The other mechanism of the saturation of the m=1/n=1 magnetic island was pointed out by Biskamp{6}. He has shown that the kinetic effect causes the saturation of the magnetic island by using the quasi-linear theory. In this workshop we show the nonlinear effect on the kinetic model due to the mode coupling.

The basic equations are given by

$$\frac{\partial U}{\partial t} + V_\perp \cdot \nabla_\perp U - e_z \cdot \nabla N \times \nabla \frac{V_\perp^2}{2} = B \cdot \nabla J + \alpha_* T_i e_z \cdot \nabla N \times \nabla U + \mu \nabla^2 U \qquad (10)$$

$$\frac{\partial \Psi}{\partial t} + V_\perp \cdot \nabla_\perp \Psi = \eta J + \alpha_* (T_e + T_i) e_z \cdot \nabla N \times \nabla \Psi \qquad (11)$$

$$\frac{\partial N}{\partial t} + \nabla \cdot (N V_\perp) = \alpha B \cdot \nabla J + \kappa \nabla^2 N \qquad (12)$$

where

$$B = B_0 e_h + e_h \times \nabla \Psi \qquad (13)$$

$$e_h = e_z + r/R_0 e_\theta \qquad (14)$$

$$J = \nabla^2 \Psi + B_0/R_0 \qquad (15)$$

$$V_\perp = e_z \times \nabla \Phi \qquad (16)$$

$$U = \nabla \cdot (N \nabla \Phi) \qquad (17)$$

$$\alpha_* = \tau_{PH} T_0/(eBa^2) \sim \omega_* \tau_{PH} \qquad (18)$$

and

$$\alpha = c/(R\omega_{pi}) \sim \alpha_*/\beta_p \quad . \qquad (19)$$

We use the same method as in section 2 by introducing the complex

variables to our code. The safety factor and the density are chosen such that

$$q(r)=(1+(r/r_0)^{2\lambda})^{1/\lambda} \tag{20}$$

and

$$N(r)=0.8(1-(r/a)^2)^2+0.2 \tag{21}$$

The parameter r_0 is determimed so that the m=1/n=1 rational surface is placed at $r_s=0.5a$.

Figure 7 shows the imaginary part of the eigenfrequency as the function of ω_*/γ_T for $\eta_0=10^{-5}$ and the different values of λ. Here γ_T is the growth rate of the m=1/n=1 resistive mode. The real part of the eigenfrequency is $\omega \sim \omega_*$. The numerical result for $\lambda=1$ (solid line) agrees with the analytic one (dashed line) given by Waddell et al.{9}. Figure 8 shows the eigenfunctions for $\omega_*/\gamma_T=5$. The lines with the large amplitude in Φ and N correspond to the real parts and $\Psi \sim i\Phi$. The eigenfunctions show that the drift wave is excited at the rational surface and propagates outward to decay rapidly. This means that the kinetic effect on the m=1/n=1 mode is apparent near the rational surface and the MHD behavior holds in other region.

In the nonlinear study we use $M \leqq 10$, $N_r=201$ and $\eta_0=10^{-5}$. The analysis with $M=1$ gives the same result as that of the quasi-linear theory given by Biskamp{6}. Next we study the effect of the higher modes. Figure 9(a) and (b) show the time evolution of the magnetic energy for $\omega_*/\gamma_T=0$ and 3, respectively. We use $M=5$ in this case. For $\omega_*/\gamma_T=0$ the internal disruption occurs at $t \sim 600\tau_{PH}$. This time is almost independent of M. For $\omega_*/\gamma_T=3$ the evolution of the magnetic energy seems to saturate. The level and time of the saturation, however, increases as M. The saturation level of the m=0 component of the magnetic energy, $-\delta M_0$, increases as M^2 (Fig.10). This fact means the impotance of the coupling with the higher modes and suggests the internal disruption even for $\omega_*/\gamma_T>1$. The time evolution of the spectra of the kinetic energy in Fig.11 also indicates the importance of the mode coupling. The solid lines denote the amplitude of the each m componetnt

of the kinetic energy for M=5 and the dashed lines are for M=10. With the lapse of time the higher mode are excited as much as M increases. To confirm our conjecture we have to take the numbers of modes up to $M \sim 50$.

4. Summary

In the analysis of the external kink mode the highly resistive region outside the plasma column describes the "vacuum" both in the linear and the nonlinear regime. Hereafter we are studying the nonlinear behavior of the free boundary modes by varying the position of the m=2/n=1 rational surface and the profile of the plasma current with the extension to the muliti-helicity simulation.

The analysis of the kinetic effect on the m=1/n=1 mode has shown the importance of the higher modes in the single helicity and suggests the internal disruption for $\omega_*/\gamma_T>1$.

References

{1} G. Kurita et al., "Major Disruption Process in Tokamak", JAERI-M 9788 (1981).

{2} M. Azumi et al., "Internal Disruption in High β_p Tokamak", JAERI-M 9787 (1981).

{3} Y. Tanaka et al.,"Numerical Study of Resistive Modes in Tokamak(II)", in *Proceedings of the Tenth Conference on Numerical Simulation of Plasmas* (San Diego, USA) 2B18 (1983).

{4} M. Azumi et al, "Numerical Study of the Resistive Internal Kink Mode" in *Proceedings of the US-Japan Workshop on 3-D MHD Simulation* (Nagoya, Japan) IPPJ-632 (1983).

{5} B. V. Waddell et al., Phy. Fluids 22 (1979) 896.

{6} D. Biskamp, Phys. Rev. Lett. 46 (1981) 1522.

{7} K. Itoh, "Magnetohydrodynamic Gross Stability of Current-Carrying Plasmas", *PhD Thesis* (1979).

{8} S. Yamamoto et al, Nucl. Fusion 21 (1981) 993.

{9} B. V. Waddell et al, "Reduction of the Growth Rate of the m=1 Resistive Magnetohydrodynamic Mode by Finite Gyroradius Effects", ORNL/TM-5968 (1977).

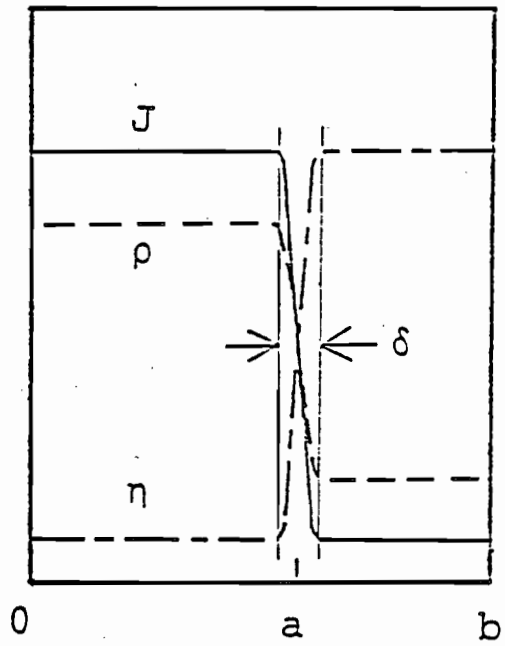

Fig.1 Model of equilibrium. The plasma current J (solid line) and the density ρ (dashed line) decrease and the resistivity η (dashed solid line) increases steeply at $r \sim a$ with the width of δ.

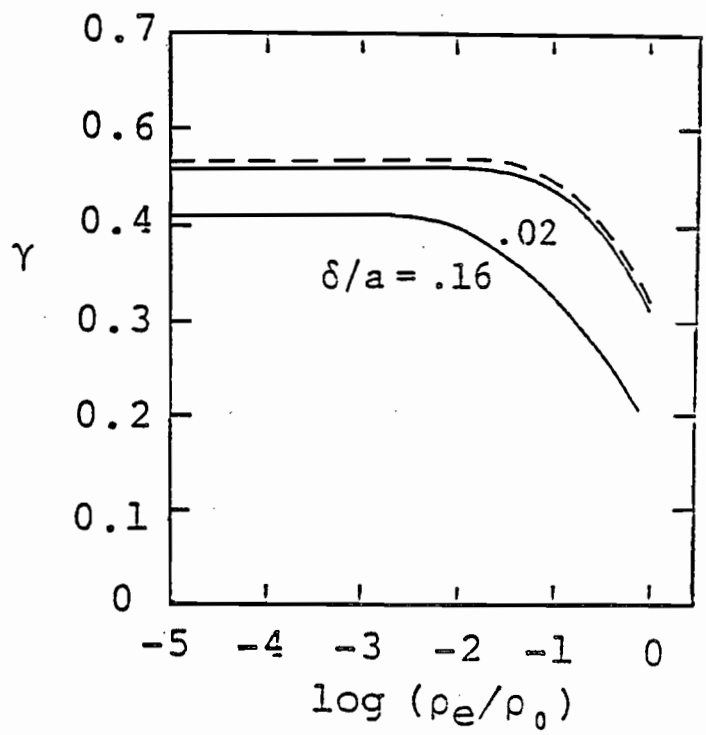

Fig.2 Growth rate, γ, vs. the density at the conducting wall, ρ_e. The dashed line is given by eq(7) and the solid line is obtained by the numerical computation for δ/a=0.02 and 0.16 ($\eta_0=10^{-7}$ and $\eta_e=1$).

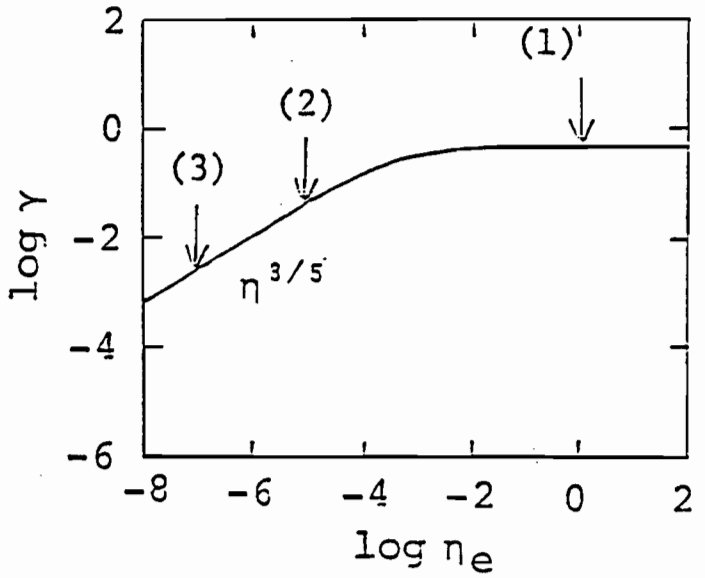

(a)

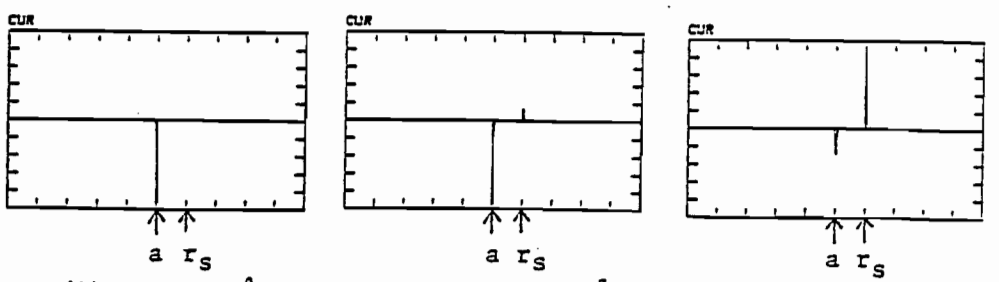

(b) (c) (d)

Fig.3 Growth rate and mode structure. The gowth rate, γ, is shown in (a) as a function of the resistivity at the conducting wall, η_e. The structure of the m=2 component of the perturbed current are shown for (b) η_e=1, (c) η_e=10^{-5} and (d) η_e=10^{-7}.

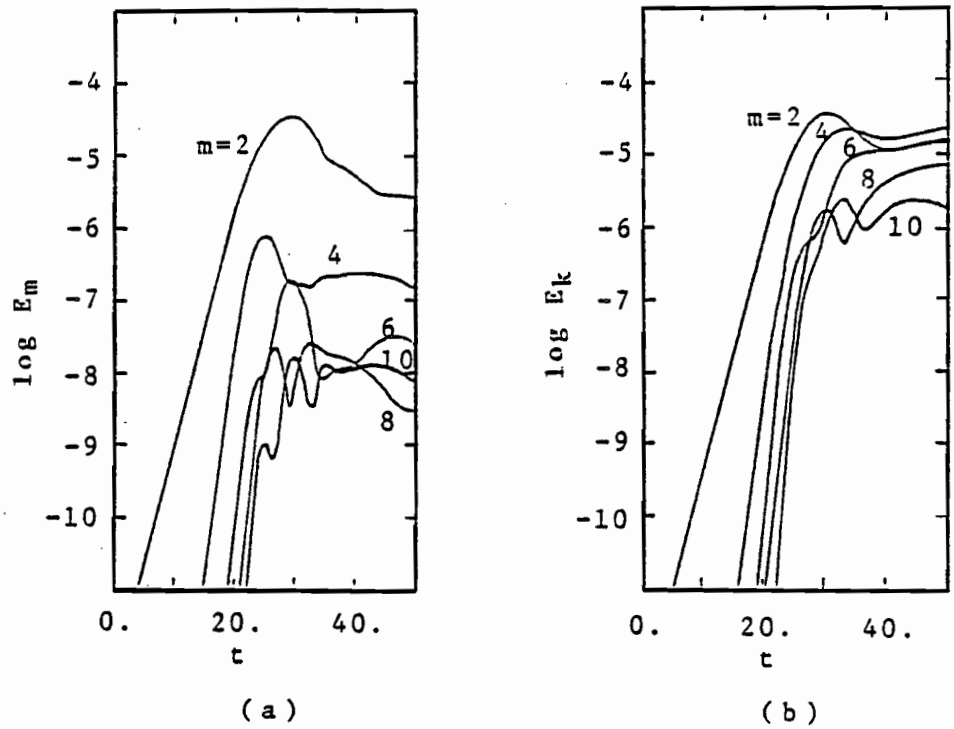

Fig.4 Time evolution of (a) magnetic energy and (b) kinetic energy for δ/a=0.1. The m=2/n=1 rational surface is placed at r=1.2a.

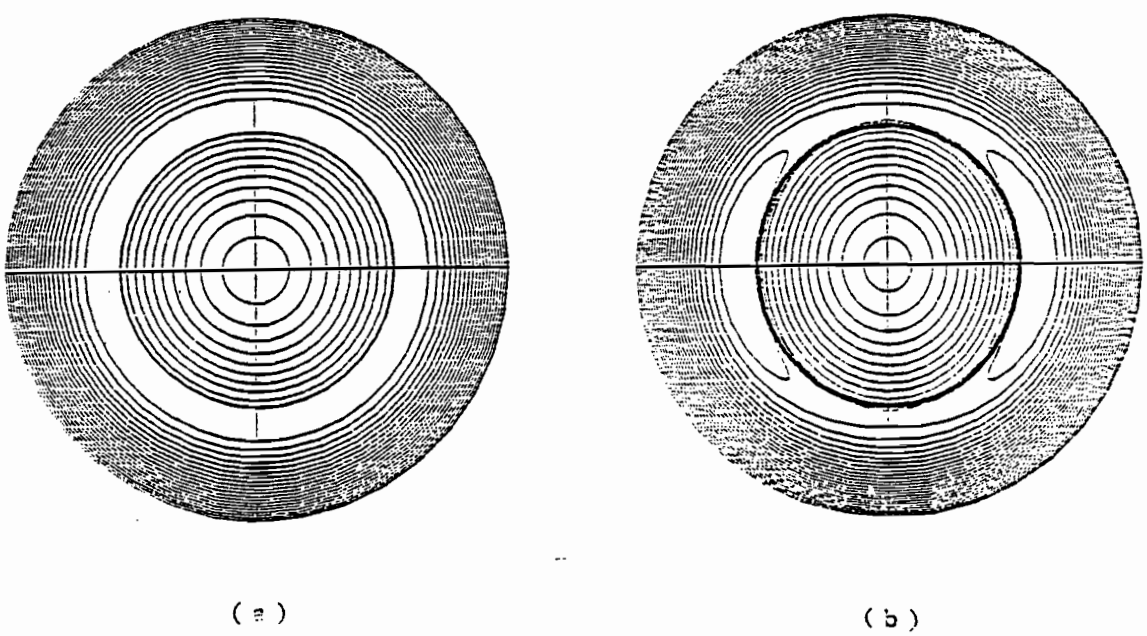

Fig.5 Time evolution of the magnetic flux surface at (a) t=0 and (b) at the time of the saturation $t=30\tau_{PH}$. The dense lines denote the contors of the resistivity.

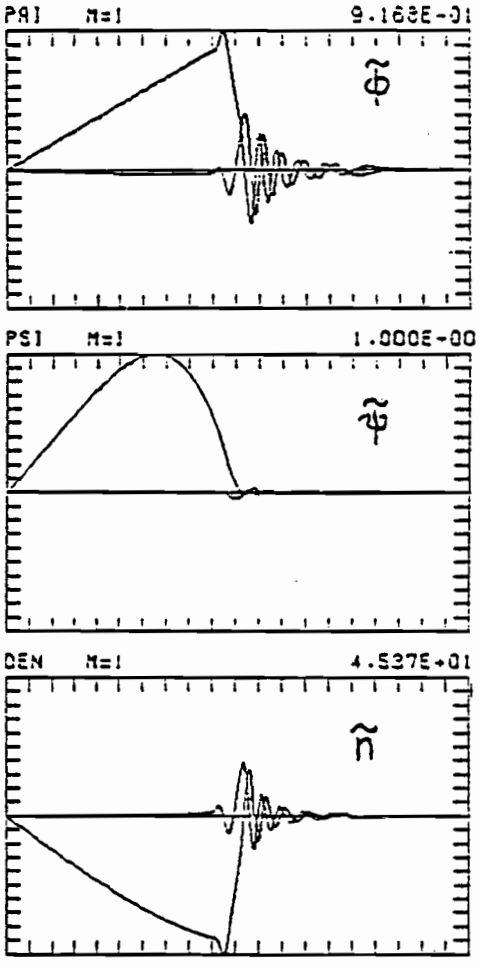

Fig.8 Eigenfunction Ψ, Φ and N for $\omega_*/\gamma_T=5$.

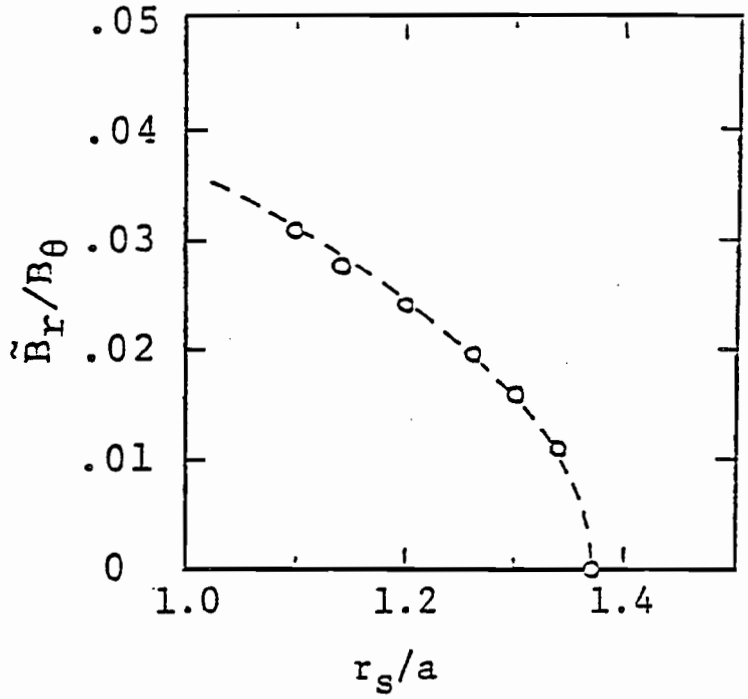

Fig.6 Amplitude of the saturated poloidal magnetic field vs. the position of the rational surface.

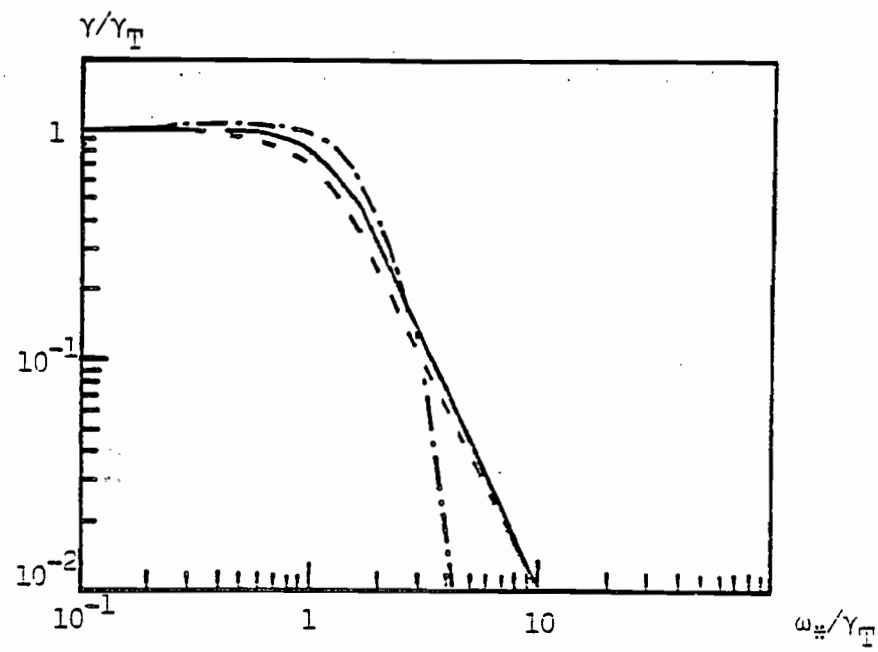

Fig.7 Imaginary part of the eigenfrequency vs. ω_*/γ_T for $\eta_0=10^{-5}$.

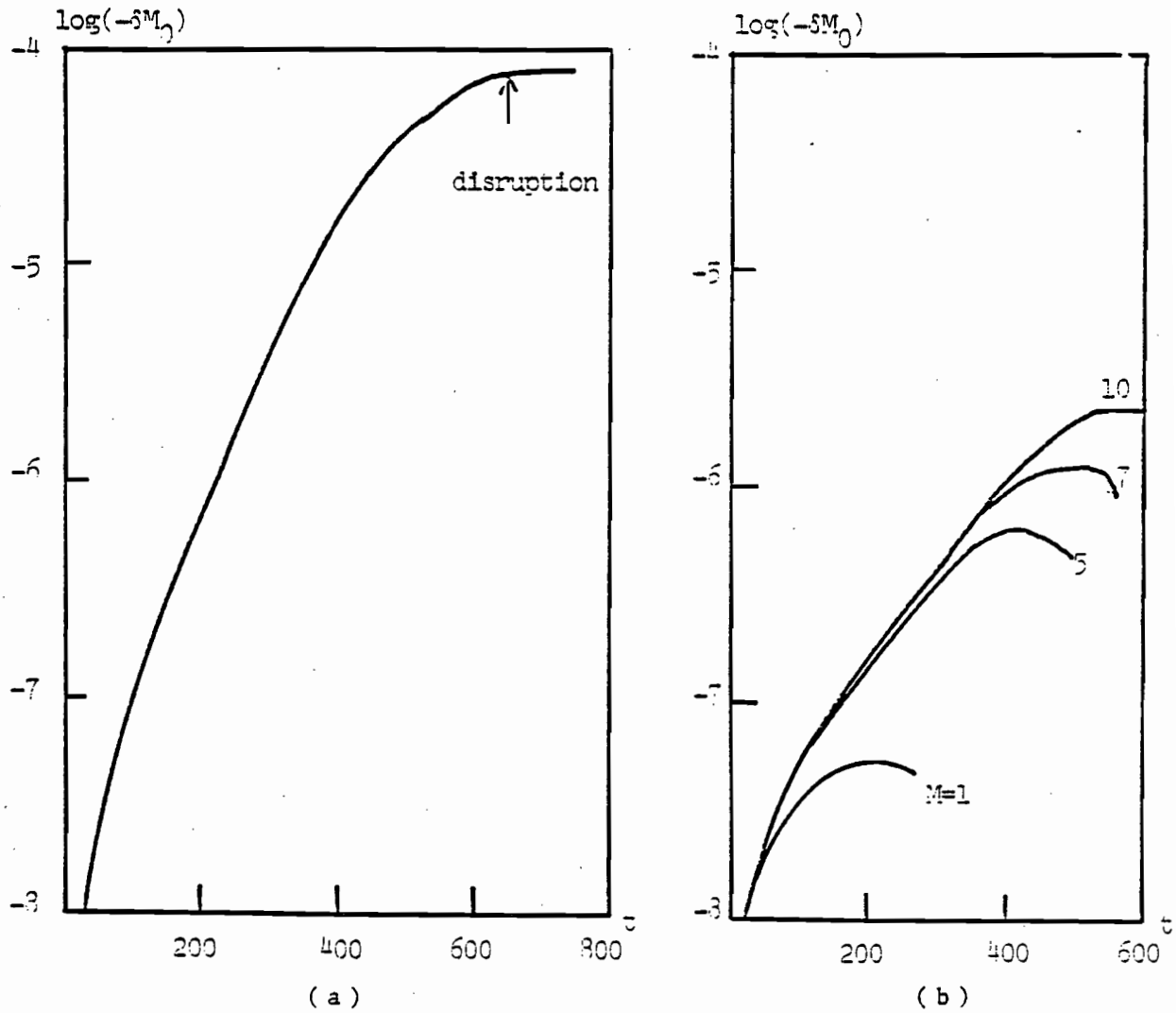

Fig.9 Time evolution of the magnetic energy for (a) $\omega_*/\gamma_T=0$ and $M=5$, and (b) $\omega_*/\gamma_T=3$, $M=1$, 5, 7 and 10.

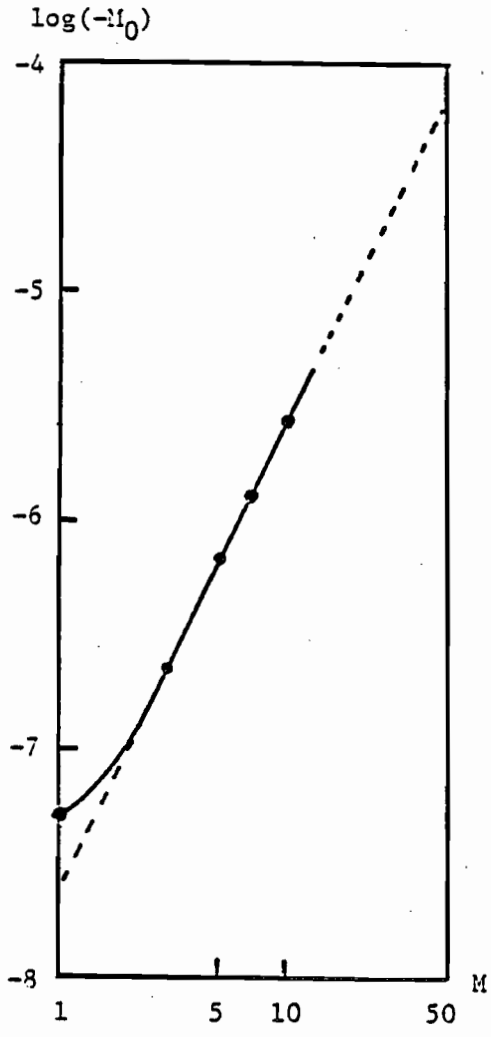

Fig.10

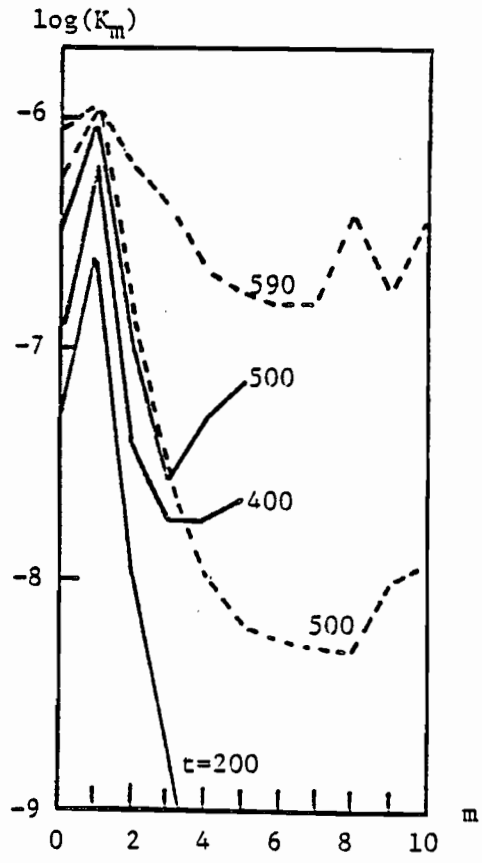

Fig.11

Fig.10 Maximum value of $-\delta M_0$ vs. M for $\omega_*/\gamma_T=3$. This value scales as M^2.

Fig.11 Spectrum of the kinetic energy at differnt t for $M=5$ (solid line) and $M=10$ (dashed line). The diamagnetic frequency is chosen such that $\omega_*/\gamma_T=3$.

By acceptance of this article, the publisher or recipient acknowledges the U.S. Government's right to retain a nonexclusive, royalty-free license in and to any copyright covering the article.

CALCULATIONS IN TOROIDAL GEOMETRY WITH FULL M.H.D. EQUATIONS*

L. A. Charlton, B. A. Carreras,** J. A. Holmes,
H. R. Hicks, and V. E. Lynch

Computer Sciences at
Oak Ridge National Laboratory
Oak Ridge, Tennessee 37831 USA

1. INTRODUCTION

A fully toroidal formalism has been developed which follows very closely that of Ref. 1. This approach uses the full MHD equations with no ordering assumptions. The fluid is, however, assumed to be incompressible. It can be used to study either ideal or resistive modes.

This formalism has been used to construct the computer code FAR, which is linear and fully-implicit. The fully-implicit nature of the numerics allows extremely fast calculations, as will be discussed below. Detailed comparisons for n=1 modes have been made with the computer code RST [2], which uses an ordering formalism due to Strauss [3].

All results presented in this paper are linear. This work, however, is viewed as a first step toward nonlinear calculations. Work, in fact, is well underway to be able to do nonlinear studies.

2. EQUATIONS

A flux coordinate system (ρ,θ,ζ) is used where ρ is a flux-surface label, θ is a poloidal angle-like variable and ζ is the toroidal angle. The angle θ is determined from the straight magnetic field line condition.

We start with the usual MHD equations,

---

*Research sponsored by the Office of Fusion Energy, U.S. Department of Energy under contract DE-AC05-84OR21400 with Martin Marietta Energy Systems, Inc.

**Fusion Energy Division.

$$\frac{\partial \mathbf{B}}{\partial t} = -\nabla \times \mathbf{E} \ , \tag{1}$$

$$\mathbf{E} + \mathbf{v} \times \mathbf{B} = \eta \mathbf{J} \ , \tag{2}$$

$$\rho_m \left[\frac{\partial \mathbf{v}}{\partial t} + \mathbf{v} \cdot \nabla \mathbf{v}\right] = -\nabla p + \mathbf{J} \times \mathbf{B} \ , \tag{3}$$

$$\mathbf{J} = \nabla \times \mathbf{B} \ , \tag{4}$$

$$\nabla \cdot \mathbf{B} = 0 \ , \tag{5}$$

and

$$\frac{\partial \rho_m}{\partial t} + \mathbf{v} \cdot \nabla \rho_m = 0 \ . \tag{6}$$

The fluid is assumed to be incompressible and the density constant in time. This implies

$$\nabla \cdot (\rho_m \mathbf{v}) = 0 \tag{7}$$

Therefore, it is useful to assume for the equilibrium mass density the following form

$$\rho_m = \rho_{m0} \left(\frac{R_0}{R}\right)^2 \ . \tag{8}$$

Eqs. (1) to (5) can be written in terms of potential functions to guarantee an exact solution of Eq. (5). To do so, the usual vector potential, defined by

$$\underset{\sim}{B} = \underset{\sim}{\nabla} \times \underset{\sim}{A} \, , \tag{9}$$

is used with the gauge defined by $A_\rho = 0$. This choice of gauge allows the remaining two components of the vector potential to be identified with the poloidal and toroidal magnetic fluxes.

The time-dependence of $\underset{\sim}{A}$ is given by

$$\frac{\partial \underset{\sim}{A}}{\partial t} = \underset{\sim}{v} \times \underset{\sim}{B} - \eta \underset{\sim}{J} + \underset{\sim}{\nabla}\alpha \tag{10}$$

with α the electrostatic potential. The above, together with some rather lengthy algebra, gives six equations for the six unknowns to be time advanced. These equations are

$$\frac{\partial \psi}{\partial t} = - \frac{\partial \alpha}{\partial \zeta} - v^\rho B^\theta + v^\theta B^\rho + \eta j_\zeta \, , \tag{11}$$

$$\frac{\partial \chi}{\partial t} = - \frac{1}{\rho}\frac{\partial \alpha}{\partial \theta} - v^\zeta B^\rho + v^\rho B^\zeta + \eta j_\theta \, , \tag{12}$$

$$\frac{\partial \alpha}{\partial \rho} = - v^\theta B^\zeta + v^\zeta B^\theta + \eta j_\rho \, , \tag{13}$$

$$\begin{aligned} \frac{\partial U^\theta}{\partial t} = S^2 \Bigg\{ & \frac{\partial}{\partial \zeta}\left(v^\theta U^\zeta - v^\zeta U^\theta\right) + \frac{\partial}{\partial \rho}\left(v^\theta U^\rho - v^\rho U^\theta\right) \\ & - \frac{\beta_0}{2\epsilon^2}\left(\frac{\partial R^2}{\partial \zeta}\frac{\partial p}{\partial \rho} - \frac{\partial R^2}{\partial \rho}\frac{\partial p}{\partial \zeta}\right) \\ & + \frac{\partial}{\partial \zeta}\left(j^\theta B^\zeta - j^\zeta B^\theta\right) + \frac{\partial}{\partial \rho}\left(j^\theta B^\rho - j^\rho B^\theta\right) \Bigg\} \end{aligned} \tag{14}$$

$$\frac{\partial U^\zeta}{\partial t} = S^2 \left\{ \frac{1}{\rho}\frac{\partial}{\partial \rho}\left(\rho(v^\zeta U^\rho - v^\rho U^\zeta)\right) + \frac{1}{\rho}\frac{\partial}{\partial \theta}\left(v^\zeta U^\theta - v^\theta U^\zeta\right)\right.$$

$$- \frac{\beta_0}{2\epsilon^2}\left(\frac{\partial R^2}{\partial \rho}\frac{1}{\rho}\frac{\partial p}{\partial \theta} - \frac{1}{\rho}\frac{\partial R^2}{\partial \theta}\frac{\partial p}{\partial \rho}\right)$$

$$\left. + \frac{1}{\rho}\frac{\partial}{\partial \rho}\left(\rho(j^\zeta B^\rho - j^\rho B^\zeta)\right) + \frac{1}{\rho}\frac{\partial}{\partial \theta}\left(j^\zeta B^\theta - j^\theta B^\zeta\right)\right\} \tag{15}$$

and

$$\frac{\partial p}{\partial t} = - v^\rho \frac{\partial p}{\partial \rho} - v^\theta \frac{1}{\rho}\frac{\partial p}{\partial \theta} - v^\zeta \frac{\partial p}{\partial \zeta} . \tag{16}$$

The six unknowns are the poloidal flux ψ, the toroidal flux χ, the poloidal velocity stream function ϕ, the toroidal velocity stream function Λ, the electrostatic potential α, and the pressure p. In terms of these quantities, the magnetic field, velocity and vorticity are given by

$$\underset{\sim}{B} = \nabla\theta \times \nabla\chi + \nabla\zeta \times \nabla\psi \tag{17}$$

$$\underset{\sim}{V} = \frac{R^2}{R_0}\left\{\underset{\sim}{\nabla}\theta \times \underset{\sim}{\nabla}\Lambda + \underset{\sim}{\nabla}\zeta \times \underset{\sim}{\nabla}\phi\right\} . \tag{18}$$

$$\underset{\sim}{U} = \underset{\sim}{\nabla} \times \underset{\sim}{v} \tag{19}$$

A perfectly conducting wall at the plasma boundary (ρ=a) is assumed which requires

$$B^\rho\big|_{\rho=a} = V^\rho\big|_{\rho=a} = 0 . \tag{20}$$

Both equilibrium and dynamic quantities are expanded in Fourier modes as in Ref. 4.

3. NUMERICAL SCHEME

Accurate results must be convergent in the number of grid points used in ρ and in the number of Fourier modes used in the expansion of both the dynamic and equilibrium quantities. In Fig. 1, the n=1 growth rate as a function of the number of radial grid points is shown and represents typical behavior. For large λ ($\sim 0.1\ \tau_{HP}^{-1}$) results are converged with ~100 grid points. For smaller λ, ($\sim 0.01\ \tau_{HP}^{-1}$), however, a convergence study is needed to extrapolate to an infinite number of points. In Fig. 2, the convergence behavior when varying the number of equilibrium modes is shown. The number needed (for errors $\leq 1\%$) varies from a few at small β to 5-10 for larger β. For the results presented later (which are n=1), dynamic modes from m=-1 to m=4 were used, which gave errors of $\lesssim 1\%$. Since the safety factor varied from 0.9 at the magnetic axis to 2.3 at the edge, this distribution gave modes through the resonant region with two additional, above and below.

In Fig. 3, a comparison with the ideal code ERATO [5] is shown. The agreement is regarded as excellent.

In order to display the results seen when the time step was varied, it is useful to define an eigenvalue and a growth rate. The linearized problem is written as

$$L \frac{\partial x}{\partial t} = Rx \ , \tag{21}$$

and the implicit time step algorithm relates the solution vector at time t to that at t+Δt by

$$\underset{\sim}{x}^{t+\Delta t} = \left(\underset{\sim}{L} - \frac{\Delta t}{2} \underset{\sim}{R}\right)^{-1} \left(\underset{\sim}{L} + \frac{\Delta t}{2} \underset{\sim}{R}\right) \underset{\sim}{x}^{t} \tag{22}$$

In the above, $\underset{\sim}{L}$ and $\underset{\sim}{R}$ denote the matrices formed from the operators L and R. In what follows, t will denote the physical time only when Δt is small. The eigenvalue λ is defined by

$$\lambda = \left\langle \frac{(\underset{\sim}{R}\underset{\sim}{x})_i}{(\underset{\sim}{L}\underset{\sim}{x})_i} \right\rangle \Bigg|_{\text{large } t} \tag{23}$$

where "large t" means that λ is independent of t and $\langle \ldots \rangle$ means an average has been taken.

The growth rate is defined by

$$\gamma = \frac{1}{\Delta t} \ln \left(\frac{|\underset{\sim}{x}^{t+\Delta t}|}{|\underset{\sim}{x}^{t}|} \right). \tag{24}$$

In Fig. 4, γ and λ are shown for a cylindrical case and as a function of step size. The eigenvalue is constant over a large range of Δt, while the growth rate undergoes a resonant behavior with the resonance occurring at $\Delta t = 2/\lambda$. Also shown is the velocity in the poloidal plane (v^{ρ} and v^{θ}). The velocities are identical for values of Δt at each end of the range shown and for a value near the resonance. The behavior for the other unknown quantities is identical. Note that for small Δt, λ and γ are identical. It is thus possible to use a very large step size and obtain a solution given by λ and the eigenfunction. This solution is identical to that found if one uses a small step size to get a solution given by γ and the eigenfunction. The number of time steps required to find an eigenfunction as a function of Δt is shown in Fig. 5. The minimum required is at the resonance given by $\Delta t = 2/\lambda$. Very careful selection of the step size can give a solution in a very few (1 or 2) time steps. In Fig. 6, the eigenvalue is shown over a much wider range of Δt than that shown in Fig. 4. Discrete changes are seen at values of $\Delta t = 2/\sqrt{\lambda_i \lambda_j}$ where λ_i is the value before the change, and λ_j is the value after the change. Also shown is the poloidal

velocity given by the eigenfunction found for each λ. The ρ component of the velocity has no nodes for the largest λ, one node for the second largest, and two for the third largest. This is typical behavior for the most unstable, second-most unstable, and third-most unstable modes. This is, in fact, what is being selected by the choice of Δt. Also shown, for reference, is the resonant values of Δt for each mode.

The numerical behavior shown in Figs. 4, 5, and 6 can be understood by assuming the set of eigenfunctions generated form a complete orthonormal set. Again we write the linear problem as

$$L \frac{\partial x(\underset{\sim}{r},t)}{\partial t} = Rx(\underset{\sim}{r},t) \ . \tag{25}$$

Each member n of the complete set of solutions to the resulting matrix problem satisfies

$$\lambda_n \underset{\sim}{L}\underset{\sim}{x}_n(\underset{\sim}{r}) = \underset{\sim}{R}\underset{\sim}{x}_n(\underset{\sim}{r}) \tag{26}$$

with the stepping algorithm given as before as

$$\underset{\sim}{x}^{t+\Delta t}(\underset{\sim}{r},t) = \left(\underset{\sim}{L} - \frac{\Delta t}{2}\underset{\sim}{R}\right)^{-1} \left(\underset{\sim}{L} + \frac{\Delta t}{2}\underset{\sim}{R}\right)\underset{\sim}{x}^{t}(r,t) . \tag{27}$$

and $\underset{\sim}{x}_n$ and $\underset{\sim}{x}^t$ related by

$$\lim_{t \text{ large}} \underset{\sim}{x}^t(\underset{\sim}{r},t) = \pm \underset{\sim}{x}_n \, e^{\gamma_n t} \ . \tag{28}$$

When Δt is small $\gamma_n = \lambda_n$, of course. The solution vector at each time step may be expanded as

$$\underset{\sim}{x}^t(\underset{\sim}{r},t) = \sum_n a_n^t \underset{\sim}{x}_n(\underset{\sim}{r}) \ . \tag{29}$$

Using Eq. (29) in Eq. (27), using Eq. (26), multiplying by $\underset{\sim}{L}^{-1}$ and projecting a_m by the assumed orthonormality gives

$$a_m^{t+\Delta t} = \frac{\left(1+\frac{\lambda_m \Delta t}{2}\right)}{\left(1-\frac{\lambda_m \Delta t}{2}\right)} a_m^t . \tag{30}$$

Thus, if Δt is properly chosen, the eigenfunction m will be selected due to the denominator in Eq. (30). A resonance will occur at

$$\Delta t = \frac{2}{\lambda_m} \tag{31}$$

as observed in Fig. 4. Using Eqs. (28), (29), and (30), λ_m and γ_m may be related by

$$\pm\, e^{\gamma_m \Delta t} = \frac{\left(1+\frac{\lambda_m \Delta t}{2}\right)}{\left(1-\frac{\lambda_m \Delta t}{2}\right)} \tag{32}$$

The results shown in Fig. 4 satisfy this relation with the plus sign being correct to the left of the resonance and the minus sign to the right.

The value of Δt for the transition from one eigenvalue to another may be found by realizing that the minus sign in Eq. 32 applies to one of the eigenvalues and the plus sign to the other giving

$$\left(1-\frac{\lambda_m \Delta t}{2}\right)\left(1+\frac{\lambda_n \Delta t}{2}\right) = -\left(1-\frac{\lambda_n \Delta t}{2}\right)\left(1+\frac{\lambda_m \Delta t}{2}\right) \tag{33}$$

or, by solving for Δt,

$$\Delta t = \frac{2}{\sqrt{\lambda_n \lambda_m}} . \tag{34}$$

This is the transition Δt shown in Fig. 6. Thus a fairly simple algebraic treatment can reproduce the numerical results shown in Figs. 4, 5 and 6.

4. STABILITY RESULTS

In Fig. 7 stability results are shown for a sequence of flux-conserving equilibria with a safety factor profile ranging from 0.9 to 2.3. In the lower figure, the eigenvalues as a function of β_0 are shown when the full equations of Section 2 are used. In the upper figure, results for the same sequence are shown when the reduced equations of Strauss [3] are used. Both ideal and $S=10^6$ results are shown for the full equations, with only $S=10^6$ results shown for the reduced equations since the reduced equations give ideal stability. The ideal peak for the full equations results from the ideal internal kink mode, which is not in the reduced equations since it is of higher order than that included. The $S=10^6$ results for the full equations are dominated by the ideal internal kink except for the points at the highest and lowest values of β_0. These two points, in fact, are in good agreement, both in eigenvalue and mode structure with the reduced equations and are eigenvalues for a tearing mode (for the lowest β_0) and a resistive ballooning mode (for the highest β_0). Thus, for n=1, the reduced and full equations agree at high and low β_0, but disagree at intermediate β_0 where the ideal internal kink is unstable. As seen in the figure, a second stability region for the internal kink exists.

We would like to acknowledge very useful conversations with M. Azumi.

REFERENCES

1. M. Azumi, et al., "Numerical Study of the Resistive Internal Kink Mode," Proceedings of the U.S.-Japan Workshop on 3-D MHD Simulation, (Nagoya, Japan) IPPJ-632 (1983).
2. J. A. Holmes, B. A. Carreras, H. R. Hicks, V. E. Lynch, and K. E. Rothe, Phys. Fluids 25 (1982) 800.
3. H. R. Strauss, Phys. Fluids 20 (1977) 1354.
4. H. R. Hicks et al., J. Comp. Phys. 44 (1981) 46.
5. R. Gruber et al., Comp. Phys. Comm. 21 (1981) 323.

FIGURE CAPTIONS

Fig. 1. Convergence with number of radial (ρ) grid points (M). The scale is M^{-2}.

Fig. 2. Convergence with number of Fourier modes.

Fig. 3. Comparison with the ideal code ERATO [4].

Fig. 4. Eigenvalue λ and growth rate γ as a function of step size Δt for the most unstable mode.

Fig. 5. Number of time steps to converge (N) as a function of step size Δt.

Fig. 6. Eigenvalue λ as a function of step size Δt.

Fig. 7. Eigenvalue as a function of β_0 for n=1 and for both the reduced and full equations.

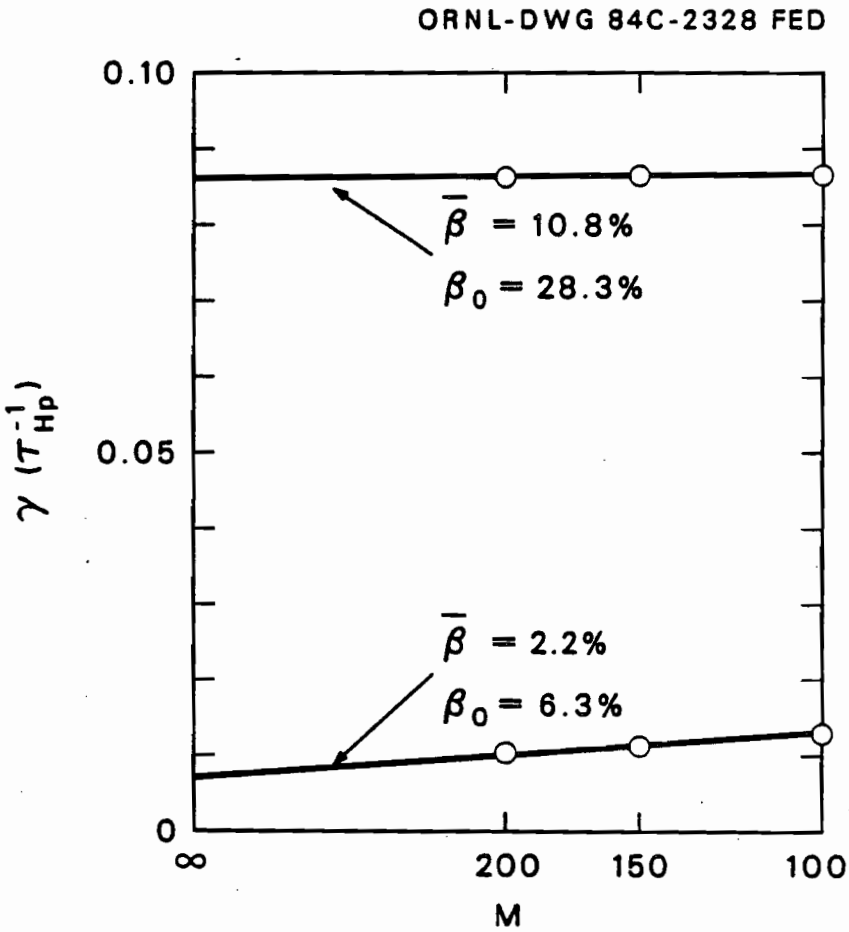
ORNL-DWG 84C-2328 FED
0.10
0.05
0
γ (τ_{Hp}^{-1})
$\bar{\beta}$ = 10.8%
β_0 = 28.3%
$\bar{\beta}$ = 2.2%
β_0 = 6.3%
∞
200
150
100
M

Fig. 1

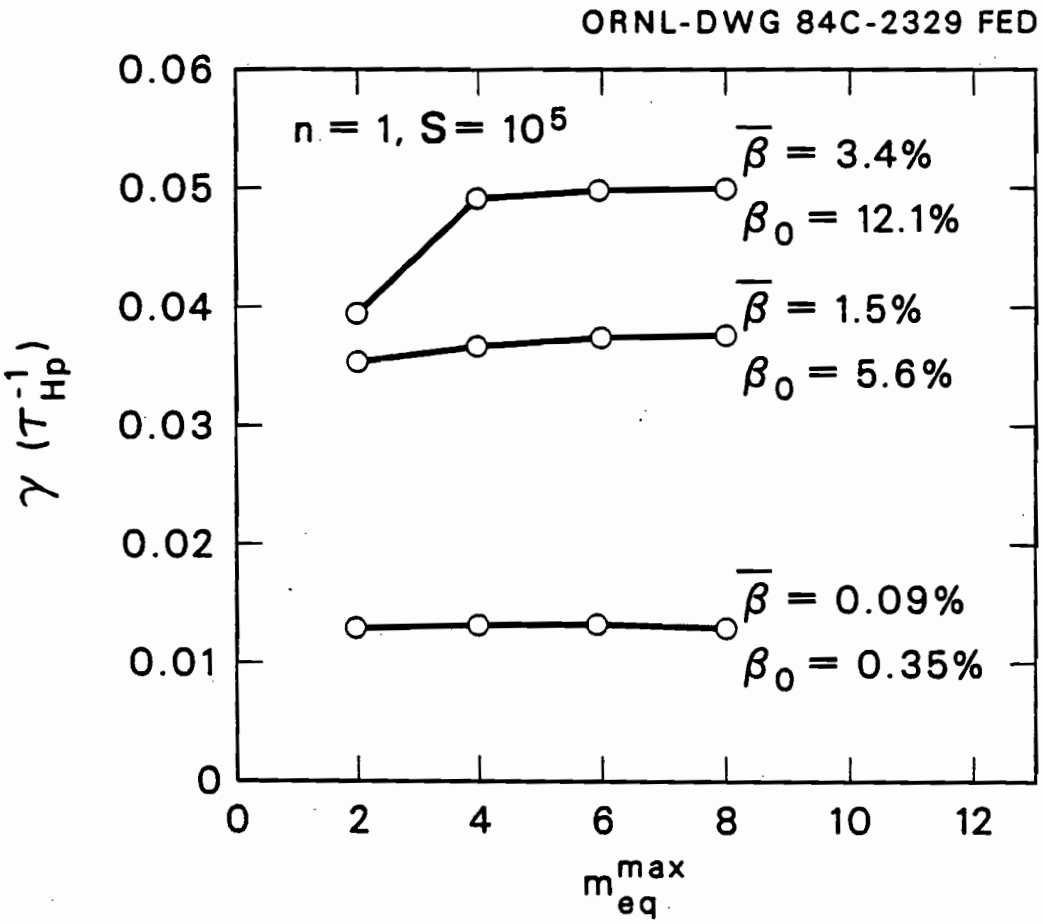
ORNL-DWG 84C-2329 FED
n = 1, S = 10^5
β̄ = 3.4%
β0 = 12.1%
β̄ = 1.5%
β0 = 5.6%
β̄ = 0.09%
β0 = 0.35%
γ (τ_Hp^-1)
0.06
0.05
0.04
0.03
0.02
0.01
0
0
2
4
6
8
10
12
m_eq^max

Fig. 2

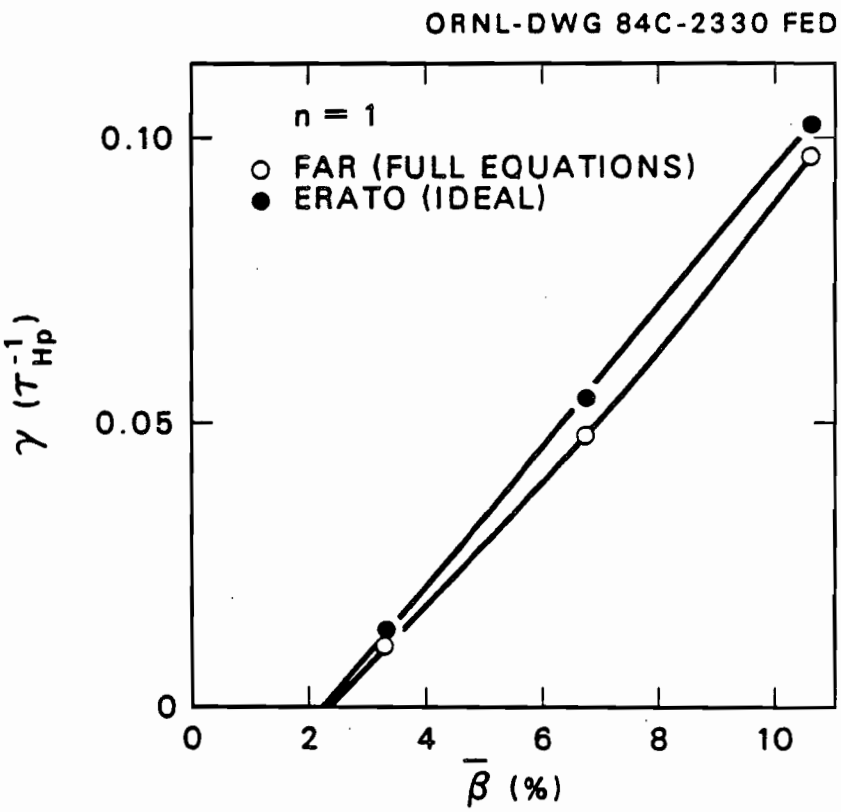
ORNL-DWG 84C-2330 FED
n = 1
FAR (FULL EQUATIONS)
ERATO (IDEAL)
0.10
0.05
0
$\gamma\ (\tau_{Hp}^{-1})$
0
2
4
6
8
10
$\bar{\beta}$ (%)

Fig. 3

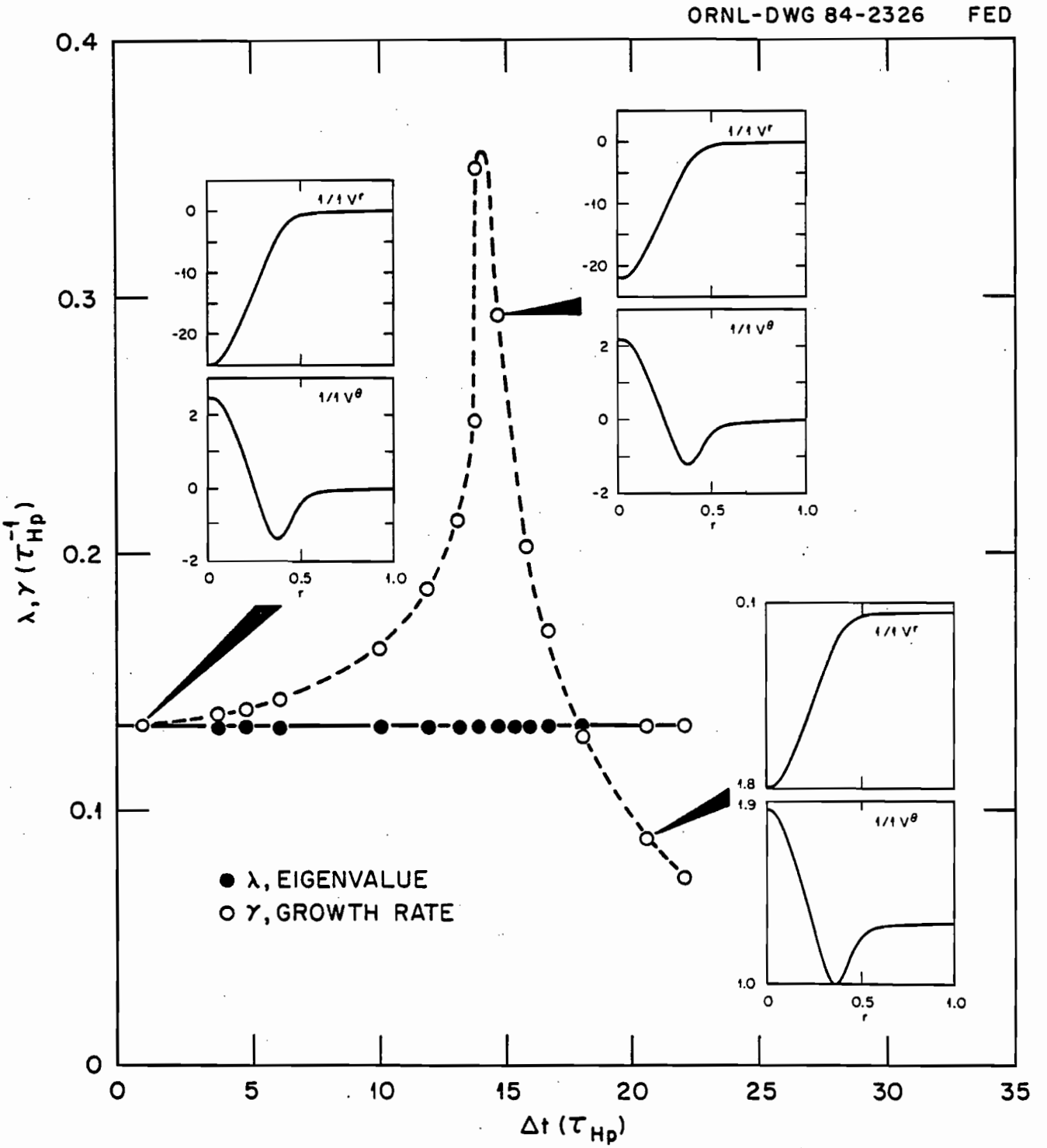
ORNL-DWG 84-2326 FED
0.4
0.3
0.2
0.1
0
λ, γ (τ_Hp^-1)
0
5
10
15
20
25
30
35
Δt (τ_Hp)
● λ, EIGENVALUE
○ γ, GROWTH RATE
1/1 V^r
1/1 V^θ
r
0
0.5
1.0
-10
-20
2
-2
0.1
1.8
1.9
1.0

Fig. 4

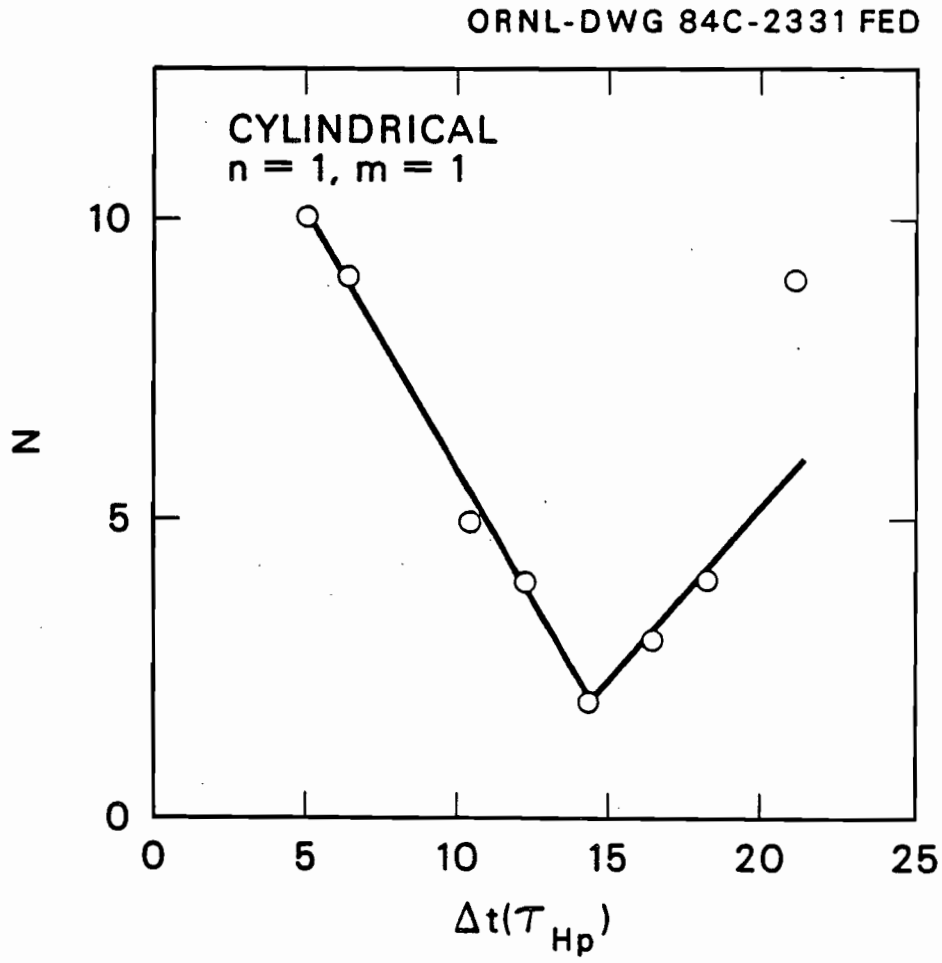
ORNL-DWG 84C-2331 FED
CYLINDRICAL
n = 1, m = 1
N
10
5
0
0
5
10
15
20
25
Δt(τ Hp)

Fig. 5

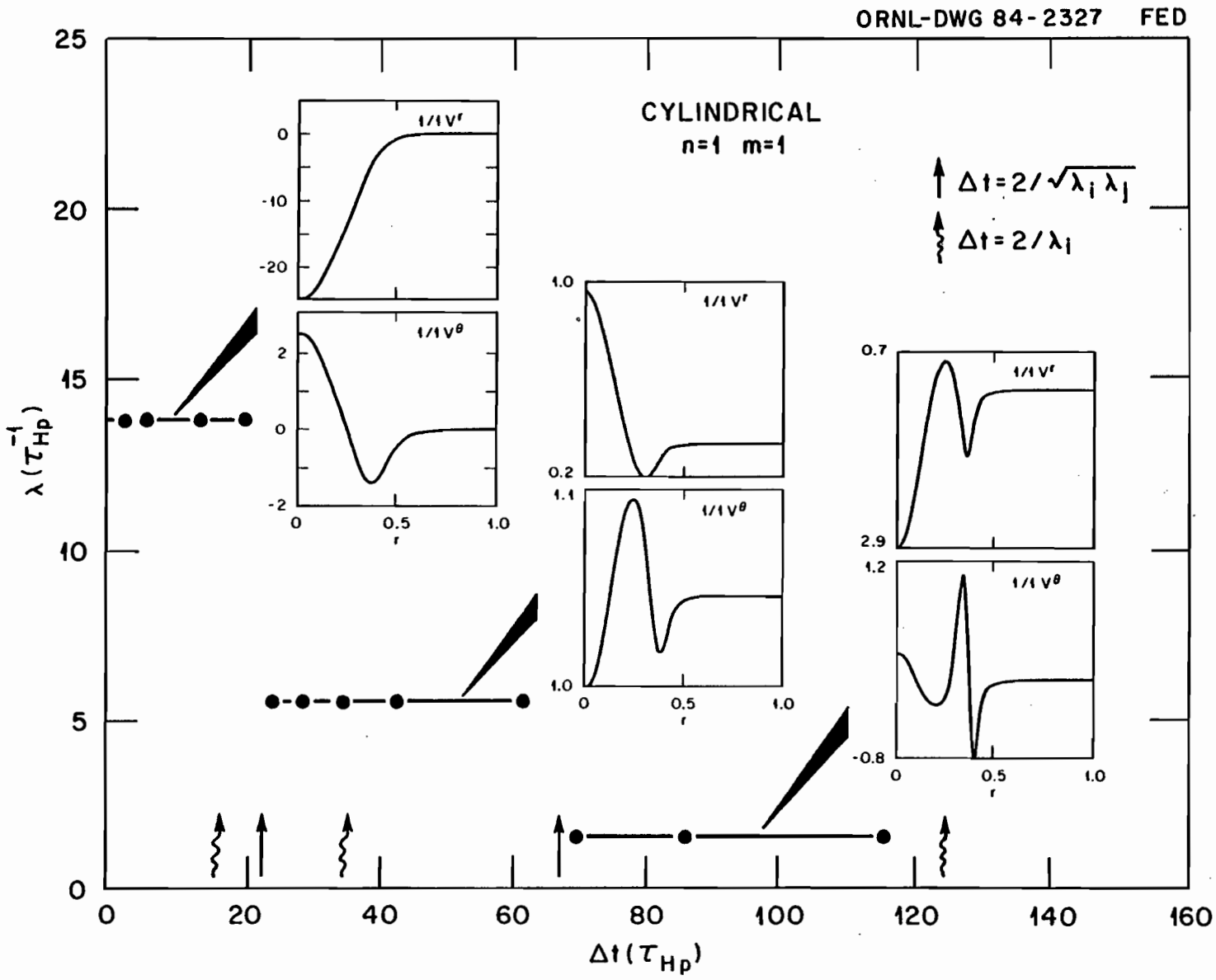
ORNL-DWG 84-2327 FED
CYLINDRICAL
n=1 m=1
$\Delta t = 2/\sqrt{\lambda_i \lambda_j}$
$\Delta t = 2/\lambda_i$
$\lambda(\tau_{Hp}^{-1})$
$\Delta t(\tau_{Hp})$
1/1 V^r
1/1 V^θ
r

Fig. 6

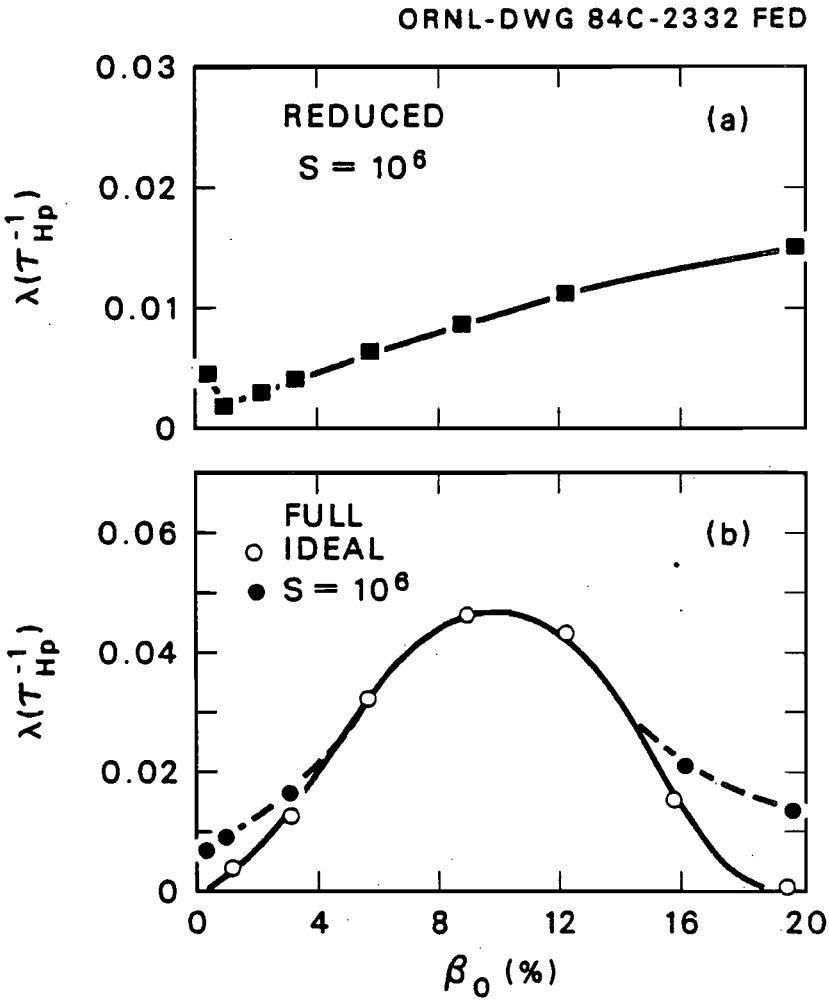
ORNL-DWG 84C-2332 FED
REDUCED
S = 10^6
(a)
0.03
0.02
0.01
0
λ(τ⁻¹Hp)
FULL
IDEAL
S = 10^6
(b)
0.06
0.04
0.02
0
0
4
8
12
16
20
β0 (%)

Fig. 7

LIST OF ATTENDEES

US-JAPAN THEORY WORKSHOP ON 3-D MHD STUDIES

Oak Ridge, Tennessee

March 19-23, 1984

Dr. M. Aizawa
Atomic Energy Research Institute
College of Science and Technology
Nihon University
Chiyoda-ku Kanda Surugadai 1-8
Tokyo, JAPAN

Dr. Daniel C. Barnes
Institute for Fusion Studies
University of Texas
Austin, Texas 78712

Dr. B. A. Carreras
Oak Ridge National Laboratory
P.O. Box Y
Oak Ridge, TN 37831

Dr. L. A. Charlton
Oak Ridge National Laboratory
P.O. Box Y
Oak Ridge, TN 37831

Dr. M. S. Chu
GA Technologies Inc.
P.O. Box 81608
San Diego, California 92138

Dr. R. A. Dory
Oak Ridge National Laboratory
P.O. Box Y
Oak Ridge, TN 37831

Professor K. Hanatani
Plasma Physics Laboratory
Kyoto University
Gokasho, Uji
Kyoto, JAPAN

Dr. T. Hayashi
Institute for Fusion Theory
Hiroshima University
1-1-89 Naka-ku
Hiroshima, JAPAN

Dr. C. L. Hedrick
Oak Ridge National Laboratory
P.O. Box Y
Oak Ridge, TN 37831

Dr. T. C. Hender
Oak Ridge National Laboratory
P.O. Box Y
Oak Ridge, TN 37831

Dr. J. A. Holmes
Oak Ridge National Laboratory
P.O. Box Y
Oak Ridge, TN 37831

Dr. Jae Koo Lee
GA Technologies Inc.
P.O. Box 81608
San Diego, CA 92138

Dr. J. F. Lyon
Oak Ridge National Laboratory
P.O. Box Y
Oak Ridge, TN 37831

Dr. Brendan McNamara
Lawrence Livermore National Laboratory
Box 5511
University of California
Livermore, CA 94550

Dr. A. A. Mirin
Lawrence Livermore National Laboratory
P.O. Box 5509
Livermore, CA 94546

Dr. D. A. Monticello
Princeton Plasma Physics Laboratory
Forrestal Campus
Princeton University
P.O. Box 451
Princeton, NJ 08540

Dr. R. A. Nebel
Los Alamos National Laboratoy
MSF 642
P.O. Box 1663
Los Alamos, NM 87545

Dr. Allan Reiman
Princeton Plasma Physics Laboratory
Princeton University
Princeton, NJ 08544

Dr. Spilios Riyopoulos
University of Texas/IFS
RLM Building
Austin, TX 78712

Dr. Tetsuya Sato
Institute for Fusion Theory
Hiroshima University
1-1-89 Naka-ku
Hiroshima, JAPAN

Dr. Dalton Schnack
Science Applications, Inc.
P.O. Box 2351
LaJolla, CA 92038

Dr. A. G. Sgro
Los Alamos National Laboratory
MSF 642
Los Alamos, NM 87544

Dr. John Sheffield
Oak Ridge National Laboratory
P.O. Box Y
Oak Ridge, TN 37831

Dr. Toshihide Tsunematsu
Japan Atomic Energy Research Institute
Tokai-mura, Naka-gun,
Ibaraki-ken, JAPAN

EXIT

AGENDA

U. S.-JAPAN WORKSHOP ON 3-D MHD STUDIES

March 19-23, 1984

Fusion Energy Design Center, Oak Ridge, Tennessee

Monday, March 19, 1984

9:00 - 9:15	Welcome
	Morning Session Chairman - K. Hanatani
9:15 - 10:00	A. Reiman, "Calculation of Island Widths in Three-Dimensional Equilibria."
10:00 - 10:15	COFFEE BREAK
10:15 - 11:00	K. Hanatani, "A 3-D Algorithm for Calculating Drift Orbits in Nonaxisymmetric Toroidal Devices."
11:00 - 11:45	T. C. Hender, "Equilibrium Studies for Helical Axis Stellarators."
12:00 - 1:30	LUNCH
	Afternoon Session Chairman - A. Reiman
1:30 - 2:15	K. Hanatani, "Analysis of a Pressure-Driven Instability in Heliotron-E."
2:15 - 3:00	J. A. Holmes, "Stellarator Expansion MHD Studies of a High Beta Torsatron."
3:00 - 3:15	COFFEE BREAK
3:15 - 4:00	M. S. Chu, "Reduced Equations in 3-D Geometry."
4:00 - 5:00	Discussion on 3-D MHD calculations for Stellarators, Chairman - B. Carreras

Tuesday, March 20, 1984

	Morning Session Chairman - T. Hayashi
9:15 - 10:00	T. Sato,"Self-Reversal Mechanism in the RFP."
10:00 - 10:15	COFFEE BREAK
10:15 - 11:00	D. D. Schnack, "Three-Dimensional MHD in the Reversed Field Pinch."
11:00 - 11:45	D. C. Barnes, "Compressible Simulations of RFP Self-Reversal."
12:00 - 1:30	LUNCH
	Afternoon Session Chairman - D. Schnack
1:30 - 2:15	T. Hayashi, "3-D Simulation of Spheromak Dynamics."
2:15 - 3:00	A. Mirin, "Nonlinear MHD Simulations of the Spheromak and the Reversed Field Pinch."
3:00 - 3:15	COFFEE BREAK
3:15 - 4:00	M. Aizawa, "Finite Element Method and Its Application to 3-D Dynamic System."
4:00 - 5:00	Discussion on 3-D MHD calculations for RFP and CT, Chairman - T. Sato

Wednesday, March 21, 1984

	Morning Session Chairman - T. Tsunematsu
9:00 - 10:00	B. McNamara, "Rapidly Convergent Algorithm for 3-D Tandem and Stellarator Equilibria in the Paraxial Approximation."
10:00 - 10:15	COFFEE BREAK
10:15 - 11:00	C. L. Hedrick and L. Owen, "Magnetic Equilibria for Square and Circular EBTs."
11:00 - 11:45	D. Monticello, "The Total De-reduction of the Reduced Equations."
12:00 - 1:30	LUNCH

	Afternoon Session Chairman - M. Aizawa
1:30 - 2:15	J. K. Lee,"3-D Simulations of Limiter Stabilization of High Beta External Kink-Tearing Mode."
2:15 - 3:00	T. Tsunematsu, "Nonlinear Evolution of External Kink Mode in Tokamak."
3:00 - 3:45	L. A. Charlton, "Calculations in Toroidal Geometry with Full MHD Equations."
4:00 - 5:00	Discussion on 3-D MHD calculations for tokamak, Chairman - D. Monticello

Thursday - Friday, March 22-23, 1984

Continue discussions at Fusion Energy Division, Bldg. 9201-2